Laser beam welding and additive manufacturing of duplex stainless steel 2205

Vom Promotionsausschuss der

Technischen Universität Hamburg

zur Erlangung des akademischen Grades

Doktor-Ingenieur (Dr.-Ing.)

genehmigte Dissertation (Monographie)

von

Anton Emil Odermatt

aus

Hamburg

2024

1. Gutachter: PD. Dr.-Ing. habil. Nikolai Kashaev
2. Gutachter: Prof Dr.-Ing Ingomar Kelbassa
Tag der mündlichen Prüfung: 22.10.2024

https://orcid.org/0000-0002-5012-8382
https://doi.org/10.15480/882.13582

Danksagung

Zuerst möchte ich meinem Doktorvater, PD Dr.-Ing. habil. Nikolai Kashaev, für seine bedingungslose Unterstützung und seinen weitsichtigen Rat danken. Auch meinem Zweitprüfer, Prof. Dr.-Ing Ingomar Kelbassa, bin ich für die genaue und fachkundige Begutachtung meiner Arbeit außerordentlich dankbar.

Vielen Dank gebührt auch meinen Kollegen am Helmholtz-Zentrum hereon für ihre Freundschaft, Unterstützung und Rat. Sie haben in großem Maße zu meiner persönlichen, sowie beruflichen Entwicklung beigetragen. Rene Dinse und Stefan Riekehr unterstützten und ermöglichten viele der experimentellen Arbeiten in dieser Dissertation. Dr. Volker Ventzke und Falk Dorn halfen mir sowohl mit praktischer Unterstützung als auch bei der Auswertung der Ergebnisse der Mikrostrukturcharakterisierung und der Rasterelektronenmikroskopie. Die Unterstützung von Dr. Nowfal Al-Hamdany, Dr. Guilherme Abreu Faria und Dr. Sebastian Degener war entscheidend bei der Durchführung und Auswertung der Experimente mit hochenergetischer Röntgenstrahlung. Ich möchte auch Lars Herold, Jürgen Knaack und Christian Knothe-Horstmann für ihre technische Unterstützung bei der Weiterentwicklung der Prozessteuerung und Durchführung von mechanischen Prüfversuchen danken. Dr. Jonathan Paul danke ich für die sprachliche Prüfung und den entscheidenden Feinschliff der Arbeit. Auch der ständige Austausch mit meinen Weggefährten zur Promotion, Dr. Sören Keller, Dr. Jan Herrnring, Dr. Frederic Bock, Dr. Irmela Burkhardt, Jannik Brumm, Jonas Lehmann, Ruslan Kulieev, Siva Teja Sala und Nadezhda Likhareva bereitete mir große Freude und half mir in großem Maße die Qualität dieser Arbeit zu verbessern.

Ich danke auch meiner Familie für ihre Unterstützung und Ermutigung. Insbesondere meine Frau Jessica hat immer an mich geglaubt, mich bei meinen Höhenflügen wieder auf den Boden geholt und über die Täler getragen.

Zuletzt möchte ich meinem Vater danken, der mich durch die Förderung meiner Neugier und Wissbegierde auf diesen Weg gebracht hat und den Abschluss leider nicht mehr miterleben konnte. Ich vermisse dich.

Lüneburg, 23.10.2024

Anton Emil Odermatt

Abstract

Duplex stainless steels exhibit a unique combination of high mechanical strength, high ductility and good corrosion resistance making them promising candidates for utilization in many industries where parts are subjected to a combined mechanical and corrosive load. In comparison to the more commonly employed austenitic stainless steels, parts can be designed thinner, resulting in savings in material for the construction and energy during the service life. The ductility as well as the corrosion resistance depend upon their ferrite/ austenite duplex microstructure, which is highly susceptible to heat input during manufacture, making the fusion processing challenging. Manufacturing processes must be optimized to obtain sound material and part properties. Additionally, possible deviations from the optimal condition need to be determined. Thereby, the robustness of the fabrication method – when optimal results cannot be achieved due to process constraints, or the results cannot be controlled adequately – can be assessed.

The present work considers laser beam welding and laser additive manufacturing of duplex stainless steels and their influence on the microstructure, quasi-static and fatigue properties. For laser beam welding with subsequent laser surface remelting, it was demonstrated that fatigue properties can be brought up to the level of the base material. For the case of additive manufacturing with laser and wire, a novel process control method was developed. The influence of process and design parameters on the material properties were investigated. Demonstrator parts were manufactured and the residual stress distribution resulting from process design choices was evaluated.

The laser beam welding process is often performed utilizing the keyhole effect. This process mode is characterized by small fusion and heat affected zones. Evaporation of material from the process may lead to the formation of porosity and poor weld surface quality. The high cooling rates inhibit the formation of austenite from the as δ-ferrite solidifying duplex stainless-steel material. The ferritic fusion zone of laser beam weldments exhibits higher strength and reduced ductility compared to the duplex base material, protecting the joint against deformation in quasi-static loading conditions. Under fatigue loading conditions, the strength is determined firstly by geometric notches, which can be alleviated by a laser surface remelting treatment, bringing the fatigue limit of specimens containing joints up to the level of the base material.

The modified geometric configuration in additive manufacturing leads to a reduced cooling rate and increased heat accumulation during the fabrication of parts. The heat accumulation can be described by limited exponential growth laws, reaching a steady state after multiple layers of the part have been deposited. The heat accumulation and process defined geometry of the part pose a major challenge during additive manufacturing. This was solved by developing a process control method based on the interaction force between wire-tip and melt-pool. The reduced cooling rates lead to a reversal of the situation from laser beam welding. High amounts of austenite are formed in the weld metal. Large variations of the microstructure could be obtained by the utilization of suitable sample geometries, which allow for good heat conduction, as well as control of the interpass

temperature. The heat accumulation led to a nearly entirely austenitic microstructure, while the reheating effect leads to the precipitation of austenite in preceding layers of the samples. Thus, the microstructure is comprised of layers with high strength and low ductility as well as less strong and more ductile layers. This arrangement as well as the texture resulting from epitaxial growth of the δ-ferrite grains along the build direction of the parts leads to strong anisotropy in the quasi-static mechanical properties with the build direction exhibiting up 100 MPa higher yield strength and half the fracture strain. The fatigue properties are governed by defects to which the duplex stainless steel is vulnerable due to its low fatigue crack propagation threshold. Process induced defects include insufficiently remolten parts of the oxide layer and lack of fusion. The formation of defects is governed by the laser intensity distribution during the additive manufacturing process. Defocusing the laser leads to a higher irradiated area and, together with the developed process control method, a reduced feedstock melting rate. This facilitates increased remelting depth into the previous layer and better contact angles. The order of layers has a higher influence on the residual stress distribution than the order of tracks in a layer.

The main findings of this thesis can be summarized as follows: Laser surface remelting can bring the fatigue properties of welded joints up to the level of the base material. This has not been shown to be possible with other post-processing methods. For laser and wire additive manufacturing, a closed-loop control method has been developed that can be implemented in almost any existing manufacturing equipment with minimal investment, ensuring process stability and accounting for differences between preset and actual layer heights. As an important step towards the future industrial application of this technology, in addition to the quasi-static properties, the fatigue properties of laser and wire additive manufactured stainless duplex steels have been investigated and evaluated using a fracture mechanics framework.

Kurzfassung

Nichtrostende Duplex-Edelstähle weisen eine einzigartige Kombination aus hoher mechanischer Festigkeit, hoher Duktilität und guter Korrosionsbeständigkeit auf. Daher sind sie vielversprechenden Kandidaten für den Einsatz in vielen Branchen, in denen Bauteile einer kombinierten mechanischen und korrosiven Belastung ausgesetzt sind. Im Vergleich zu den gebräuchlicheren austenitischen Edelstählen können die Teile dünner ausgelegt werden. Dies führt zu Materialeinsparungen für die Konstruktion und Energie während der Einsatzdauer. Die Duktilität sowie die Korrosionsbeständigkeit hängen von ihrer Ferrit-/ Austenit-Duplex-Mikrostruktur ab, die sehr anfällig gegenüber Wärmeeintrag ist. Dies macht die schweißtechnische Verarbeitung zu einer Herausforderung. Fertigungsprozesse müssen daher optimiert werden, um einwandfreie Material- und Bauteileigenschaften zu erhalten. Darüber hinaus muss die mögliche Abweichung vom optimalen Zustand bestimmt werden, damit die Robustheit der Herstellungsmethode beurteilt werden kann, wenn aufgrund von Prozesszwängen keine optimalen Ergebnisse erzielt oder die Ergebnisse nicht angemessen kontrolliert werden können.

Die vorliegende Arbeit betrachtet das Laserstrahlschweißen und die laseradditive Fertigung von Duplex-Edelstählen und deren Einfluss auf das Gefüge, die quasistatischen und die Ermüdungseigenschaften. Für das Laserstrahlschweißen wurde eine Kombination mit anschließendem Laseroberflächenumschmelzen demonstriert, mit der die Ermüdungseigenschaften auf das Niveau des Grundwerkstoffs gebracht werden können. Für die additive Fertigung mit Laser und Draht wurde ein neuartiges Verfahren zur Prozesskontrolle entwickelt. Der Einfluss von Prozess- und Designparametern auf die Materialeigenschaften wurde untersucht. Auch wurden Demonstratorbauteile hergestellt und die Eigenspannungsverteilung, die sich aus dem Prozessdesigns ergibt, ermittelt und bewertet.

Das Laserstrahlschweißverfahren wird häufig mit dem Tiefschweißeffekt durchgeführt. Dieser Prozessmodus zeichnet sich durch kleine Schmelz- und Wärmeeinflusszonen aus. Die Verdunstung von Material aus dem Prozess kann zur Bildung von Porosität und schlechter Qualität der Schweißnahtoberfläche führen. Die hohen Abkühlraten hemmten die Bildung von Austenit aus der als δ-Ferrit-erstarrenden Duplexlegierung. Die ferritische Schmelzzone von laserstrahlgeschweißten Bauteilen wies im Vergleich zum Duplex-Grundmaterial eine höhere Festigkeit und reduzierte Duktilität auf und schützte die Verbindung vor Verformung unter quasistatischen Belastungsbedingungen. Unter Ermüdungsbelastung bestimmten geometrische Kerben die Festigkeit., Durch die Laseroberflächenumschmelzbehandlung konnten diese so weit reduziert werden, dass die Ermüdungsfestigkeit von Proben mit Schweißnähten auf das Niveau des Grundmaterials gebracht wurde.

Die modifizierte geometrische Konfiguration in der additiven Fertigung führte zu einer reduzierten Abkühlrate und einem erhöhten Wärmestau während der Fertigung. Die Wärmeanreicherung kann mittels begrenzten exponentiellen Wachstumsgesetzen beschrieben werden und erreicht einen stationären Zustand, nachdem mehrere Schichten des Teils aufgetragen wurden. Der Wärmestau und die prozessdefinierte Geometrie des

Bauteils stellen eine große Herausforderung bei der additiven Fertigung dar. Dies wurde durch die Entwicklung einer Prozessregelungsmethode gelöst, die auf der Wechselwirkungskraft zwischen Drahtspitze und Schmelzbad basiert. Die reduzierten Abkühlraten führten zu einer Umkehrung der Herausforderungen gegenüber dem Laserstrahlschweißen. Im Schweißgut bildeten sich große Mengen an Austenit. Hohe Variationen der Mikrostruktur wurden durch Kontrolle der Zwischenlagentemperatur und durch die Verwendung geeigneter Probengeometrien, die eine gute Wärmeleitung ermöglichen erzielt. Der Wärmestau kann zu einer fast vollständig austenitischen Mikrostruktur führen, während der Wiedererwärmungseffekt zur Bildung von Austenit in den vorhergehenden Schichten der Proben führt. Das Gefüge besteht somit aus Schichten mit hoher Festigkeit und geringer Duktilität sowie aus Schichten mit geringerer Festigkeit und höherer Duktilität. Diese Anordnung sowie die Textur, die sich aus dem epitaktischen Wachstum der δ-Ferritkörner entlang der Aufbaurichtung der Bauteile ergab, führten zu einer starken Anisotropie der quasistatischen mechanischen Eigenschaften. Die Aufbaurichtung wies eine um 100 MPa höhere Streckgrenze und die Hälfte der Bruchdehnung auf. Die Ermüdungseigenschaften wurden durch Defekte bestimmt, für die der Duplex-Edelstahl aufgrund seines geringen Widerstandes gegen Ermüdungsrissausbreitung anfällig ist. Zu den prozessbedingten Defekten gehörten unzureichend geschmolzene Teile der Oxidschicht und Anbindungsfehler. Die Entstehung von Defekten wurde durch die Laserintensitätsverteilung während des additiven Fertigungsprozesses bestimmt. Die Defokussierung des Lasers führte zu einer größeren bestrahlten Fläche und gemeinsam mit der entwickelten Prozesssteuerungsmethode zu einer reduzierten Abschmelzrate des Ausgangsmaterials. Dies erhöhte die Einschmelztiefe in die vorherige Schicht und verbesserte den Kontaktwinkel. Die Reihenfolge der Schichten hatte einen höheren Einfluss auf die Eigenspannungsverteilung als die Reihenfolge der Schweißnähte in einer Schicht.

Die wichtigsten Ergebnisse dieser Arbeit lassen sich wie folgt zusammenfassen: Durch das Umschmelzen von Laserschweißnähten können die Ermüdungseigenschaften von Schweißverbindungen auf das Niveau des Grundwerkstoffs gebracht werden. Dies war mit anderen Nachbearbeitungsmethoden bisher nicht möglich. Für die additive Fertigung mittels Laser und Draht wurde ein Prozessregelungsverfahren entwickelt, welches mit minimalen Investitionen in nahezu jede bestehende Fertigungsanlage integriert werden kann. Das Verfahren gewährleistet die Prozessstabilität und kann effektiv Unterschiede zwischen voreingestellter und tatsächlicher Schichthöhe ausgleichen. Als wichtiger Schritt in Richtung der zukünftigen industriellen Anwendung dieser Technologie wurden neben den quasistatischen Eigenschaften auch die Ermüdungseigenschaften von mittels Laser und Draht additiv gefertigten rostfreien Duplexstählen untersucht und mit bruchmechanischen Methoden bewertet.

List of Symbols

a	half crack length
a_{wire}	deflection of the wire guide
$\sqrt{area}$	area parameter for the crack size
$\|b\|$	Burgers vector
d	distance (lattice spacing, characteristic size)
d_0	initial distance (stress free lattice spacing, specimen size)
ΔK	stress intensity factor range
$\Delta K_{th,eff}$	intrinsic threshold stress intensity factor range
$\Delta K_{th,LC}$	long crack threshold stress intensity factor range
$\Delta\sigma$	stress range
Δx	lateral offset
E	Young's modulus
ϵ_m	assumed measurement emissivity
ϵ_{act}	actual emissivity
ε_f	fracture strain/ elongation at break
η	dynamic viscosity
f	ferrite fraction
$F_{process}$	interaction force between wire tip and substrate
F_{guide}	force on the wire guide
g	grain size
h	cooling rate
h_i	prescribed initial height offset
h_o	prescribed height offset
h_{ss}	prescribed steady state height offset
I_{mot}	motor current
k_h	exponential growth constant (layer height)
k_m	torque constant
k_n	speed constant
k_P	exponential growth constant (power)
l	half-length of the wire guide
l_t	half-length of the tool center point path in one layer
λ	wavelength
K_P	proportional constant
k_t	exponential growth constant (time)
M	Taylor factor
$\vec{M}$	motor torque
n	revolutions per time
N	number of cycles
p	phase boundary density
P_{el}	electrical power
P_i	initial power of the laser

P_J	resistive losses
P_{laser}	power of the laser
P_{mech}	mechanical power
P_{ss}	power of the laser in the steady-state
ϕ	specimen facing direction
ψ	specimen tilt angle
R	Resistance
R_a	Surface roughness (average of height deviations from mean line)
Re	Reynold's number
R_f	load ratio
R_{mf}	low cycle fatigue strength
$R_{p0,2}$	0.2% offset yield strength
R_t	surface roughness (maximum peak to valley height)
ρ	density
σ_{max}	maximum stress
σ_{uts}	ultimate tensile strength
t	time
$t_{12/8}$	time for cooling from 1200°C to 800°C
T_{corr}	corrected temperature value
T_{ip}	interpass temperature
$T_{ip,ss}$	interpass temperature in the steady state
$T_{ip,start}$	interpass temperature at the start of the deposition process
T_m	measured temperature value
θ	diffraction angle
U_{mot}	motor voltage
v	velocity
v_{TCP}	tool center point velocity
v_{wire}	wire feed rate
Y	geometry factor

List of Abbreviations

bcc	body-centered cubic
CPT	critical pitting temperature
DSS	duplex stainless steel
EDX	energy-dispersive X-ray spectroscopy
EBSD	electron backscatter diffraction
fcc	face centered cubic
FEM	finite element method
HCF	high cycle fatigue
hcp	hexagonally closest packed
LBW	laser beam welding
LCF	low cycle fatigue
L-DED-wire	laser directed energy deposition with wire
LDF	laser defocus
LoF	lack of fusion
ND	normal direction
PID	proportional-integral-derivative
PTA	plasma transferred arc
PREN	pitting resistance equivalent number
RD	rolling direction
RoI	Region of Interest
TD	transverse direction
WAAM	Wire arc additive manufacturing

Table of Contents

1 Introduction

1.1 Motivation

According to estimates of the World Corrosion Organization the annual costs of damage caused by corrosion amount to approx. 3% of the gross domestic product in industrialized nations [1]. For sustainability and economic reasons, such damage needs to either be avoided or at least mitigated. Consequently, in case the of damage, a timely replacement of parts is essential to mitigate costly downtime of machinery. At the same time there is an ever-growing pressure to reduce industrial manufacturing and operating costs in industry, necessitating the introduction of more efficient materials and manufacturing processes. The properties of materials, structures and their manufacturing processes are irrevocably interlinked. Therefore, the relevant material properties, which are the result of new and innovative manufacturing technologies, need to be characterized.

There is great industrial interest in the laser processing of duplex stainless steels (DSSs) for the chemical, pharmaceutical, food-processing and biotechnology industries. DSS alloys exhibit a combination of high resistance against general, pitting, crevice and stress corrosion cracking. In general DSSs are more resistant against chloride induced stress corrosion cracking and exhibit superior technically useable strength than other stainless steels [2]. Especially in comparison to austenitic stainless DSSs possess a higher yield and ultimate tensile strength. Therefore, parts can be designed thinner, which results in savings in weight and energy [2–4].

The reduced lead-time is the main advantage of additive manufacturing from an economic viewpoint. By using new production technology, the dependence on raw material suppliers can be reduced. This is especially relevant for the above-mentioned industries, where plant downtime due to component failure can cost between 300,000 € and 1,000,000 € per day[1]. In addition, material utilization can be increased by using additive manufacturing processes compared to conventional machining. While the weldability of duplex stainless steels is generally considered to be satisfactory, the microstructural properties – and therefore the corrosion and mechanical properties – are very sensitive to processing conditions like heat input, cooling rate and shielding gas composition among others. The same is true for the fatigue properties, where even small defects from the manufacturing process can lead to a large reduction in useable strength [6–9]. For duplex stainless steels the resulting austenite/ ferrite ratio and the formation of the intermetallic σ and χ-phases are of special interest. The sensitivity of the alloy to the processing conditions in the scope of additive manufacturing poses an interesting scientific challenge [10,11].

Because of their properties, DSSs are used for building pipes, pumps, ventilators, centrifuges, pressure vessels, valves and tanks in the above mentioned industries as well as in seawater environments [3,12]. DSSs find application in other industries as well, for example in architecture, biofuel manufacturing and waste water treatment plants [4]. Duplex stainless

[1] This example applies to a propylene production plant. The numbers vary due to plant size and market prize [5].

steels are frequently employed in machinery, which is subjected to vibratory or fatigue loads like pumps or tubing [13,14]. A typical part, where the utilization of additive manufacturing methods is economically worthwhile, is the production of impeller wheels or other parts used for flow control as shown in Figure 1. For example, in pumps conforming to the ASME B73 standard the pump wheel is regularly made from cast standard duplex stainless steel [15], when the equipment is scheduled to be used for mildly corrosive or abrasive media. This part exhibits distinct geometric features. The most important one is a topology optimized for creating efficient flow of process media. This results in high machining costs using conventional subtractive machining or for mold fabrication. For additive manufacturing the most important features are varying wall thickness and the complex geometry of the blades. These features must be manufactured using different manufacturing strategies, resulting in inhomogeneous processing conditions, most notably variations in cooling rates due to changes in heat conduction. This results in geometry dependent material properties [16].

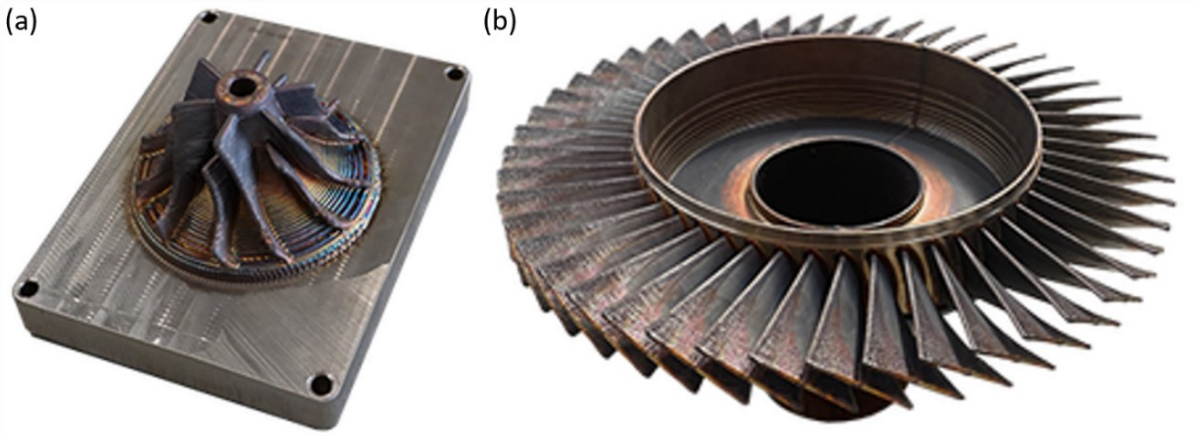

Figure 1: (a) Example of a turbo impeller and (b) blisk made from 316L stainless steel using L-DED-wire (images provided by MELTIO) [17].

In addition to wear and corrosive load such parts are often subjected to vibratory loads, which can lead to fatigue induced failure [14]. The main focus of research into additively manufactured duplex stainless steels has been on the microstructural, quasi-static mechanical and corrosive properties [10,11,16]. This work addresses an essential gap in the knowledge regarding the interaction between process control strategies, microstructure, mechanical properties, fatigue performance, defects and damage tolerance.

1.2 Objectives

The overarching question of the thesis is the influence of the laser beam welding and the laser directed energy deposition process with wire on the microstructure and mechanical properties of duplex stainless steels.

The main challenge of the laser beam welding process is the high cooling rate, which is often significantly higher than the recommendations for fusion welding of the material. This results in either narrow I-shaped joints, with small heat affected zones and high ferrite contents in the weld metal or joints. When appropriate heat inputs for austenite formation are realized, the fusion and heat affected zones resemble those of the arc welded condition. In addition, the laser beam welding process often leads to the formation of gas porosity and geometrical notches due to over- or underfill of the weld metal. The research objective is therefore to evaluate how the geometrical notches and the non-optimal weld microstructure influence the mechanical properties, while still preserving the benefits of laser beam welding and how the mechanical properties of the welded joint can be improved.

The directed energy deposition process with laser and wire poses a different set of challenges. Here the heat accumulation due to many repeated cycles of heat input as well as the changed heat conduction condition lead to slow cooling rates resulting in high austenite contents. Additionally, the process cannot be performed with constant parameters for the fabrication of even low complexity parts. Therefore, suitable process control methods must be developed. It's effectiveness beyond the production of material samples needs to be demonstrated. Consequently, the process parameters must be evaluated for their influence on the microstructure and the mechanical properties. Once the relevant process parameters have been identified, the range of producible microstructures and their influence on the mechanical properties must be characterized. Due to the great flexibility of the directed energy deposition process, the influence of process design choices on the relevant part properties like the residual stress distribution should also be investigated.

The objectives of this work can be regarded as milestones for the maturation of laser directed energy deposition with wire as a viable technology for the fabrication of duplex stainless-steel parts. This ambitious and fundamental work will be the basis for future applications relying on laser processes. This will contribute – especially in the case of additive manufacturing – to a reduction of material utilization and therefore more sustainable manufacturing.

1.3 Structure of the Thesis

To present the results in a consistent way conforming to the global scientific approach, while promoting the reader to follow the reasoning for the choice and order of experiments performed the thesis is organized chronologically with regard to the publications during its creation. The last publication does not consider duplex stainless steel. However it demonstrates the application of the fracture mechanics concept, which was also used in this work, to additively manufactured material.

1) Odermatt, A. E.; Pan, L.; Ventzke, V.; Kashaev, N.: Influence of laser welding defects on the high cycle fatigue behavior of stainless duplex steel 1.4462. In: 4th International Symposium on Fatigue Design and Material Defects. Potsdam (D), 26.05.2020 - 28.05.2020, 2020. [18]
2) A. E. Odermatt, V. Ventzke, F. Dorn, R. Dinsé, P. Merhof, N. Kashaev, Effect of laser beam welding on microstructure, tensile strength and fatigue behaviour of duplex stainless steel 2205, Journal of Manufacturing Processes 72 (2021) 148–158. [19].
3) A. E. Odermatt, N. Kashaev, Evaluation of steady state via thermography during laser and wire based directed energy deposition. In: Lasers in Manufacturing Conference Proceedings 2021, 2021 [20].
4) A. E. Odermatt, F. Dorn, V. Ventzke, N. Kashaev, Coaxial laser directed energy deposition with wire of thin-walled duplex stainless steel parts: Process discontinuities and their impact on the mechanical properties, CIRP J. Manuf. Sci. Technol. 37 (2022) 443–453. [21].
5) European patent application: A. E. Odermatt, Method for operating a wire-based material deposition device and wire-based material deposition device, EP 4 349 600 A1 (2022), Helmholtz-Zentrum Hereon GmbH [22].
6) A.E. Odermatt, L. Vázquez, P. Álvarez, N. Kashaev, On the prediction of fatigue life of WAAM-processed Ti-6Al-4V under consideration of manufacturing defects, International Journal of Structural Integrity 2024 (under review) [23].

Additionally, three master theses were supervised during this thesis. Relevant results from these works are included in this thesis.

7) Sebastian Frederik Roth, Thermomechanical FEM-simulation of the laser-additive manufacturing process with duplex stainless-steel wire. Hamburg University of Technology, 2021 [24]
8) Yasin Balur, Microstructural characterization of additively manufactured duplex stainless-steel structures. Leuphana University Lüneburg, 2021 [25]
9) Aljoscha Repczuk, Development and validation of two manufacturing strategies for the wire-based laser metal deposition of a hydrogen pressure tank with a Cr-Ni duplex stainless steel. Hamburg University of Technology, 2022 [26].

In addition, the already published work is extended by presenting still unpublished results regarding the fatigue properties of the additively manufactured material and residual stress distribution of additively manufactured parts. Comprehensive conclusions regarding the

similarities and differences between the laser processes are presented. In summary, the thesis is organized as follows:

Chapter 2: State of the Art

The literature relevant to factors influencing the properties of duplex stainless steels, laser beam welding, additive manufacturing and process control in additive manufacturing is evaluated in this chapter. The origin of the singular combination of high strength and ductility as well as good corrosion resistance of duplex stainless steels and the influence of fusion processing and especially laser beam welding on these properties are examined. The challenges resulting from the combination of the alloy composition and the laser beam welding process are analyzed. The same analysis is performed for the laser and wire additive manufacturing process. Lastly, process control methods are reviewed. The literature review is leveraged to identify gaps in the scientific knowledge, which this thesis aims to address.

Chapter 3: Methods

In this chapter, the experimental procedures, as well as the theoretical concepts employed in this work are summarized. Firstly, the laser beam welding process is described. The description of the experimental procedures is organized chronologically with regard to the additive manufacturing experiments. While the methodology for the laser beam welding experiments could be defined beforehand, the methodology for the additive manufacturing experiments developed during the work on this thesis. Some results of preliminary studies are briefly described qualitatively so that the reader can follow the decision-making process. First the investigation of the heat accumulation effect and the resulting open loop control strategy is presented. Secondly, the feedback control method addressing the shortfalls of open loop control method is presented. Thirdly, the experiment design using the feedback process control method employed to produce specimens with high microstructural variation and the influence of process design on the residual stress distribution is described. Consequently, the characterization methods including extraction positions for tensile and fatigue specimens are described. The methods chapter concludes with a summary of the fracture mechanics concept used for the assessment of the fatigue tests performed during this work.

Chapter 4: Results and Discussion

This chapter is divided between the laser beam welding section and the additive manufacturing section. The laser beam welding section gives a complete overview over the obtained weld quality, the microstructure of the material and the resulting quasi-static and fatigue properties of the joints. The additive manufacturing section is further subdivided following the approach of the methodology chapter: Firstly, the results of the investigation into heat accumulation are presented. Consequently, the results from the open loop control strategy are analyzed. Following this, the benefits and challenges of the force feedback control method are discussed. Lastly, the results from the application of the open and the closed loop control are demonstrated by the fabrication of samples with large variation in

microstructure and demonstrators, where the influence of process design on the residual stress distribution is analyzed.

Chapter 5: Summary and Outlook

The most prominent results regarding the laser beam welding and laser and wire additive manufacturing of duplex stainless steels are summarized comprehensively. The fullfillment of the research objectives is evaluated. Similarities, differences and limitations between the processes are discussed. Recommendations for further research activities in this field are proposed.

2 State of the Art

2.1 Duplex Stainless Steels

The choice of material always needs to be tailored to the use case and the design of the engineering solution. The material must bear mechanical, thermal, corrosive, or other loads or a combination of them. During design of the structure all these loads must be considered. At the same time a structure or design must be producible. Therefore, the material needs to be machined and/-or welded. Finally, the choice of material needs to be economical. Steel is a group of materials, which can be made to fulfill nearly all but the most severe requirements. Because of their polymorphic microstructure, which depends on the alloying and processing, a wide range of material properties can be achieved. At the same time their cost is in most cases manageable.

Figure 2 shows an overview of different groups of steels with regard to their fracture strain and tensile strength [27]. The left side is taken by conventional steels possessing high fracture strains and low strength. Typical representatives belong to the groups of interstitial free and mild steels. Higher strength steels are comprised of bake hardening steels, heat treatable quenched and tempered steels (CMn) and high-strength, low alloy (HSLA) steels. The third category belongs to the advanced high strength steels and is made up of transformation-induced plasticity steels (TRIP), dual phase (DP) and complex phase (CP) steels. Martensitic steels exhibit even higher strength. Press-hardening (PH) steels are a prominent representative of the ultra-high strength steels. The perfect steel would exhibit both high fracture strain and strength. This would result in superior formability, damage tolerance behavior, and allow for material savings due to high strength, resulting in energy savings during service life. Construction materials exhibit one or the other or an average of both these characteristics.

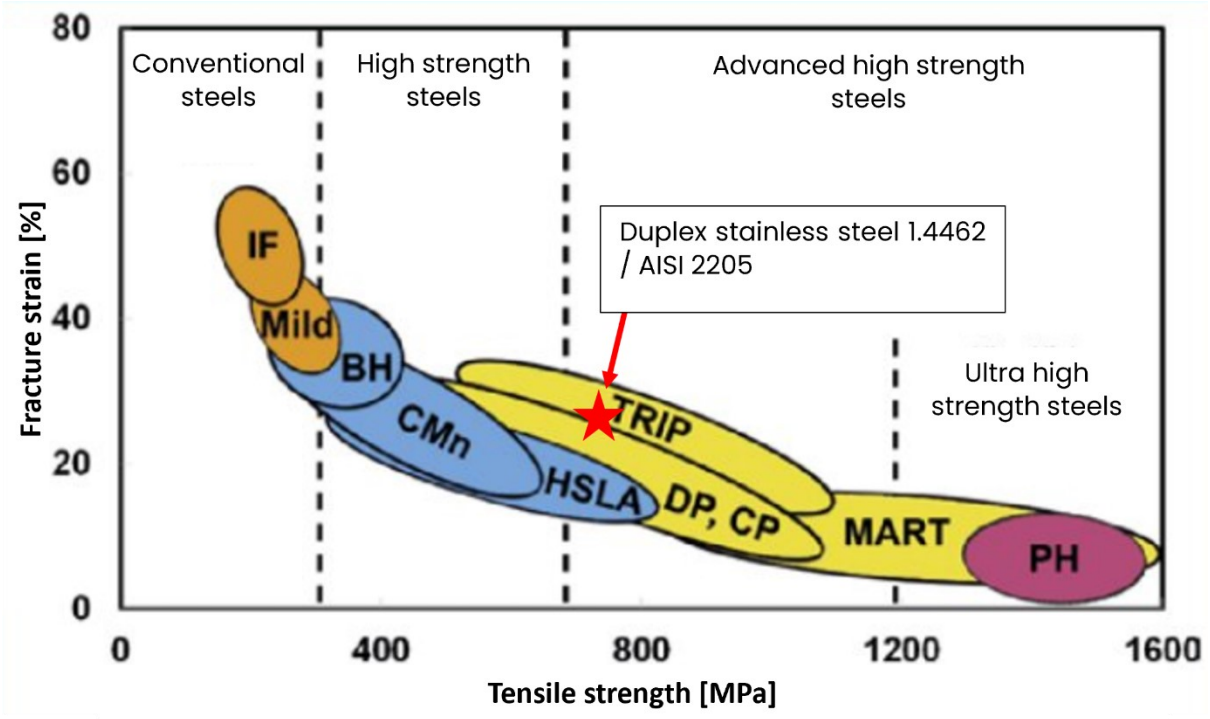

Figure 2: Fracture strain vs. tensile strength for different groups of steels (Depicted and adopted according to [27]).

This is because the mechanisms which increase strength in metallic materials are based on the impediment of dislocation movement, whereas plasticity in metallic materials is based upon the movement of dislocations. A dislocation is a mobile line defect in the metallic lattice. In metallic materials there are several mechanisms influencing the dislocation movement. The most important factor is the crystal lattice of the material. Atoms in metallic materials typically assemble in either face-centered cubic (fcc), body-centered cubic (bcc) or hexagonally closest packed (hcp) structures. The polymorphism of iron-based alloys is based on the ability to organize into fcc, bcc and, with the right alloy composition and heat or mechanical treatment, a tetragonally distorted lattice referred to as martensite. The crystal lattice controls the number of available orientations for easy glide of dislocations and thus the ability to deform under load. Typically, the fcc lattice deforms under lower loads than the bcc lattice due to the closer packing density and the higher number of available glide systems. The tetragonally distorted lattice exhibits close to no plasticity and very high strength. [28]

In addition, there are four main strengthening mechanisms for metallic materials: Forrest hardening, foreign atoms, precipitation hardening and lattice distortion. Forrest hardening occurs due to interaction of dislocation with each other during deformation of the material leading to the pinning and formation of new dislocations and thus increasing strength with increasing deformation (strain or work hardening). Foreign atoms lead to imperfection in the crystal lattice, which locally deform the lattice and consequently increase the resistance against dislocation movement. This is achieved by creating a mixed crystal with elements of different sizes, point defects or interstitial atoms. Precipitations are particles, which are harder than the surrounding matrix or possess crystal lattices and glides systems, which are

incompatible with their surrounding matrix. Thus, a dislocation is prevented from gliding past the precipitation. The last main strengthening mechanism is the amount and constitution of grain boundaries. Often multiple dislocations pile up at grain boundaries before they are forced to cross them. Their strain fields lead to stress hardening of the material. The change in direction of dislocation movement at grain boundaries also increases the impact resistance considerably. [28]

Duplex stainless steels are alloys, which combine the properties of the highly deformable austenitic fcc-lattice and the deformation resistant ferritic bcc-lattice. The typical microstructure of sheet material in the as received condition and after various heat treatment procedures is shown in Figure 3. In the hot rolled condition (Figure 3 (a)) the alloy exhibits approx. equal fractions of ferrite and austenite, which are aligned as a result of the rolling process. Solution heat treatment at 1050°C (Figure 3 (b)) preserves the fraction of the two phases, while resulting in some grain growth. In some cases, heat treatments between the temperature ranges for intermetallic phase formation and 475°C embrittlement (Figure 3 (c)) can be performed for very limited periods of time as a stress relieve treatment. This is generally not recommended, due to the hazard from the formation of detrimental intermetallic phases [2,28]. Prolonged times at temperatures above 1300°C (Figure 3 (d)), where the material is fully ferritic, lead to severe grain coarsening by growth of the ferritic phase.

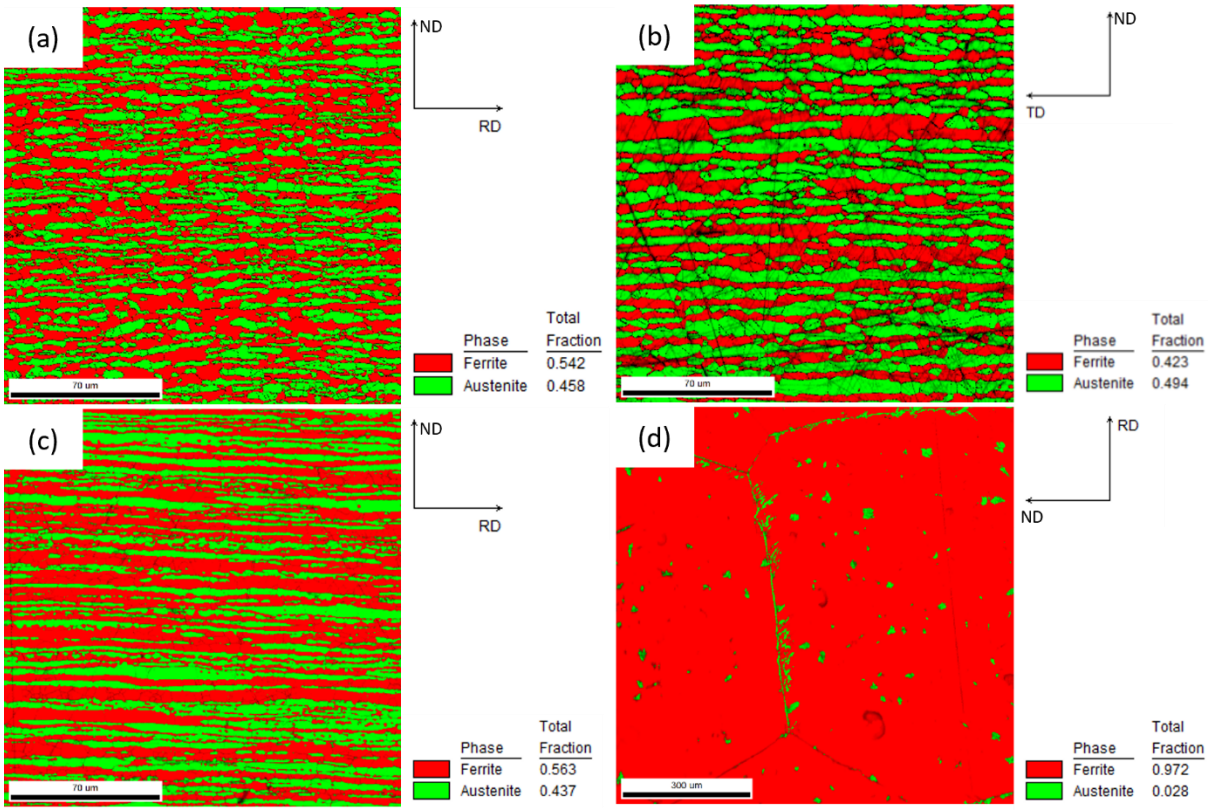

Figure 3: Duplex stainless steel 1.4462 sheet material (d=4 mm) in different heat-treatment conditions: (a) As received, (b) heat treated at 1050°C for 2 h, (c) heat treated at 650°C for 30 min and (d) 1350°C for 2 h. All samples were cooled under forced convection with air. (RD: rolling direction, TD: transverse direction)

The DSS alloy class was introduced in the 1970s. The earliest duplex alloys contained chromium, nickel and molybdenum as alloying elements. Due to the development of the argon-oxygen decarburization process, alloying with nitrogen was performed for the first time in 1968 [2]. The addition of nitrogen stabilizes the austenitic phase, which significantly increases the toughness and corrosion resistance in the as-welded state [2,28]. This is important, because, in order to prevent chromium carbides from forming and to preserve the corrosion resistance, duplex stainless steels cannot be alloyed with carbon to increase the strength [28]. Alloy 2205 (EN 1.4462) is considered the standard DSS alloy. Additionally, there exist lean duplex alloys, which are not alloyed with molybdenum, super duplex alloys, with Pitting Resistance Equivalent (Nitrogen)-(PREN)-values between 40 to 45 and hyper duplex with PREN values greater than 45. The PREN value is an empirical method to estimate the resistance against pitting corrosion for stainless steels. The optimal microstructure is achieved by balanced alloying with the elements chromium, nickel, molybdenum and nitrogen [2] and by heat treating the material at approx. 1050°C and consequently rapidly cooling it to freeze the desired microstructure and prevent the formation of the σ- and χ-phases (Figure 4).

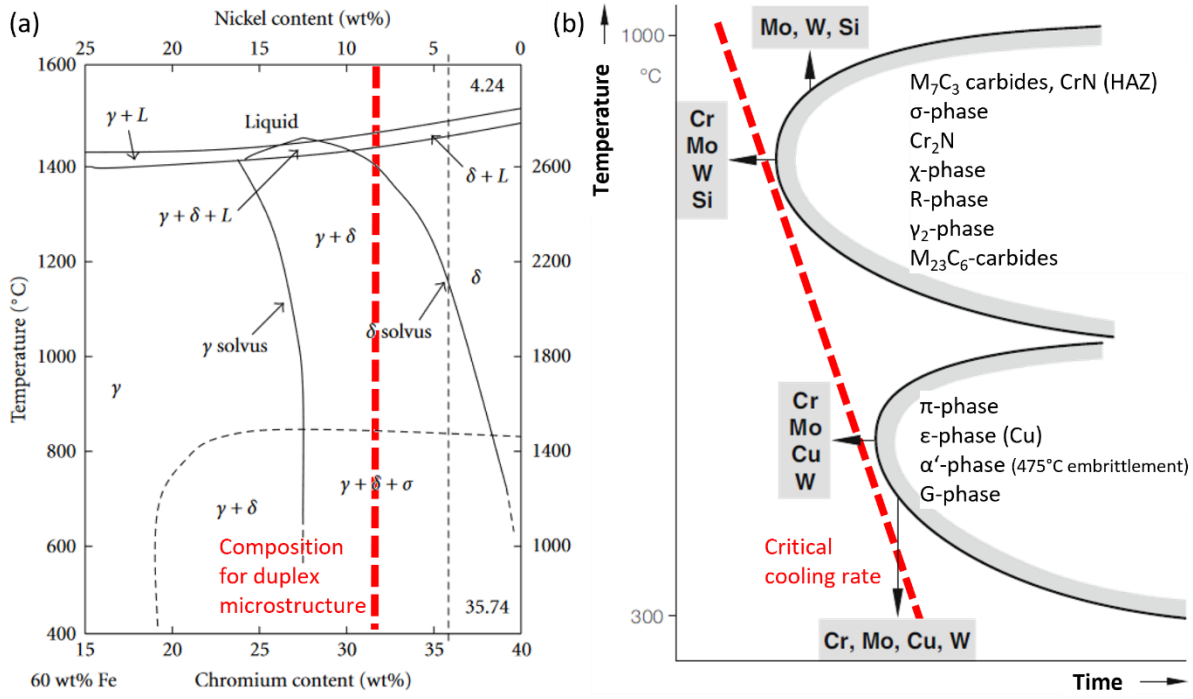

Figure 4: (a) Cut through the ternary Cr-Ni-Fe phase diagram at 60 wt.-% Fe [29] showing the high temperature region, where the duplex microstructure is stable and (b) isothermal transformation diagram for duplex stainless steels showing the temperature ranges, where the σ and χ-phase form and the α'-embrittlement takes place [28].

Chromium stabilizes the ferritic phase and – with a minimum concentration of 10.5 wt.-% – forms a passivating layer, which is the reason for its atmospheric corrosion resistance [28]. The passive layer is comprised of a 1 nm to 20 nm thick chromium oxide layer. Therefore, the corrosion resistance is only stable under oxidizing conditions, where the passive layer is constantly reformed. Under reducing condition such as in sulphuric or hydrochloric acid the

formation of the passive layer is impeded or impossible. Surface corrosion occurs under these conditions [28]. Chromium also improves the corrosion resistance at high temperatures. The corrosion resistance increases with increasing chromium concentration. Increasing the chromium concentration also promotes the tendency for the formation of the undesirable intermetallic σ- and χ-phase. These phases are undesirable, because their presences reduces the ductility of the material and due to their high chromium content (approx. 45 at.-% [28]) – in the same manner as chromium carbides [28] – deprive the surrounding matrix of chromium. They typically form in the temperature range between approx. 700°C to 1000°C. In standard duplex stainless steels the chromium content is usually at least 22 wt.-% [2]. In alloys containing between 10 wt.-% and 85 wt.-% chromium the ferrite matrix decomposes into chromium rich δ'-mixed crystals and chromium depleted δ-mixed crystals at temperatures below 600°C. This phenomenon is called the 475°C embrittlement because it is fastest at this temperature [28]. Due to 475°C embrittlement the operating temperature is limited to 250°C. Heat treatments at around 550°C and 650°C, which are commonly employed for austenitic stainless steels, are generally discouraged. Instead solution heat treatment is performed at around 1050°C. [28]

Molybdenum is also a ferrite stabilizer and increases the resistance against pitting and crevice corrosion. Molybdenum – in the same manner as chromium – promotes the formation of intermetallic phases and is therefore limited to a maximum of 4 wt.-% [2]. The addition of chromium and molybdenum improve the tensile strength, the yield strength and ductility through solid solution strengthening [30]. Nickel and nitrogen stabilize the austenitic phase and impede the formation of intermetallic phases [2,28]. In the case of nickel, it reduces the diffusion rate due to stabilization of the austenitic phase. Nitrogen is not soluble in the σ-phase and carbides. Therefore, these phases are prevented from forming when the matrix is saturated with nitrogen.

The face centred cubic structure of the austenitic phase is the reason for the high toughness of DSS [2]. Nitrogen increases the stacking fault energy and increases the work hardening inclination of the austenitic phase [2] and increases the strength through solid solution hardening [2,30]. Additional alloying elements are manganese – commonly employed as a deoxidizing agent – and silicon, which improves the oxidation resistance [31]. In the presence of oxygen these elements may lead to the formation of spinel, rhodonite and amorphous phases, which are rich in manganese, silicon and oxygen [32]. In summary, the DSS 2205 alloy is characterized by high strength, high toughness and good resistance against pitting, crevice and stress corrosion [2,3].

Compared to other stainless steels (Figure 5) DSSs possess a unique combination of high resistance against corrosion – indicated by the PREN values for the alloys – and high yield strength. They are superior to ferritic stainless steels (when comparing PREN-values) and exhibit competitive mechanical properties with superior corrosion resistance compared to martensitic stainless steels.

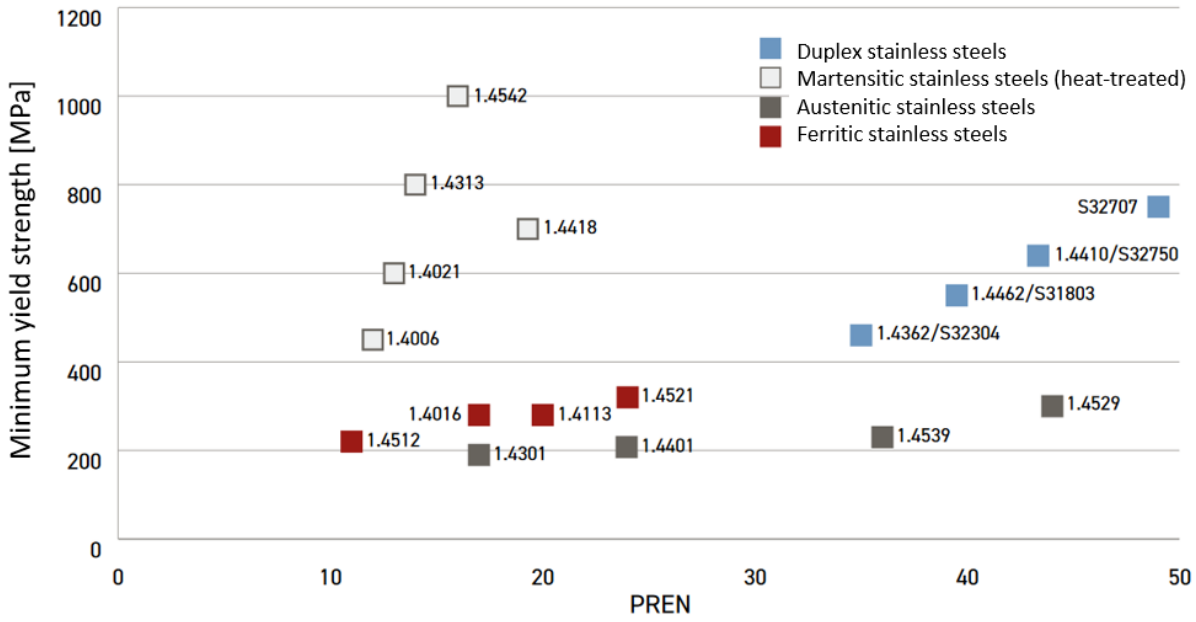

Figure 5: Yield strength and pitting resistance equivalent number for the different classes of stainless steels (depicted and adopted according to [33]).

In comparison to austenitic stainless steels, DSSs possess a higher yield and ultimate tensile strength, so that parts can be designed thinner. This results in savings in weight and energy [2–4]. Additionally, the resistance to tribocorrosion is increased. Due to their superior weight specific strength, DSSs are frequently employed in machinery, which is subjected to vibratory or fatigue loads [13].

The fatigue performance of wrought duplex stainless steels has been investigated extensively. Mateo et al. [34] studied the mechanical properties of DSS 2205 wrought material in sheet and bar form. They found a positive correlation between the fatigue limit and the Taylor factor of the ferritic phase of the material and concluded, that the probability of individual grains to be aligned for easy slip has a significant impact on the high cycle fatigue (HCF) resistance.

In addition to the crystallographic texture, the phase composition also influences the fatigue response. De Lacerda et al [35] annealed DSS 2205 sheets at 1060°C, 1200°C and 1300°C to achieve non-optimal phase compositions and then characterized their mechanical properties. With increasing annealing temperature, the grain size and the ferrite volume fraction increased and the tensile strength and fatigue limit decreased. The decrease in fatigue limit was attributed to a transfer of plastic deformation to the austenitic phase and a reduction of the ferrite-austenite interfaces. The reduction of tensile strength is contrary to the results of Floreen and Hayden [36], who found increased tensile strength for increased ferrite contents. It must be noted, that Floreen and Hayden [36] achieved different phase compositions by altering the chromium and nickel contents of the alloy rather than employing different annealing regimes.

Slow cooling rates lead to the precipitation of undesirable phases like the σ and χ-phases [2,37,38]. A critical parameter for the structural integrity of duplex steels is the 475°C

embrittlement by precipitation of the δ'-Phase. The presence of this phase considerably reduces the ductility, leading to a significant reduction of both fracture strain and fracture toughness [2,28]. The fatigue properties are also influenced. Sahu [39] found an increased fatigue life for increased phase fractions of δ'-phase at low strains and a reduced fatigue life at high strains. The crack initiation mechanism during cyclic loading of DSS base material has been investigated extensively [40–44]. In high cycle fatigue, the origin of fatigue cracks at stress levels below the yield strength and in the absence of defects is localized at dislocation pileups in the softer austenitic phase. Therefore, controlling the amount and size of the austenitic phase is crucial for optimal fatigue properties.

2.2 Laser Beam Welding of DSS

The weldability of DSSs and strength of the resulting weld metal are generally regarded positively [3,12,45–49]. They are less prone to hot-cracking than their austenitic counterparts due to the primarily ferritic solidification and less prone to severe grain coarsening than their ferritic counterparts due to austenite impeding grain growth [28]. The main challenge is a heat management adapted to the metallurgy of the alloys [28,50]. There needs to be at least 30% austenite in the weld metal to ensure sufficient corrosion resistance. Additionally, the formation of intermetallic phases and 475°C embrittlement need to be avoided [45,51].

The ferritic part of the microstructure is prone to several detrimental mechanisms during fusion processing. In the temperature range between 700°C and 900°C σ-phase formation can occur after just a few minutes. Increased chromium contents increase the severity of this problem. Because the solubility of carbon and nitrogen is lower in ferrite than in austenite high amounts of ferrite also promote the formation of nitrides and carbides. Lastly, the ferritic phase has a tendency for excessive grain growth, which lowers the yield strength of the material. [28]

The formation of a sufficient austenite content during welding is promoted by the utilization of feedstock materials containing increased amounts of nickel and nitrogen. Nitrogen reduces the susceptibility for sigma phase formation and increases the temperature for the ferrite to austenite transformation. Nitrogen contents in the weld metal should not be below 0.12 wt.-%. [28]

The resulting microstructure is not readily predicted with conventional methods like the Schaeffler, DeLong or WRC-diagrams. All material experiencing temperatures above 1300°C is fully transformed into ferrite. This leads to a coarse-grained microstructure. Due to the distinct ability to be undercooled, the ferrite is often not fully transformed to austenite. Increased cooling rates result in a shift of the phase fraction after cooling from a 50/50 fraction to a 70/30 fraction or worse. This leads to enhanced embrittlement of the fusion zone. The austenite fraction, which is responsible for the ductility and the corrosion resistance forms primarily between 1200°C and 800°C. Due to this, the $t_{12/8}$ cooling time from 1200°C to 800°C is a representative quantity. This time should be sufficiently long for austenite formation, but short enough, so that the ferrite does not coarsen excessively and metal carbides or other phases are prevented from forming. [2,28]

Due to the complex metallurgy of the DSS alloys, several different aspects need to be considered during fusion processing. In some cases, nitrogen containing shielding gases need to be used to prevent nitrogen loss from the molten metal. According to Schulze, 2009 [28], the cooling time $t_{12/8}$ should be longer than 10 seconds. 15 seconds is often recommended. This is achieved by appropriate heat inputs of 1.2 kJ/mm to 2.5 kJ/mm. The ESAB [50] recommends cooling times – in order to facilitate sufficient austenite formation – between 8 and 10 seconds, which corresponds to line energies between 0.5 kJ/mm and 2.5 kJ/mm for joining procedures. Parts should not be preheated above 150°C and the inter layer temperature should not be higher than 200°C [28] (250°C [50]). Where high cooling

rates or high stresses due to constructive measures are expected austenite enriched filler materials should be used to ensure sufficient deformability. For this reason, I-joints should be avoided. Due to the sensibility of the alloys the tolerance field of the filler alloy composition is reduced compared to other classes of stainless steels. [28]

The only typical metallurgical defects that rarely occur are solidification cracks. Cracking of the heat affected zone is nearly never observed. High concentrations of hydrogen in the weld metal may lead to the formation of cracks and low amounts may already lead to a loss in ductility. Low to temperature annealing to remove hydrogen is generally not economic because of its low diffusion rate in the austenite. [28]

Generally, welded parts are not heat treated. Forged and repaired parts, which are welded, are solution heat treated between 1050°C and 1150°C for 1h and rapidly cooled. Depending on the size of the part this can range from cooling with air under forced convection to water quenching. [2,28] Thereby, the intermetallic phases are dissolved, the 475°C embrittlement is reversed, a homogenization of the chemical composition is achieved and welding residual stresses are reduced. If heat treatment is to be applied the filler material must be of the same composition as the parent alloy. Heat treatment in air leads to the formation of a very dense and resistant oxide layer, which must be removed by either mechanical or chemical methods for optimal corrosion resistance [2,28].

The previous paragraphs described the general metallurgical aspects of fusion processing of duplex stainless steels. High speed laser beam welding is characterized by the keyhole effect (Figure 6 (a)). In comparison to other welding processes, which use an electric arc or plasma torch to melt the material, using a laser beam the energy can be focused on a much smaller area. As a result – once the critical irradiance is surpassed – material starts to vaporize. The loss of material as well as the vapor pressure cause a depression of the molten pool. Inside this depression the laser beam is reflected onto the walls of the depression, resulting in a sudden increase in absorption. A vapor capillary forms, leading to deep penetration of the energy into the material along the axis of the laser beam. As a result, deep and narrow welds can be created using comparatively little energy input using laser beam welding. The resulting welds are almost always I-shaped (Figure 6 (b)). The low energy input leads to very narrow heat affected zone and comparatively low residual stresses. However, laser beam welding poses several distinct challenges. The joint preparation needs to be much more precise, because a smaller volume of material is molten. The smaller fusion zones lead to poorer gap bridging capabilities of the laser beam welding process compared to arc welding processes. Due to the deep and narrow vapor capillary, gas can be trapped inside the material, if the keyhole is unstable. Furthermore, the welding depth plays an important role. The porosity may increase considerably, if the keyhole is open at the bottom of the joint [52]. Maintaining the correct depth and stability of the vapor capillary is crucial. Metal vapor from the process may deflect some of the incoming energy and, especially if the shielding gas coverage is insufficient, burn in the surrounding atmosphere. To prevent this, pressurized air is often used to blow the smoke from the beam path. Feedstock material can be fed into the molten pool, to alter the chemical composition of the welded joint and

to add material to prevent underfill from the evaporation loss. The high velocity of the metal vapor escaping the keyhole as well as the comparatively fast solidification of the material often leads to worse surface quality and increased spatter compared to arc welded joints.

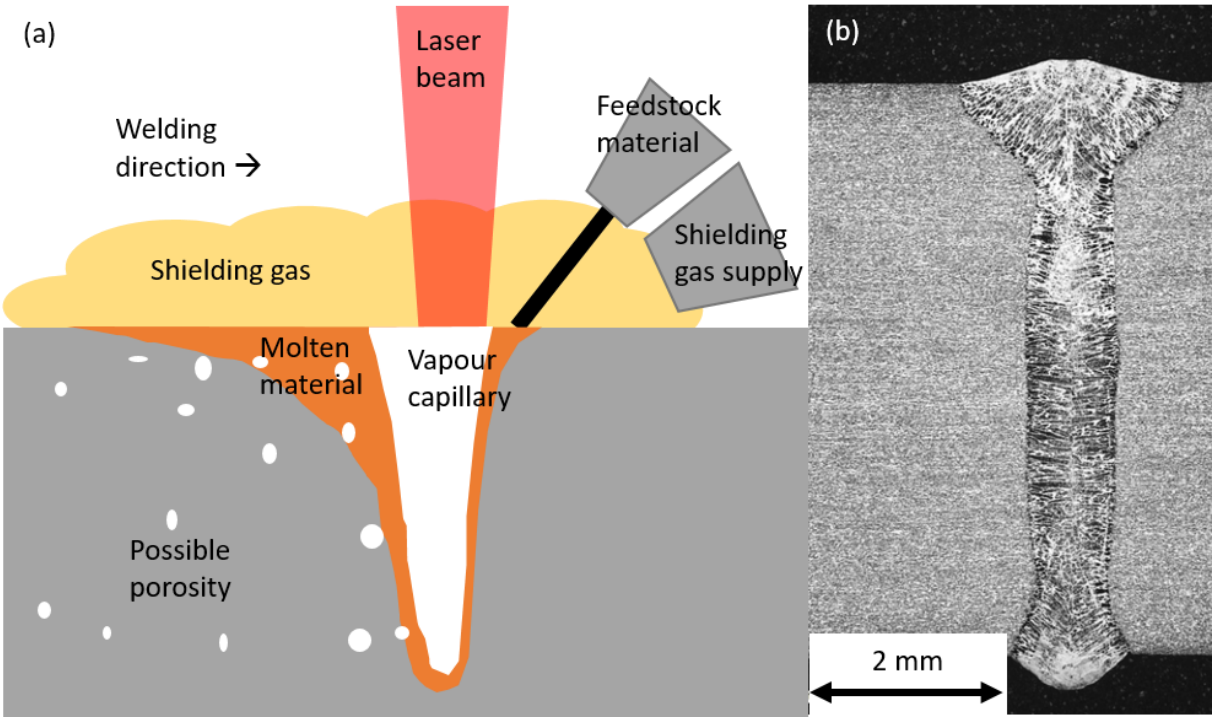

Figure 6: (a) Schematic of the laser beam welding process and (b) cross-section of a laser beam weldment in 6 mm thick duplex stainless steel (depicted and adopted according to [53]).

In industrial settings keyhole welds in DSS structures are mostly produced by electron beam welding. Electron beam welding has historically been preferred since the power output of the equipment can be modulated from zero to the maximum without affecting the beam quality, thus allowing the welding of parts with varying thickness on the same machine. Additionally the certification requirements, especially for food processing equipment, are more stringent when the welds have been performed by laser as compared to electron beam. [54] The necessity for a high vacuum makes the process costly and inflexible [55]. Therefore, there is considerable economic interest in the laser beam welding of DSSs. Additionally, the high vacuum leads to a loss of nitrogen during welding [56], possibly reducing the corrosion resistance and ductility of joints. The biggest challenge to the application of LBW to DSSs is the quality of the weldments and the resulting mechanical and corrosion properties. Historically CO_2 lasers, where the laser beam is guided by a series of copper mirrors, have been used for the welding process [57]. In the case of solid-state or diode lasers, the laser beam can be guided via a laser fibre, thus making the operation of a welding setup more manageable.

Keyhole welding with laser is characterized by high welding speed and precision, when performed on CNC machines or by robots, resulting in small fusion and heat-affected zones, low thermal deformation and low residual stresses. The LBW of DSS is regarded critically because of the high ferrite fraction in the weld metal, which is detrimental to the corrosion

resistance and the fracture toughness [58]. The weldability and strength are regarded positively [3,12,45–49]. The optimal process route for achieving good mechanical and corrosion properties as well as sufficient surface finish of the welds is still under investigation.

A metallographic investigation by Winkel and Fett [45] on welded joints of DSS 2205 showed that the austenite content in laser beam welded joints was between 6 vol.-% and 10 vol.-% in dependence of the location (radiation exposure side or weld root side). An increase in the incident energy through a combination of laser beam and metal active gas process led to an increase of the austenite content to 18 vol.-% to 21 vol.-%, depending on the position in the weldment [45]. In tungsten inert gas weldments of DSS 2205 the austenite content varied between 20 vol.-% and 60 vol.-% [45]. Corrosion in a 6% Fe-II-chloride solution occurred preferentially at the ferritic parts of the duplex microstructure in the root and top region of the tungsten inert gas weldment [45]. In the case of the laser beam weldment, the corrosion occurred exclusively in the weld root region. In the hybrid weldment, it occurred in both the root and radiation exposure side and in the tungsten inert gas weldment in the root region and in the base material. The corrosion damage was visible by the dissolution of the ferritic phase around the austenitic grains [45]. Measurements of the critical pitting temperature (CPT) revealed, that the LBW weldment exhibited the lowest CPT (30°C) in comparison to the hybrid (35°C-40°C) or the tungsten inert gas weldment (35°C) [45]. The application of LBW results in a non-optimal ratio of ferrite to austenite in the heat affected zone and fusion zone with regard to corrosion resistance. The reasons are mainly the high cooling rates [3,45], which oppose the recommendations of [28,50,51]. However, the corrosion resistance is not the sole criterion for the assessment of welded duplex joints, because mechanical stresses are also relevant [45].

Mourad et al. [3] compared the properties of tungsten inert gas and LBW joints of DSS 2205 and came to the conclusion, that the ferrite to austenite ratio is not critical for the strength of the joint but rather the width of the fusion zone and heat affected zone. In the LBW joints, the width of fusion zone and heat affected zone were lower than in the tungsten inert gas joints. This was controlled by the amount of energy introduced into the butt joint, which was lower in the case of laser beam welding. Lower energy inputs together with higher cooling rates led to narrower fusion zones and heat affected zones and a higher ferrite content compared to the base material. In the tensile test, the butt joints showed ductile fracture with clearly visible necking close to the region of the heat affected zone. In some joints necking also occurred in the base material. The tungsten inert gas and laser beam welded joints exhibited – even though they possess different austenite to ferrite ratios in the joint region – similar values for the ultimate tensile strength and fracture strain [3]. Mourad et al. [3] attribute this to the increased internal stresses in the case of the tungsten inert gas weldments compared to the LBW weldments.

The presence of weldments in DSS generally does not impair the tensile strength, but reduces the fracture strain [59,60]. The influence of weldments in parts on their fatigue properties is more pronounced. For welded structures, the additional heat input, solidification, cooling and utilization of special feedstock material may lead to a deviation

from the previously optimal microstructure [53]. Excess or missing material may lead to geometric notches and stress concentrations. Some research activities have covered these aspects.

Singh and Shahi [61] found an increased resistance against fatigue crack growth for higher ferrite contents and larger grain sizes in joint material produced by electron beam welding. They attributed the reduced fatigue crack growth rate to the higher deflection of the crack path. Sołtysiak [62] determined the fatigue lives of DSS 2205 specimens containing autogenous laser beam welded butt joints, which were manufactured using an Nd:YAG disk laser without post-processing steps. The shape of the fusion zone was found to depend on the focus position of the laser beam. The joints possess a slight excess of weld metal. The fatigue lives of joints created by two different LBW parameter sets as well as the base material were measured at two distinct stress levels (0.66 $R_{p0.2}$ and 0.57 $R_{p0.2}$) under a load ratio of R_F=1 and a frequency of 1 Hz. Due to the low frequency, all specimens were tested in the low cycle fatigue (LCF) regime. Sołtysiak [62] reported fatigue cracks originating in the base material as well as in the fusion zone. The geometric and structural notches of the joint reduced the fatigue lifes of the specimens by 24.6% or 33.5% depending on the LBW parameters used [62]. Sołtysiak [62] extrapolated the results of the LCF tests to estimate the fatigue limit at 2×10^6 cycles and concluded a reduction of the fatigue limit by 2.8% or 4.9% depending on the laser beam welding parameter set. Björk et al. [63] studied the influence of a high-frequency mechanical impact treatment on the fatigue properties of gas metal arc welded butt and X-joints in DSS 2205 and DSS 2507. They had limited success at improving the fatigue properties, because the high-frequency mechanical impact treatment generated microcracks, where fatigue cracks were initiated. They observed fatigue crack initiation at the coarse ferritic zone in the heat affected zone of the weldments.

In summary, the fatigue properties of laser welded duplex stainless steels have been investigated. It has been found that the presence of weldments generally reduces the fatigue performance of the material due to either geometric or microstructural notches. Some effort has been undertaken to determine post processing procedures to improve the fatigue performance, but the results show room for improvement. Up to now, it has not been possible to increase the fatigue performance up to the level of the base material.

2.3 Laser Directed Energy Deposition

Figure 7 shows an overview of the metal additive manufacturing technologies. The additive manufacturing processes can be characterized by the form and supply method of the feedstock material, the energy source for the process and the method for joining the feedstock material. The feedstock can be either a powder, a wire or a metal powder bound in a thermoplastic granulate or filament. Energy sources commonly used are laser beam, electron beam, plasma torch, electric arc or heated nozzles for the thermoplastic carrier material. The feedstock material can be directly molten and solidified in a near net shape. Using other methods a part or a green body is produced, which must be sintered. Laser and wire additive manufacturing is classified within the directed energy deposition methods. Methods using powder as a feedstock material and/or an electron beam or electric arc as an energy source serve as the closest reference for the material properties due to the process similarities.

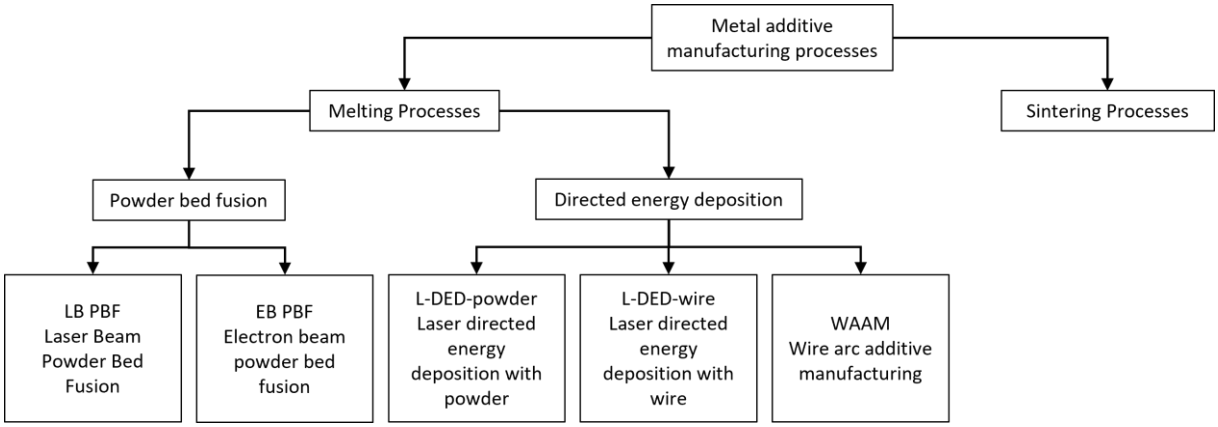

Figure 7: Overview of the metal additive manufacturing technologies according to [64].

During laser directed energy deposition with wire, a metal wire is continuously molten using a laser as an energy source. The resulting melt-pool is fused onto a substrate. This way a near net shape part can be produced, or features can be added to existing parts in a layer-wise manner [65] or damaged parts can be repaired. Generally additive manufacturing with laser beam and wire can be performed on the same equipment as conventional laser beam welding with feedstock material, if a sufficiently large defocus distance to avoid keyhole formation can be achieved. The dimensional accuracy of the directed energy deposition (DED) method is usually much lower than powder bed methods, but the deposition rate is at least an order of magnitude higher [66]. The benefit of DED with laser and wire over DED processes with powder is the avoidance of difficulties with powder handling and a near 100% material utilization rate. Compared to methods using an electric arc to melt the material, the energy can be introduced into the process in a more focused way, resulting in a smaller melt-pool with less heat being introduced into the part. This means, that more filigree structures can be produced and the residual stresses and microstructure of the material can be controlled more precisely [67–73].

The main difference between laser beam welding as a joining procedure and laser and wire additive manufacturing is the process mode. For high-speed laser beam welding the

keyhole effect is used. For additive manufacturing keyhole formation should be avoided. Here, as much material as possible needs to be deposited with the best possible quality. This often means, that excessive heat input and deep remelting depth are unwanted. Additionally, the problems regarding porosity and surface quality when a vapor capillary is formed need to be avoided in additive manufacturing. The material loss due to evaporation is also detrimental. Figure 8 (a) shows a schematic of the laser directed energy deposition process with coaxial wire feeding and Figure 8 (b) shows the cross-section a duplex stainless steel weld bead produced with laser directed energy deposition with lateral wire feeding [74].

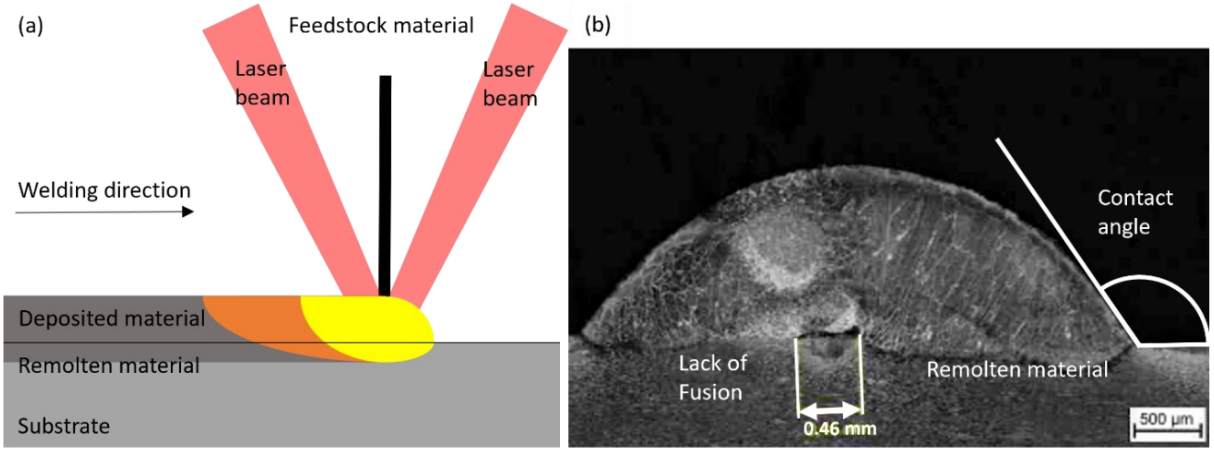

Figure 8: (a) Schematic of the coaxial L-DED-wire process and (b) cross-section of a weld bead produced with laser directed energy deposition with wire [74].

The energy input is often limited to the absolute minimum required for melting of the feedstock material in order to limit the remelting depth, while still ensuring proper bonding with the previous layer. Insufficient energy inputs or distributions can lead to lack of fusion defects or acute contact angles and improper fusion at the edges of the deposit (Figure 8 (b)).

The thermal management during the deposition process is critical for the quality of the final part [75,76], because the process stability is very sensitive to changes in boundary conditions and process parameters. The height of individual welding tracks is not constant over the height of a structure. The shape of individual layers is dependent upon the temperature of the melt-pool, temperature distribution within the melt-pool, cooling and solidification rates. Due the change in geometry, the thermal boundary conditions of the melt-pool change with increasing height of the deposit. Due to the changing boundary conditions, the energy input needs to be adjusted with increasing build height to prevent overheating or undercooling of the melt-pool. Additionally, – together with the changed cooling rate – the changing shape from the substrate to the finished structure leads to a change in the shape of the welded tracks, requiring adjustments in the offset per layer or feed rate of the material to ensure a constant relative position between part and tool. [76–78]

The placement of the wire with regard to the melt-pool has a great influence on the geometry of the deposited track [22]. Syed and Li [22] concluded that during front feeding with a lateral wire feed the optimal clad geometry is obtained when the wire is placed at the front of the melt-pool so that it is molten by the dissipated heat from the melt-pool. When the window for optimal clad generation is missed, discontinuities like non-uniform weld tracks and serrations on the track surface may form [23], which may also be accompanied by lack-of-fusion defects [19]. Additionally, the angle between the laser and wire influences the size of the stable process window, with the window becoming smaller as the angle becomes steeper [19].

Another important factor is the free length of wire between the wire-nozzle and the melt-pool [77]. When the focus position is elevated above the substrate, the free length of wire is longer. As a result, the laser beam is focused on the wire and top of the melt-pool, leading to a more focused laser spot and a hot-spot in the melt-pool. The relative position between focus and substrate is subject to change when the pre-programmed offset height per layer is different from the actual height of the deposited tracks. This can cause a shift to the droplet transfer mode (Figure 9 (first row)) [77] or to the wire evaporating completely before it reaches the melt-pool. When the distance becomes smaller, the energy transmitted to the wire may be insufficient for stable melting. This results in the solid wire stubbing into the bottom of the melt-pool, buckling, if enough force is applied. The wire then plunges through the melt-pool and protrudes out on the sides of the deposit (Figure 9 (third row)) [21,77].

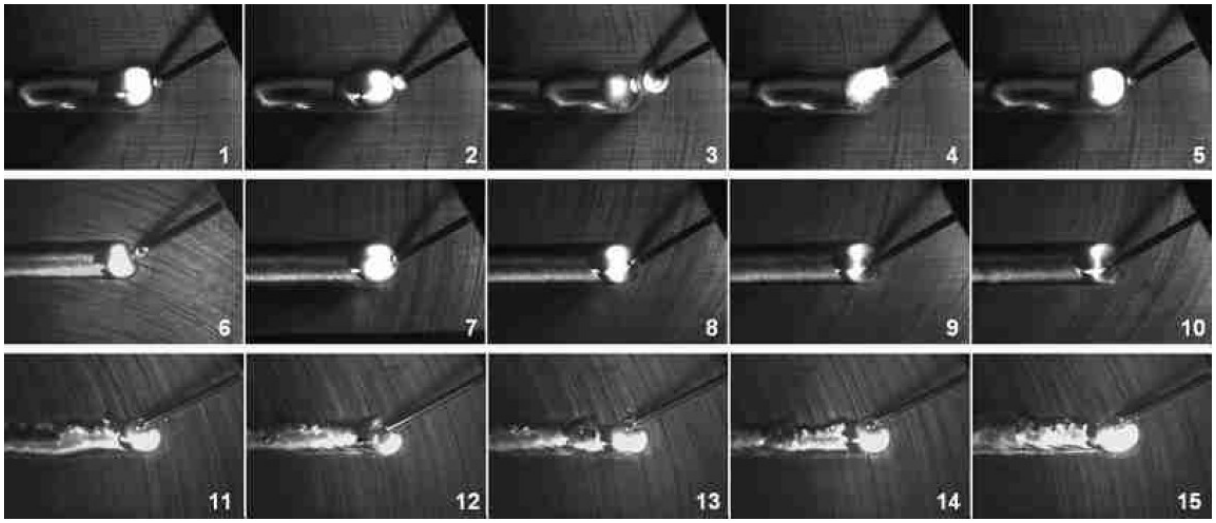

Figure 9: Material transfer modes between wire and melt-pool [77]. First row: Droplet transfer, second row: Liquid bridge, third row: Stubbing.

The thermal history during additive manufacturing has a large impact on the quality and properties of the final structure [75,79]. The exact amount of energy, which is introduced into the part as well as the resultant thermal history, are difficult to quantify, since the relevant physical quantities — such as the absorption, radiation and convection coefficients, thermal conductivity, specific heat and latent heat associated with phase transformations — are temperature dependent [80] and difficult to measure [75]. The most important quantity is the power of the laser, but less obvious factors may also exert great influence. For example,

by defocusing the laser beam, the beam irradiance can be adjusted. Thereby, it is possible to influence the aspect ratio and the temperatures of the melt during the L-DED-wire process [67]. Even if constant process parameters for additive manufacturing are chosen, the temperature distribution and process behaviour can constantly change because of heat conduction and accumulation [81]. In order to obtain uniform microstructures and mechanical properties within the structure, a steady state during the L-DED-wire process is sought, where the temperature field is constant and no further adjustment of the process parameters is needed. Knowledge of the actual temperature distribution enables not only control by process parameter adjustments but also allows assessment of the quality of the structure.

The material properties of specimens taken from regions where a steady state has been reached are likely to be more representative than those from structures where the process has been terminated prematurely. The cooling rate in the first few layers close to the substrate is very different from the cooling rate in the upper regions of the part. This results in differences in microstructure and, variations in mechanical properties along the height of additively manufactured structures. DED processes are envisaged to produce large-scale parts so that the production of small samples, which have material properties that can be compared to those of larger structures, is relevant for scientific and certification purposes.

For example, the standard DIN/TS 17026:2020-10 [82] issues the instruction that the interpass temperature should not vary by more than a certain temperature range for the certification of a parameter set. The interpass temperature has a great influence on the remelting depth, solidification and cooling rate. These parameters affect the grain size and morphology, which, in turn, determine the mechanical properties [83].

The remelting depth into the previous layer and the cooling rate is strongly influenced by the energy introduced and the temperature of the preceding layer during the L-DED-wire process and needs to be controlled [84]. If the interpass temperature is too low, problems with insufficient bonding with the previous layer may occur. If it is too high the cooling rate may be too low, causing unwanted microstructural changes [85–87] or overheating of the melt pool and process instability [75].

From a metallurgical standpoint additive manufacturing with duplex stainless steels is challenging due to the necessity of achieving the correct phase balance and avoiding the formation of intermetallic phases within the scope of changing thermal boundary conditions. During the solidification and cooling process, phase evolution occurs in multiple stages. The phase composition is fully ferritic after solidification [37,38,88]. Austenite begins to form at the ferrite-ferrite grain boundaries in the temperature range from 1350°C to 800°C [89]. This is followed by austenite needles growing into the ferrite grains at temperatures between 1100°C and 750°C, which have a near Kurdjumov-Sachs orientation relationship [90]. This type of austenite formation is accompanied by elemental partitioning, resulting in a lower concentration of Cr, Mo and N in the austenite needles and a higher concentration of Ni than in the grain boundary austenite [91]. In the temperature range from 1000°C to 600°C intermetallic phases like the σ-phase precipitate, which can lead to a deterioration

of the toughness of the material. Low heat inputs during welding and high cooling rates may lead to the formation of Cr_2N and CrN. [91]. Some work has been performed on directed energy deposition with duplex stainless steels. Most publications focus on optimization of the austenite-ferrite balance [92,93]. Figure 10 shows an overview of the research activities regarding additive manufacturing with duplex stainless steels.

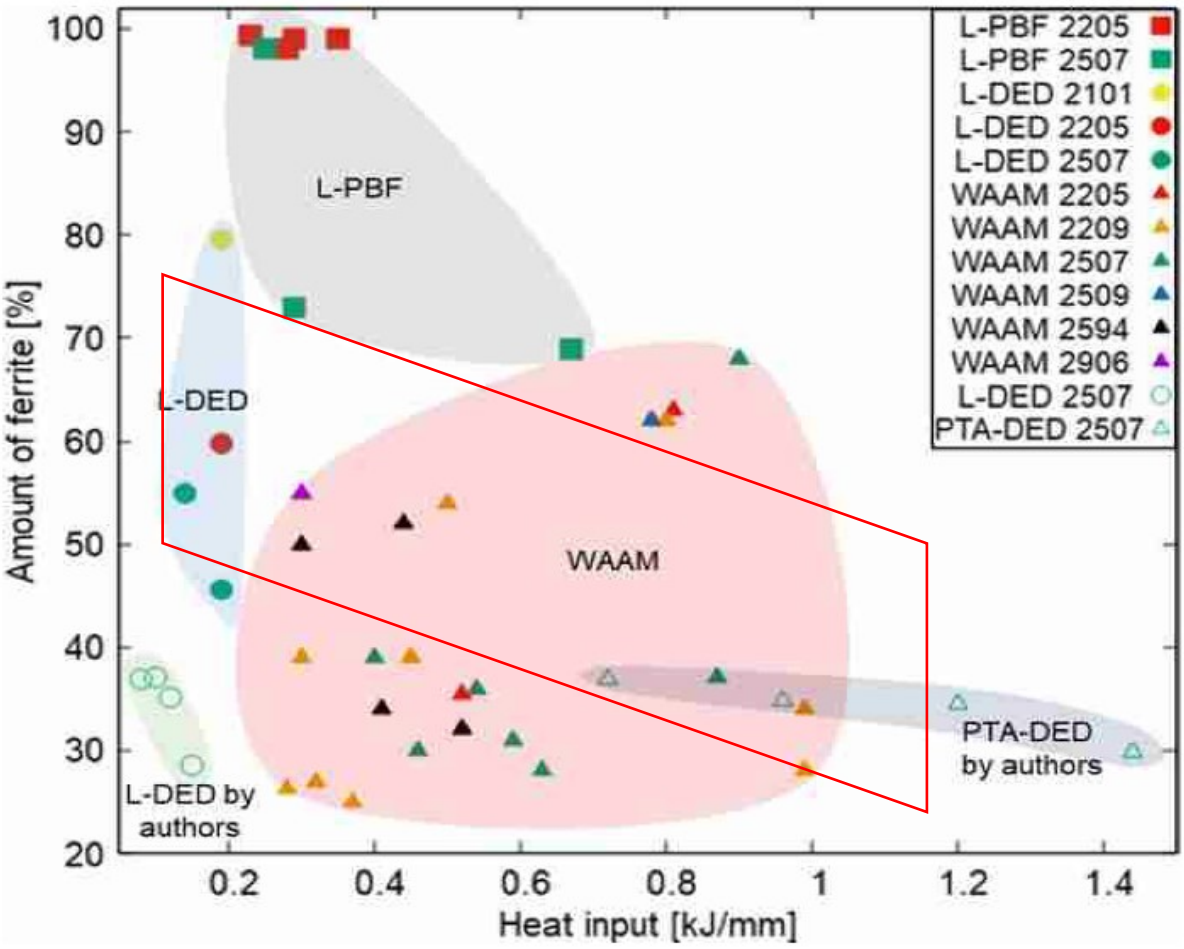

Figure 10: Overview of research activities in additive manufacturing of duplex stainless steels [11]. The red box represents the approximate process window of the equipment employed for this thesis. (Plasma transferred arc welding is abbreviated as PTA)

In directed energy deposition with laser and powder, the grade of duplex stainless steel (lean, standard (Figure 11 (b)), or super) has a great influence on the phase composition, with the final fraction of austenite ranging from 16.1 ± 1.1 vol.-% (lean) to 58.3 ± 0.1 vol.-% (super) [94]. The variations in austenite content reflect in the hardness of the material with the lean and super grade reaching a Vickers microhardness of 208 ± 8 HV and 294 ± 9 HV respectively [94].

Posch et al. [95] reported ferrite contents between 26 vol.-% and 29 vol.-% (Figure 11 (a)) in blade-like geometries made via wire arc additive manufacturing with the cold metal transfer process and a DSS 2209 welding wire. The resulting hardness of the material (266 HV1 - 270 HV1) was within the typical range of hardness for duplex stainless steel weld metal and the tensile properties met those described by the wire producer [95].

Another critical aspect in the directed energy deposition of DSS is the shielding gas atmosphere. As nitrogen is a strong austenite stabilizer, the atmosphere surrounding the melt-pool has a large influence on the final phase fractions of the part. Bermejo et al. [96] reported austenite contents of approximately 54 vol.-% (Figure 11 (c)) and 70 vol.-% (Figure 11 (d)) using argon and nitrogen shielding gas respectively, during directed energy deposition with laser and a DSS 2209 wire.

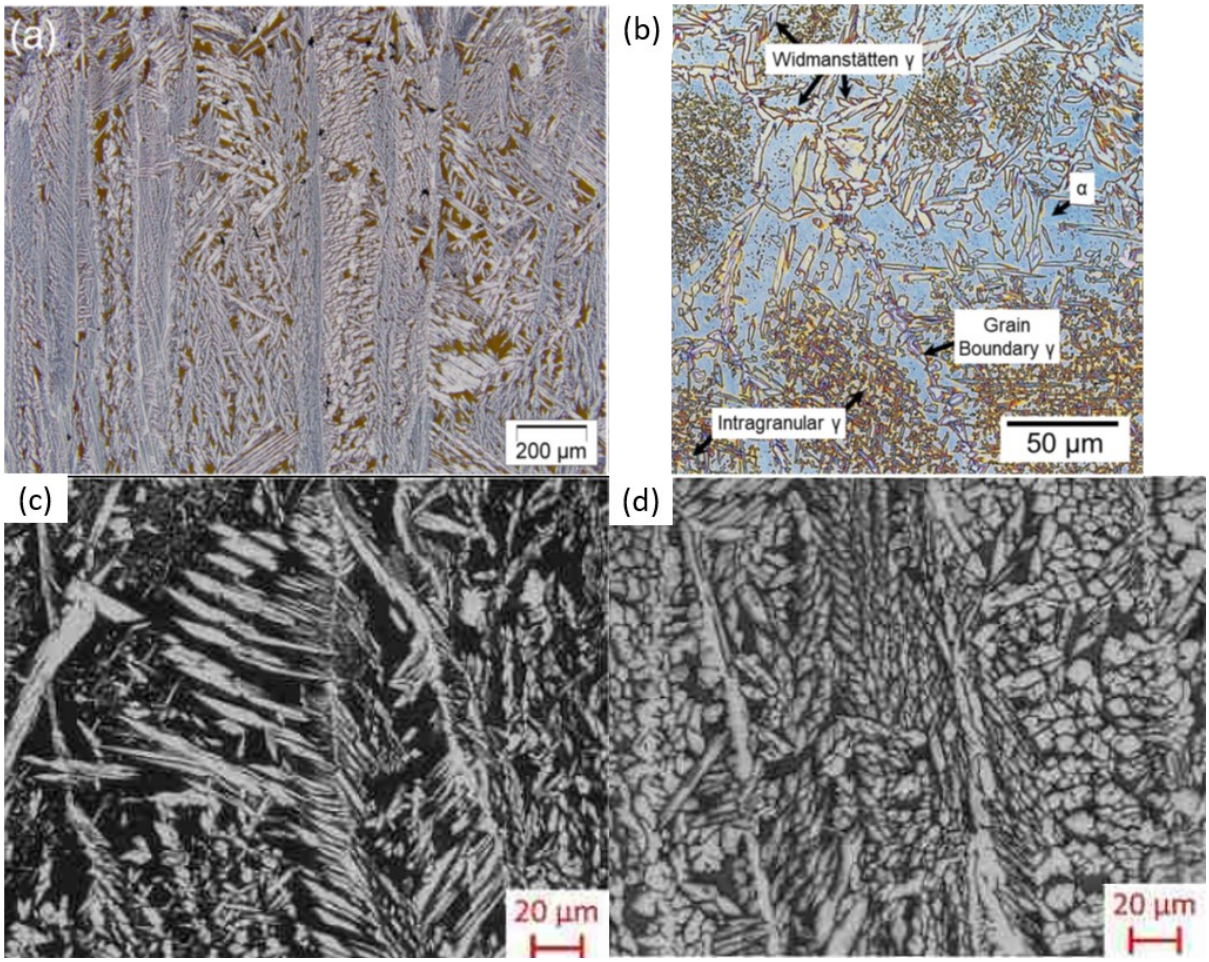

Figure 11: AM microstructures in standard DSS (a) WAAM [95], (b) L-DED-powder [94], (c) and (d) L-DED-wire with argon and nitrogen shielding gas respectively [96].

Pacheco et al. [11] and Zhang et al. [10] reviewed recent research activities regarding the additive manufacturing of duplex stainless steels. Pacheco et al. [11] identified the optimization of the processing so that post-production heat-treatments can be avoided as a critical step for the uptake of the manufacturing methods in industry. Zhang et al. [10] outlined five critical points for the adaptation of additive manufacturing of duplex stainless steels.

1) The alloy composition must be tailored to the heat-input of the manufacturing method so that the production of suitable microstructures is more easily guaranteed.

2) The process control needs to be improved. Influencing variables such as heat input, shielding gas and interpass temperature should be investigated and controlled *in operando*.
3) The interaction between alloy composition, microstructure and properties needs to be characterized further. Especially the corrosion mechanisms, typical defects and residual stresses should be quantified.
4) The process simulation needs to be improved for the case of DSS additive manufacturing, so that relevant process parameters for control of the microstructure and properties can be identified.
5) The structural design of parts must be properly adapted to the manufacturing method.

In summary a lot of work has been performed on the characterization of quasi-static mechanical properties and corrosion behavior of additively manufactured duplex stainless steels. The fatigue properties and residual stress distribution in AM-parts have received less attention so far.

Sales et al. [7] used the WAAM-cold metal transfer process to fabricate thin-walled samples of super DSS ER2594. Adhering to interpass temperatures of 150°C led to a phase fraction of 43 vol.-% austenite and 57 vol.-% ferrite. They performed fatigue tests at a frequency of 10 Hz and an R_F–ratio of 0.1. They report a fatigue limit of approx. 350 MPa (upper stress, σ_{max}) for the horizontal and 195 MPa for the vertical direction. The fatigue cracks originated at gas porosity and lack of fusion (LoF)-defects. In their subsequent study [6] they adjusted the interpass temperature to 100°C. This led to an increase of the austenite content to 64 vol-%. The fatigue limit in horizontal direction remained unaffected while the fatigue limit in vertical direction increased to approx. 280 MPa. An investigation into the fatigue crack propagation rates of the material [97] showed, that fatigue crack growth rate is equal for the horizontal and vertical direction in term of the effective stress intensity factor. However, the crack in the horizontal direction along the welded tracks exhibited higher crack closure and higher crack opening stress intensity factors. This led to a slower fatigue crack growth rate at the same applied load and a longer fatigue life.

Kunz et al. [9] produced samples of DSSs 2205 and 2507 using laser powder bed fusion. They investigated the properties of the material in the as-built, solution annealed and hot-isostatic pressed and solution annealed state. The fatigue properties were characterized in rotating bending tests at a frequency of 100 Hz and an R_F–ratio of -1. The hot-isostatic pressing led to a significant reduction in pore size. In the as-built state the material was nearly entirely comprised of ferrite. Solution annealing and hot-isostatic pressing led to austenite phase fraction of 36.2 vol.-% and 39.5 vol.-% for the DSS 2205 material respectively as well as 43.3 vol.-% for both procedures for the 2507 super DSS material. The yield strength of the DSS 2205 material was 773 MPa, 558 MPa and 548 MPa in the as-built, solution annealed and hot-isostatic pressed conditions respectively. The super DSS material exhibited values of 912 MPa, 670 MPa and 607 MPa. In DSS 2205 the as-built, solution annealed and hot-isostatic pressed condition exhibited fatigue limits of approx. 225 MPa,

413 MPa and 495 MPa respectively. For the super duplex grade, the fatigue limits were determined as approx. 422 MPa, 500 MPa and 518 MPa respectively. Failures originated from internal defects such as porosity and lack of fusion. The increase in fatigue limit with increasing austenite fraction is attributed to a reduction in notch-sensitivity due to the higher ductility of the austenite. The reduction of pore size had a larger impact than the microstructural composition.

To the authors knowledge the fatigue properties of duplex stainless steels produced with laser directed energy deposition with wire have not been reported in the literature. Also, the fatigue performance has not been assessed in a fracture mechanics framework.

One use case under investigation is the utilization of DSS alloy 2205 for hydrogen storage tanks. For mobile applications, the material needs to exhibit a combination of high specific strength, good resistance to hydrogen corrosion and a competitive price. [98] DSSs possess some resistance to hydrogen corrosion, due to their passive layer and mix of bcc and fcc crystal structures, as well as high strength. The storage of hydrogen in metal hydrides is attractive because hydrides allow the highest storage density per volume. For charging and discharging of the hydride, active temperature management is needed. The heat exchanger elements are integrated into the tank geometry using additive manufacturing techniques. Hydrogen — due to its small size — has a special affinity to diffuse into prestrained material, causing a deterioration of the mechanical properties [99].

A common way of mitigating the formation of strain mismatch in parts is preheating the build plate, so that the temperature difference across the part during manufacturing is reduced. This approach is not recommended for DSSs [2,28], as low interpass temperatures are needed to ensure high cooling rates for achieving the correct phase composition and impede the formation of intermetallic phases.

Stress relieve by heat treatment is the most common way of diminishing residual stresses. For duplex stainless steel this is performed as a solution heat treatment at approx. 1050°C [2,28] with subsequent quenching. Especially for large parts this is linked with large costs and the possibility of warping due to stress relief [16], creep [28] and uncontrolled inhomogeneous cooling. Residual stress design is therefore an essential component of the part design process with duplex stainless steels.

2.4 Process Control

Optimizing the process parameters (especially offset per layer and laser power in dependence on the height or the number of tracks) to produce large structures is often achieved by a time- and material-consuming trial and error approach [93,100]. Analytical or numerical models are not sufficiently accurate to predict track heights over tens or hundreds of layers, where small errors quickly add up and predictions are often very sensitive to the assumed boundary conditions and parameter settings [101,102].

In the absence of sufficient predictive models and process control systems for the adjustment of laser power and height increment, the correct processing parameters for each layer must be determined in time-consuming trial and error experiments. In addition, overheating of the part [17], changes of the surrounding environment like insufficient shielding gas atmosphere, blockages or slippages in the wire feeding mechanism, or distortion of the part during the deposition process [24] may lead to localized process instabilities. The production of large parts is time-consuming, taking hours or days. Process instabilities and the resulting discontinuities are therefore related with great costs and need to be avoided.

There exist many different approaches for process control in directed energy deposition with laser. Cai et al. [103] reviewed the state of the art regarding process control. For laser directed energy deposition they identified the following control variables:

- Laser power
- Laser output mode
- Travel speed
- Wire feed rate
- Shielding gas flow rate
- Scan pattern and direction
- Spot size
- Wire diameter

The control laws are based on correlations between process signals (Figure 12) and corresponding material or work-piece properties. The following types of signals are commonly used to control aspects of the additive manufacturing process:

- Thermal radiation
- Vision signals
- Electrical signals
- Force signals

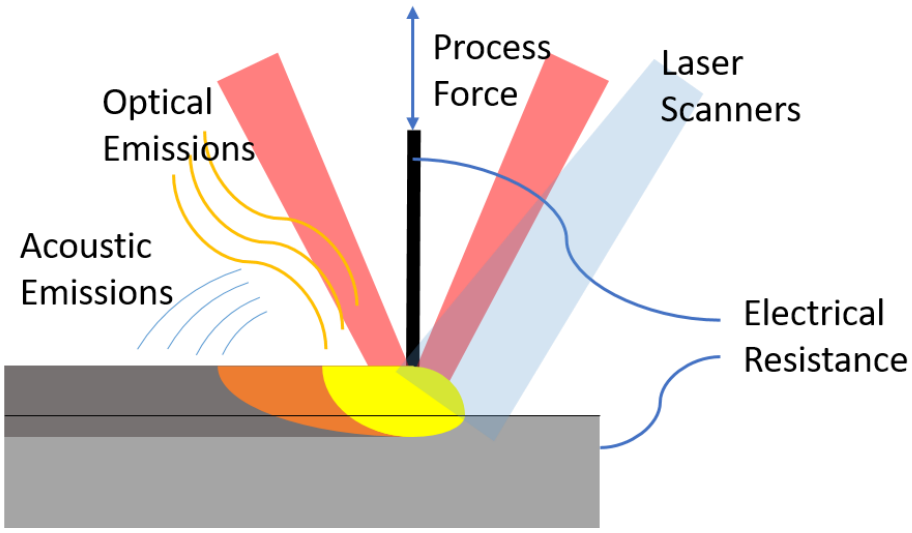

Figure 12: Process signals commonly recorded during the additive manufacturing process.

For laser directed energy deposition with powder mainly approaches that aim to influence the temperature or shape of the melt-pool for geometric control of the final part were investigated [104,105]. Control variables included the laser power, welding speed, feed-rate, laser focus and relative position between laser focus and feedstock focus [106–112]. For geometric control imaging devices are mainly used. Based on the image evaluation traditional control algorithms like PID-control are most often employed [113].

For the determination of the melt-pool temperature infrared cameras [86] and pyrometers [114] are used. Some approaches use the interpass temperature [115] or welding speed [85] to control the cooling rate and ultimately the technological properties. Especially the second approach led to reduced porosity and increased corrosion resistance for AISI 316L stainless steel [116]. Some approaches use multiple control and correcting variables. Tyralla et al. [117] used two independent PI-controllers to control the overlap and laser power based on signals from a laser-line sensor and an infrared camera during laser directed energy deposition with powder.

For laser wire processing geometrical and temperature signals are employed as well [118–121]. For example, the layer height can be controlled by correcting the wire feed [122] rate based on optical measurements [123]. Furthermore there exist some approaches for in-situ resistance and force measurement [124–127]. Hagqvist et al. [124,125] measured the distance dependent electrical resistance of the wire feedstock between nozzle and melt-pool to determine the stand-off distance. Through correction of the wire-feed-rate height discrepancies could be effectively eliminated. Teichman et al. [126] adapted a wire feeding mechanism for soldering with integrated force-sensing for coaxial laser directed energy deposition with wire. They used a two-point controller to switch the wire-feed mechanism on and off based on a threshold force on the wire during the process. Steiner et al. [127] describe a setup for the measurement of electrical resistance between wire-nozzle and substrate. However, they were unable to determine a clear correlation between measured

resistance and the stability of the liquid bridge. The control of the layer height is essential for process stability of laser directed energy deposition with wire [128].

In summary, process control solutions for some aspects of the L-DED-wire process have been described in the literature. The most important issues that a control method must solve is to account for variation in layer height and to stabilize the melt-pool temperature to prevent overheating or undercooling. At the same time the measurement of the process and setting of the control variable must be realized on the equipment in an economic manner.

3 Methods

In this chapter the experimental procedures as well as the theoretical concepts employed in this work are described.

3.1 Materials

The base material (DSS 2205, 1.4462) for laser beam welding experiments consisted of sheets with dimensions 290 mm × 100 mm × 4 mm (transverse direction, TD × rolling direction, RD × normal (thickness) direction, ND), which were welded in the butt joint configuration in the as-received condition. The orientation of the weldment was perpendicular to the rolling direction. The joint surfaces were milled to achieve an optimal fit of the surfaces. Before welding, the surfaces were cleaned with ethanol to remove residual fluids from the milling process.

The welding procedure was performed using a filler wire of type ER2209 with a diameter of 0.8 mm purchased from METAL TECHNOLOGY CANTERBO GMBH (MTC). The use of filler wire is beneficial in reducing the hot cracking tendency of the material and preventing under-fill of the weldments [55]. The feedstock materials for the welding of DSSs are typically over alloyed with nickel in order to achieve optimal phase compositions under the fast cooling conditions of welding processes, when no post weld heat treatment is planned. The chemical composition of the base material and wire (measured via energy-dispersive X-ray spectroscopy (EDX)) is given in Table 1.

Table 1: Chemical composition of the feedstock and base material for the laser welding experiments measured via energy-dispersive X-ray spectroscopy.

Specimen	Si [wt.-%]	Mo [wt.%]	Cr [wt.-%]	Mn [wt.-%]	Fe [wt.-%]	Ni [wt.-%]
base material (DIN EN 10088-2 [129])	1.0	2.5 – 3.5	21.0 – 23.0	2.0	balance	4.5 – 6.5
base material	0.37	3.42	21.93	0.80	67.81	5.6
ER2209 (MTC)	0.66	3.00	20.07	1.05	65.42	9.69

Additive manufacturing was performed using the same filler-wire as for the LBW procedure as well as an additive manufacturing alloy with reduced Ni content purchased from voestalpine Böhler welding group GmbH. The 3Dprint AM 2209 welding wire, which was used for some of the additive manufacturing experiments, has a larger Diameter (1.2 mm). Larger wire diameters are beneficial for the process control method developed during this work. The composition is given in (Table 2). All additive manufacturing experiments were performed on either 40 mm thick substrates of 316L or 10 mm thick substrates of material conforming to the German classification of V2A depending on availability and convenience.

The welding wire for additive manufacturing has increased contents of ferrite forming elements chromium and molybdenum and a reduced content of the austenite forming element nickel. This leads to higher ferrite contents in the weld metal after directed energy deposition [16] and a reinforced passive layer.

Table 2: Nominal feedstock wire composition as specified by the manufacturer and measured via EDX for the 3Dprint AM 2209 alloy by voestalpine Böhler welding.

Condition	Si [wt.%]	Mo [wt.%]	Cr [wt.%]	Mn [wt.%]	Fe [wt.%]	Ni [wt.%]
Nominal (3Dprint AM 2209 [130])	0.5	3.0	23.0	1.6	balance	9.0
3Dprint AM 2209	0.82	3.5	24.6	1.5	60.5	8.3
ER2209 (MTC)	0.66	3.00	20.07	1.05	65.42	9.69

3.2 Laser Beam Welding

Laser beam welding was performed using an 8 kW Yb:YAG fibre laser (YLS-8000 by IPG laser systems). The laser beam was guided to a Precitec YW52 laser welding head through a fibre optic cable with a core diameter of 200 µm. The laser welding head contains a collimating lens and a focusing lens with focusing lengths of 120 mm and 300 mm respectively. The resultant in focus spot has a diameter of approximately 500 µm. The laser welding head was mounted on a KUKA KR30HA 6 axis robot. The workpiece was clamped on an aluminium clamping block with a slot below the joint region. Argon shielding gas was supplied through the slot beneath the joint and a nozzle placed ahead of the wire-nozzle (Figure 13) in order to inhibit oxidation of the weld metal on both the root and top side of the joint.

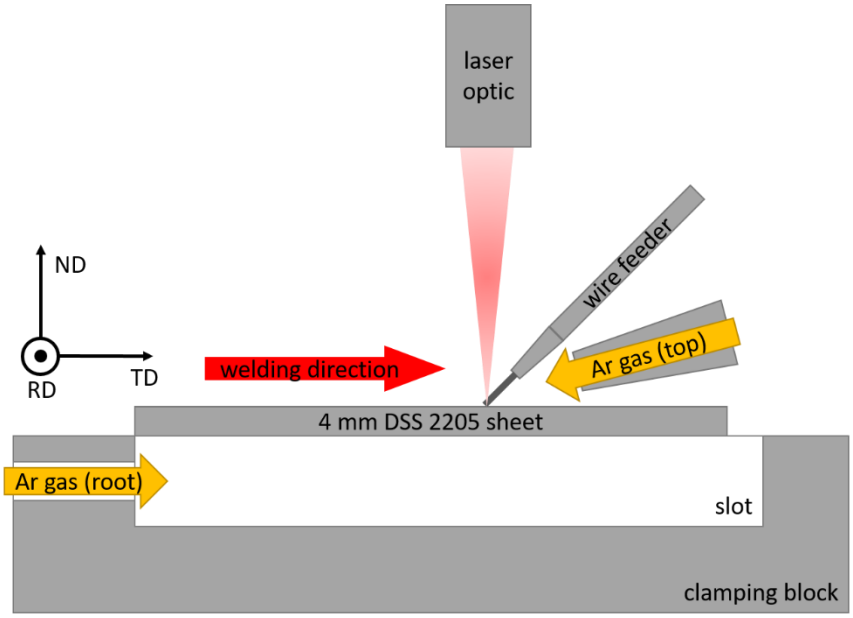

Figure 13: Schematic of the LBW setup.

The weldments were created with a focal distance of 0 mm from the top surface using filler wire. Selected weldments received a laser surface remelting treatment with reduced laser power and welding speed, for which the focus position was elevated 80 mm above the surface of the sheet material. Under these conditions no keyhole formation took place, resulting in a very smooth surface of the weld metal. The welding parameters were optimized according to visual inspection in the laser-surface-remelted condition. This way very flat weldments with a low notch factor could be produced. The optimized process parameters for the welding and laser surface remelting treatment are shown in Table 3

Table 3: LBW parameters

LBW-condition	Power [W]	Welding speed [m/min]	Ar flow (top/root) [l/min]	Wire feed rate [m/min]
As-welded (as-welded)	3800	3.0	18/10	3
laser-surface-remelted	2500	1.7	18/10	-

3.3 Additive Manufacturing

Laser directed energy deposition was performed using the same laser, robot and wire feeding mechanism as in laser beam welding. Additionally, a KUKA DKP 2-axis positioner was used for manipulation of the workpiece, when the orientation between the tool and track was essential. For the additive manufacturing procedures a 600 µm diameter fiber with a laser optic for laser cladding and additive manufacturing set-up developed by the Fraunhofer IWS [131] were used. The path planning for the deposition process was done using the DCAM software by SKM Informatik.

A schematic of the deposition process, including the local coordinate system used for presenting the results in this thesis is shown in Figure 14. In the laser optic the laser beam is split three ways. The three resulting beams intersect in one volume below the wire feeding nozzle (Figure 15). This way a higher degree of direction independence compared to lateral wire feeding is achieved since the process is more or less independent of laser beam orientation. As a result of the steep angle between the wire and the laser beams the window for stable melting of the wire is considerably reduced compared to a setup with lateral wire feeding [77].

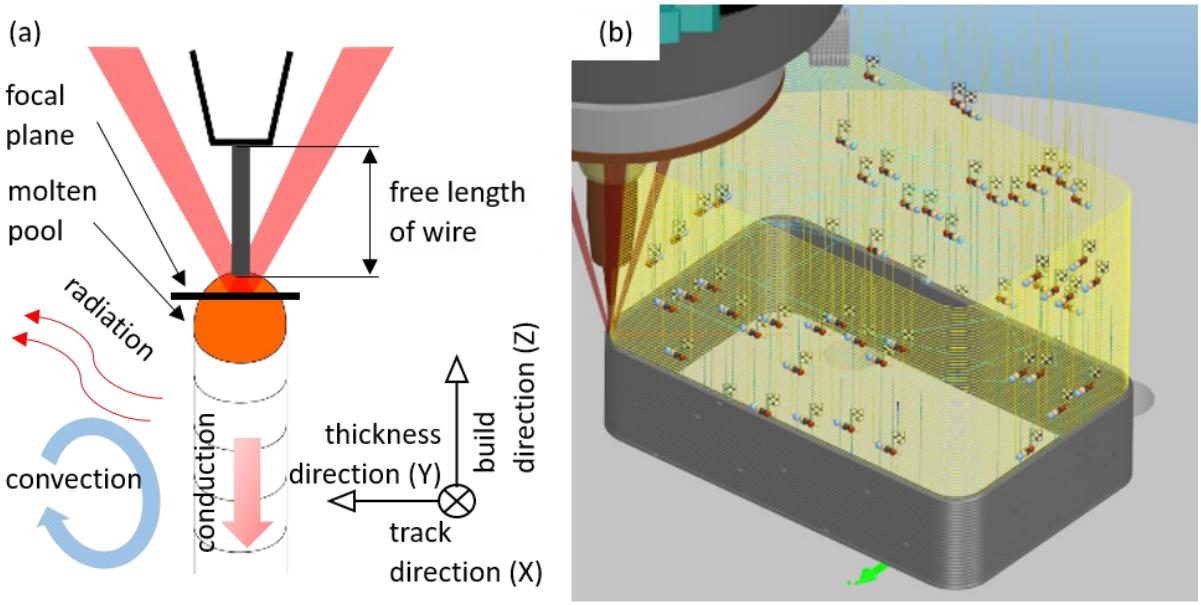

Figure 14: (a) Schematic of process conditions defining the stability of the process, (b) process planning in the CAD Software. The tool with the three laser beams is visible in the top left corner. The grey volume represents the already built structure at the time of the process simulation. The toolpath is represented by the yellow lines, with the start and endpoints being marked by the dots and finish flags.

The temperature of the melt-pool is determined by the power of the incident and emitted energy. The incident energy is determined by the power level of the laser and the focus position. When the focus position is elevated above the substrate and the free length of wire is longer the laser beams are focused on the wire and top of the melt-pool. This leads to a more focused laser spot and – at constant wire feed rate - a hotter melt-pool (Figure 15).

With this principle, the amount of wire that can be molten as well as the remelting depth into the previous layer can be influenced.

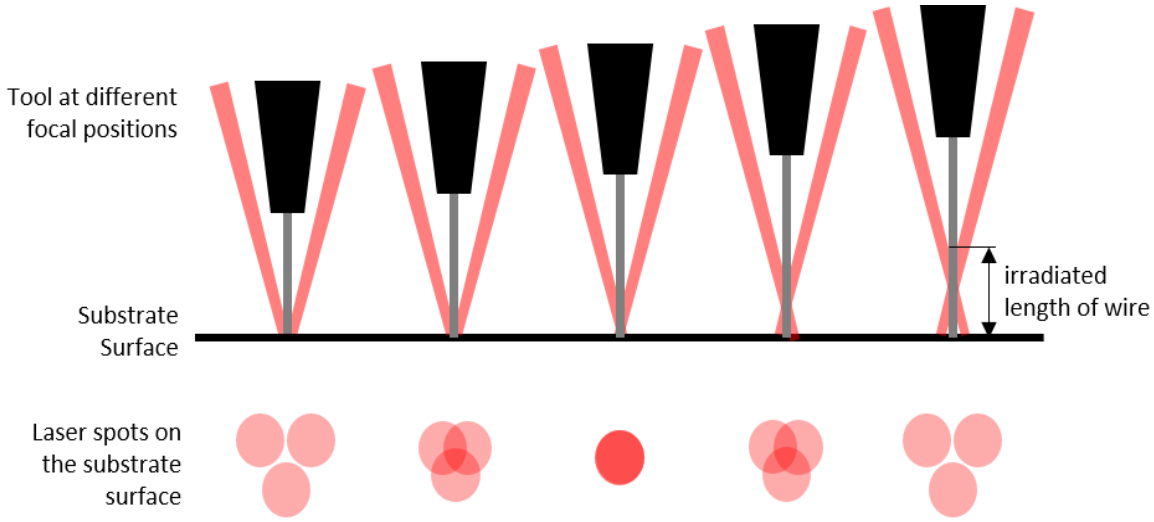

Figure 15: Irradiated length of wire and focal spot geometry in dependence of the focal position relative to the substrate. The third laser beam is out of plane.

At the start of this work the necessary adjustment of process variables was determined by trial and error experiments. A stable process for parts like the one presented in Figure 14 (b) was achieved by adjusting the preset layer height and laser power in a layer wise manner. All other process parameters were kept constant. In the beginning the layer height and laser power were adapted manually based on the observation of the previous layer. While some samples with acceptable properties could be produced this way, several problems with this approach were identified:

- The observations leading to an adjustment of process parameters and the adjustment of the process parameters are not traceable.
- The pauses for reprogramming of the L-DED-wire robot cell are not of equal length and do not to need to occur at regular intervals, depending on the quality of the parameter adjustment. Therefore, control of the part temperature is nearly impossible.
- In some cases the results are not reproducible due to rarely occurring process errors influencing the deposition sequence.
- Since the variation of process parameters is not systematic, linking cause and effect is not always possible.

3.3.1 Heat Accumulation and Steady-State Evaluation

The first challenge was to find a strategy to account for the heat accumulation during the AM-process. With thermocouples the temperature can only be acquired for fixed positions. The addition of thermocouples into the additively manufactured parts *in operando* is complex [132,133]. In particular, optical temperature measurement techniques proved to be advantageous for additive manufacturing since the successively changing geometry prohibits the use of thermocouples for the determination of temperatures of the additively

manufactured structures [134]. Therefore, an infrared (IR) camera (Optris PI 450), which was calibrated by the manufacturer for the recording of temperatures up to 1500°C, was used to study heat accumulation [20].

During the L-DED-wire process, alignment of the tool relative to the toolpath was kept constant by the motion of the robot and positioner, which leads to the part being rotated relative to the camera and the tool mostly moving laterally in relation to the camera. The experimental setup and process planning are shown in Figure 16 (a) and (b) respectively. The constraint to lateral movement was achieved by the specification of a working plane in the computer-aided manufacturing software. The result is that the XZ plane of the tool coordinate system is always kept parallel to the working plane indicated in Figure 16 (b).

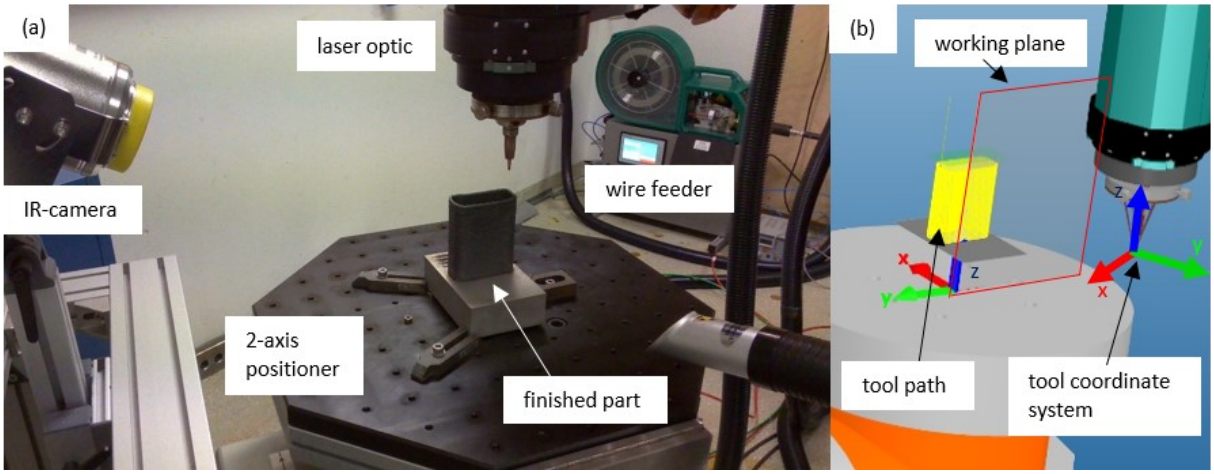

Figure 16:(a) experimental setup; (b) process planning in the CAM software.

The part made using L-DED-wire had a rectangular footprint (80 mm × 35 mm) with a radius of 10 mm at the corners and a height of approximately 100 mm. The tool path was screw-like with an offset of 1 mm per layer, which resulted in a total of 100 layers. The wire (1.2 mm, 3Dprint AM 2209) feed rate was set to 2 m/min and the tool speed was 0.5 m/min. The power of the laser was held constant at 3.15 kW.

The infrared camera is equipped with a 38° lens and offers a resolution of 382 by 288 pixels. The camera was positioned in such a way that the entire part was visible for the whole duration of the process. The distance from camera to part was 450 mm leading to a resolution of just under 0.9 mm per pixel. The wall of the final part has a thickness of 4.8 mm, not considering the surface roughness. Therefore, a resolution of at least 5 pixels over the thickness of one track is achieved. This resolution would likely be too low to capture the thermal gradients in the melt-pool or the vicinity of the melt-pool but is sufficient to capture the interpass temperature in accordance with our measurement principle, since the temperature gradients on the side of the structure opposite to the melt-pool are much lower. The data acquisition rate was 1 fps.

A value of 0.65 for the emissivity was assumed for the data acquisition. This value is within the range suggested by the manufacturer (Optris GmbH) for steel surfaces in the expected temperature measurement range. It is likely to be a good estimate for the surface of the

substrate. Since the oxidized surface of the additively manufactured part and the melt-pool are likely to have different emissivities, the emissivity for temperature measurement on the L-DED-wire part was calibrated by comparing the optically measured temperature to a thermocouple measurement. To achieve a temperature similar to the deposition process, the finished part was heated with the defocused laser beam. The best agreement between the measurements from the thermocouple and the camera was obtained with an emissivity value of 1.0. This high emissivity can be explained by the rough and dark surface of the part and the influence of background radiation from the melt-pool. The emissivity value determined for the additively produced surfaces was used to correct the measured temperature values via the Stefan-Boltzmann law (Equation (1)). The corrected temperature T_{corr} in Equation (1), measured with the assumption of an arbitrary emissivity ε_m, can be calculated from the measured temperature T_m if the real emissivity ε_{act} is known.

$$T_{corr} = \sqrt[4]{\frac{\varepsilon_m}{\varepsilon_{act}}} T_m \tag{1}$$

The interlayer temperature (T_{ip}) was found to conform to a limited exponential growth law according to Equation (2).:

$$T_{ip} = T_{ip,ss} - \left(T_{ip,ss} - T_{ip,start}\right) e^{-k_t t} \tag{2}$$

Here, $T_{ip,ss}$, $T_{ip,start}$, k_T and t denote the steady state temperature, the starting temperature, the growth constant and the time respectively.

3.3.2 Open Loop Process Control

The layer wise adjustment of the layer height and laser power were modeled using the same limited exponential growth law (Equation (3) and Equation (4)) to account for the influence of the variable interpass temperature on the geometry and heat conduction of the deposited matrial and melt pool:

$$P_{laser}(N) = P_i - (P_i - P_{ss}) e^{-k_P (N-1)} \tag{3}$$

$$h_o(N) = h_i - (h_i - h_{ss}) e^{-k_h (N-1)} \tag{4}$$

Here, P_{laser} is the current laser power, P_i is the initial laser power for the first layer, P_{ss} is the steady-state value of the laser power, N is the number of the current layer and k_P is an exponent describing the rate at which the laser power was changed. The offset height of the current layer can be described in an analogous manner through the parameters h_o, h_i, h_{ss} and k_h.

An initial guess for the process parameters was generated by fitting the exponential growth laws to manually determined parameters. Those process parameters were tested for the build of thin-walled, rectangular parts, which are 80 mm wide, 130 mm long and 90 mm high. The height requirement comes from the objective to extract fatigue specimens that contain a representative number of ferrite grains. The samples were manufactured with a constant tool orientation regarding the weld direction. This was achieved by using the rotational axis of the 2-axis positioner table. The constant tool orientation was used to

eliminate any influence of the tool orientation on the deposition sequence. The corners of the part were rounded to a radius of 10 mm so that the rotational acceleration of the positioner was sufficient to keep the tool-path velocity as constant as possible. The welding speed was 500 mm/min. The wire (0.8 mm, ER 2209) feeding rate was kept constant at 3 m/min and argon gas was used locally with a flow rate of 7.5 l/min, to protect the melt-pool from the atmosphere. The parameter sets needed to be fine-tuned. The procedure is described in Section 4.2.3 together with the results. Initial parameter sets for variation of welding speed and power to produce material with different cooling rates were defined and fine-tuned in the same manner.

This approach has several drawbacks:

- A significant amount of experimental work for the generation of new parameter sets.
- The disturbance rejection capabilities (for example from effects of the acceleration of the positioner table) are low.
- The single-track wide walls showed little microstructural variation, so that the influence of process parameters could not be studied.
- The fabrication of structures more than one track wide would necessitate the integration of another parameter describing the additional height due to lateral overlap of welded tracks.

To achieve a higher difference in cooling and solidification rate the sample geometry was changed to approx. 12 mm wide and 130 mm long blocks. The reason for the higher variation in cooling rate is that the ratio of surface to volume is lower for the block like structures, so that less heat loss occurs by radiation and convection. Figure 17 shows the influence of the wall width on the ferrite content of additively manufactured multiple track wide walls. The cooling rate is increased, because the local heat flow from the melt pool occurs in 2 dimensions instead of 1 (Figure 17 (b)).

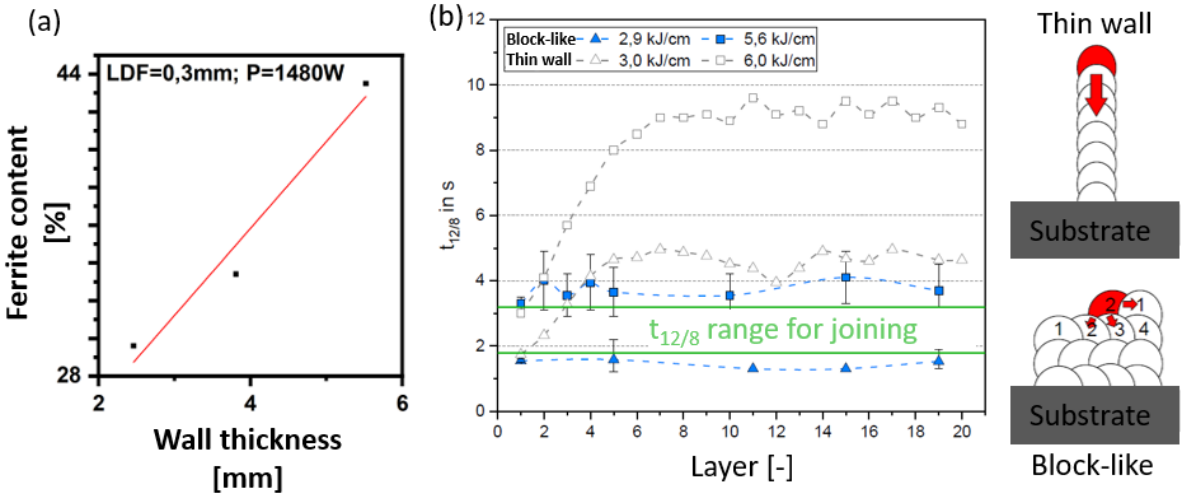

Figure 17: (a) Relationship between wall thickness and ferrite content for multi-layer walls made from duplex stainless steel [26] and (b) difference in $t_{12/8}$ time for different heat inputs and geometry for wire arc additive manufacturing with cold metal deposition. [16]

The manufacture of more than one track wide structure poses two additional challenges:

1) The lateral distance between or the overlap of individual weld-tracks makes the occurrence of lack of fusion defects more likely (Figure 18 (b)).
2) The overlap of consecutive neighboring weld-tracks creates a "ramp"-effect, where the height increases from the first to the last welded track (Figure 18 (a)).

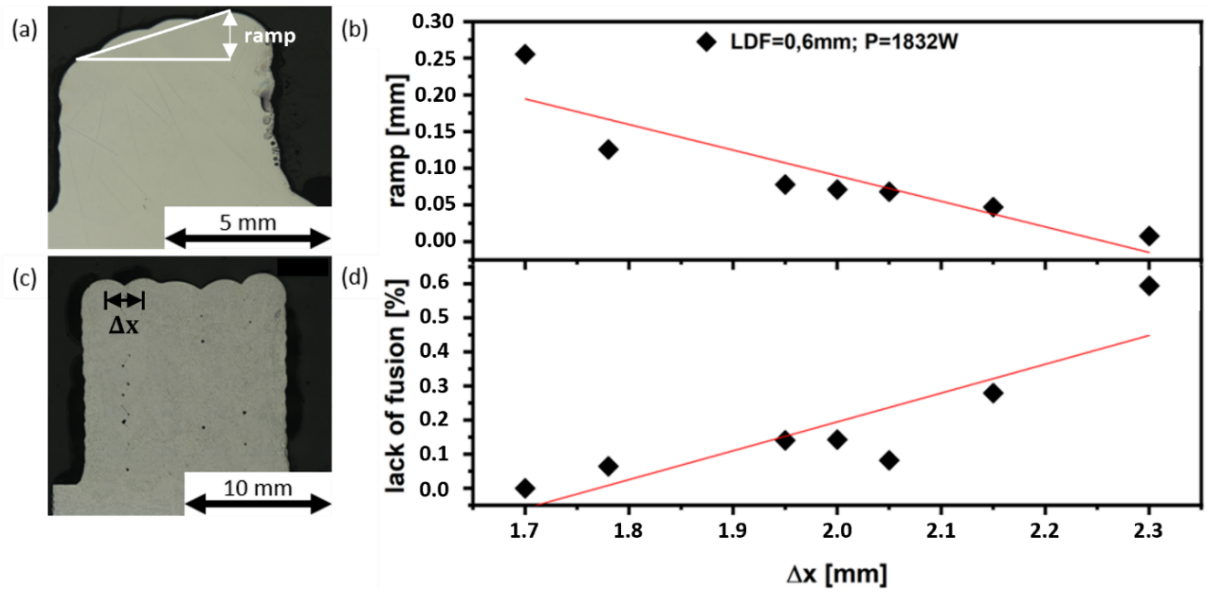

Figure 18: (a) Specimen showing the ramp-effect, (b) height increase from lowest to highest point in multi-track walls, (c) lack of fusion independence of lateral distance (Δx) of the weld tracks and (c) specimen with LoF defect due to too high lateral offset (Δx). [26]

To reliably produce specimens with repeatable properties there are two requirements for the process control method:

- The temperature of the part needs to be controlled.
- A process control method needs to be developed, that accounts for the variation in layer height and controls the melt-pool temperature.

The first requirement was fulfilled by automated part temperature evaluation via the infrared camera. The interpass temperature was in this case defined as the part temperature at the start-point for the next deposition sequence. For the second requirement a process control method based on the interaction between wire-tip and melt-pool was developed.

3.3.3 Closed Loop Process Control

For a stable process in L-DED-wire a stable liquid bridge between wire and substrate needs to be ensured at all times. The mass specific energy is minimal, when the wire speed is maximized while still being always fully molten. An interaction force between the wire and the viscous melt-pool characterizes this process mode. When the force is too high, "stubbing" of the wire occurs, which can lead to lack of fusion defects. When an appropriate force is always realized, the deposition process can be stabilized without the occurrence of defects [126]. For this purpose, the interaction force between the melt-pool and the wire

needs to be measured as accurately as possible. The force at the tip of the wire needs to be balanced, by corresponding forces on the guide mechanism and the feeding mechanism. Therefore, the interaction force can be determined either by measuring the force on a part of the guide mechanism or by the force that the wire feeding mechanism exerts. The first is complicated by the influence of friction on the measurement results but can be implemented downstream of the wire feeding mechanism, thereby eliminating the influence of disturbances from drawing the wire from the feedstock reservoir (Figure 20). The second is implemented more easily [126], but change of the resistance from the feedstock reservoir cannot be eliminated.

Motor Torque Controlled Processing

In the electrical motor of the wire feeding mechanism electrical energy (P_{el}) is transformed into mechanical energy (P_{mech}) and heat through resistive losses (P_J) according to Equation (5).

$$P_{el} = P_{mech} + P_J \tag{5}$$

In more detail this relationship can be written as [135]:

$$U_{mot} \times I_{mot} = \frac{\pi}{30000} \times n \times M + R \times I_{mot}^2 \tag{6}$$

Here, U_{mot}, I_{mot}, n, $\vec{M}$ and R are the voltage, current, revolutions per minute, torque and electrical resistance of the motor respectively. Two important metrics of this transformation are the speed (k_n) and torque constants (k_M).

$$n = k_n \times U_{mot} \tag{7}$$

$$\vec{M} = k_m \times I_{mot} \tag{8}$$

In essence, the motor torque is proportional to the motor current. The motor in the feeding mechanism has a torque constant of k_m=52.5 mN·m/A. With a gear ratio of 18:1 and a diameter of the feeding rolls of approx. 10 mm this leads to a force constant of approx. 94.5 N/A for the interaction force in a normal direction from the substrate between wire and substrate.

A current measuring transducer (WAGO 857-550) was inserted into the current carrying wire between front feeding and control unit of the DINSE wire feeding mechanism. A feedback control algorithm using the following control law (Figure 19) was realized on the KUKA KRC 4 controller using the inbuilt signal manipulation tools. The implemented control law exhibits PI-behavior. Due to limitations in signal processing by the KRC 4 controller, the integrative constant could not be set independently.

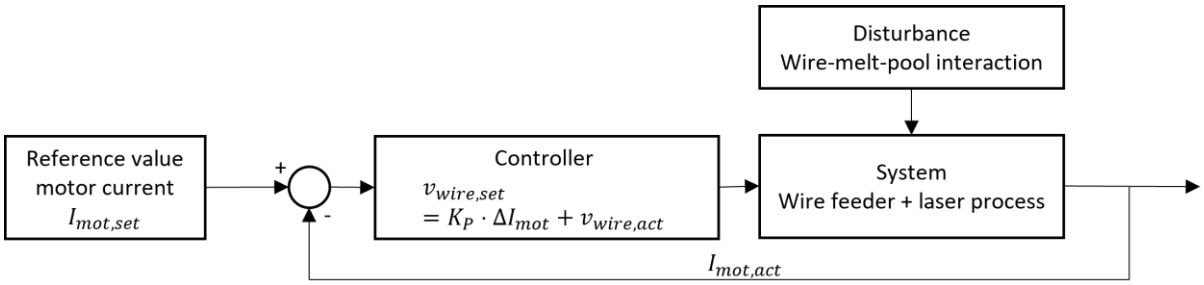

Figure 19: Schematic of the controller, where $I_{mot,set}$, $v_{wire,set}$ P, ΔI_{mot}, $v_{wire,act}$ and $I_{mot,act}$ represent the setpoint value for the controller, the setpoint value for the wire feeding mechanism, the proportional parameter, the control error, the actual wire speed and the actual value of the motor current respectively.

An appropriate reference value for the motor current was chosen by measuring the idle current when no process resistance impedes the wire feed speed. According to the above determined force constant an interaction force of approx. 5 N to 10 N was targeted by setting the reference current approx. 50 mA to 100 mA above the idle current. To achieve this the controller manipulates the set-point for the wire feed rate in dependence of the difference between the set-point and actual motor current. The signals and behaviour of the control circuit were recorded using the inbuilt "Trace"-function from the KRC4-Controller.

Direct force-controlled process control

To eliminate the influence of friction on the motor torque necessary for drawing of the wire from the feedstock reservoir, a system for measurement of the force on the guide mechanism was developed and implemented in the L-DED-wire system. To generate a force on the wire guide, the wire was deflected downstream of the front feeding mechanism by the distance a_{wire} (Figure 20) at the half distance l between wire feeder and laser optic. The resulting idealized dependence of the force on the deflected portion of the wire on the process force $F_{process}$ is given in Equation (9).

$$F_{guide} \sim F_{process} \times \frac{a_{wire}}{l} \tag{9}$$

To obtain a good signal, a_{wire}/l should be maximized while also maximizing the bending radius of the wire to prevent plastic deformation of the feedstock. The proportional dependence was validated experimentally. Typical values for a_{wire}/l that were achieved with the available hardware were around 0.3. A setup including a 200 N tension and compression load cell by A.S.T. Dresden GmbH and a MGCplus measuring amplifier by Hottinger Baldwin Messtechnik was connected to a Beckhoff programmable logic controller on which a proportional-integral-derivative-(PID) controller running at 1 kHz real time was implemented. The PID-control parameters were tuned experimentally. The force on the guide mechanism could reliably be reduced to below 2 N with this setup.

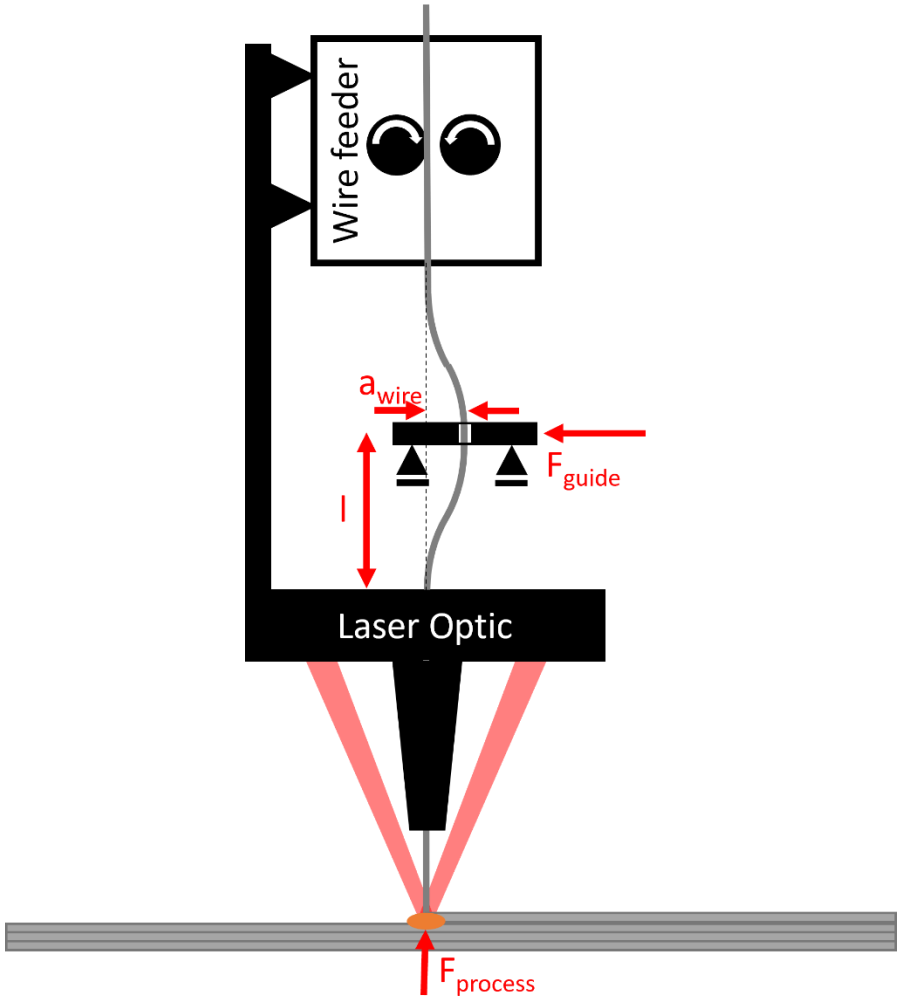

Figure 20: Measurement principle for force controlled L-DED-wire-process [22].

Layer Height Control

For coaxial laser directed energy deposition a self-balancing of the layer height can be achieved by this control method. A longer irradiated section of wire leads to more energy introduced into the wire relative to the substrate. Consequently, the wire melting rate is increased, leading to more material being deposited while the amount of energy available for the remelting of the substrate is reduced. Thus, a balance must be achieved between sufficient energy input for proper bonding and mass specific energy efficiency. In practice a preprogrammed layer height was set and adjusted until a stable process with a lack of fusion free deposit was achieved.

The developments were used for the fabrication of multiple track wide walls, freeform demonstrator parts and demonstrator parts for pressure tanks. The influence of interpass temperature on the microstructure and mechanical properties of the multiple track wide walls was investigated extensively using the instrumented indentation method. A much wider variation in austenite ferrite ratios was produced this way. Specimens for fatigue tests were extracted from the parts. The pressure tank demonstrator parts were built to investigate the influence of weld track order on the residual stress distribution.

3.3.4 Residual Stress Design

In additive manufacturing design parameters, like the order of deposition sequences, determine the residual stress state of the part. Newly deposited material solidifies, cools and contracts. The substrate or already deposited material is at a lower temperature than the deposited material. Due to the difference in temperature, thermal contraction is inhomogeneous, resulting in strain mismatch and therefore residual stresses. These stresses reduce the useable load range of parts, increase the damage from corrosion and wear and therefore need to be considered in the design phase. Stress concentrations and their interaction with additional operational demands like wear and corrosion are of special interest. Designing the layer build order during tank manufacture for example, so that the media facing side is placed under compressive, or at least not tensile stresses might aide in improving the performance.

The sample tank geometry is shown in Figure 21 (a). It has a square footprint (80 mm × 80 mm) with round corners (5 mm radius) and a height of approx. 80 mm. Rounding of the corners was performed to reduce stress concentrations and improve producibility. The residual strain measurement locations were chosen so that the expected residual stress field could be validated and the maximum residual stresses could be determined.

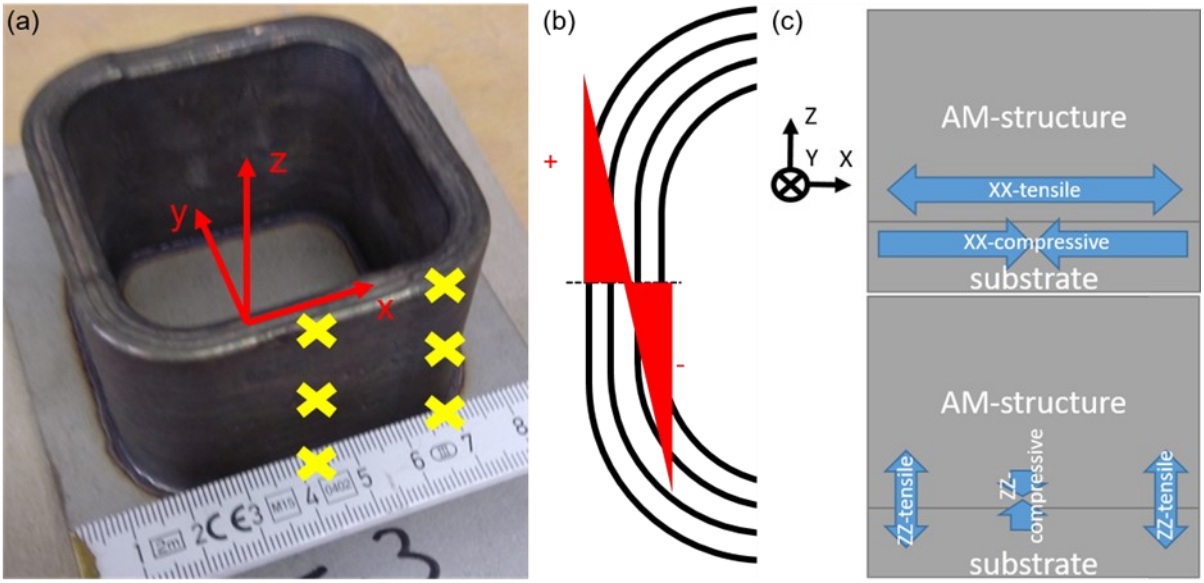

Figure 21 (a) Sample geometry with strain measurement locations, (b) expected residual stress distribution in a single layer, (c) global residual stress distribution in the whole part.

The tank geometry was deposited in the following way: For every layer three tracks were deposited with the order from the inside to the outside of the sample. The layer height and the lateral offset between layers were 0.85 mm and 1.8 mm respectively. A laser power of 2 kW and welding speed of 1 m/min were employed. The wire (3Dprint AM 2209 wire) feed rate was controlled via the motor current. The inside track was deposited directly after the outside track of the layer below. For the center and outside tracks waiting times were implemented, so that the interpass temperature was kept below 300°C.

The general stress distributions, that are expected are shown in Figure 21 (b) and Figure 21 (c). During deposition of the cross section the outer layers contract, placing the inner layers under compressive stresses, while themselves being kept in a tensile stress state. Viewed from a side, the contraction of the deposited material causes tensile stresses in the horizontal direction of the deposited material along the track direction, which are balanced by compressive stresses in the substrate. This stress distribution leads to an upward bending of the substrate, which is accompanied by tensile stresses in the vertical direction at the outer edges of the part and compressive stresses in the center of the wall.

3.4 Microstructure Analysis

In the following sections the methods for the analysis of the microstructure of the material produced with laser beam welding and laser beam and wire additive manufacturing are presented. The samples were investigated metallogaphically using optical and scanning electron microscopy as well as using high energy X-ray diffraction.

3.4.1 Optical Microscopy

The samples were prepared by polishing with emery paper from 360 grit to 2500 grit. Then the samples were polished using a diamond suspension with particle sizes of 6 µm, 3 µm and 1 µm. As a final step the samples were polished using a silicon oxide polishing suspension. For optical microscopy, the samples were etched in a Beraha II solution with half the nominal acid content for 1 to 7 seconds until a slight blue color could be observed. The etching results depend on the alloy composition and the process parameters. Therefore, no etching procedure could be determined, that worked equally well on all samples.

Optical microscopy was performed on a LEICA DMI5000 M, Keyence VHX-7000 digital microscope and Leica M80 stereo microscope depending on the availability of the microscope and characterization task. Optical Microscopy was used to determine the geometric features of weldments and additive structures, validate the presence of defects in the additively manufactured material and observe phase composition, microstructural features and the morphology of fracture surfaces. The microstructure of laser beam welded and additively manufactured samples was analyzed by optical microscopy in the as-built condition and after the tensile tests.

3.4.2 Optical Measurement of Phase Composition

Optical micrographs were taken using a Keyence VHX-7100 digital microscope in monochromatic mode (Figure 22 (a)) at magnification of at least 400x [136]. High magnifications are necessary to accurately image the small intragranular austenite. The greyscale images were transformed to black and white images using a uniform threshold (Figure 22 (b)). The threshold was determined according to Otsu's method [137], where the intra-class variance is minimized.

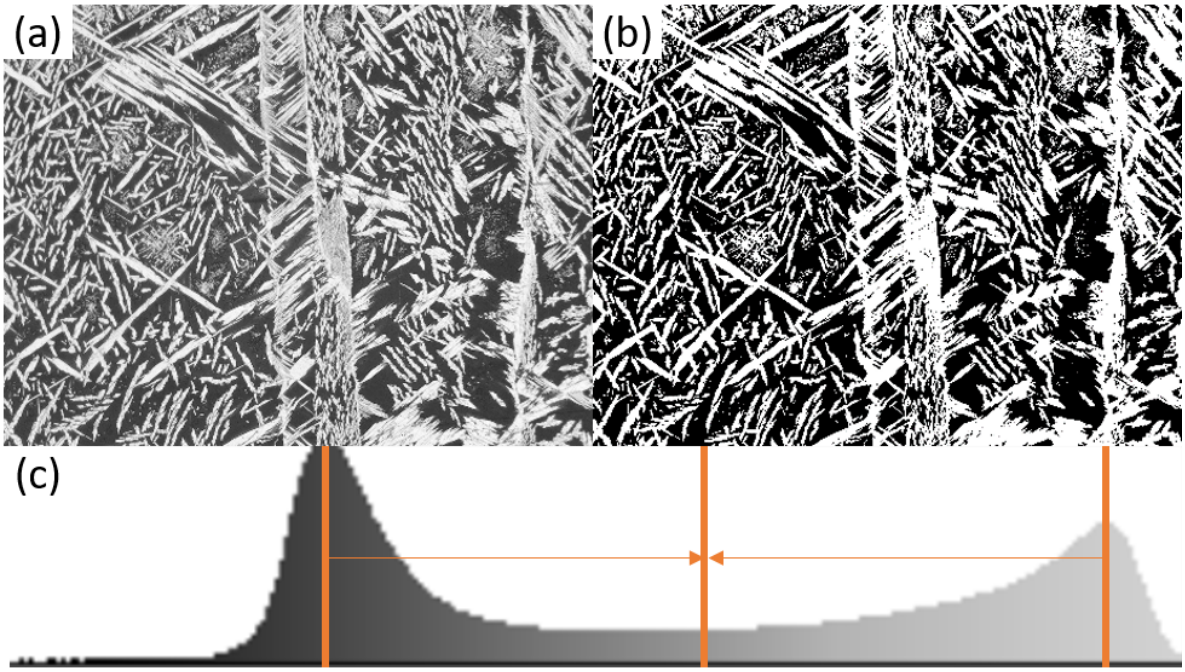

Figure 22: Evaluation of the optical micrographs for quantification of ferrite/ austenite fraction (400x magnification), (a) original greyscale image, (b) binarized image and (c) histogram of grey values for the original image.

The high magnification leads to high variance with regard to the phase fraction in individual images. The local phase fraction — for example at prior ferrite-ferrite grain boundaries — can vary quite substantially from the bulk fraction. To improve the accuracy of the measurement at least 10 images per sample were evaluated. In most cases a line scan along the entire height of the sample was performed. This allows for an assessment of the spatial variation of microstructure. The thresholding procedure together with the motorized stage of the digital microscope allows for automated evaluation of large numbers of images, offering a faster method than the electron backscatter diffraction (EBSD) [25]. However, the measurements are heavily dependent on the quality of the color etching (Figure 23). Especially under-etched ferritic parts of the microstructure are problematic since they will often be falsely identified as austenite. Therefore, all micrographs were checked manually and all images with falsely identified regions were discarded. Manual adjustment of the threshold was not performed since the threshold has a large influence on the measured size of the small intragranular austenite and the bias introduced this way is not reproducible.

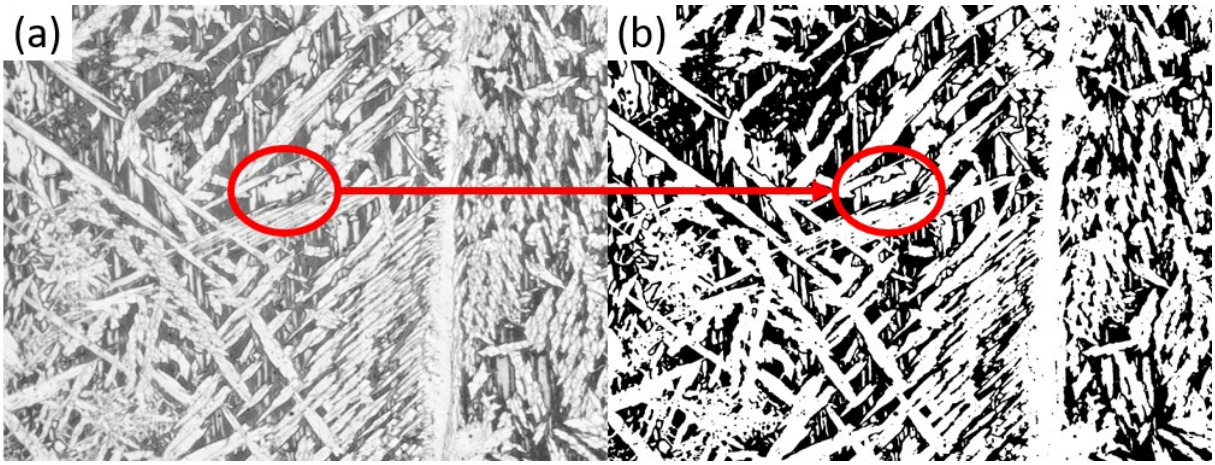

Figure 23: Influence of the etching quality on the results of the automated segmentation process (a) greyscale image with light colored austenite and darkly colored ferrite. (b) Automatically thresholded image.

3.4.3 Scanning Electron Microscopy

The microstructures of the base material, heat affected zone and fusion zone of the welded joints were characterized via electron backscatter diffraction (EBSD) using a scanning electron microscope (SEM) (JEOL JSM-6490LV). EBSD phase maps of these regions were created to analyze the phase composition and grain structure. Microtexture measurements were performed to analyze the differences in crystallographic orientation of the base material, heat affected zone and fusion zone.

The magnification, acceleration voltage, working distance and sample tilt for the additively manufactured samples were chosen according to the characterization task. The grain orientation calculations were performed based on the generalized spherical harmonic expansion method. Energy dispersive X-ray spectra were obtained to discern the spatial variation of chemical composition in the microstructure of the material.

3.4.4 Microstructural Investigation via High Energy X-Ray-Diffraction

Due to the large prior grain size of the duplex weld metal, only a single digit number of ferrite grains could be observed via EBSD while also still resolving the intragranular austenite. To verify the validity of the microtexture measurements and phase fractions determined via EBSD high energy X-Ray diffraction experiments were performed. The measurements were performed at the high energy materials science beamline station P07b at DESY with the following parameters (Table 4):

Table 4: Parameters for the phase and texture analysis using Rietveld refinement.

Parameter	Value
Wavelength	0.142353 Å
Detector Type	Perkin Elmer
Sample to detector Distance	1005 mm
Beam size	0.5 mm × 0.5 mm
Rotation	-90° to 90° data collected every 5° (37 images)
Exposure time	1 s per 5° rotation

High energy X-ray diffraction is one of the most versatile methods of investigating material characteristics. The texture, phase fraction and residual stresses can be determined non-destructively and often *in-situ*. The measurement principle is based on the concept of Bragg-diffraction, where the wavelength (λ), the lattice spacing (d) and the diffraction angle (θ) are related through Bragg's law (Equation (10)):

$$n\lambda = 2d\,sin\theta \tag{10}$$

Using monochromatic X-ray radiation on a polycrystalline material the result are ellipse shaped diffraction patterns, called Debye-Sherrer rings (Figure 24). In untextured materials the Debye-Sherrer rings exhibit uniform brightness. Increasing texture of the material leads to a reduction of the Debye-Sherrer rings to several points according to the crystal symmetry of the material. Thus, the texture of individual crystallographic directions can be computed from the intensity distribution of the diffraction data. Integration along the rotation axis and plotting versus the diffraction angle gives results in a spectrogram as shown in Figure 24 (c). The relative peak size can be analyzed for example using Rietveld refinement. The relative intensity of the peaks is directly related to the amount of the corresponding phase in the material [138]. In addition, residual stresses can be determined from the diffraction data, as strain leads to a change in the lattice spacing and therefore the diffraction angle, causing the Debye-Sherrer rings to change shape and size.

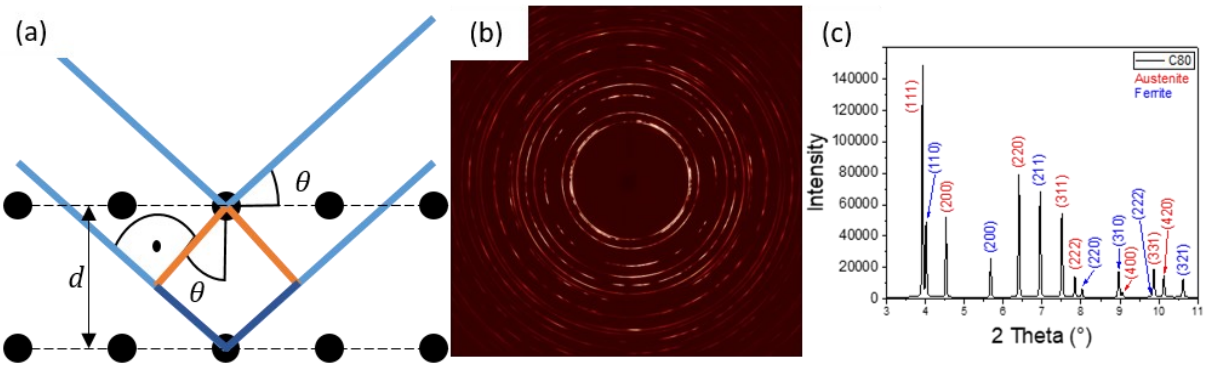

Figure 24: (a) Bragg diffraction, (b) Debye-Sherrer rings and (c) integrated intensity vs diffraction angle.

3.5 Residual Stress Determination using High Energy X-ray Diffraction

Polychromatic X-ray radiation was used for the measurement of residual strain in additively manufactured tank structures. The beamline P61A at DESY was chosen due to the high energy radiation, which allows measurements on materials with high absorption coefficient and thicknesses of multiple millimeters. The $sin2\psi$-method was used in the experiments to calculate residual stresses. The P61Atoolkit [139] was used to analyze the data. In contrast to monochromatic X-ray radiation the utilization of polychromatic X-ray radiation necessitates a different detector setup. The incoming and diffracted beam are limited by system of slits, so that only the diffracted beam from a small gauge volume reaches the detector. The detector is held at a fixed angle with regard to the incoming beam. The sample is then rotated or translated to investigate stress gradients with regard to direction and position. The energy dispersive technique was used, where the number of photons and their energy, which is closely related to their wavelength, were recorded.

Procedure at P61A

The residual strains along the wall thickness of additively manufactured duplex stainless steel specimen were investigated. The residual strain profiles were measured in two regions: At the middle of the sample and at the start of the radius section (Figure 25).

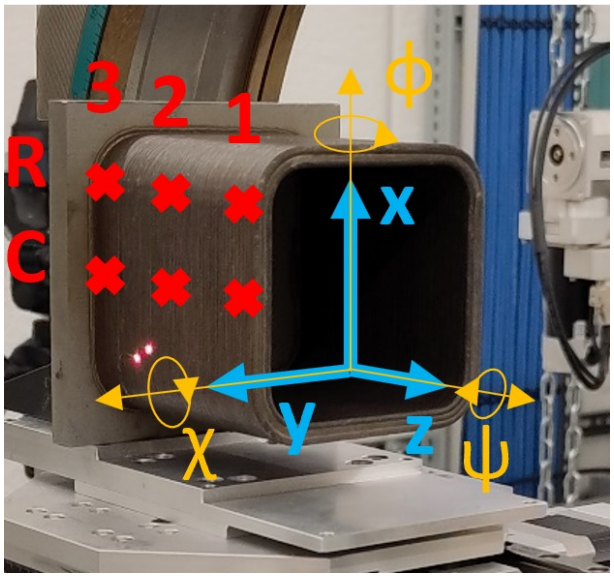

Figure 25: Experimental setup at P61A.

For each region the residual strain profiles were measured in three positions (5 mm from the bottom, in the middle and 5 mm from the top surface of the additively manufactured structure (denoted as C1 to C3 (center) and R1 to R3 (radius)). For each of the six measurement positions 7 points were measured through the wall thickness direction of the sample. For the evaluation the innermost and outermost measurement volume were discarded, so that the remaining five gauge volumes ensured to be fully within the sample. Wiggling in the plane of the walls of the sample with an amplitude of 5 mm in both directions (Y and Z) was employed to reduce the effects of the large grain size. The experimental parameters for each of the measurement positions are given in Table 5. For each in-depth position, the specimen was tilted from 0° to 90°. For each tilt angle, the diffraction patterns

were recorded at 90° and 270°. The 2θ-angles were approx. 6.51° and 7.80° for the 0° and 90° detectors respectively.

Because the duplex microstructure is in different non-quilibrium states depending on the location in the sample, the composition of austenite and ferrite might vary. A variation in chemical composition for high-alloyed materials is accompanied by changes in the lattice spacing. Therefore, the variation in the stress-free lattice spacing was measured on a second sample, where one weld track high and wide, stress-free lamella were cut by electrical discharge machining. For the d_0 sample measurements were made at three positions on the sample and three points along the depth for each position resulting in nine measurements and rotating around chi in 39 steps and counting for 20 seconds while wiggling along the stress-free lamella of the samples.

Table 5: Measurement positions and experimental parameters.

Position	ϕ angles	χ-steps	Time [s]
R1	90, 180	45	20
R2	90, 180	90	20
R3	90, 180	90	20
C1	90, 180	90	30
C2	90	90	30
C3	90, 180	9	20

The material of the sample is very coarse-grained and has a strong texture. Therefore, the resulting spectra are noisy and strongly dependent on the χ-angle. Automatic peak identification is therefore error prone and the stress results are expected to have high uncertainty.

Residual Stress Determination

Due to the high X-ray absorption of the material the noise to signal ratio was not optimal. In Figure 26 (a) the noise from the measurement setup is visible between the peaks whereas for the integrated spectrum the noise is reduced considerably (Figure 26 (b)). Due to the strong texture of the material most of the lattice directions (represented by their photon energies) and their corresponding intensity exhibited a strong dependence on the χ-angle indicated by the large peaks in the spectra.

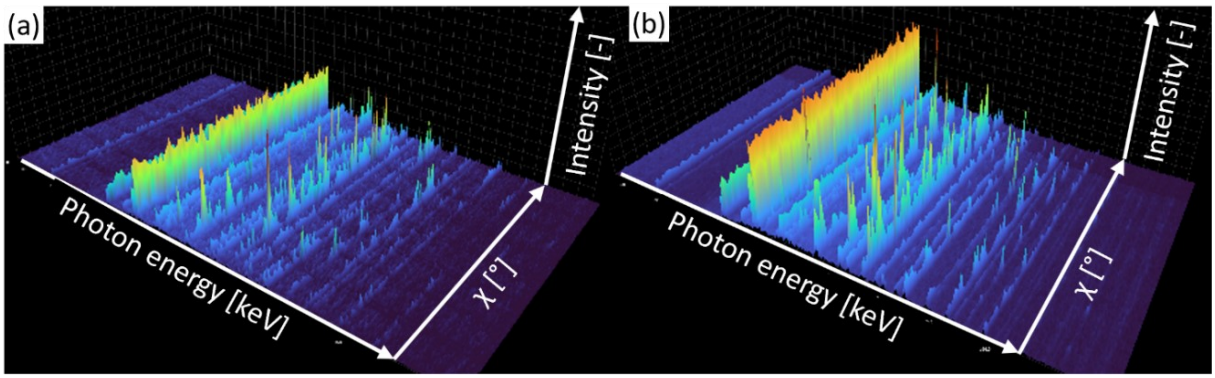

Figure 26 (a) Spectrum before integration and (b) Spectrum after integration.

To account for these challenges the data was integrated over a range of 10°. This considerably improved the noise to signal ratio and decreased the influence of texture. Afterwards, the data was checked manually and photon energies (lattice directions) with high noise and low isotropy were discarded. For each measurement location the stresses from all remaining photon energies were first averaged and then the stresses from both detectors were averaged. The X-Ray elastic constants supplied with the P61A-Toolkit for bcc and fcc iron were used to calculate the residual stresses.

3.6 Mechanical Properties

In the following sections the methods for the determination of the mechanical properties are described. The local properties of the weld metal were investigated using hardness and microhardness testing as well as the instrumented indentation method according to DIN SPEC 4864 [140]. Tensile and fatigue life tests were performed on the laser beam welded joints and the laser and wire additively manufactured material to determine the mechanical properties and measure important engineering quantities like the yield stress, ultimate tensile strength as well as the fatigue life and fatigue limit. Fatigue crack growth tests with load shedding were performed on the additively manufactured material to assess the material properties using the fracture mechanics concept presented in section 3.8.

3.6.1 Hardness and Microhardness

Vickers hardness measurements with a weight of 0.2 kg were performed on the laser beam welded samples using an INNOVATEST® Falcon 5000 machine to characterize the difference in mechanical properties between the base material and the weld metal. 40 indents were made at a depth of 2 mm from the surface across the weldments with a spacing of 180 µm to stay within the specifications of DIN EN ISO 6507 [36].

The Vickers microhardness line scans and maps of the additively manufactured material were measured on the same equipment with a weight of 0.1 kg to characterize the spatial variation of the material properties the of structures. Line scans were performed along the entire height of additively manufactured structures. Hardness mapping was performed to characterize the spatial distribution of material properties within representative regions of the material. Vickers macrohardness measurements (Hv10) were performed using the same equipment to compare the material properties between different additively manufactured specimens.

3.6.2 Instrumented Indentation Test (DIN SPEC 4864)

For the instrumented indentation test an indenter is pushed into the sample orthogonally to the surface until the reference force is achieved. After a defined hold-time the indenter is retracted. The deformation around the indent is measured using an appropriate measurement tool. A simulation model is created, which realistically maps the physical indentation experiment. Important aspects are for example the constitutive material model, the boundary conditions and the indenter sample interaction. The constitutive material model parameters are adjusted iteratively until the difference between the calculated and measured residual deformations is minimized. This procedure results in the computation of stress-strain curves, from which important engineering quantities like the yield strength, ultimate tensile strength and fracture strain, can be extracted. [140]

The instrumented indentation tests were performed on the additively manufactured material to investigate the spatial variation of the mechanical properties. The tests were performed according to DIN SPEC 4864 using an i3D R/BVR automated testing equipment by Imprintec GmbH. For the experiments minimizing the force was imperative to test a small volume of material and reduce the necessary distance between indents. A testing force of 10 kg (98.07 N) was used with a type B [140] indenter. The surface was ground with 500 grit

emery paper. Under theses condition the lowest force with reliable deformation measurement was achieved.

3.6.3 Tensile Testing

Tensile tests on LBW weldments were performed on specimens with the same geometry as the fatigue specimens (Figure 27) to estimate reasonable stress ranges for the fatigue tests. Tensile tests were conducted on specimens from the base material and in the as-welded and laser-surface-remelted condition at a strain rate of 4.17×10^{-4} s^{-1}. Only the contour of the specimens was machined. The flat surfaces were kept in the as-received, as-welded and laser surface remelted conditions respectively. The edges were rounded to a radius of 0.5 mm.

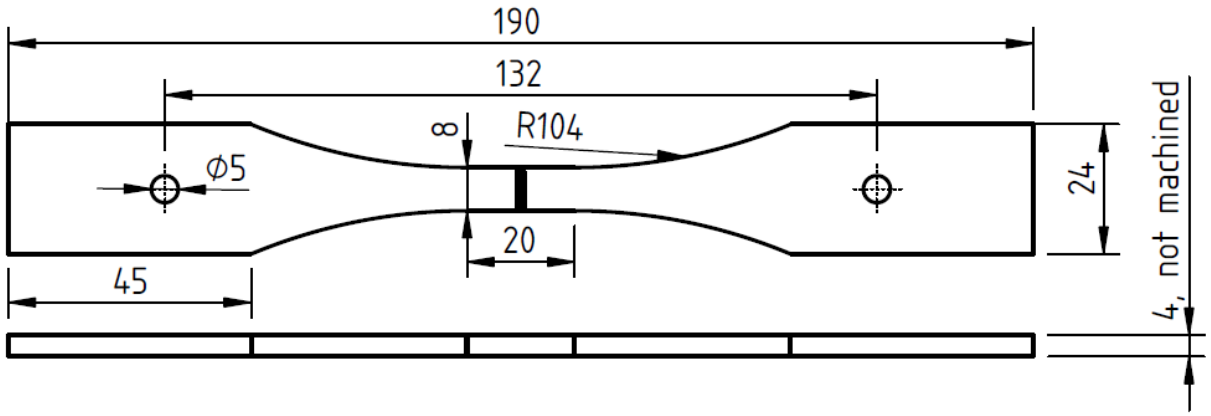

Figure 27: Specimen geometry for fatigue and preliminary tensile tests.

The tensile specimens containing welded joints fractured in the base material region at higher forces and thus stresses than the base material specimens. Due to this inconsistency, additional tensile tests in the as-welded state with twice the recommended gauge length (DIN EN 2002-001, Figure 28) were performed.

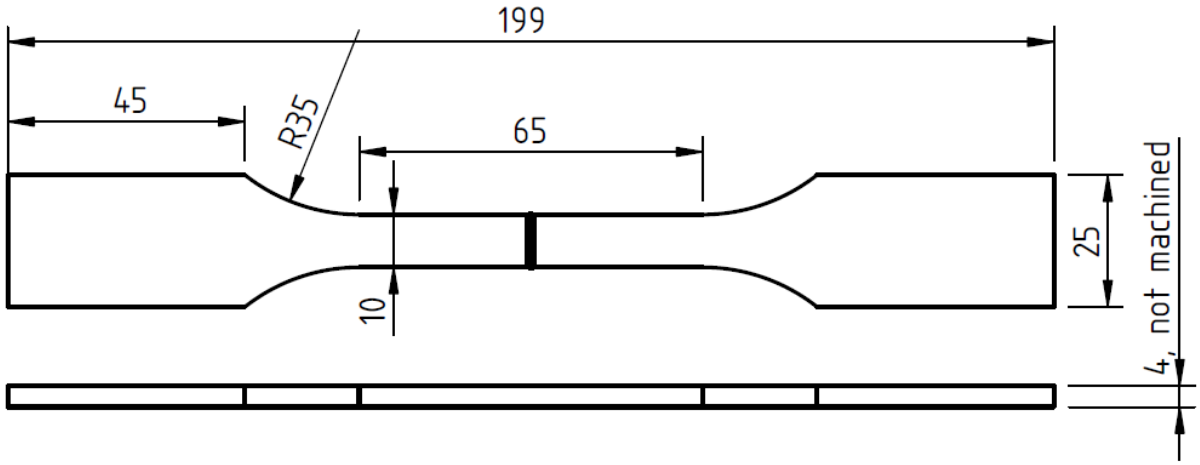

Figure 28: Specimen geometry for the additional tensile tests with twice the recommended gauge length.

The samples from the additively manufactured material were manufactured by extracting rectangular coupons containing the future specimens by cutting with a diamond wire saw,

band saw, water jet or electric discharge machining depending on the tolerances. The final geometry was manufactured by milling. Surface irregularities were removed by milling the specimens from the as built thickness after the process to a final thickness of 1.5 mm. The specimen shape was chosen based on DIN EN ISO 6892-2 [141] because of the short head section of the sample geometry, which allowed extraction of specimens closer to the base of the structure without having to cut into the substrate. The specimen geometry is shown in Figure 69 (e) together with the extraction position. The tests were performed on a ZwickRoell tensile testing machine at a strain rate of 4.63×10^{-4} s^{-1} with a laser extensometer by ZwickRoell for the extension measurement.

3.6.4 Fatigue Tests

Uniaxial fatigue tests on the welded samples were performed under stress control on servo-hydraulic testing machines (INSTRON) with 25 kN and 60 kN load cells at frequencies between 10 Hz and 20 Hz. The frequency was increased for lower loads to reduce the runtime of the fatigue tests. The fracture surfaces from the fatigue tests were investigated under a Leica M80 stereomicroscope to analyse the failure mechanism.

Fatigue testing on additively manufactured material was performed on a 100 kN resonant testing machine from Russenberger Prüfmaschinen AG at approx. 80 Hz to 100 Hz depending on the specimen stiffness and at an R_F–ratio of 0.1. Fatigue tests were performed to determine the fatigue limit by starting at a fixed stress level and increasing the stress level every 2×10^6 cycles. The last stress level at which no break occurred is considered the fatigue limit of the specimen. Additional fatigue tests were performed on a 50 kN resonant testing machine from Russenberger Prüfmaschinen AG at approx. 1000 Hz at an R_F–ratio of 0.1 to increase the testing throughput.

Fatigue samples were extracted from the additively manufactured rectangular hollow parts according to Figure 29 (a). These samples were produced in a layer wise manner. Multiple parts with a variation of laser power and welding speed were produced.

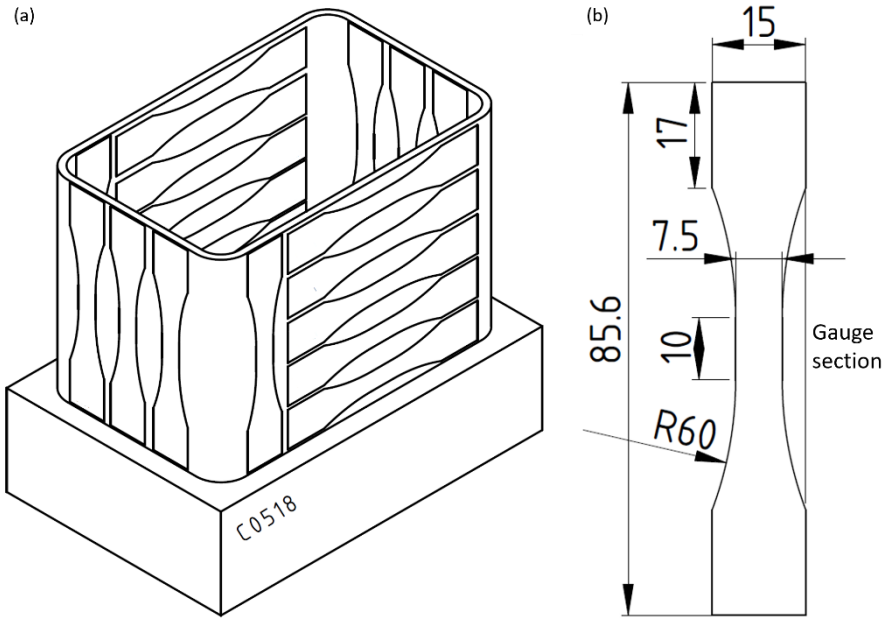

Figure 29: (a) Cutting plan for extraction of the fatigue specimens and (b) dimensions of the fatigue specimens (The final thickness was obtained by grinding the surfaces until the AM surface was fully removed).

Cutting of the specimens resulted in 10 horizontal specimens and 7 vertical specimens from the additively manufactured part, as one of the vertical specimens material was reserved for metallographic investigation across the height of the deposit. Coupons were pre-cut from AM-specimens. The fatigue specimens' contour was machined by milling. The planar surfaces were prepared by grinding using aluminum oxide-based grinding wheels until the AM-surface was fully removed.

Round fatigue specimens were extracted from the block-like samples according to Figure 30. The specimen surface was ground to a maximum roughness below $R_t = 1\ \mu m$ using emery paper.

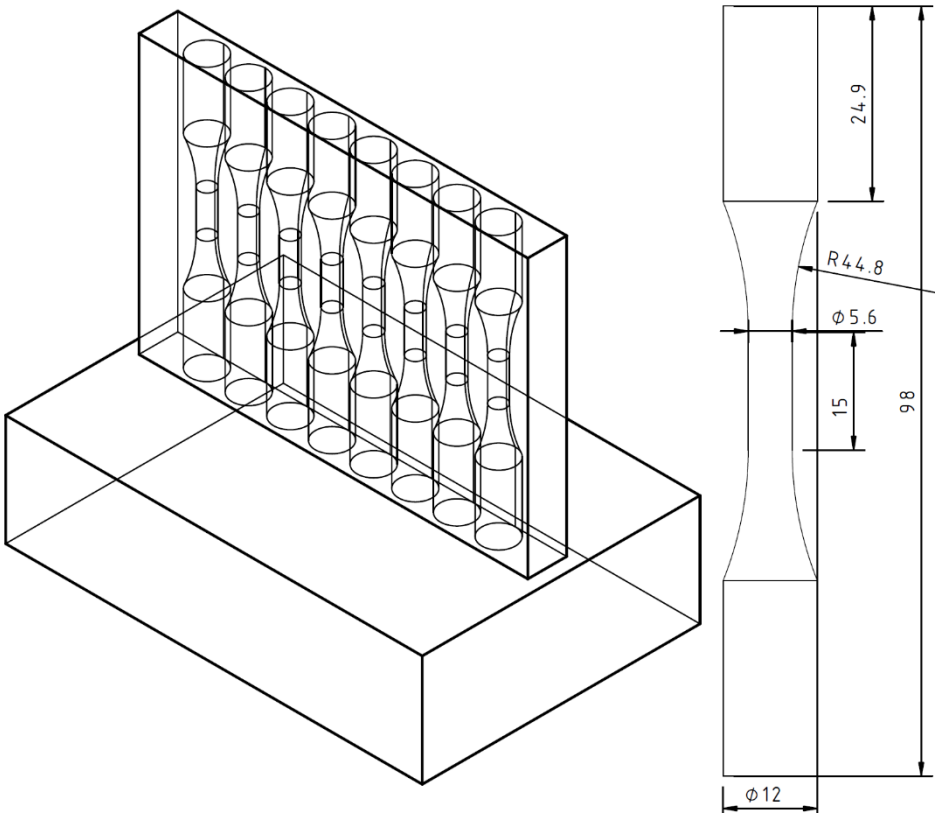

Figure 30: Extraction plan and specimen drawing for the fatigue samples from the block-like samples.

Correction of Nominal Stress

Due to defects created during manufacturing of the samples as well as from the AM-process some samples broke outside of the 10 mm long gauge-section (Figure 29 (b)). These samples were included in the evaluation by correcting for the stress at the initial failure site. The stress distribution in the samples was determined via a simulation using the finite element method (Figure 31). The defect location with regard to the specimen length and width were measured using an optical microscope. Consequently, the stress correction factor was applied to the nominal stress to determine the stress at the failure site.

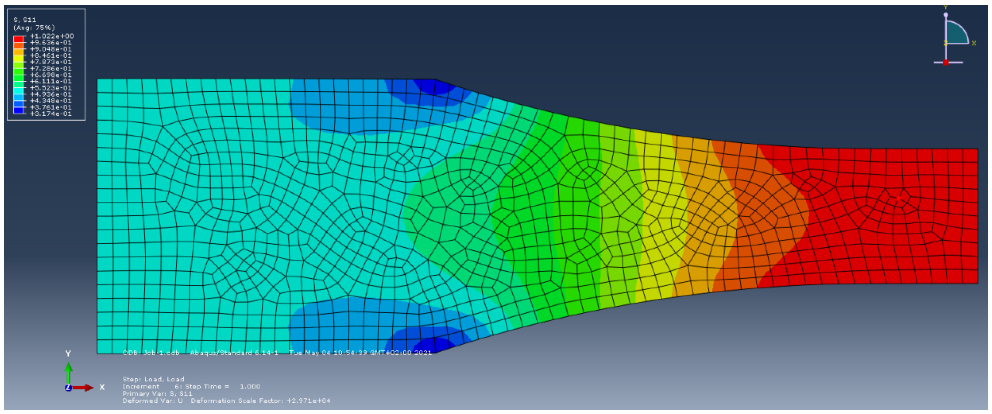

Figure 31: Stress distribution in one half of a flat fatigue specimen for the evaluation of specimens, which did not break in the test section.

Fatigue Crack Propagation Tests

C(T)-50 specimens were extracted from the block-like samples so that the fatigue crack runs along the horizontal plane along the weld track direction (Figure 32). A Testronic 100-kN resonant testing machine of Russenberger Prüfmaschinen AG was used for the load-controlled fatigue crack propagation tests. The tests were performed in accordance with ASTM E466-07 at a resonant frequency of approximately 80 Hz and a load ratio R_F = 0.1 and at room temperature. C(T)-50 specimens with a width of 3 mm and 10 mm were used depending on the dimensions of the primary material. A FRACTOMAT crack length measuring system was used for the measurements of the fatigue crack growth. This measuring system is based on the indirect potential drop method and continuously indicates the measuring values. It generates an accurate measurement of the crack length within the single-digit micrometer range and can also be used to control the propagation of the crack. For determination of the long crack threshold stress intensity range the load-shedding procedure from ASTM E466-07 with continuous load-decrease was employed.

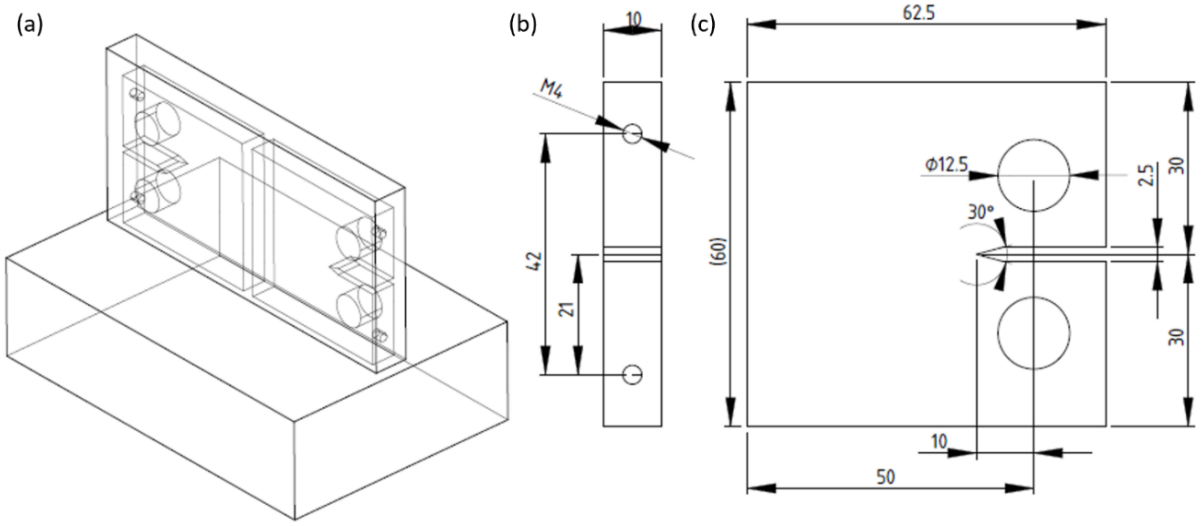

Figure 32: Extraction scheme for C(T)-50 specimens from block-like structures.

3.7 Radiographic Inspection

The weldments were inspected via X-ray radiography on a COUGAR VXP micro-focus device. An acceleration voltage of 100 kV and a current of 275 µA were employed with a distance of 74 mm from the source to the specimen and 315 mm from the specimen to the detector. The acceleration voltage was chosen to stay within the specifications of DIN EN ISO 17636-2 [142].

The porosity of the additively manufactured samples was investigated on the same equipment. For the radiographic inspection specimens taken from the sides of the part, as shown in Figure 29, were extracted. The surfaces were milled so that surface irregularities did not superimpose on any internal defects. The remaining thickness was 1.5 mm. The equipment was operated with an acceleration voltage of 110 kV and a current of 100 µA.

An array of images was combined using the automated acquisition and image stitching feature implemented in the software of the machine. This way large volumes of material could be examined while still achieving a reasonable resolution. Due to the working principle of microfocus X-ray devices only material thicknesses up to approx. 5 mm could be examined. In materials with larger thicknesses the edge distortion leads to a degree of blurring that hinders the detection of defects in the material.

3.8 Fracture Mechanics Concept

The fatigue life of a specimen or structure can be roughly divided into three stages: Fatigue crack initiation, fatigue crack propagation and failure upon surpassing the critical stress intensity of the material. Figure 33 shows the stages of fatigue life with the corresponding length scales extended by the three different stages of fatigue crack growth. When a material is defect free, it can spend a significant portion of its fatigue life in the initiation stage [143]. After an initial crack is formed in the material, the crack begins to grow along a convenient direction depending on the load case and the surrounding microstructure. It is hindered or accelerated by the orientation of slip systems in the grains it crosses, grain boundaries, inclusions, reinforcing particles and residual stresses. At this stage the crack growth rate is highly irregular, as the propagation of the crack front is dependent upon local microstructural features [41,144,145]. When the crack grows the number of microstructural features it interacts with at any time increases, making the propagation rate more even. The stress intensity at the crack tip increases, increasing the plastic deformation ahead of the crack tip. The stage of mechanically or physically short cracks is determined by the crack being of a similar size as the plastic deformation zone around the crack tip. In the final stage the crack length is much larger than the plastic zone size at its tip. In this regime, the conditions at the crack tip can be accurately described by linear elastic fracture mechanics concepts. The crack grows in this mode until the stress intensity at maximum force approaches the critical stress intensity. When this values is surpassed the crack growth becomes unstable. [146]

Generally, the material spends decreasing amounts of time in the later regimes of crack growth as the fatigue crack propagation rate increases by orders of magnitude as the growth mechanism changes and the stress intensity at the crack tip increases. For this reason, the first stages of crack growth are the most important for an accurate prediction of the fatigue failure.

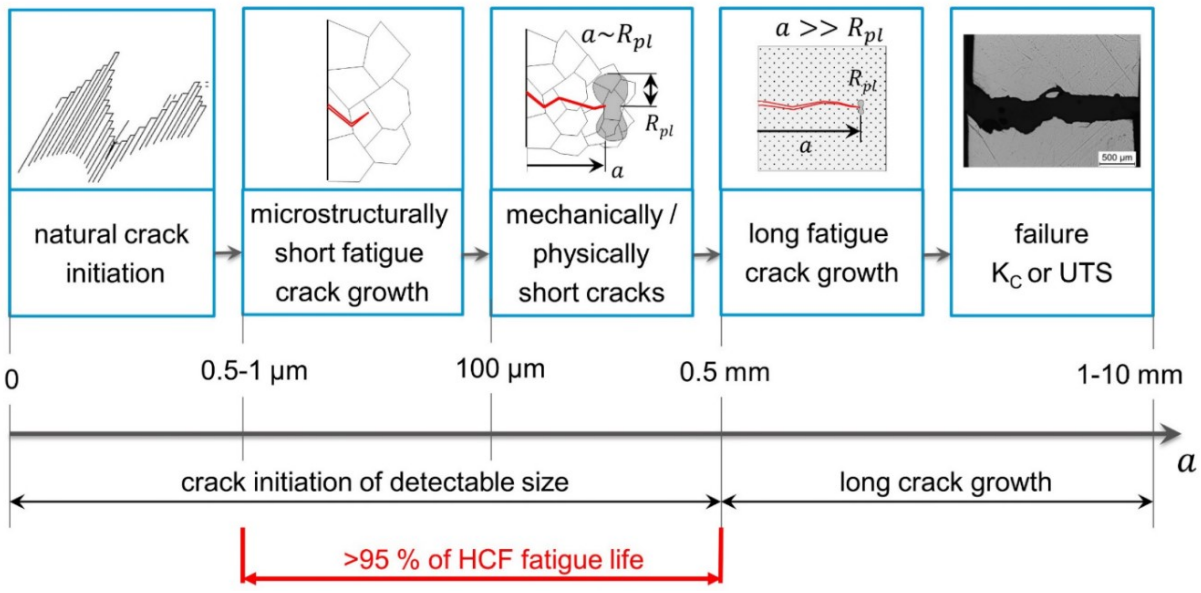

Figure 33: Stages of fatigue life [52] see also [146].

The assessment of the local stress state at the crack tip plays a crucial role in the determination of the fatigue resistance and remaining fatigue life of structures [147]. Usually, the loading conditions of a part lead to a somewhat uniform distribution of stress across the cross section of material. When there is a feature, that does not carry load, such as a pore or an inclusion, a stress inhomogeneity occurs. The stress at an infinitely sharp crack tip mathematically approaches infinity (Figure 34 (a) [148]). Generally, the loading condition is described by the stress intensity factor range ΔK for fatigue cracks (Equation (11)).

$$\Delta K = Y \Delta\sigma \sqrt{\pi a} \tag{11}$$

Here, Y is a geometry factor, $\Delta\sigma$ is the remotely applied stress range and a is the characteristic crack size. The stress intensity factor has been determined analytically and numerically for a wide range of defect types and applications [148–150]. Murakami [151] proposed an alternative expression for irregular defects in the form of Equation (12).

$$\Delta K = Y \Delta\sigma \sqrt{\pi \sqrt{area}} \tag{12}$$

In this case $\sqrt{area}$ is the square root of the area of the defect and Y is a geometry factor, which is 0.5 for internal and 0.65 for surface defects.

In any analysis of a fatigue problem the relationship between applied load, often described by the stress intensity factor range ΔK and the resulting fatigue crack propagation rate (Figure 34 (b)), is vital. For long cracks three typical regions can be determined. The value of stress intensity factor range where the fatigue crack propagation rate asymptotically approaches zero is the long crack threshold stress intensity factor range $\Delta K_{th,LC}$. At growing ΔK there exists a region, where the logarithm of the stress intensity factor range is proportional to the logarithm of the fatigue crack propagation rate often called the Paris-Erdogan-Regime [152]. When the critical stress intensity factor is exceeded, the crack growth is unstable and the material fractures spontaneously. Naturally initiated short cracks and cracks from already existing defects deviate from this behavior. They must overcome the microstructural barriers and barriers from the build-up of the plastic zone before conforming to the behavior of long cracks. Short cracks might even grow for some time and then be stopped by the build-up of resistances against crack growth. [153]

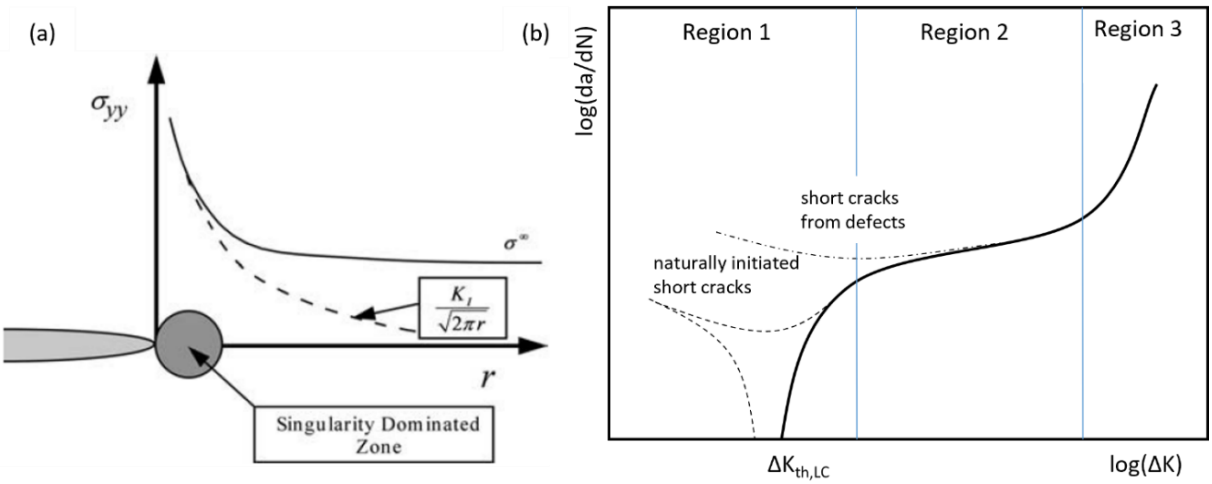

Figure 34: (a) Stress intensity at the tip of a sharp crack [148] and (b) regimes of the fatigue crack propagation rate.

Methods for describing the build-up of resistance against fatigue crack propagation and the fatigue strength of materials containing cracks include the Kitagawa-Takahashi diagram (Figure 35 (a)) and the cyclic R-curve (Figure 35 (b)). [144,147,153] Both methods describe the varying resistance of a material in dependence of the characteristic defect size and the applied load. They have different advantages and drawbacks. To create a Kitagawa-Takahashi diagram many specimens containing defects of different size must be tested in time-consuming fatigue-limit tests. The cyclic-R-curve is very difficult to determine directly, as crack extensions in the single micrometer range needs to be accurately measured [144,146,154]. Its application is less straightforward than the Kitagawa-Takahashi diagram. To determine whether a fatigue crack will grow from a given defect it must be determined whether the curve of applied load and the cyclic-R-curve will intersect. Therefore, an accurate determination of the stress intensity factor and its dependence on the crack extension is also critical for the application of the concept [23].

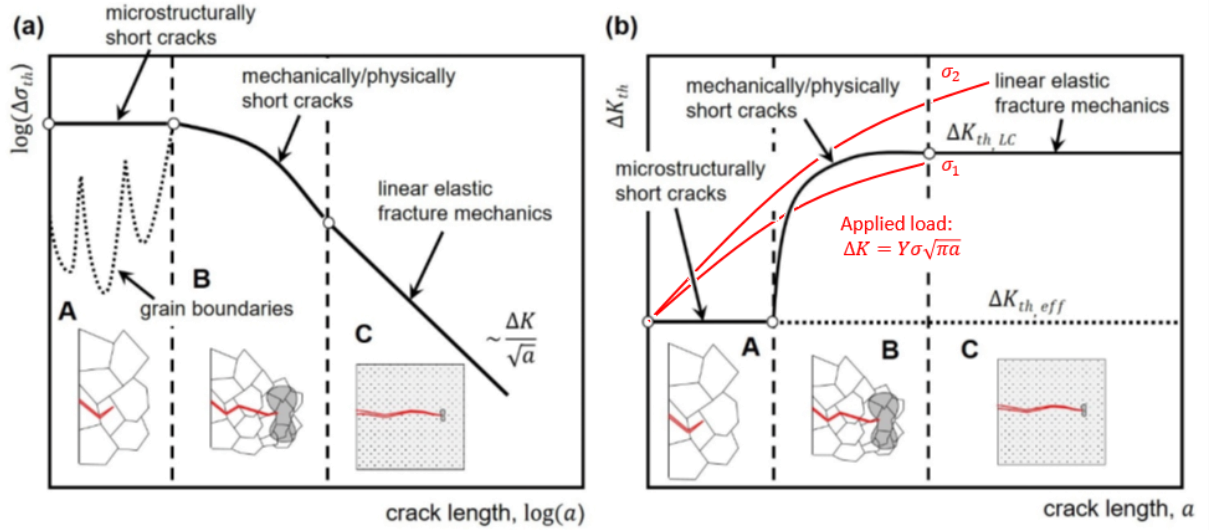

Figure 35: Comparison between the Kitagawa-Takahashi Diagram(a) and the cyclic R-curve (b). [52]

All material possess an intrinsic resistance against crack growth [155,156]. Below this value no cracks will grow. The intrinsic threshold stress intensity range ($\Delta K_{th,eff}$) can be estimated according to Equation (13) [144] or Equation (14) [144,157], where E and $|b|$ represent the Young's Modulus and burgers vector respectively.

$$\Delta K_{th,eff} \approx 1.6 \cdot 10^{-5} \cdot E \tag{13}$$

$$\Delta K_{th,eff} \approx \frac{3}{4} E \sqrt{|b|} \tag{14}$$

The value mainly depends on the Young's Modulus E. Consequently, for steels with a Young's Modulus between 190 GPa and 210 GPa values from 3.0 $\mathrm{MPa}\sqrt{\mathrm{m}}$ to 3.6 $\mathrm{MPa}\sqrt{\mathrm{m}}$ are to be expected from Equation (12) and 2.4 $\mathrm{MPa}\sqrt{\mathrm{m}}$ to 2.6 $\mathrm{MPa}\sqrt{\mathrm{m}}$ from Equation (14).

4 Results and Discussion

4.1 Laser Beam Welding

In this section the results of the systematic experimental work regarding the laser beam welding of duplex stainless steel are presented. The objective was to improve the fatigue properties while also keeping the cost for post processing steps minimal. The work focused on the influence of a laser remelting procedure on the fatigue properties. The results were published in [19]. The possibility to improve the balance of austenite and ferrite with subsequent passes during electron beam welding is well known [13]. The additional heat input without keyhole formation leads to additional austenite formation and therefore improved corrosion resistance and ductility. The influence of surface remelting on the fatigue properties was investigated for the first time as part of this work. Based on the literature the main reason for fatigue crack initiation, especially in the high cycle fatigue regime are geometric notches. Only when no such notches are present, are large and conveniently oriented austenite grains responsible for crack initiation. Therefore, any joining procedure and post processing should focus on excluding features that facilitate those two origins of failure. Therefore, high welding speeds with comparatively low heat inputs were preferred for the welding and laser surface remelting procedures. The parameters were listed in Section 3.2.

4.1.1 Visual Inspection of the Laser Beam Weldments

The optimization of the process parameters was performed based on visual inspection in the laser-surface-remelted state. As Fomin et al. [52,158] has shown, the geometric notch at the surface of weldments in high strength Ti-6Al-4V material has the largest influence on fatigue behavior. Therefore, the primary focus was the elimination of geometric notches. For the as-welded condition the parameters were chosen, so that a sufficient and nearly equal amount of excess weld metal remains on both the top and weld root side (Figure 36 (a)). Consequently, both sides could be remelted so that no underfill occurred without the use of filler wire (Figure 36 (b)).

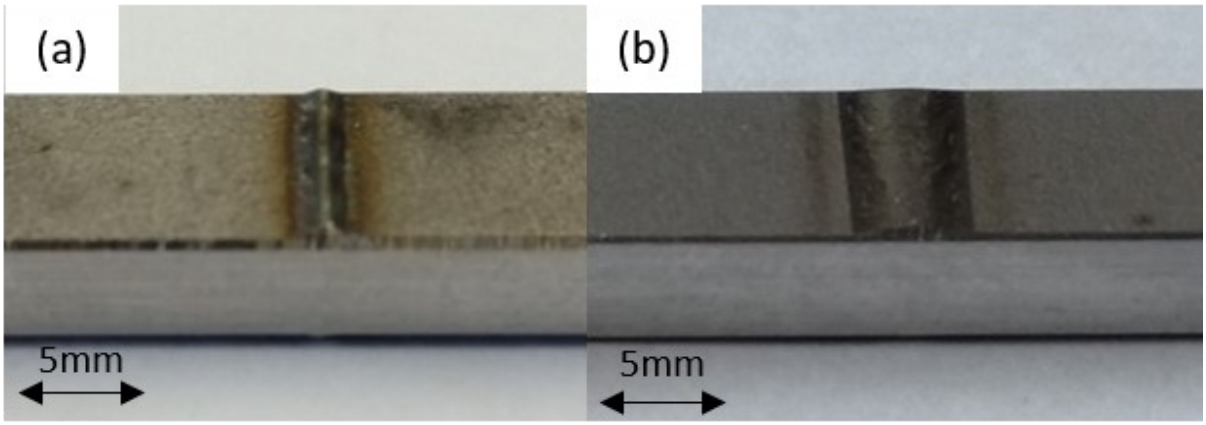

Figure 36: Test section of a fatigue specimen in the (a) as-welded and (b) laser-surface-remelted condition.

The results show that it is possible to create laser beam welded butt joints in DSS 2205 without weld imperfections such as underfill or large amounts of excess weld metal using filler wire and a laser surface remelting treatment with the defocused laser beam. The laser surface remelting treatment for smoothening the weld surface can be performed on the same equipment as the welding process, thus eliminating the need for additional machining steps of the weldment.

4.1.2 Radiographic Inspection

The radiographic inspection showed the weldments to be nearly porosity free. An example weldment for the laser-surface-remelted condition is shown in (Figure 37). Only six pores between 10 µm and 25 µm diameter could be discerned over a 20 mm length of the weldment. The size of the pores is very close to the limit of the resolution of the X-ray micrographs. Therefore, it can be concluded, that the weldments are free of macro-pores, but the existence of micro-porosity below 10 µm in size cannot be excluded. Figure 37 further shows that the examined weld seam is free of cracks. Overall, the laser-surface-remelted weld is almost free of defects and discontinuities.

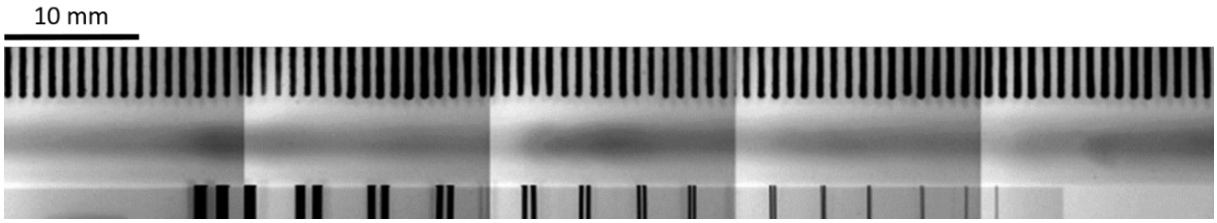

Figure 37: X-Ray image of and laser-surface-remelted weldment before extraction of the specimens. Above the weldment an X-ray ruler is visible for scale. Below the weldment an image quality indicator (EN 462-5) is shown. Sharpening and contrast enhancement filters were employed.

4.1.3 Hardness Measurements

Vickers hardness measurements were performed across the weldments along the rolling direction of the material on the neutral axis of the sheet material. The hardness measurements were performed to validate the assumption, that the weldment is of higher strength than the surrounding material and therefore protects the joint area against deformation under static and dynamic loading conditions. The results of the Vickers microhardness measurements on weldments in the as-welded and the laser-surface-remelted conditions can be seen in Figure 38.

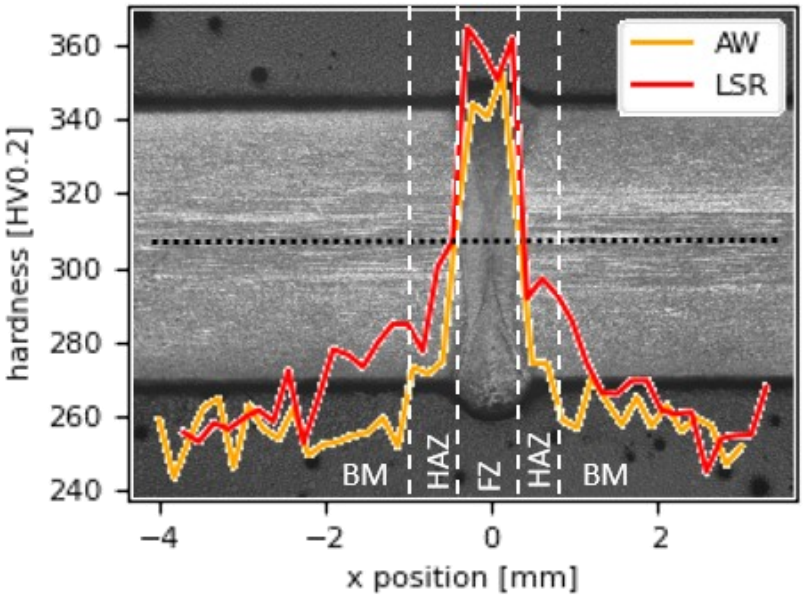

Figure 38: Microhardness profile across the weldments in the as-welded and the laser-surface-remelted conditions. The location of the hardness measurements is shown by the dotted black line. The approximate transitions between fusion zone, heat affected zone and base material are marked by white, dashed lines. [19]

The measurements show a distinct increase of the hardness in the fusion zone of the joint and a slight increase in the heat affected zone. The microhardness of the base material is 262±19 Hv0.2. In the heat affected zone, an average microhardness of 284±10 Hv0.2 and 299±7 Hv0.2 were measured in the as-welded and laser-surface-remelted condition respectively. The fusion zone exhibited a microhardness of 338±25 Hv0.2 and 359±8 Hv0.2 in the as-welded and laser surface remelted conditions respectively.

Based on the microhardness measurement a significant increase in strength of the fusion zone can be expected. A detailed evaluation of the influence of microstructure with regard to the literature on the hardness of weld metals is given in Figure 45.

4.1.4 Microstructural Investigation

The microstructure of the joint was investigated extensively using optical microscopy and EBSD to correlate the results from the hardness, tensile and fatigue tests with the microstructure of the material. Macrographs of the test sections of fatigue specimens in the as-welded and laser-surface-remelted conditions can be seen in Figure 39. The as-welded condition is marked by a higher (0.531 mm) and narrower (1.18 mm) excess weld metal with a lower notch root radius. The laser-surface-remelted condition exhibits flatter (0.35 mm) and broader (4.09 mm) excess weld metal. The remelting treatment has significantly smoothed and expanded the weld surface and reduced the notches at the weld-top and root since mainly the excess weld metal has been remolten. The microstructure in the centre of the weld and morphology of the weld in the interior remain unaffected by the remelting

procedure. The weldments interior morphology can be regarded as for typical laser beam welded butt joints.

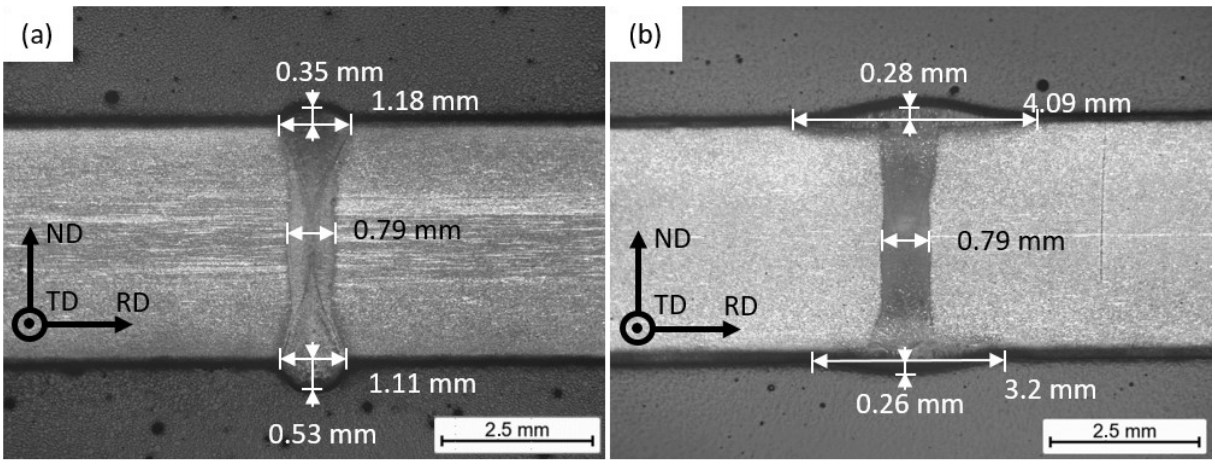

Figure 39: Macrographs of the tests section containing weldments. The samples were etched for approx. 4 seconds with Beraha II etchant. a) Test section of a fatigue-specimen in the as-welded condition, b) test section of a fatigue-specimen in the laser-surface-remelted condition. [19]

On the macrographs a heat-affected zone in the weld metal from the remelting procedure can be discerned by the lighter colour near the weld cap and root, which indicates an increased austenite content in those areas. The increase in austenite content in the heat affected zone from the laser surface remelting treatment is shown in Figure 44 in more detail.

Phase analysis via EBSD revealed that the ferrite fractions in the head sections of fatigue specimens from different batches of base material varied between 54.2 vol.-% and 61.4 vol.-% (Table 6). The standard DIN EN ISO 17781:2017-11 requires a ferrite fraction of 35% to 60% for the base material. The ferrite fraction of batch B of the base material is thus outside of this requirement. This may result in higher strength and reduced ductility and corrosion resistance. Accordingly, the austenite phase fractions were between 38.6 vol.-% and 45.8 vol.-% (Table 7). Figure 40(a) shows for example, that the grains of both phases are arranged row-wise as a result of the rolling process and therefore an aspect ratio $\beta=g_{min}/g_{max}<0.5$ (Table 7). The plate-like austenite and ferrite grains possess aspect ratios of 0.4 ± 0.2 and 0.2 ± 0.2 respectively.

The phases are not homogeneously distributed, because the austenite grains lie close together. The grains of the ferritic phase are coarser than those of the austenite phase. The length of the major axis of the ferrite grains ($g_{maj(\delta)}$) varies between 7.9 µm and 13.5 µm, whereas the variation of the minor axis ($g_{min(\delta)}$) is lower (Table 7). Such variations do not appear in the major axis of austenite grains ($g_{maj(\gamma)}$). From Figure 40 (a) it can be deduced, that the austenite grains exhibit annealing twins, which may influence the grain size determination and probably are the cause for the finer-grained appearance of the austenite phase.

Table 6: Ferrite content in the head section of specimens from different batches of base material.

Specimen	Ferrite content [vol.-%]
Base material A	54.2
Base material B	61.4
As-welded	57.1
laser-surface-remelted	54.4

Table 7: Microstructural features of DSS 2205 base material and weldments determined from an analysis of the EBSD measurements with the software of the scanning electron microscope.

Condition	Ferrite content [vol.-%]	Austenite content [vol.-%]	$g_{may(\delta)}$ [µm]	$g_{min(\delta)}$ [µm]	$g_{may(\gamma)}$ [µm]	$g_{min(\gamma)}$ [µm]	$g_{min(\delta)}/g_{maj(\delta)}$	$g_{min(\gamma)}/g_{maj(\gamma)}$	$M_{TD(\delta)}$	$M_{RD(\delta)}$	$M_{TD(\gamma)}$	$M_{RD(\gamma)}$
Base material	54.4 – 68.3	31.7 – 45.8	13.5 ±3.9	1.9 ±0.5	5.4 ±2.2	1.1 ±0.4	0.2 ±0.2	0.3 ±0.2	3.36	3.42	3	3.14
Fusion zone	96.2	3.8	84.8 ±29.9	14.5 ±4.8	4.0 ±1.5	1.6 ±0.3	0.2 ±0.2	0.3 ±0.2	-/-	2.97	-/-	3.07

The (1 0 0)-, (1 1 0)- and (1 1 1)-pole figures of the ferritic phase are nearly axis and point symmetric with regard to the pole density distribution. The Taylor factors for the ferritic phase in the rolling and transversal directions are nearly identical since the $(1\,1\,0)_\delta$ planes are perpendicular to those directions (see Figure 40(a) and (b)). In this orientation dislocations with the Burgers vector $|b|=d/2\langle 1\,1\,1\rangle$ in the glide system $\{1\,1\,0\}\langle 1\,1\,1\rangle$ cannot be activated because the Burgers vector $|b|$ is parallel to $(1\,1\,0)_\delta$ and the shear stress is therefore zero. For the austenite phase, the difference in the calculated Taylor factors is greater between the rolling direction and transverse direction. In the transverse direction the load would be perpendicular to the $(1\,1\,1)_\gamma$ planes. In the rolling direction the load would be at a slight angle (Figure 41), which is the reason why dislocations with the burgers vector $|b|=d/2\langle 1\,1\,0\rangle$ in the gilde system $\{1\,1\,1\}\langle 1\,1\,0\rangle$ can be more easily activated in the rolling direction than in the transverse direction.

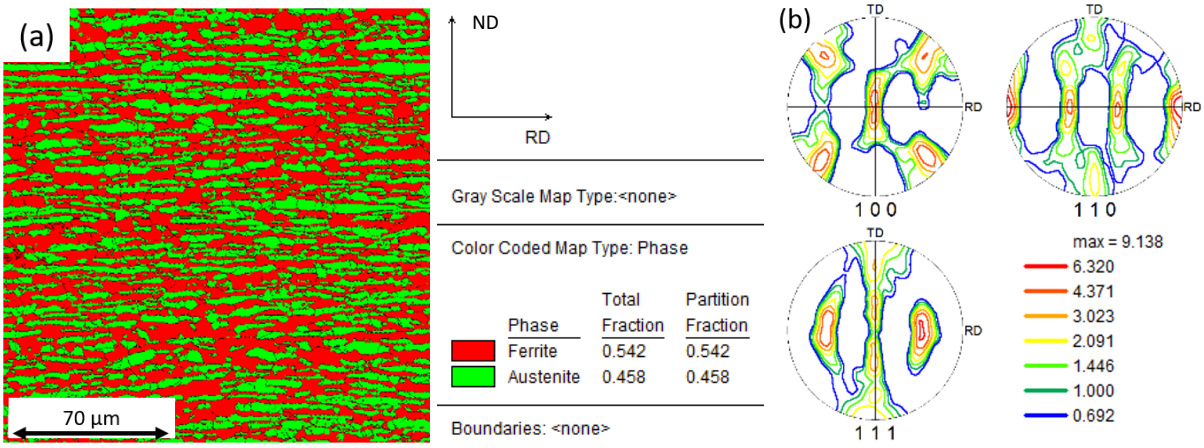

Figure 40: (a) EBSD phase map of the base material of DSS 2205 and (b) ordinary pole figure of the ferritic phase. [19]

In context with the austenite-martensite transformation, the Kurdjimov-Sachs and Nishiyama-Wasserman ($(-1\,1\,1)_\gamma//(0\,1\,1)_\delta$) relationships are well known [2,30], which are also present in the rolled DSS 2205 sheet. If the $(1\,1\,1)_\gamma$-pole figure of the austenite phase (Figure 41) is superimposed on the $(1\,1\,0)_\delta$-pole figure of the δ-Fe-phase (Figure 40 (b)), they are nearly congruent. From this congruence the above-mentioned orientation relationships can be derived, whereby the $(1\,1\,1)_\gamma$ and the $(1\,1\,0)_\delta$ planes are nearly parallel to each other.

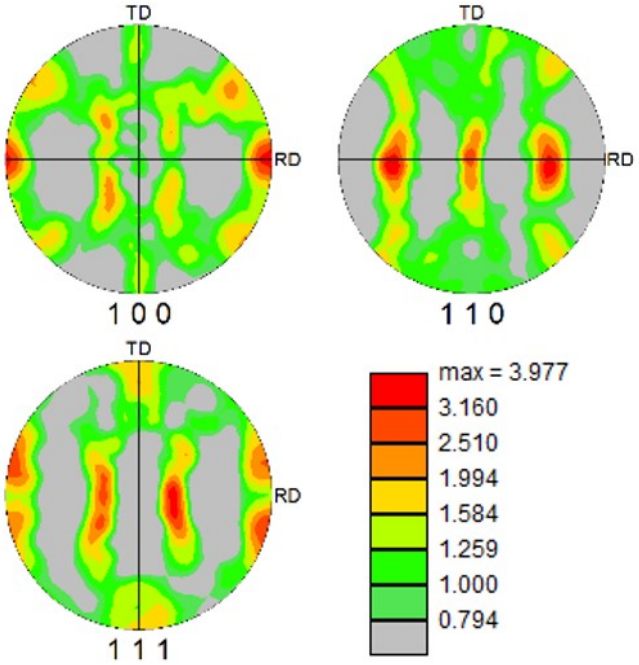

Figure 41: Ordinary (1 0 0)-, (1 1 0)- and (1 1 1)-pole figures of the austenitic austenite phase in the base material. The $(1\,1\,1)_\gamma$ and $(1\,1\,0)_\delta$ (Figure 4(a)) exhibit nearly equal pole density distributions. [19]

The microstructure of the fusion zone is nearly fully ferritic (Figure 42 (a)) and the ferrite fraction in the heat-affected zone (Figure 42 (b)) is slightly increased compared to the base material in Figure 40. The ferrite grains in the fusion zone are much coarser than in the base material. They are dendritic beginning at the border to the heat affected zone and become nearly globular in the middle of the heat affected zone. Small austenitic grains precipitated at the grain boundaries of the ferrite grains throughout the fusion zone. This is usually the first mode of austenite formation in DSS welds [89]. No indication of austenite needles, intragranular austenite or sigma phase could be found in the centre of the weldment. In addition, no indication of sigma phase could be observed in the heat affected zone of the weldments.

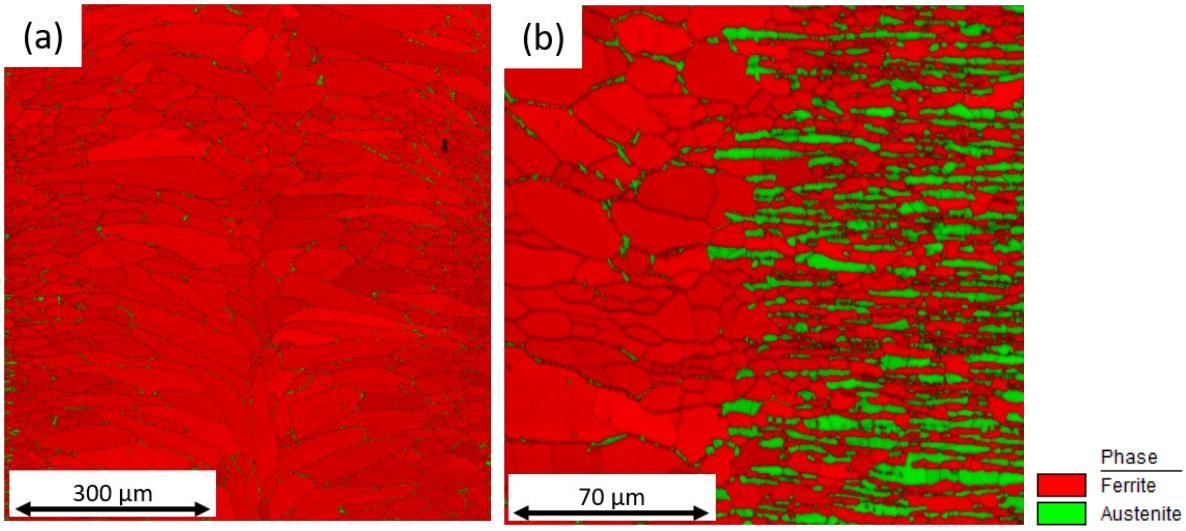

Figure 42: (a) EBSD phase map of the fusion zone exhibiting 97.7 vol.-% ferrite and 2.3 vol.-% austenite and (b) EBSD phase map of border between fusion zone and heat affected zone showing the slight grain coarsening and increased ferrite content in the heat affected zone. [19]

The fusion zone is clearly separated from the heat affected zone shown by the large difference in ferrite content. The ferrite content as well as the grain size in the heat affected zone is slightly increased compared to the base material. The ferritic phase in the fusion zone exhibits the same texture components as the base material combined with a solidification texture component but this is less intense. Additionally, the Taylor factor with regard to the rolling direction (2.97) is lower compared to the base material (3.42). Figure 43 shows the ordinary pole figure for the weld metal in the laser surface remelted condition. The pole distribution density is reduced compared to Figure 40 (b).

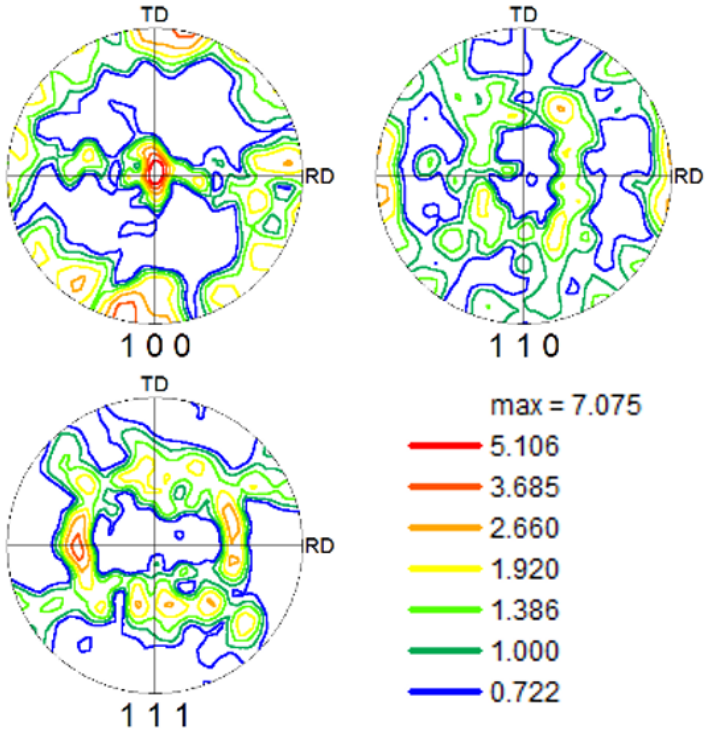

Figure 43: Ordinary pole figures of the ferritic phase in the laser-surface-remelted condition. [19]

Optical micrographs, which are shown in Figure 44, revealed that the laser remelting procedure resulted in a nearly fully ferritic cap at the top and bottom of the weldments. The laser surface remelting treatment produced a heat affected zone in the weldment and the connected base material. In the weld metal, the additional heat input led to the precipitation of finely dispersed austenite grains in the ferrite matrix. Some increase in the width of the grain boundary austenite is also noticeable. Austenite lamellae, which started to grow from the grain boundaries into the ferrite grains, can also be observed. The austenite content in the heat affected zone is increased to approximately 20%. At the border between remelted weld cap and base material, an approximately 80 µm wide zone of globular ferrite grains formed. From this substrate dendritic ferrite grains grew from the bottom of the melt-pool to the outside of the joint, forming their elongated shape.

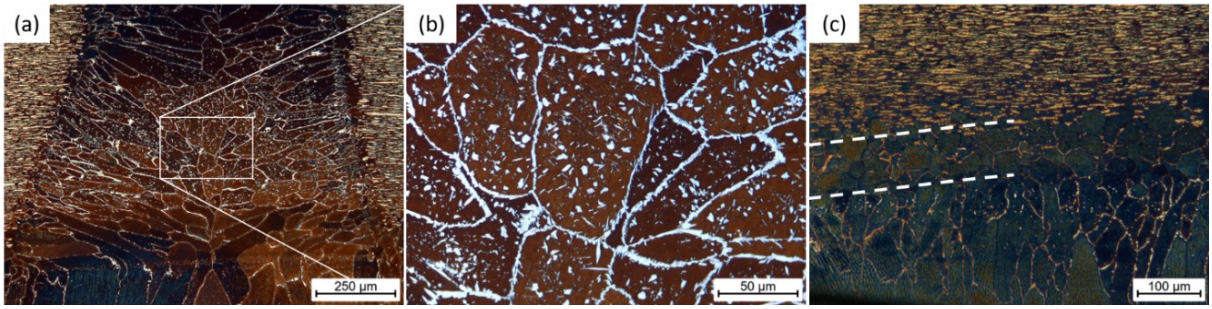

Figure 44: Optical micrographs of the heat affected zone from the remelting procedure on the bottom of a sample. (a) Overview of the heat affected zone inside the weld metal, (b) magnified view of the heat affected weld metal microstructure. (c) The transition region from the base material (top of image) to the remelted region (bottom of image) is separated by globular ferrite grains (inside the white lines). [19]

The laser beam welded joints show typical features for keyhole welded material [13]. The joint geometry is narrow, the ferrite content is high and the laser surface remelting led to increased austenite formation in its heat affected zone.

The increased ferrite content in the heat affected zone of the weldments in this work is a result of the high temperatures and the fully ferritic equilibrium phase composition at temperatures just below the solidus temperature [28,37,38] combined with the high cooling rates typical for the laser beam welding process. The material spends insufficient time in the temperature range from 1200°C to 800°C for significant amounts of austenite to precipitate [13]. The very sharp transition in terms of the crystal structure at the boundary between the fusion zone and heat affected zone was also observed by Bolut et al. [53]. Compared to other publications on this topic (Figure 45 (a)) the parameters employed in this work yielded high hardness and ferrite contents [3,46,49,53,58,60,62,159–164]. However, the aspect ratio of the joint is higher, resulting in less weld metal and a much smaller heat affected zone. Due to the high cooling rates during laser beam welding the microstructure of the weld metal is nearly entirely ferritic. The laser remelting procedure is also suitable for bringing the phase composition closer to optimal values.

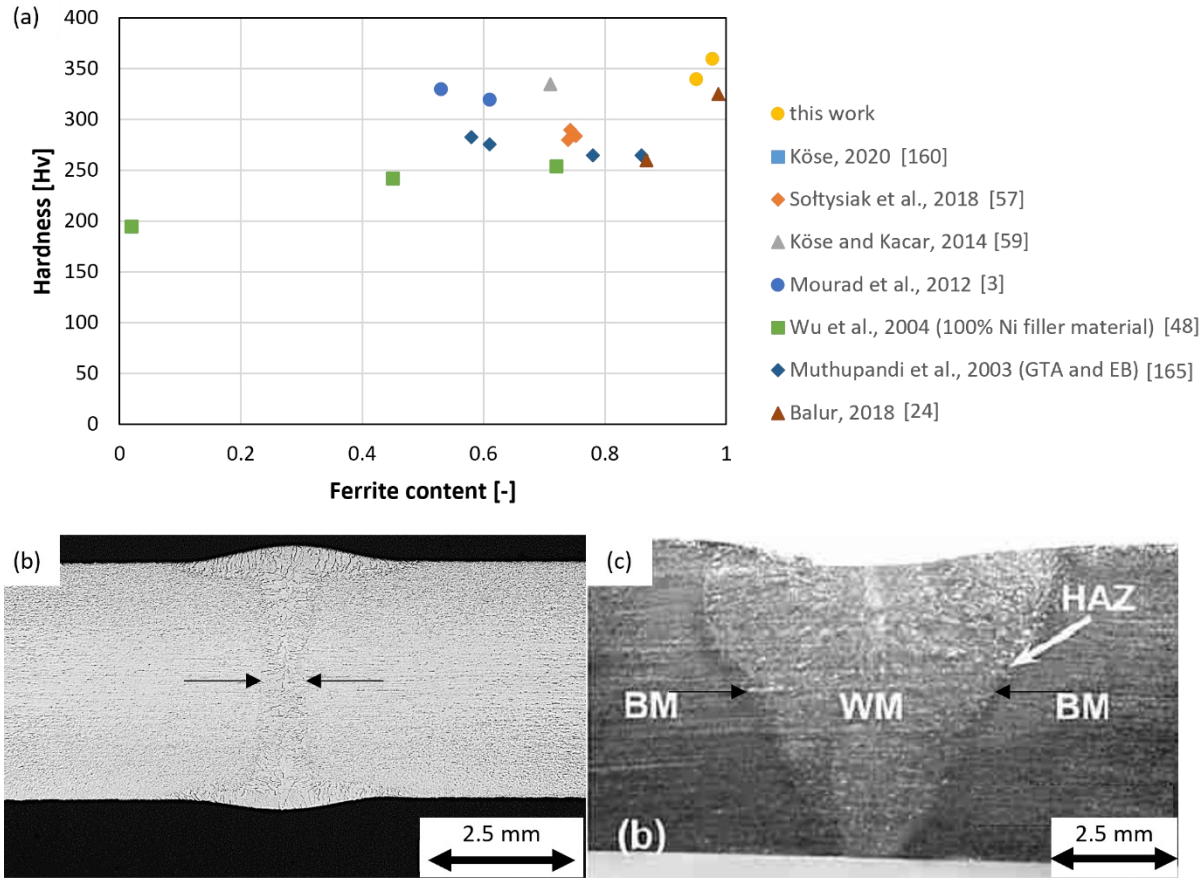

Figure 45: (a) Composed data from literature regarding the correlation between ferrite content and hardness in welded joints (GTA: Gas tungsten arc, EB: electron beam). When not otherwise indicated the results stem from LBW weldments. (b) Weldment with laser surface remelting from this work and (c) laser beam weldment from Mourad et al. [3].

4.1.5 Tensile Tests

The stress-strain curves from the tensile tests are shown in Figure 46. All specimens failed in the base material. The relevant properties determined from the stress-strain curves are summarized in Table 8.

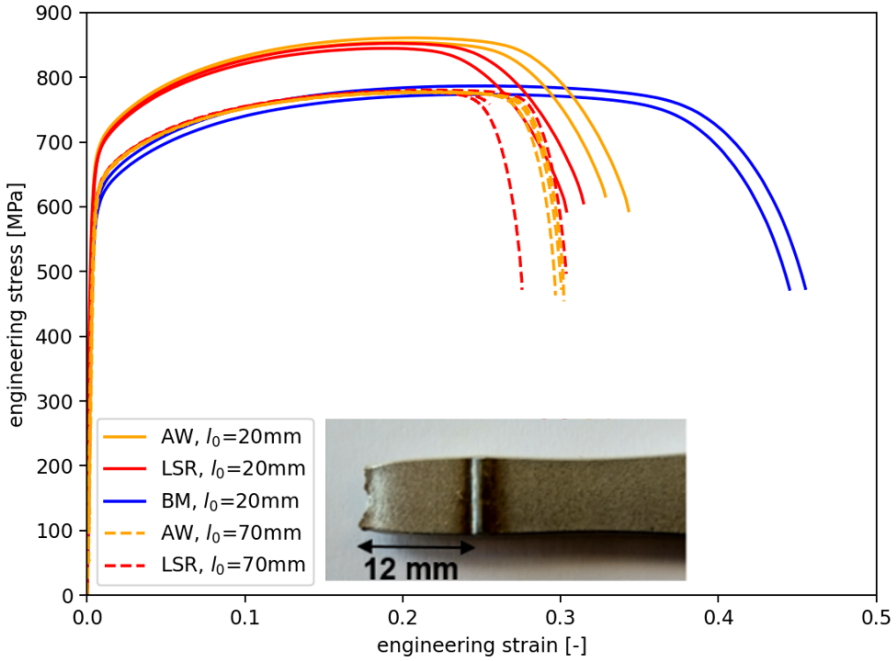

Figure 46: Results of the tensile tests; tensile tests were only performed on batch A of the base material, the as-welded (AW) and laser-surface-remelted (LSR) condition. The resulting fracture location of a tensile test sample with low gauge length is also shown.

The sub-size specimens containing weldments exhibit a higher yield strength, ultimate tensile strength and reduced fracture strain compared to the base material. The strength in the as-welded condition is nearly the same as in the laser-surface-remelted condition, but the fracture strain is slightly higher. Samples with a weldment and an extended gage length exhibit similar yield and ultimate tensile strength as the base material but show significantly reduced fracture strain.

Table 8: Mechanical properties determined from the tensile tests on the fatigue specimens and specimens with extended test-section.

Condition	Gauge length [mm]	Yield strength [MPa]	UTS [MPa]	Fracture strain [-]
base material	20 mm	563	781	0.45
as-welded	20 mm	663	858	0.34
laser-surface-remelted	20 mm	652	849	0.31
as-welded	70 mm	546	779	0.30
laser-surface-remelted	70 mm	536	777	0.27

Hardness measurements were performed along the axis of the broken samples from the tensile tests to assess the amount of work hardening of the material in different areas of the test section. Additionally, the reduction in thickness of the samples was measured and micrographs of the etched microstructure near the fracture surface of samples from the tensile test were taken.

The hardness measurement on the sub size tensile test samples (Figure 47 (a)) revealed a strong increase in hardness near the failure site to a hardness of over 400 HV1. For the base material, the hardness reduces quickly, as the distance from the failure site increases, dropping to a value of 330 HV1 before increasing again to values higher than 350 HV1 at a distance of approx. 5 mm to 14 mm from the fracture surface on the deformed sample and then gradually approaching the base material level. Considering the deformation of approximately 0.45 engineering strain, the region of increased hardness extends approximately up to the region, where the radius of the specimen starts.

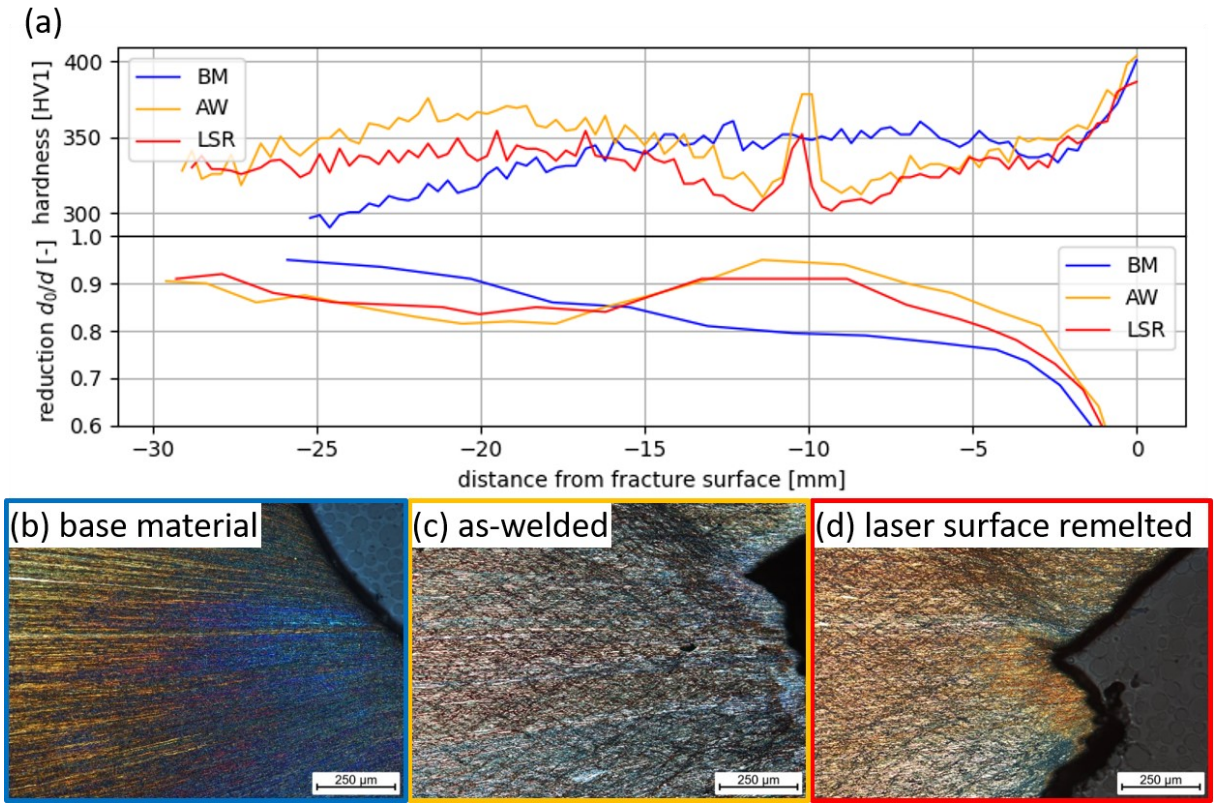

Figure 47: Investigation into the deformation and work hardening behavior of the tensile specimens etched with Beraha II. (a) Hardness changes and thickness reduction, (b) deformed base material, (c) deformed material from a specimen with as-welded joint and (d) deformed material from a specimen with laser-surface-remelted joint. All micrographs were taken on the neutral axis of the specimens. [19]

The specimens containing weldments possess fundamentally different hardness distributions compared to the base material specimens. The hardness near the fracture surface is nearly the same. However, the hardness reaches its lowest value next to the weldment and increases again on the other side of the weldment in the base material. In the case of the welded samples, the increase in hardness (up to 374 HV1) is significantly

higher than the hardness measured on the base material specimen outside of the necking zone. The maximum hardness was measured approximately 10 mm from the weldment. Considering the engineering strain of approx. 0.31, this places the hardness maximum at the end of the radius section of the specimens. The hardened volume of material protrudes well into the radius section for the specimens containing weldments.

The hardness measurements correlate well with the reduction in thickness (Figure 47 (a)) of the specimens. The specimens exhibit increased hardness, where the reduction in thickness – and as follows the deformation – was high. Overall, the reduction of thickness near the fracture surface was highest for the base material specimen that did not contain a welded joint.

The micrographs of the material near the fracture surface show distinct modes of deformation for the base material (Figure 47 (b) and the welded specimens (Figure 47 (c) and (d)) respectively. In the case of the base material specimen, uniform necking and fracture strain of the aligned microstructure can be observed. In the case of specimens containing weldments, deformation lines form a rhombic pattern.

The reduced fracture strain of the tensile specimens containing weldments can be attributed to the ferritic fusion zone and the increased ferrite content in the heat affected zone, which take up a significant volume of the test section. The increased ferrite content leads to increased strength and a reduced ability to accommodate deformation. The fracture strain in the laser-surface-remelted condition is slightly lower than in the as-welded condition since the width of the weldment at the surface is slightly higher. The increased strength of the material in the fusion zone is evident in the increased microhardness in this region. The assumption of increased strength is supported by the results of Floreen and Hayden [36], but contrary to the findings of Lacerda et al.[35]. Köse et al. [60] also observed base metal failure during uniaxial tensile tests for butt joints created by welding with a CO_2 laser, even when the phase composition of the weld metal was more balanced. Xie et al. [59] reported base material failure with increased strength, reduced fracture strain of samples with multi-pass arc welded joints of DSS 2205 with DSS 2209 filler wire. This supports our findings of improved strength of specimens containing weldments. The failure of the base material, rather than the joint region or the heat affected zone is typical for DSS weldments. Due to the high deformability of the duplex microstructure, the strain mismatch between the overmatched joint, heat affected zone and base material does not lead to failure, causing the base material to be the weakest link. Xie et al. [59] attributed the increased strength to refined grain structures. The higher strength of our specimens containing weldments is a result of the relatively short test sections of the specimens. The high strength of the weld metal in the fusion zone obstructs the deformation of the adjacent base material and leads to higher work hardening since the test section is not under strictly uniaxial stress, thus increasing the strength. [28] This proposition is supported by the hardness measurements on deformed specimens (Figure *47* (a)) and the difference in deformation patterns in the necking zone (Figure *47* (b) to (c)) The obstruction of deformation extends more than 10 mm away from the weldment into the radius section

of the specimen, stressing the importance of choosing specimen geometries with sufficient gage length for uniaxial tensile tests on materials containing weldments.

The presence of weldments does not reduce the strength of the specimens under tensile loading conditions since the material in the fusion zone and heat affected zone is stronger than in the base material due to the increased ferrite phase fraction and Taylor factor with regard to the load and rolling direction. Weldments are detrimental to the fracture strain, due to the reduced ductility. The presence of weldments in the test section impedes the deformation in the adjacent base material leading to higher strength of the specimens.

4.1.6 Fatigue Tests

Two sets of fatigue life specimens with a 20 mm long test section were extracted without further modification from different batches of base material (base material A & base material B). These sets of specimens serve as the reference state. Tests specimens with a 20 mm long test section for tensile and fatigue life tests were extracted from the welded sheets in the as-welded and laser-surface-remelted condition, so that the load direction of the specimens was parallel to the rolling direction, perpendicular to the weldment and the weldment was situated in the middle of the test section.

The results of the fatigue life tests are shown in Figure 48. The fatigue life tests show a significant variation of the fatigue properties with regard to the LBW-procedure and also between different batches of base material. In the low cycle fatigue (LCF) regime all specimens fractured in the base material, whereas in the high cycle fatigue (HCF) regime all specimens containing weldments began to fracture at the root of the weldments. LCF failure was accompanied by a reduction of area near the failure site.

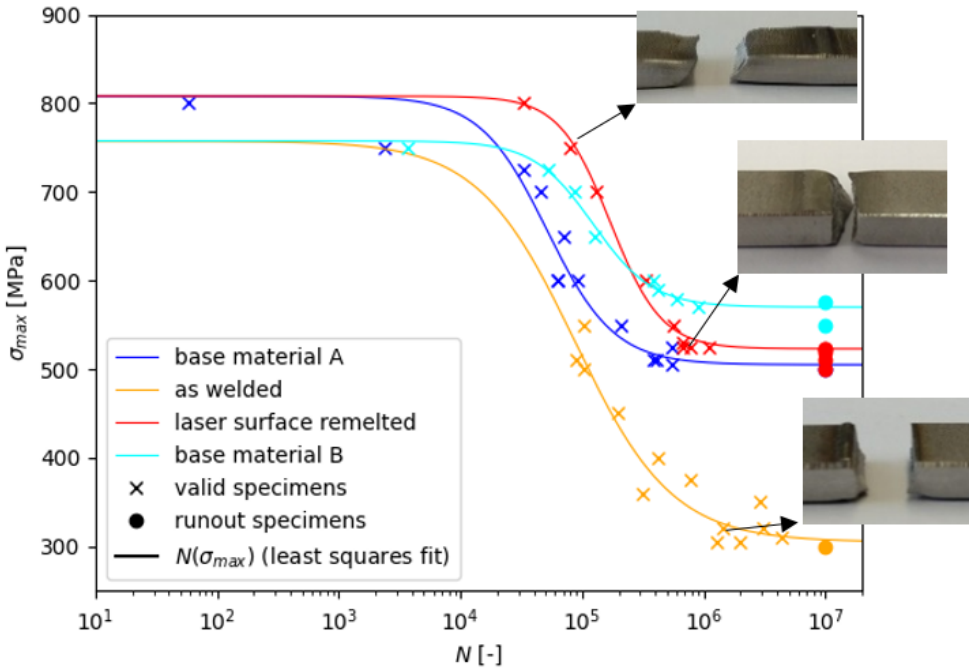

Figure 48: Results of the fatigue tests. All tests were performed at an R_F-ratio of 0.1. [19]

The two batches of base material, as well as the laser-surface-remelted condition exhibited a well-defined fatigue limit, where specimens either broke before 2×10^6 cycles or did not

break before the test was stopped at 10^7 cycles. The scatter of the fatigue lifes at similar loading conditions was also much more pronounced in the as-welded condition compared to the base material and laser-surface-remelted conditions. The fatigue limit was determined by the least squares fit of Equation (15) [165] to the results of the tests. Here, N represents the number of cycles, σ_{max} describes the maximum stress, R_{mf} is a "LCF strength" and σ_e is the endurance limit. N_0 and κ are free parameters defining the shape of the curve.

$$N(\sigma_{max}) = N_0 \left(\frac{R_{mf} - \sigma_{max}}{\sigma_{max} - \sigma_e} \right)^{\kappa} \quad (15)$$

The resulting fatigue limits and "LCF strengths" are summarized in Table 9. The fatigue limits show a difference of 65 MPa between the two batches of base material. The base material batch, where a higher ferrite content (base material A: 54.2%, base material B: 61.4%, Table 6) was measured in the head section of a specimen exhibited a higher fatigue limit. The fatigue limit is not as well defined for the as-welded condition. The fatigue limit in the as-welded condition lies 200 MPa below or at 60.4% of the lower value for the base material. Compared to the laser-surface-remelted condition, the fatigue limit is reduced by 218 MPa or at 58.3% of the laser-surface-remelted value. The fatigue limit of the laser-surface-remelted condition is within the range of the two sets of base material.

The fatigue life tests show that LBW joints, which received a laser surface remelting treatment, are not necessarily detrimental to the fatigue properties of the component, because the fatigue properties of the specimens are within the range of the base material.

Table 9: Fatigue limits and LCF strengths

Material condition	Fatigue Limit (σ_{max}) [MPa]	LCF strength (R_{mf}) [MPa]
base material 1	505	808
base material 2	570	758
as-welded	305	757
laser-surface-remelted	523	808

4.1.7 Fracture Surface Analysis after Fatigue Testing

Under LCF loading conditions, multiple crack origins (Figure 49 (a)) can be observed. Under HCF loading conditions, one crack was always the dominant one (Figure 49 (b)). The point of origin is clearly visible on the fracture surface (Figure 49 (c)).

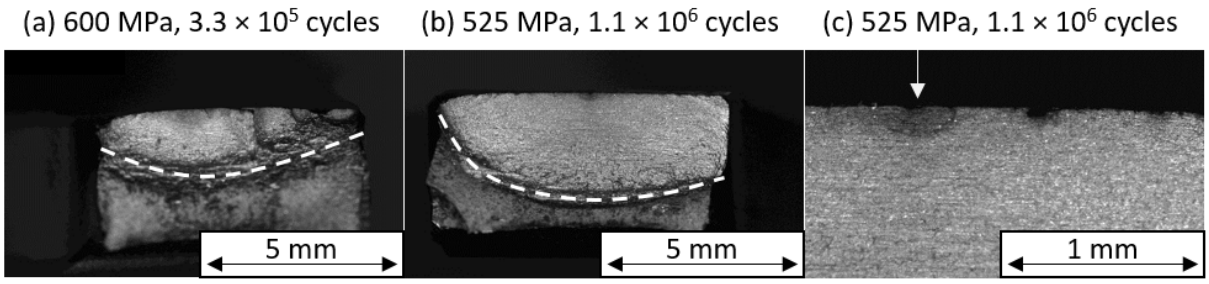

Figure 49: Fracture surfaces of specimens after the fatigue test that underwent laser surface remelting treatment under stereomicroscopy; the fatigue fracture surface and area, where the final rupture occurred are separated with a dotted white line. (a) LCF fracture with multiple crack fronts, (b) HCF fracture with a single crack origin and (c) enlargement of the origin from (b). The white arrow designates the origin point of the crack. [19]

The observation of the fracture surfaces revealed that the fatigue cracks grew from the surface of the specimens and were not initiated at internal defects, such as inclusions, porosity, or large grains. While the location, where the crack was initiated can be clearly discerned by the different reflectivity of the fracture surface near the origin, no defect from which the crack was initiated could be discerned under optical microscopy. The different appearances of the fracture surfaces near the origin and the rest of the fatigue fracture surface (Figure 49 (c)) suggest, that a change in crack growth mechanism from short to long cracks takes place in this region.

LCF properties are less sensitive to notch effects and more sensitive to plasticity phenomena like cyclic hardening and softening than HCF properties. The ferritic fusion zone and the ferritically enriched heat affected zone of the material are protected against plastic deformation and therefore exhibit less plastic deformation during LCF loading, leading to faster initiation and growth of cracks in the base material regions. The assumption of higher strength in the fusion zone and heat affected zone is supported by the hardness measurements. The reduction of deformation near the weldments observed during the tensile tests is likely to also occur during fatigue tests in the LCF-regime, albeit to a lesser degree.

For all material conditions tested in this study, the fatigue limit is below the yield strength. Therefore, no global plastic deformation of the specimens should occur under HCF loading conditions. Instead, stress concentrations at the root of the weldments – where the border between fusion zone and heat affected zone is located – facilitate crack initiation. Björk et al. [63] concluded that fatigue cracks in gas metal arc welded X-joints initiate preferentially at the coarse-grained ferrite in the heat affected zone. The results show increased scatter of fatigue lives in the as-welded condition in the HCF regime compared to the laser-surface-remelted condition. Here, non-uniformly distributed radii (Figure 39 (a)) at the weld-root lead to a variation in notch factors between the specimens, which lead to the increased scatter of the as-welded condition compared to the laser-surface-remelted and base material conditions (Figure 48), where the notch effects are much more uniform or present at all. It can be concluded, that for HCF loading conditions, the notch at the weld-root is the governing factor for the fatigue properties of the specimens containing

weldments. When the notch effect of the weld root is reduced enough, the higher ferrite content in the fusion zone and heat affected zone protects the joint area against HCF loading conditions. This finding is supported by the higher resistance to crack growth at higher ferrite contents measured in electron beam weld material by Singh and Shahi [61], the hardness measurement presented in this work and the correlation of the fatigue limit with the Taylor factor observed by Mateo et al. [14]. This stands contrary to the observations by Lacerda et al. [35], but can be explained by the absence of austenite in the weldments from this work, which precludes fatigue crack initiation. Arc welded joints with a more balanced microstructure were shown to decrease the fatigue performance compared to the base material [59]. When the focus is solely on fatigue performance, the combination of a high ferrite content and laser surface remelting treatment are a superior alternative.

While the static properties of LBW joints in DSS 2205 are nearly unaffected by the laser surface remelting treatment, the fatigue limit can be nearly doubled compared to the as-welded condition. The improved fatigue performance can be attributed to a weldment geometry with a reduced notch factor. In combination with the increased strength of the material in the fusion zone and heat affected zone this leads to welded joints, which have similar fatigue limits as the base material.

4.2 Additive Manufacturing

In this section the results using laser directed energy deposition with wire as a means to additively manufacture duplex stainless steel material are presented. The results were published in [20] and [21]. Additionally, a patent application was filed for the process control method, which was developed to produce some of the samples in the later stages of this thesis [22]. The presentation of published work is extended by the investigation of the fatigue properties and the residual stress state of the additively manufactured material. Some aspects of the fracture mechanics concepts were also applied in [23].

4.2.1 Optimization of Shielding Gas Flow Rate

To exclude the shielding gas flow rate as a parameter to be varied during the experiments, the shielding gas flow rate was optimized in preliminary trials. Argon was used as a shielding gas. An optimal shielding gas coverage is achieved, when the flow rate is maximized, so that the maximum amount of air is displaced and the workpiece is covered well, without introducing turbulent flow and drawing air into the shield gas flow. The Reynolds number (*Re*) according to Equation (16) is a good indicator of laminar or turbulent flow.

$$Re = \frac{\rho v d}{\eta} \tag{16}$$

Here, ρ, v, d and η indicate the density, velocity, characteristic size and dynamic viscosity. The gas velocity was calculated from the shielding gas flow rate, the shielding gas nozzle diameter and wire nozzle diameter. The characteristic size was set as the distance from the shielding gas nozzle to the work piece. From this relationship it can be expected that high shielding gas flow rates and large distances between the workpiece and nozzle lead to more turbulent flow. Consequently, a larger shielding gas flow rate might yield worse results.

Three single track wide samples of 50 mm height and 90 mm length were deposited at a laser power of 3 kW, a welding speed of 1 m/min, a layer height of 0.8 mm and shielding gas flow rates of 5 l/min, 10 l/min and 15 l/min. Between deposition sequences the samples were cooled with compressed air. The interlayer wait time was adjusted, so that an interlayer temperature of approx. 100°C was achieved. Samples were taken by sawing with a band saw from the middle of each structure in 3 height increments near the bottom, middle and top. The samples including the oxide layer were measured for the oxygen and nitrogen content using carrier gas hot extraction (LECO ONH836). The microstructure was evaluated using the methods described in section 3.4.2. The results are shown in Table 10.

Table 10: Results of the optimization experiment for shielding gas flow rate.

Shielding gas flow rate [l/min]	Reynold's number [-]	Average ferrite content [-]	Oxygen content [-]	Nitrogen content [-]
5	2466	0.43	0.186%	0.166%
10	4932	0.38	0.218%	0.167%
15	7399	0.41	0.223%	0.167%

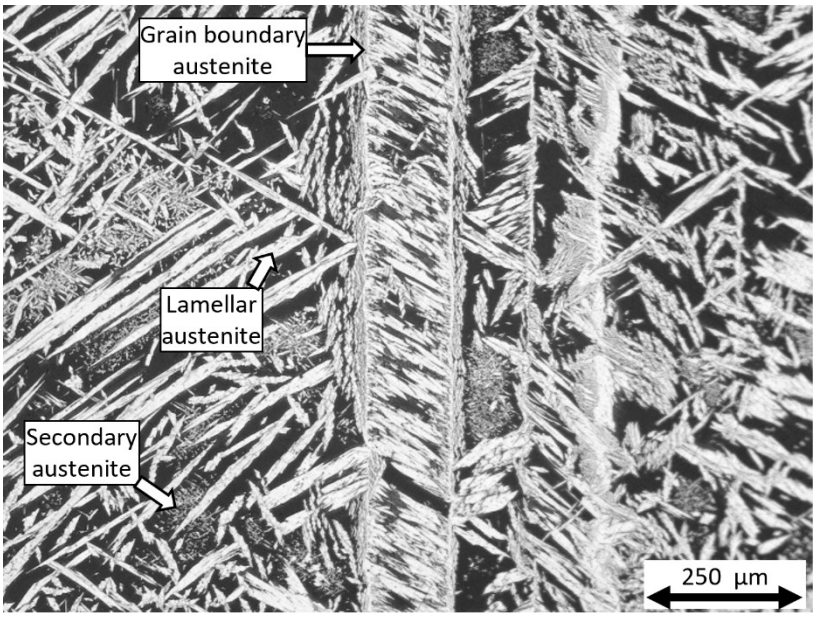

Figure 50: Greyscale micrograph at 500x magnification. The material was color etched with Beraha II for approx. 5s.

The samples exhibited typical microstructure with epitaxially grown prior ferrite grains, grain boundary, lamellar and intragranular austenite. High contents of intragranular austenite were noticeable, probably stemming from the combination of a medium line energy and low height increment, leading to highly defocused welding conditions with significant reheating of the previous layer.

The nitrogen content was constant for all shielding gas flow rate settings, while the oxygen content increased monotonically with increasing shielding gas flow rate. The nitrogen content of the weld metal is well above the recommended 0.12% [28]. Therefore, adding nitrogen to the shielding gas was not considered. Reasons for the decrease of shielding gas coverage with increasing flow rate can be an increase in turbulent flow with an increased amount of ambient air being drawn into the shielding gas through the Venturi effect as supported by the higher Reynold's number for increased flow rates.

4.2.2 Steady State in Additive Manufacturing of Thin-Walled Parts

In this section the results of the thermographic measurements during the additive manufacturing process, which were published in [20], are described. During the additive manufacturing process heat accumulates in the parts due to the repetitive addition of molten metal. The part temperature has a direct influence on the solidification rate and therefore on the shape of the deposited weld tracks. Knowledge of the way heat accumulates in the part is imperative if open loop methods are to be used to adapt the layer height to compensate for this effect.

Owing to the coordinated motion of the robot and positioner and because of the constraint to the working plane (Figure 16 (b)), the process zone is always located in the upper part of the thermal images (Figure 51 (a)). When a temperature profile along the y-axis of the thermal images is extracted, the side opposite to the current process zone is always

included and not obscured by the wire-feeding nozzle (green arrow in Figure 51(a)). The position of the evaluation line was identified as the median value of the x-position of the pixels with the highest temperature values. The entire height of the thermal images was evaluated to ensure that the additively manufactured part is always within the region of interest (RoI). Since the emissivity of the melt pool is much lower, compared to the solidified and oxidized material, the temperature of the liquid metal is underestimated during acquisition of the images.

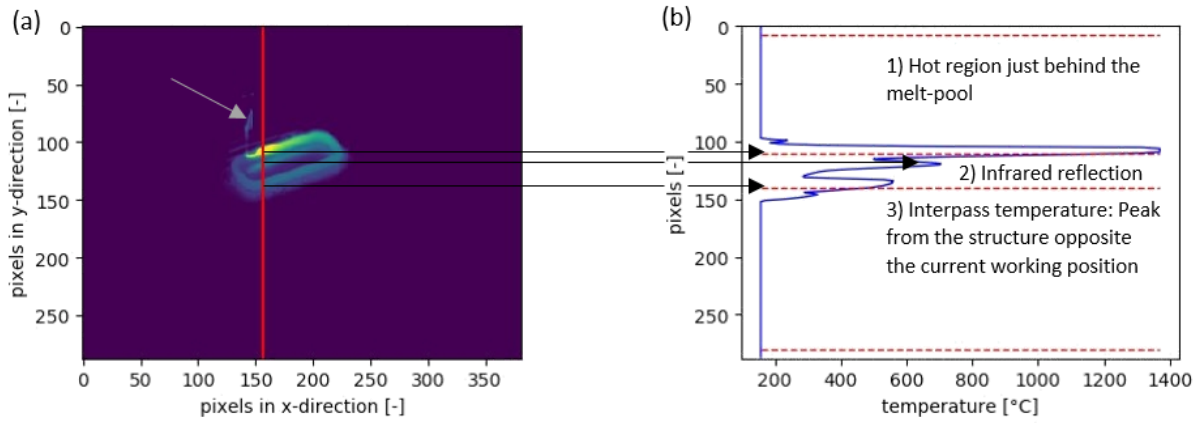

Figure 51: (a) Thermal image from the L-DED-wire process. A red line highlights the evaluation line. Some reflections of the thermal radiation on the substrate and the wire nozzle (green arrow) are visible. (b) Thermal profile extracted from the process at t=180 s [20]

A temperature profile was extracted along the evaluation line (Figure 51 (b)). This temperature profile exhibits multiple characteristic peaks. The highest peak is the evaluation position. At the beginning of the L-DED-wire process, there are three peaks in the data shown in Figure 51 (b): the first one from the evaluation position, the second one from thermal radiation and reflection near the base of the part under the process zone and the third one from the opposite side. These peaks were identified by their width. Hence, the peak belonging to the current interpass temperature (Figure 51 (b)) could be identified using the "find_peaks" function from the "scipy.signal" Python package [166,167]. The function identified the peaks by performing a continuous wavelet transform with the expected width (wall thickness in pixels) and identifying the ridge lines in the wavelet transform matrix.

Owing to the rectangular shape of the structure built in this study, the evaluated position is not always the same distance along the tool path from the current working position. When the temperature is evaluated more on the left side in the thermal image (Figure 51 (a)), lower temperatures are measured than on the right side. Hence, the measured interpass temperature oscillates (Figure 52 (a)). To flatten these oscillations, a continuous function (Equation 2) is fitted to the measured time-temperature data ($T_{i,m}$, Figure 52 (a)). The parameter optimization was performed based on the least squares method. The development of the fit parameters over time — indicating when a reliable prediction is possible — is shown in Figure 52 (b).

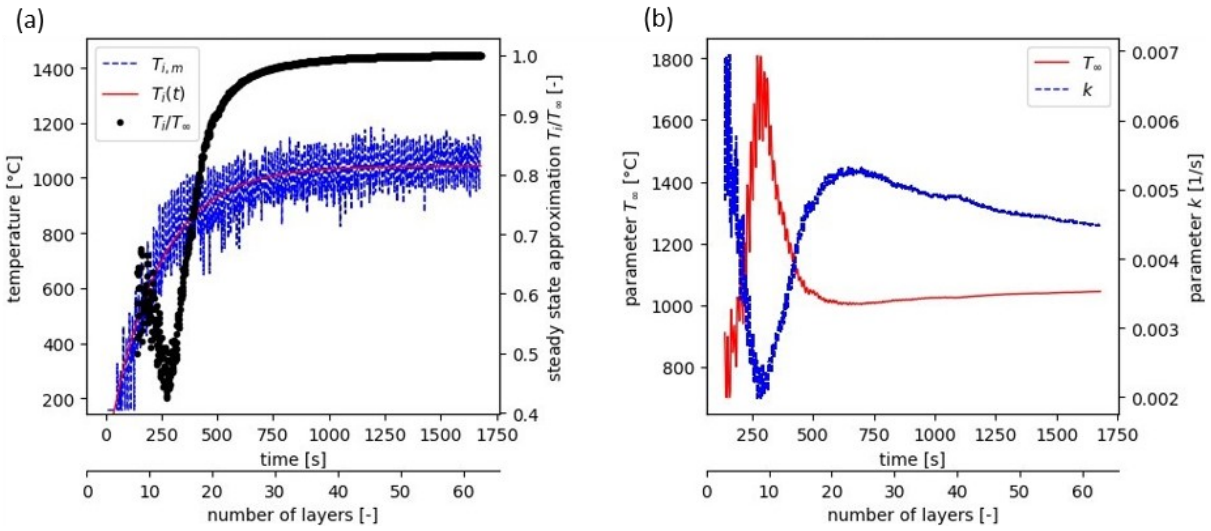

Figure 52: (a) Measured interpass temperature (blue line), fit function to the measured temperature (red line) and the steady state approximation (current temperature divided by the upper limit determined by the current value of the fitting parameters). The change in the steady state approximation at the beginning of the build corresponds to a change in the fitted steady state value T∞. (b) Evolution of the current value of the fitting parameters with time. Only the first 60 layers are shown to achieve better visibility of the transitive regime. [20]

At the beginning of the L-DED-wire process, the optimized values for the free parameters change considerably. After about 700 seconds, or 25 layers, the interpass temperature reaches 95% of the steady state temperature and the predicted threshold temperature nearly converges.

From the maximum temperature (solidus temperature, T_{max}), the current interpass temperature ($T_i(t)$), welding speed (v_s) and length of the tool path for half a revolution (l_t) a cooling rate (h) can be derived through Equation (17) (Figure 53 (a)):

$$h(t) = \frac{(T_{max} - T_i(t))v_{TCP}}{l_t} \tag{17}$$

During the build the cooling rate reduces from ca 73 K/s to 25 K/s which corresponds to $t_{12/8}$ times of approx. 5 to 16 seconds. This is an almost threefold reduction. The cooling rate is compared to the microstructure formed at the base and approx. half the height of the sample (Figure 53). Representative cross-sections from the bottom and the top of the deposited structure are presented in Figure 53 (b) and (c) respectively. The solidification and cooling rates influence the partitioning of elements during the formation of the microstructure [28], leading to non-uniform reaction to the etching agent.

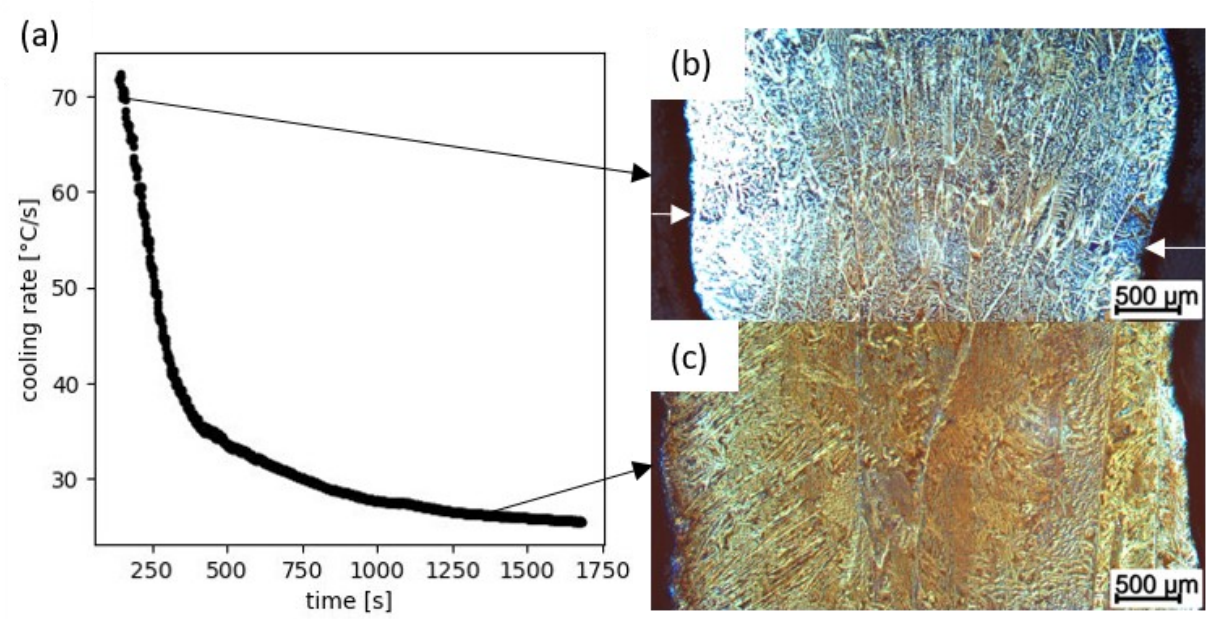

Figure 53: (a) Cooling rate between solidus temperature and current interpass temperature, (b) fine-grained prior ferrite grains from the bottom of the structure and slightly darker layer bands (white arrows), (c) coarse-grained epitaxially grown prior ferrite grains from the top of the structure. [20]

The microstructure at the bottom of the structure (Figure 53 (b)) consists of prior ferrite grains, which marked by the austenitic grain boundaries separating them, and a network of austenitic needles in the prior ferrite grains. There are between 15 and 20 prior ferrite grains across the cross-section from the bottom of the additively manufactured part. In the cross-section from the top of that part, the number has reduced to five at most (Figure 53 (c))). While the height of the prior ferrite grains in the bottom is less than one layer height, the height at the top can be much larger than several layers. Near the substrate darker bands, separating individual deposited layers were observed (white arrows in Figure 53 (b)). These are no longer visible near the top of the structure (Figure 53 (c)). Microstructural defects such as lack of fusion, solidification cracks or porosity are not visible in Figure 53 (b) and (c).

The predictions of the steady state value of the interpass temperature for the process at hand converged after about 600 s, while the interpass temperature reached 95% of the steady state value (1020°C) after 700 s. During the first 500 s of the process, the results of the least-squares fit change considerably. A good prediction of the steady state, based on the transitive regime of the process is, therefore, unlikely. The remelting depth is likely increased with increasing height because of the increased temperature of the substrate material, which explains the disappearance of the darker bands between layers. The epitaxial grain growth across layers and the resulting increase in grain size and aspect ratio has been reported on in [168].

The transitive behaviour of the part temperature has been indirectly reported on by other researchers. Kledwig et al. [169] reported a transition from an initial temperature signal from the melt pool to a steady state signal during the laser directed energy deposition with powder of an austenitic stainless steel (X2CrNiMo17-12-2). They found that a steady state

signal from thermal images of the melt pool was reached after about 400 s of the process. The tool path for one revolution was slightly longer (314 mm) than in the present study (213 mm), but the final height of the part was smaller. In combination with the slightly higher power and material addition rate used, this leads to a 177% higher power per unit length of revolution ((5.7 W/mm vs. 10.1 W/mm). After 700 s of process in the present study the temperature is close to (>95%) approaching the steady state. This is 175% longer than reported in [169]. Since the structures in the work of Kledwig et al. [169] are slightly larger compared to the structures in this study, there is a larger area where energy can be transmitted to the surroundings via radiation and convection. At the same time, a lower power of the energy source leads to a lower temperature, at which the thermal equilibrium is reached. In addition to the time to a steady state process, part level thermography can measure the actual interpass temperature and calculate a cooling rate, which can be directly linked to material properties through the resultant microstructure and the remelting depth.

The measurement of optical radiation from the melt-pool is more challenging than for a part because of the higher temperatures, strong temperature dependency of emissivity and high resolution required to capture the actual temperature distribution. In addition, if the laser power is controlled via temperature measurements of the melt pool, the optical emission is likely to stay more constant throughout the process. Therefore, the certainty of reaching a steady state is hindered by the adjustment of the power. A part-level evaluation is then more promising.

Chechik et al. [79] computed cooling rates of the melt-pool during a DED process with laser and powder from infrared images of the melt pool [79]. They found that the cooling rate decreased to a plateau over the first 20 layers, with the effect being more pronounced when a high line energy is employed. This gives merit to application of an exponential growth law like Equation 2 to DED processes. In addition, the hardness of their structures correlates with their computed cooling rate.

The computation of cooling rates from the temperature field of the melt-pool should not be the only parameter with which microstructure is predicted. The interpass temperature could have stronger correlation with the remelting depth and the probability of lack of fusion defects. In addition, when the laser power is controlled to keep the melt-pool temperature constant, attempts to judge whether a steady state process has been reached cannot be made based on temperature measurements of the melt-pool.

In summary, the rate of convergence to a steady state process and the actual temperature values mainly depends on three parameters: the laser power, the size of the structure and the surface-to-volume ratio. The laser power controls the amount of energy introduced into the structure and the size along with the surface-to-volume ratio control the power that can be radiated and convected away from the structure.

4.2.3 Open Loop Control

The following paragraphs describe the results when height offset and laser power are adjusted to account for the changing boundary conditions of the process when starting from a cold substrate and manufacturing a thin-walled structure with a layer wise repeating geometry like that shown in (Figure 14 (b)). The parameters tested for manufacturing the 90 mm high rectangular parts are presented in Table 11. P1 are the parameters obtained from a fit of Equation 3 and Equation 4 to the manually determined process parameters.

Table 11: Parameter sets for open loop control following a limited exponential growth law.

Parameter set	Parameters					
	P_i [W]	P_{ss} [W]	k_P [-]	h_i [mm]	h_{ss} [mm]	k_h [-]
P1 (measured + fit)	1630	1480	0.3	1.450	1.075	2.15
P2	1530	1300	0.5	1.450	1.065	2.15
P3	1530	1390	0.75	1.450	1.100	0.5
P4	1530	1340	0.5	1.450	1.080	1
P5	1530	1370	0.75	1.450	1.085	0.5

A build in a continuous fashion without breaks was attempted using parameter set P1 but failed. The absence of pauses resulted in excessive heat accumulation, leading to overheating of the melt-pool and evaporation of the wire feedstock through a combination of reduced layer height and excess laser power. Consequently, the laser power and layer height were reduced to the values given in parameter set P2. The parameter P_i for the set P2 was determined by lowering the laser power until stable melting barely occurred and the process was close to the stubbing mode. The remaining values of P2 are an initial guess for the subsequent iterations for the determination of suitable parameters. The parameters P_{ss} and h_{ss} were lowered so that undercooling of the melt-pool was assured at some point during the build according to the operators' experience. Achieving undercooling was imperative to have the process bounded by the two discontinuities that can occur. The value of the k_p coefficient was increased slightly to reflect the more gradual change in interpass temperature. In the case of the interrupted build, the cooling rate was much higher for each individual layer and therefore the temperature stabilized more quickly. The overall decrease in energy led to insufficient melting of the wire after the first layer. For parameter set P3, the laser power in the steady-state was adjusted to be the average of parameter sets P1 and P2, while the offset height in the steady-state was increased from 1.065 to 1.100. The combined increase in layer height and laser power caused the process to become unstable through overheating. This also occurred in a later stage of the deposition process when using parameter set P1 for continuous deposition. In the next tests, the laser power and height offset in the steady state were adjusted following the bisection method until the stable parameter set P5 was found. The variables k_P and k_h were adjusted slightly to improve the process in the first 15 to 20 layers, but slight changes here did not influence the steady-state behavior significantly.

As an extension to the published work, the steady-state process parameters of laser power and welding speed were varied systematically from 1.5 kW to 3 kW and 0.35 m/min to

1 m/min respectively, to understand their influence on the deposited material. The wire feed rate was adjusted proportionally to the steady state laser power to keep the mass specific energy input constant. The interpass temperature was not controlled. Pauses in the deposition sequence only resulted from the tool moving to the starting point of the next deposition sequence. The materials microstructure was analyzed via optical microscopy and samples were taken for fatigue tests.

4.2.4 Appearance of the Additively Manufactured Samples

The stability of the process is highly dependent on the offset per layer, which controls the distance between the focal plane of the laser beams and the melt-pool. Even differences of a few hundredths of a millimeter can make an initially stable process unstable after many layers. Ideally, it would be advantageous to measure the height of the deposit during the process. In the absence of such capabilities, one needs to resort to trial and error to find the correct processing parameters. An initial guess for the layer-dependent height offset was obtained by measuring the height in between layers. However, this did not always produce a stable parameter set for the continuous case, because the interpass temperature was higher when there were no breaks between the layers, resulting in a lower track height due to the decreased solidification rate.

Depending on the parameters chosen for the adjustment of the offset and laser power, the process evolved in three different ways with increasing the height of the deposit (Figure 54). When the combination of laser power and offset was too high, the process became unstable due to overheating and vaporization of the melt-pool (Figure 54 (b)). When the combination of laser power and height offset is too low, the part height increased faster than the prescribed offset. This led to a reduction of the free length of the wire, thus increasing the amount of energy needed to achieve stable melting. When stable melting was no longer possible, the wire plunged through the melt-pool and came out of the side of the wall (Figure 54 (c)), taking some of the molten material with it. This led to a reduction of the local layer height. When the height offset and laser power were too high, the melt-pool overheated and partially vaporized when the tool passed this position on the subsequent deposition sequence. This led to a localized instability, since less material was deposited, lowering the height of the deposited tracks even further. When the process is optimized sufficiently these phenomena can be avoided altogether.

The substrate employed in this study was 10 mm thick. Therefore, the bending deformation from thermal strain was significant. Consequently, some remaining wires that stuck out on the left and right sides of the final part could not be avoided. Additionally, the limited acceleration of the two-axis positioner led to some process instabilities due to the increased amount of material deposited at the start of each corner. The final height could be reached for the “cold” processing routes indicated in Figure 54 (c) and the final, optimized processing route indicated in Figure 54 (d). The optimized processing route was used to build a smaller cube-like (65 mm × 65 mm × 50 mm, length × width × height) structure for the extraction of additional tensile specimens to determine the scatter of the mechanical properties.

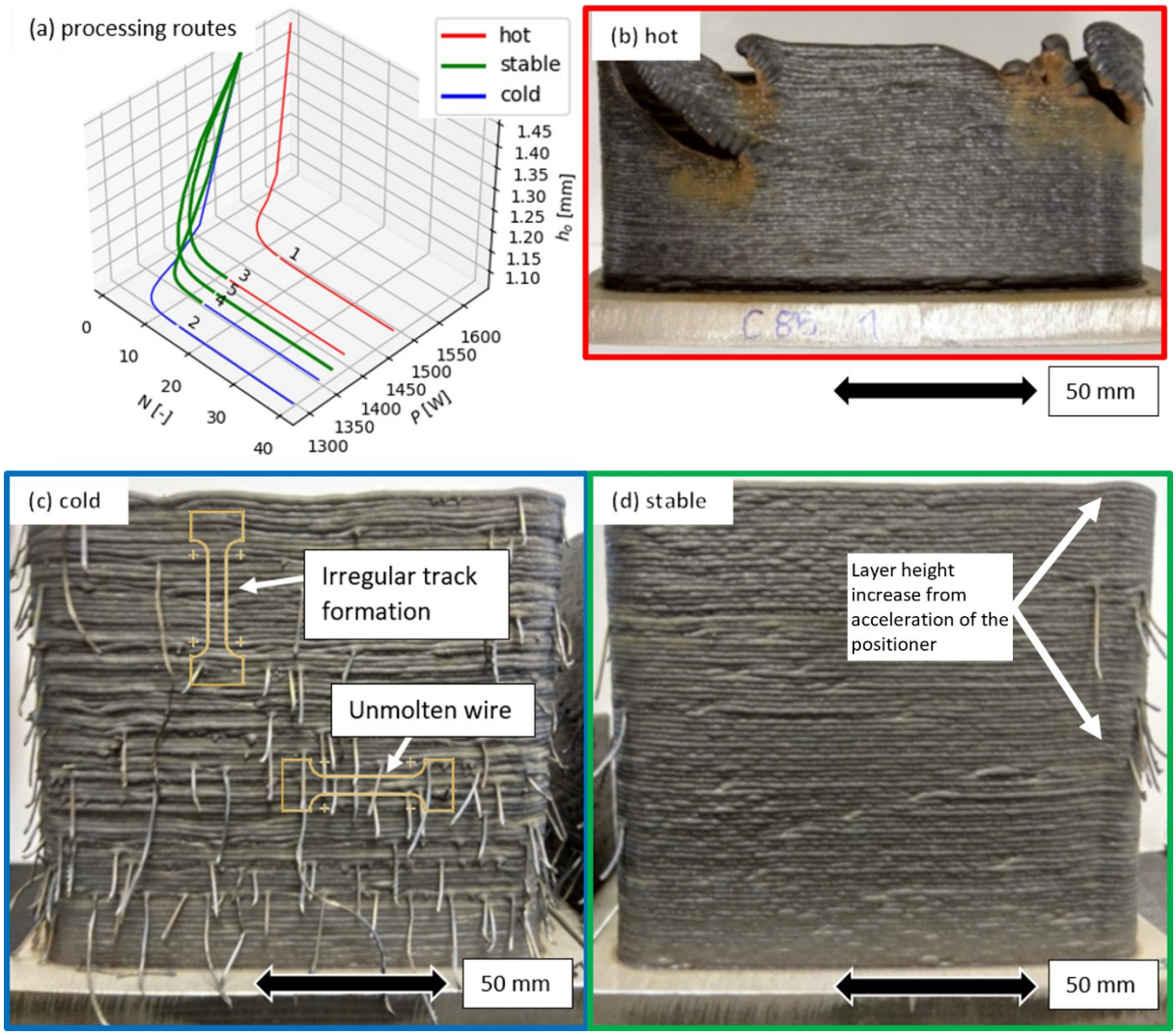

Figure 54: Processing routes and the resulting part qualities: (a) Laser power and offset height in dependence of the number of layers. (b) Result of either too high laser power or offset: The build had to be aborted before reaching the full height of 90 mm due to excessive vaporization of the material. (c) Result of too low laser power or offset: Unmolten wire plunged through the melt-pool and protrudes out of the sides of the structure. (d) Result of optimized stable processing route: Some amount of wire sticking out of the left and right sides of the structure could not be avoided because of substrate bending. The extraction location for tensile test specimens, so that potential defects are within the gage section, is shown exemplarily with orange outlines in (c). [21]

The behavior of the coaxial process is analogous to that during the L-DED-wire process with side feeding, in that a high height offset or laser power leads to a process behavior similar to the droplet transfer mode described by Heralić [128]. When the laser power is focused on the wire, uneven tracks are formed, the wire feedstock may partially evaporate and the process will become unstable. The opposite case, where laser power and offset are too low, leads to insufficient melting of the wire, which is similar to the plunging behavior described by Heralić [128] and the behavior during rear feeding described by Syed and Li [170]. Syed and Li [170] discussed increased resistance of the wire feeding due to interaction with the solidifying trailing edge and resultant force on the wire feeding mechanism as a reason for

irregular track formation. In our case, such a pushback also existed, but the system reacted by buckling of the wire and plunging through the melt-pool.

Allowing the substrate and part to deform is beneficial as it prevents the formation of high residual stresses at the base of the part [171]. This is especially important for materials, where heat treatments have a great influence on the microstructure of the material [2]. Additionally, the surface morphology of the parts manufactured via DED often requires a post-processing step, where a small amount of additional work to remove the remains of wires is probably not considered detrimental to the economic feasibility of the processing chain [172].

A stable processing route for the coaxial laser metal wire deposition of thin duplex stainless steel specimens can be established with open loop control, when the height offset per layer and laser power are adjusted according to an exponential growth law. Two kinds of instabilities – the undercooling or overheating of the melt-pool – can occur, of which only the second one leads to unusable parts. When the laser power or offset per layer is too low, the unmolten wire plunges through the melt-pool. When the laser power and/or offset are too high, the wire evaporates, before it connects with the substrate.

Oxide Layer on Additively Manufactured Samples

It is desirable to employ additively manufactured parts in their as-built state without any post processing to save on machining costs. Due to the slow cooling rates, heat accumulation of the material and local shielding gas concept, some oxidation of the surface cannot be avoided. The oxides on the surface might be detrimental to the corrosion properties of the material [28]. Additionally, the surface oxide film is not mechanically stable and might thus contaminate material it comes in contact with. The surface oxidation was analyzed in terms of its thickness, distribution and chemical composition. Representative areas of the oxide layer were identified on the surface and in the cross section for an approx. 100 mm high sample (Figure 55) using a scanning electron microscope. The oxide layer appeared nonuniform in nature. In all areas that appeared different EDX measurements were carried out to determine the chemical composition. The investigated regions are shown in Figure 56 and the corresponding values are given in Table 12.

Figure 55: Sample for the investigation of the surface state.

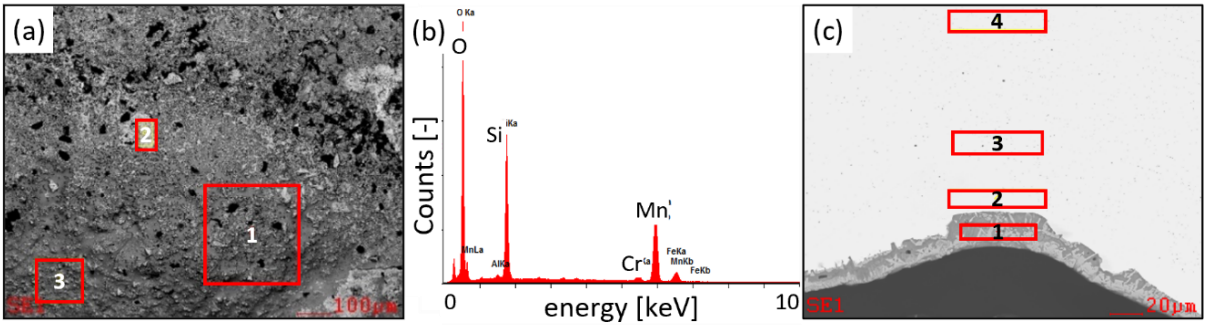

Figure 56: EDX-analysis of the oxide layer: (a) Oxide layer, (b) EDX-spectrum corresponding to measurement region one (indicated in red) and (c) cross-section of the oxide layer with respective measurement regions.

Table 12: Results of the EDX-measurements on the regions indicated in Figure 56 (c).

Location	O [wt.-%]	Fe [wt.-%]	Cr [wt.-%]	Ni [wt.-%]	Mo [wt.-%]	Mn [wt.-%]	Si [wt.-%]
1	24.68	1.20	34.15	-	0.26	20.67	17.34
2	0.41	62.24	23.85	7.71	4.15	0.59	1.05
3	0.39	60.88	24.78	7.58	4.15	1.14	1.09
4	0.81	61.20	24.02	8.36	3.37	1.47	0.78

The oxide layer formed due to a long dwell time at high temperatures in contact with the atmosphere. The oxides consisted of silicon, chromium and manganese oxides. No chromium or molybdenum depletion of the surface layer could be determined. The molybdenum content in the areas examined was slightly increased compared to the composition of the welding wire (24.6% Cr, 3.5% Mo, 8.3% Ni), while the nickel content was reduced. However, the results should be viewed with caution, as the size of measurement regions was similar to the phases components. It is therefore possible that only the ferritic phase, that is enriched with chromium and molybdenum, was measured. The results show that the additively manufactured parts can likely be used in the as-built state if a smooth surface is not required due to functional reasons. Only the oxide layer needs to be removed because it is not mechanically stable. A chromium or molybdenum depletion from the surface oxidation compared to the composition measured for the welding wire and bulk of the structure was not observed. The stress concentration from the notches at the bottom of every deposited layer needs to be considered when evaluating the load capacity, especially in case of fatigue loading.

X-Ray radiography

the result of the radiographic inspection for a cold processing route (Figure 54 (c)) is shown in Figure 57. Multiple pictures were taken in a rectangular grid at high magnification and stitched together by the stitching algorithm of the equipment. The radiographic inspection shows the specimens to be porosity-free. Only one defect could be observed near the bottom of the sample. The defect is marked with a rectangular box. The energy input during the deposition process is sufficient to achieve the required remelting depth, so that no lack of fusion defects formed at the bottom of the melt-pool.

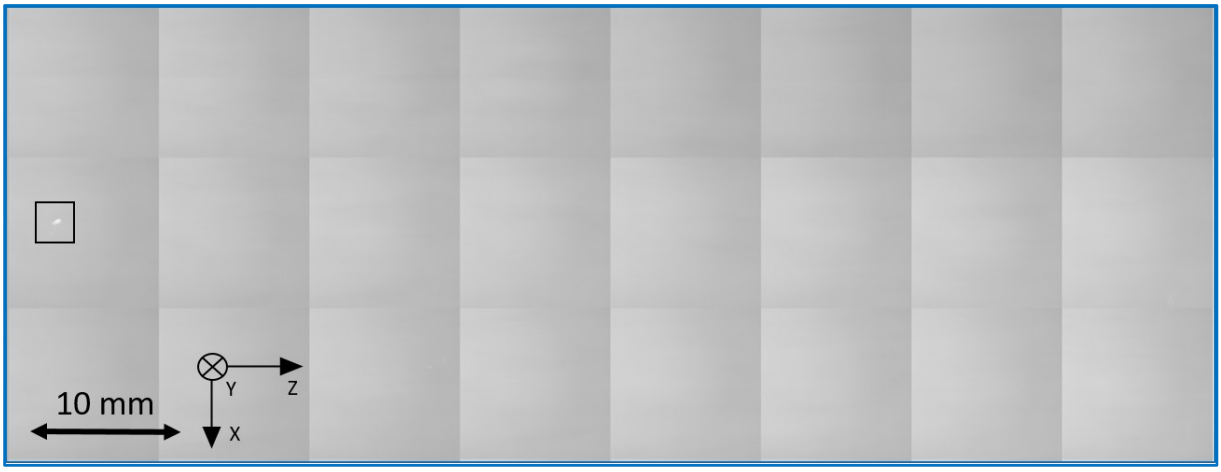

Figure 57: Radiographic inspection of an 80 mm x 30 mm area of the side wall of specimens manufactured with parameter set 4. The surfaces of the walls were milled before the inspection to make the detection of small pores possible. The build direction is to the right. Multiple high-resolution pictures were stitched together to examine a large area at high magnification. The only defect that could be found is marked by the black box. [20]

4.2.5 Microstructural Characterization

In this chapter the results from the microstructural investigation using optical and scanning electron microscopy as well as high energy X-ray diffraction are presented. The results are analysed and discussed with regard to the literature.

Optical and Scanning Electron Microscopy

Macro- and microstructures resulting from P2 (undercooling), P4 (malformed tracks) and P5 (optimized) are shown in Figure 58. For each condition images that are representative of the respective region and magnification level were chosen. While a quantitative analysis of the microstructural features is difficult due to the irregularity of the constituent phases and their inhomogeneous distribution, several qualitative observations can be made. The macrostructure as well as the microstructure exhibit banded layers. The banded layers of the microstructure coincide with the thinnest section of the macrostructure. All deposits exhibit a minimum width of at least 2.1 mm at the thinnest point. The height of an individual layer is between 1.07 and 1.09 mm, which agrees with the prescribed offset. The macrostructure is dominated by epitaxially grown prior ferrite grains, which are marked by the austenitic seams at prior ferrite/ferrite grain boundaries. At higher magnification (Figure 58 (50x)) the layer boundaries and centers of the layers could be differentiated by differences in ferrite content and the presence of fine, needle-like austenite agglomerates. For evaluation of the phase fractions sufficiently high magnifications should be chosen for

a good resolution of the small austenite agglomerates [28]. At such high magnification, the measurements vary considerably between individual frames, because of the small area of evaluation and the inhomogeneity of the austenite/ferrite distribution. In the layer boundaries an approximately equal fraction of austenite and ferrite was found, whereas the centers of the layers consisted of approximately 70% austenite and 30% ferrite. In addition to the fine austenite needles, the layer boundaries contain slightly coarser austenite grains than the centers of the layers. The size of the austenite needles varies by over one order of magnitude from under 5 µm to over 200 µm.

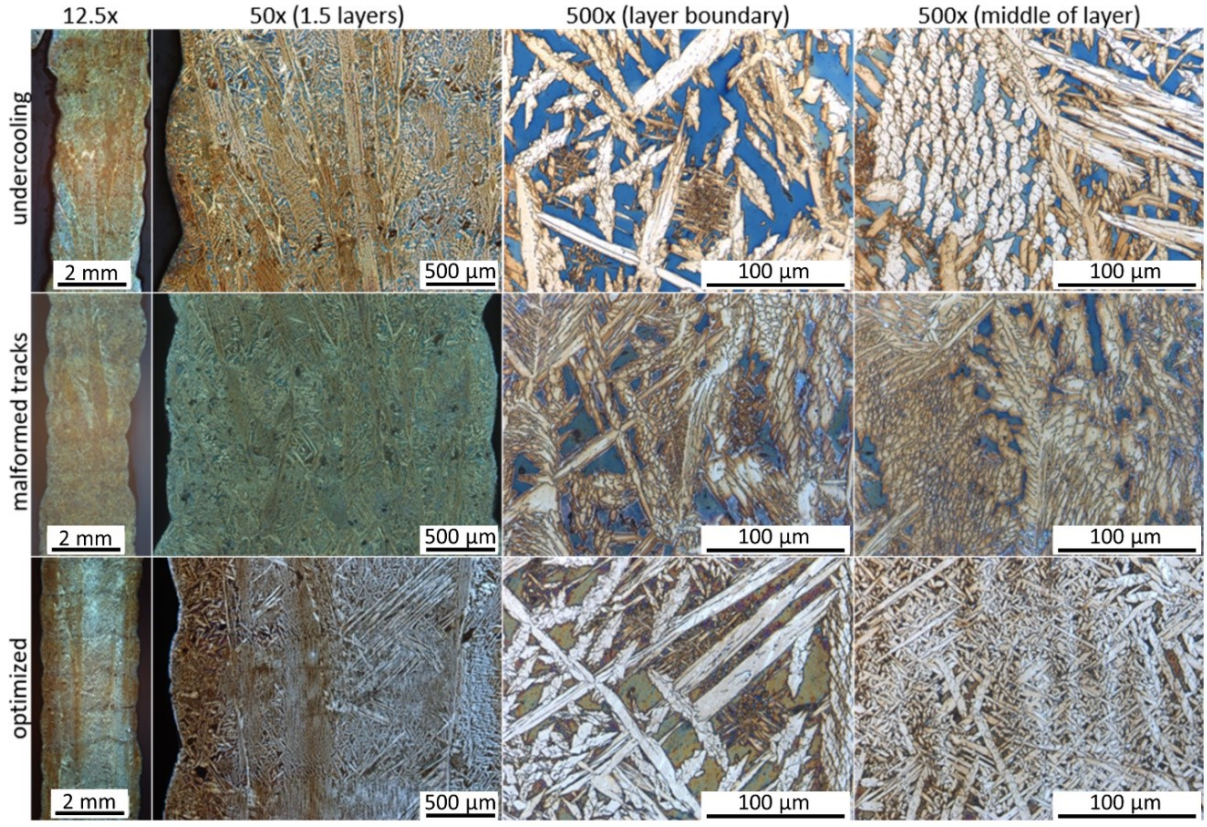

Figure 58: Macro and microstructure resulting from P2 (undercooling), P4 (malformed tracks) and P5 (optimized) parameters sets and conditions. For each parameter set the macrostructure, an overview of approx. 1.5 layers and enlarged views from the layer boundary region and the middle of a layer are shown. [21]

A wire-plunging site was investigated in more detail (Figure 59). Some disturbance of the microstructure but no lack of fusion defects due to the wire plunging through the melt-pool or lack of material could be found on the macro or micrographs. The macrograph (Figure 59 (a)) reveals epitaxial grain growth of prior ferrite grains across multiple different layers. The austenite development appears to be unaffected by the wire plunging site. At the base of the protrusion site, a small crack (approx. 100 µm) was found. Such small cracks were removed during machining of the surface.

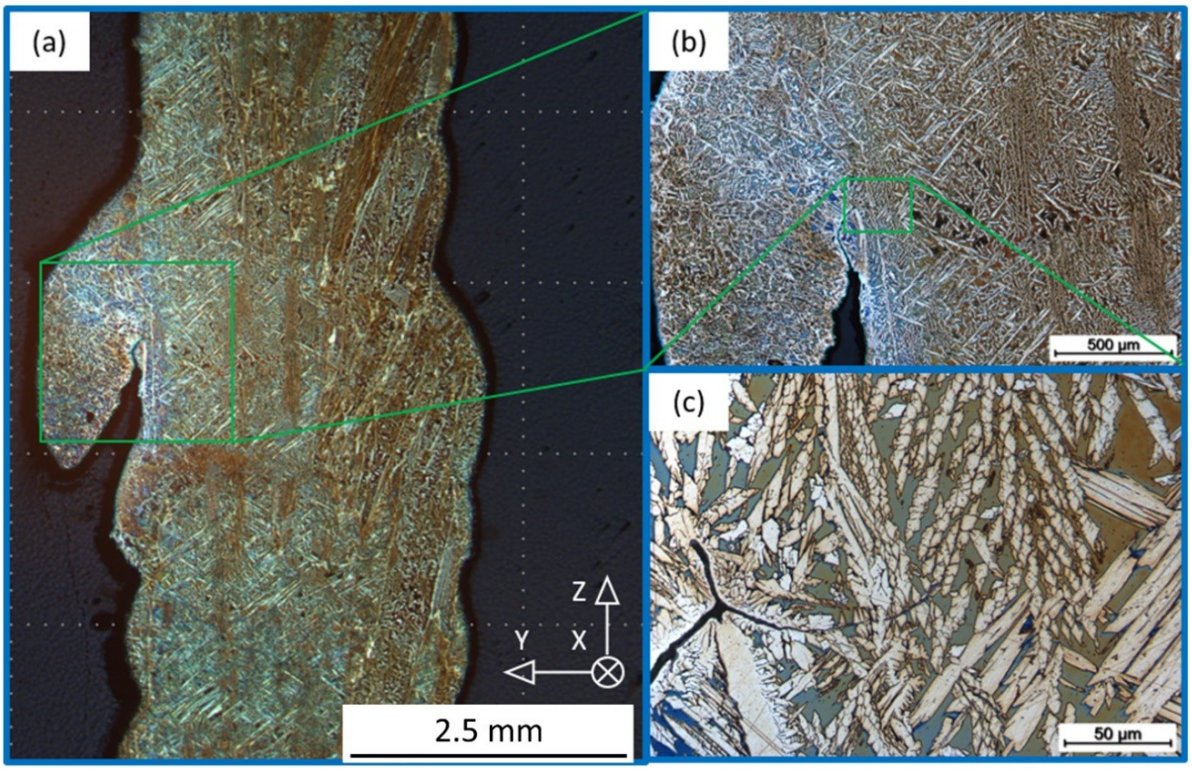

Figure 59: Macro- and microstructure near a site of a wire protruding out of a structure built with parameter set 2: (a) Macrograph showing that the microstructure is dominated by elongated prior ferrite grains and largely undisturbed by the wire plunging, (b) enlarged section showing the microstructure and (c) detailed view of a small crack at the base of the wires protrusion location. [21]

An SEM image, that was taken from the optimized processing route, is shown in Figure 60. The difference in intensity of the microstructural features stems from material and orientation contrast, which is the result of crystal orientation and spatial variation in chemical composition. The chemical compositions at the measuring locations, which are marked in Figure 60, as derived from the EDX spectra, are summarized in Table 13. Measurement locations one to six exhibit chemical compositions, which are close to the nominal composition of the alloy. Location one exhibits an increased content of the ferrite stabilizing elements chromium and molybdenum and decreased levels of the austenite stabilizing element nickel compared to the alloy composition (reference analysis (Table 2)). The locations 2 to 6 exhibit increased concentrations of nickel. Locations 7 to 9 exhibit high concentrations of oxygen, silicon and manganese compared to the remainder of the material.

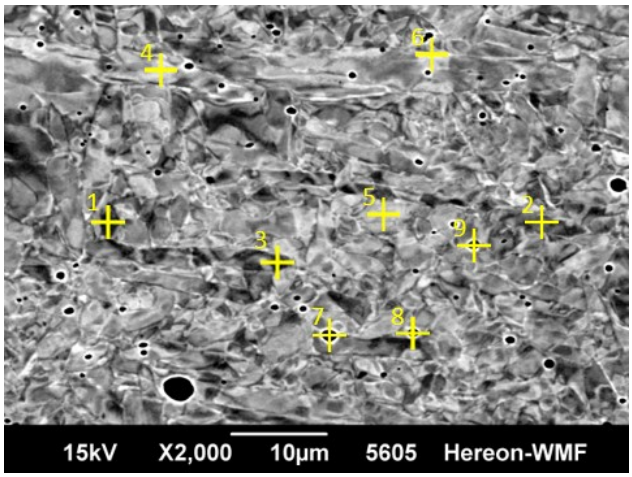

Figure 60: SEM image of a sample from the optimized processing route. EDX measurement locations are shown in yellow. The results are summarized in Table 13. Locations 1 to 6 serve as reference to locations 7 to 9. [21]

Table 13: Chemical composition derived from the EDX spectra collected at the locations shown in Figure 60.

Loc.	%O	%Al	%Si	%Mo	%Cr	%Mn	%Fe	%Ni
Reference analysis [29]			1.0	2.5-4.0	21.0-24.0	2.5	Bal.	7.0-10.0
1			1.15	4.4	26.2	1.4	60.9	6.1
2			0.81	2.7	22.0	1.6	62.5	10.4
3			0.69	2.5	21.7	1.7	62.4	11.0
4			0.66	2.9	22.9	1.5	62.6	9.4
5			0.83	2.9	22.5	1.7	61.9	10.3
6			0.7	3.0	22.0	1.7	62.0	10.6
7	23.5	0.58	10.3	1.8	18.9	23.8	19.1	2.0
8	19.7	0.66	1.0	2.1	32.5	15.3	25.7	3.0
9	17.3	0.46	10.0	4.2	12.8	24.6	27.5	3.4

The evaluation of the EDX spectra from the material revealed partitioning of ferrite and austenite stabilizing elements and the formation of spots rich in manganese, silicon and oxygen. The composition measured in these spots leads to the conclusion, that these are inclusions rather than microporosity, as the composition is similar to the one measured by Iams et al. [32] for duplex stainless steel fabricated via laser directed energy deposition with powder.

The samples produced to investigate the effects of variation in laser power and welding speed were investigated in a similar manner. The hardness was measured along the build direction. The phase fraction was determined according to Section 3.4.2. The evaluation of the phase fraction from optical micrographs allows the investigation of larger areas than time-consuming EBSD measurements while yielding comparative accuracy [25].

The parameter settings tested during the systematic variation of process parameters, the resulting average hardness values and the average ferrite contents are shown in Table 14.

The average ferrite fraction and average hardness showed little influence on the linear heat input (Figure 61).

Table 14: Process parameters tested for the fabrication of thin-walled rectangular parts.

P_{SS} [W]	v_{TCP} [m/min]	0.25		0.5		1	
		Hardness [HV10]	Vol.% ferrite	Hardness [HV10]	Vol.% ferrite	Hardness [HV10]	Vol.% ferrite
1500		248	37	248	49	-	-
2000		-	-	248	41	256	39
3000		240	37	251	32	246	41

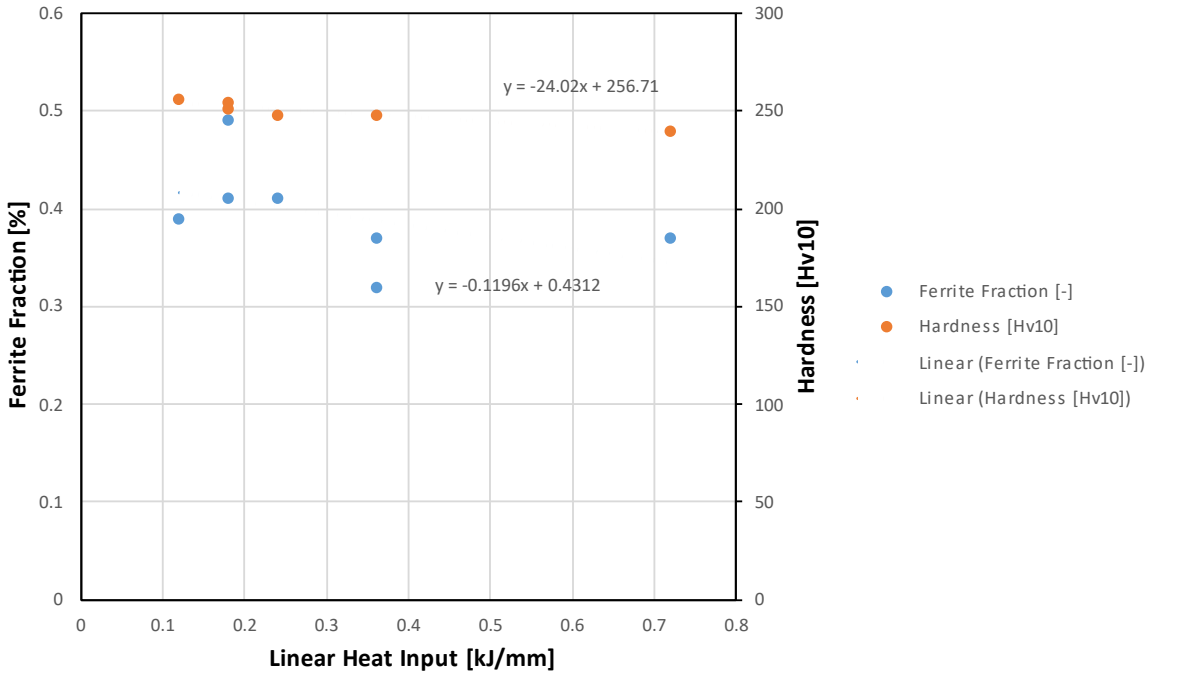

Figure 61: Correlation between the linear heat input, hardness and ferrite fraction for the parameter variation with open loop control.

Representative microstructures from the parameter sets, where a high cooling and solidification rate (P_{Laser}=1500 W, v_{TCP}=0.5 m/min, 0,18 kJ/mm) as well as the lowest solidification rate (P_{Laser}=3000 W, v_{TCP}=0.25 m/min, 0,72 kJ/mm) that can be expected due to the combination of energy input and welding speed are shown in Figure 62. The difference in line energy is 4-fold between the two samples.

There are no qualitative differences of the microstructure morphology. The microstructures exhibit the same features consisting of epitaxially grown prior ferrite grain separated by austenitic grain boundaries. Lamellar austenitic grains formed inside the prior ferrite grains. Below the fusion lines some agglomerates of secondary austenite can be observed. The lack of variation in microstructure with cooling rate can be attributed to the steady state reached during fabrication. After approx. 25 layers, a thermal equilibrium between the part and heat sink is reached, which determines the cooling rate, so that laser power and welding speed only have a minor influence. All combinations of process parameters suffered from heat accumulation in the same manner, so that the cooling rate was governed not by the

process parameters but rather by the temperature gradient to the heat sink, which was the substrate in this case. Lack of fusion defects associated with plunging [128] could not be observed for the coaxial L-DED-wire process with duplex stainless steel.

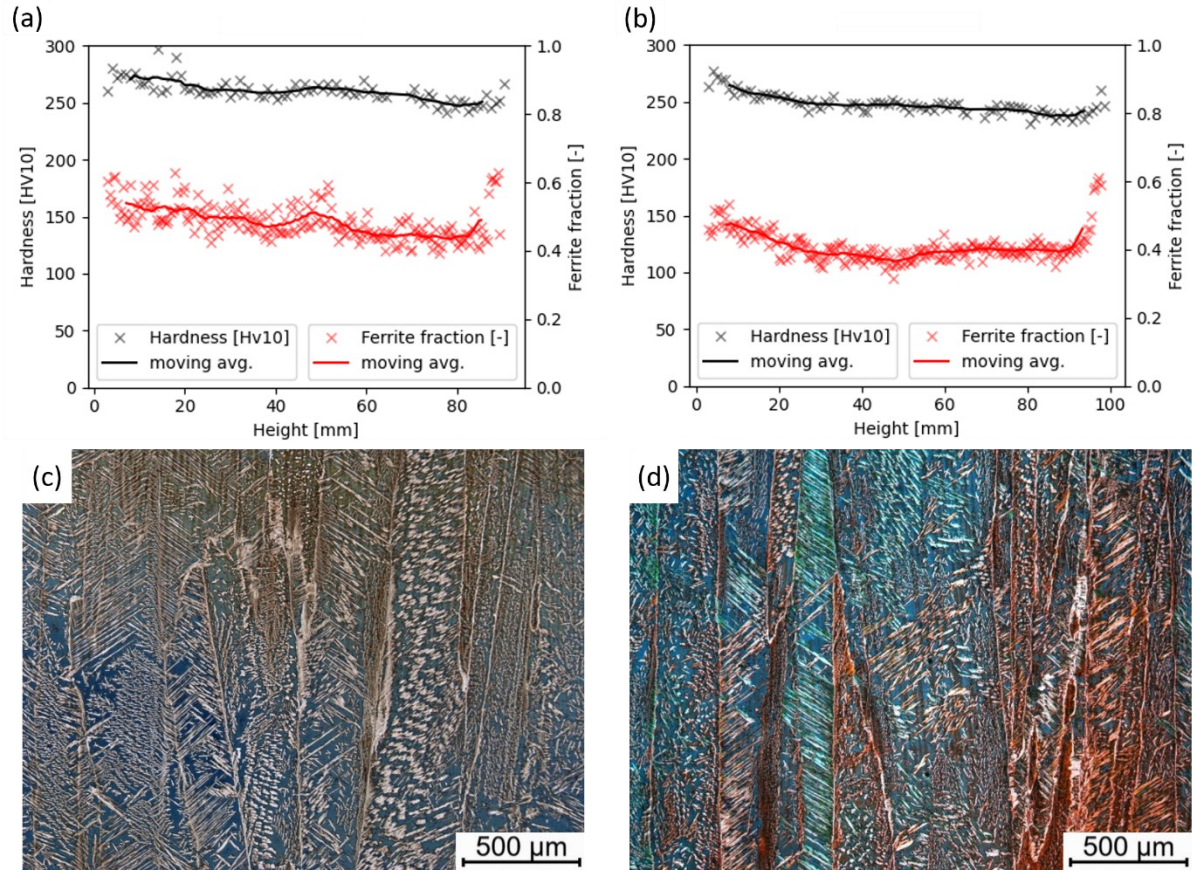

Figure 62: (a) Hardness and ferrite fraction for (P_L=1500 W, v_{weld}=0.5 m/min), (b) hardness and ferrite fraction for (P_L=3000 W, v_{weld}=0.25 m/min), (c) and (d) optical micrographs from (a) and (b) corresponding to a linear heat input of 0.18 kJ/mm and 0.72 kJ/mm.

EBSD Analysis

EBSD-Analysis was performed on samples from the discontinuous deposition of rectangular parts. The microstructure consists of 59.7% austenite and 38.3% ferrite in the selected micro-area. It appears that 2.0% sigma phase was also present (Figure 63). However, since no precipitates can be discerned the amount of sigma-phase can also be a result of misidentification at grain boundaries. Estimating the mean grain diameter gives g_d= 35.5 ±7.3 µm for the austenitic phase and g_d= 43.5 ±8.9 µm for the ferritic phase. The respective phases and crystallites are formed within former ferrite.

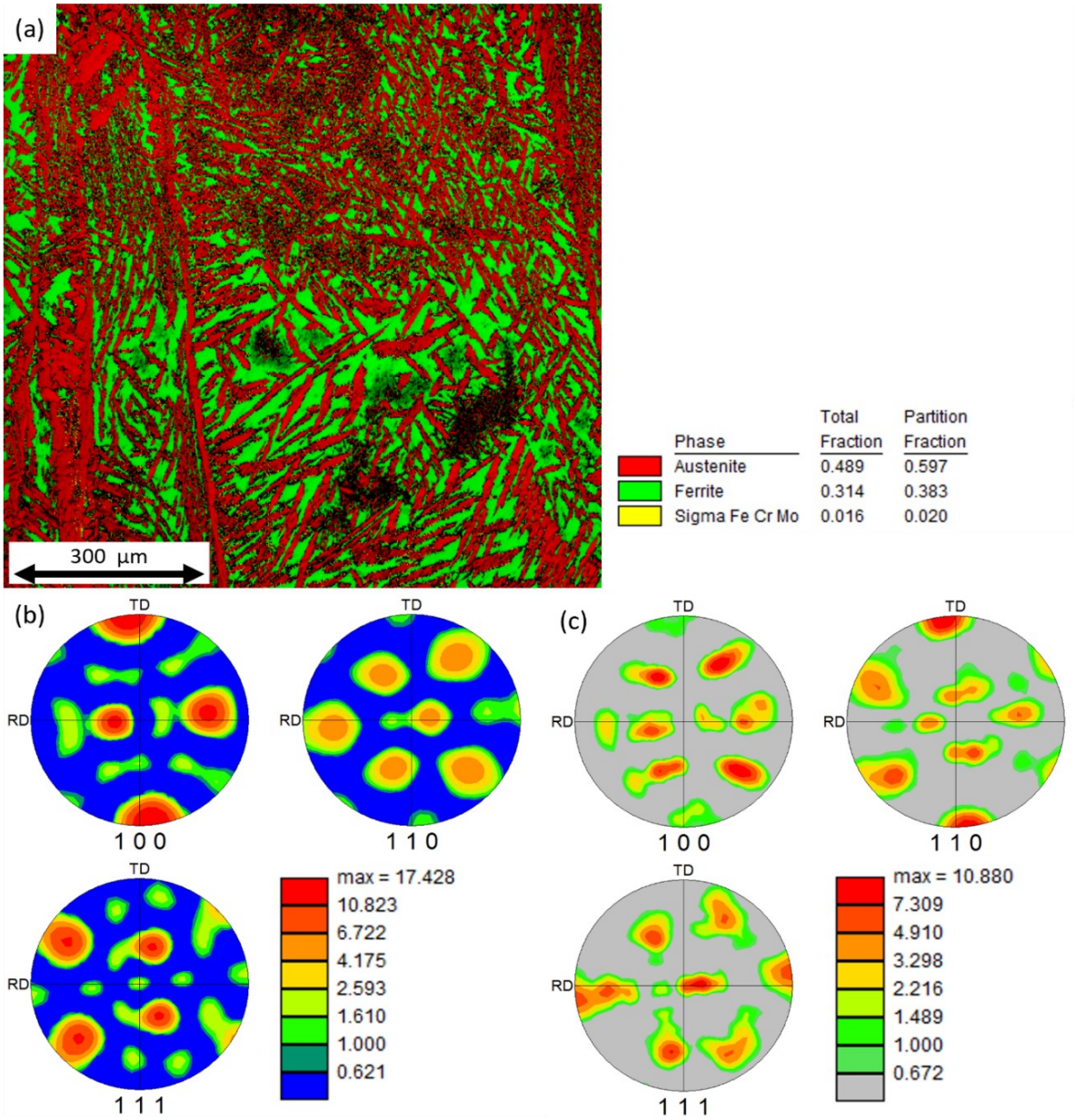

Figure 63: (a) representative cross section of a thin-walled specimen, (b) ordinary pole figure of the ferritic phase and (c) ordinary pole figure of the austenitic phase.

In the selected micro-area, the ferrite phase exhibits the <1 0 0> fiber texture and the inverse Goss orientation (1 1 0)[0 1 1]. However, the respective microtexture components are rotated 7° around ND and 13° around TD. $\langle 1\ 0\ 0\rangle_{\delta}$ and $\langle 1\ 1\ 0\rangle_{\gamma}$ are the preferred crystal growth directions of the ferrite and austenite phases, i.e. the transformation of the melt into the solid phase is orientation dependent. The directions of growth mentioned above are thus almost parallel to the direction of build-up or perpendicular to the direction of welding. The relation between the ferrite and austenite phases is $(1\,1\,1)_{\gamma}//(1\,1\,0)_{\delta}$. With regard to the pole densities, there is almost congruence between the $(1\,1\,1)_{\gamma}$ and $(1\,1\,0)_{\delta}$ pole figures (Figure 63 (b) and (c)).

The calculation of the Taylor factors (Table 15) was based on the slip systems (1 1 0)[1 -1 1] and (1 1 1)[1 -1 0] for the body-centered cubic δ-ferrite or face-centered cubic austenite phase. With uniaxial tensile stress parallel to the RD axis, the following mean Taylor factors result in: M0° = 2.97 ±0.25 for the ferritic phase and M0° = 3.15 ± 0.37 for the austenitic phase (Figure 64). Two distinct maxima of 2.85 and 3.45 occur in the distribution of Taylor factors. Figure 64 (a) makes it clear that the crystal directions ⟨1 0 2⟩//[0 0 1] and ⟨1 0 1⟩//[0 0 1] that occur separately in the selected micro-range are the reason for the maxima in the Taylor factor distribution. Figure 64 (b) shows that the distribution of the Taylor factors ranges from 2.31 to 3.65. Differences in Taylor factors between the respective microscale grains are an indicator of strain incompatibilities, which can lead to stress concentrations.

Considering the case of uniaxial tensile stress at an angle of 45° between RD and TD, a Taylor factor of $M_{45°}$ = 3.33 ±0.10 results for the ferritic phase and $M_{45°}$ = 3.07 ±0.41 for the austenitic phase (Table 15). For a stress angle of 90° the following results can be obtained: $M_{90°}$ = 2.41 ± 0.08 for the ferritic phase and $M_{90°}$ = 3.39 ± 0.40 for the austenitic phase (Figure 64).

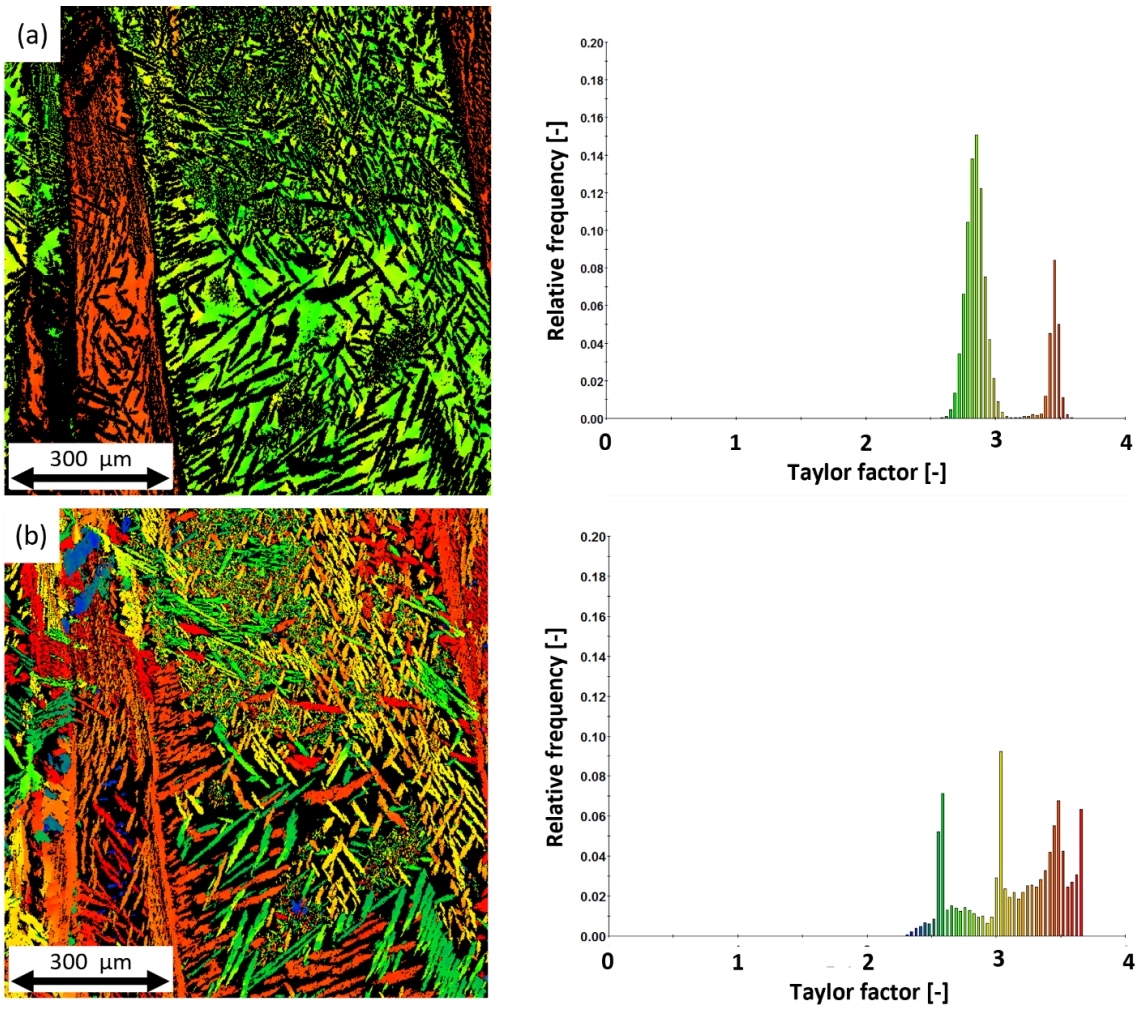

Figure 64: Taylor factor distribution. (a) ferritic phase, (b) austenitic phase.

Table 15: Taylor factor by phase with regard to the RD-direction (perpendicular to the build direction).

0° (RD, horizontal, weld direction)		45°		90° (TD, vertical, build direction)	
δ	γ	δ	γ	δ	γ
2.97 ±0.25	3.15 ±0.37	3.33 ±0.10	3.07 ±0.41	2.41 ±0.08	3.39 ±0.40

The Taylor factor of the ferritic phase is calculated from essentially two prior ferrite grains in the selected micro-area (Figure 64 (a)). For the austenitic phase a wider range of grain orientations is present in the same micro area. Due to the Nishiyama-Wassermann and Kurdjimov-Sachs orientation relationships the orientation of the slip-systems in the austenitic phase are coupled to the parent ferrite grain. Therefore, either more EBSD measurements for sufficient statistics need to be performed or it must be shown, that the selected micro-area is representative of the whole material despite the small number of evaluated grains.

Microstructural Characterization using high energy X-Ray Diffraction

In order to validate the micro-area EBSD-results regarding the phase fraction and micro-texture measurements and the derived Taylor factors larger volume measurements were performed at the high energy materials science beamline at DESY. This is essential, as the ferritic phase is composed of large grains. Using EBSD it is not possible to find a resolution, where both the fine secondary austenite are resolved and simultaneously a good statistic of the ferrite grains is obtained.

A representative spectrum and the measurement locations resulting from the measurements at P07b are shown in Figure 65. The sample dimensions were approx. 3 mm × 3 mm × 30 mm. For the P1 specimen the measurement location was 10 mm from the top surface. For the P5 sample, the measurement locations were 0 mm, 5 mm, 10 mm, 15 mm, 20 mm and 25 mm from the base. Analysis using Rietveld refinement yielded ferrite fractions of 0.33 ± 0.007 and 0.34 ± 0.008 austenite fractions of 0.67 ± 0.007 and 0.66 ± 0.008 for the two investigated specimens respectively.

Ordinary pole figures for the P1 and P5 specimen are shown in Figure 66 and Figure 67 respectively. The distribution of the orientation relationships shows both the Kurdjomov-Sachs and Nishiyama-Wassermann $(1\,1\,1)_\gamma//(0\,1\,1)_\delta$ orientation relationships. The δ-ferrite solidifies preferentially in the [100] direction and the austenite precipitates according to the above-mentioned specific relationship with the surrounding ferrite matrix. The material is increasingly textured along the height of the welded sample because of the preferential solidification along the [100] direction.

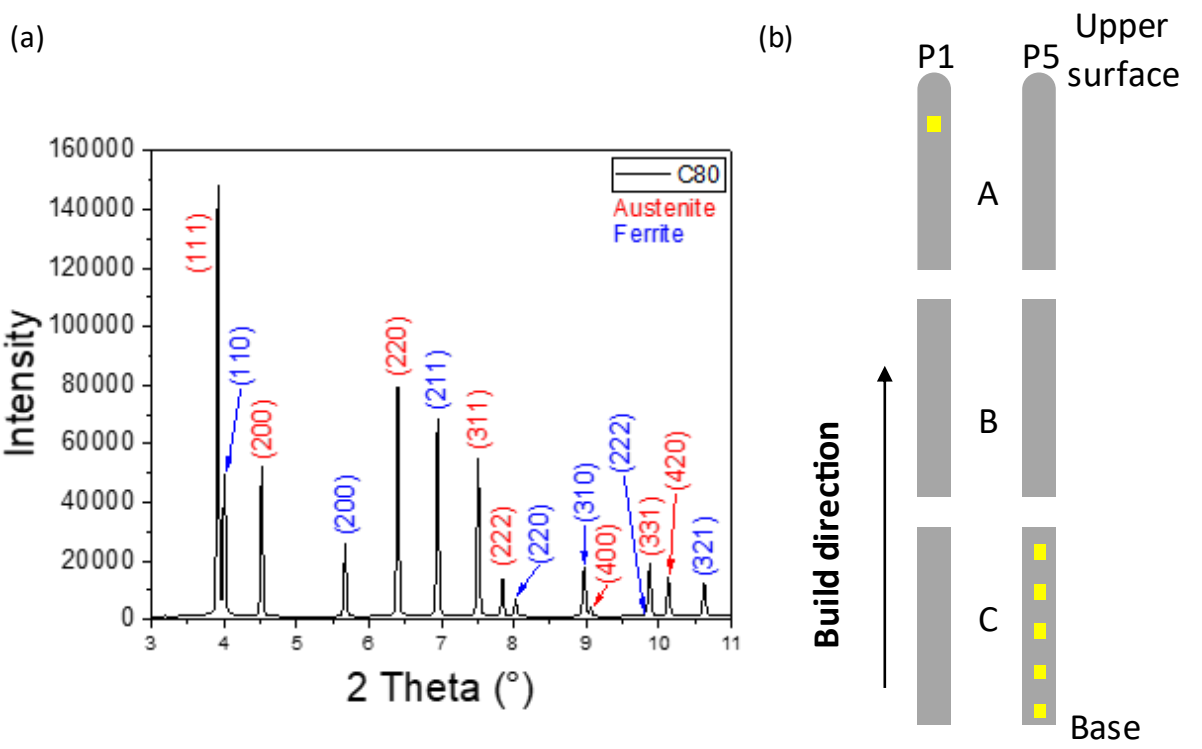

Figure 65: (a): Spectrum from the measurement at P07b and (b) measurement locations on the sample.

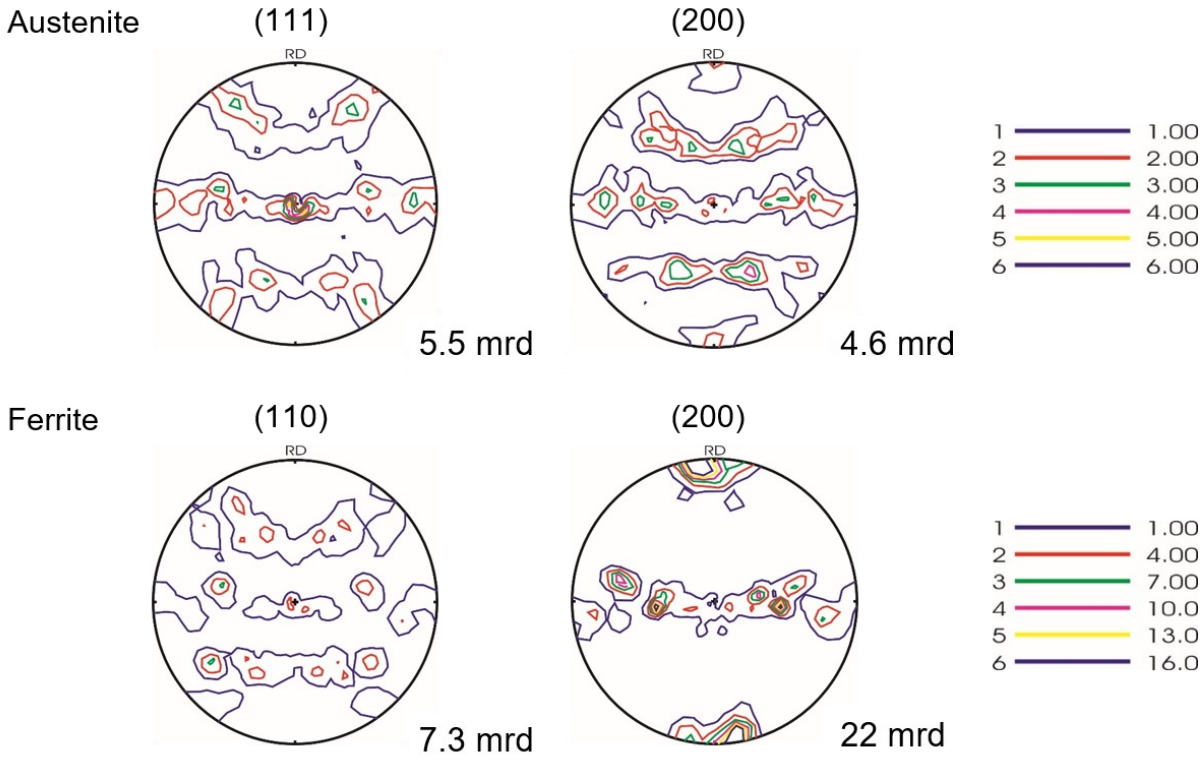

Figure 66: Ordinary pole figures showing the macrotexture of the P1 specimen.

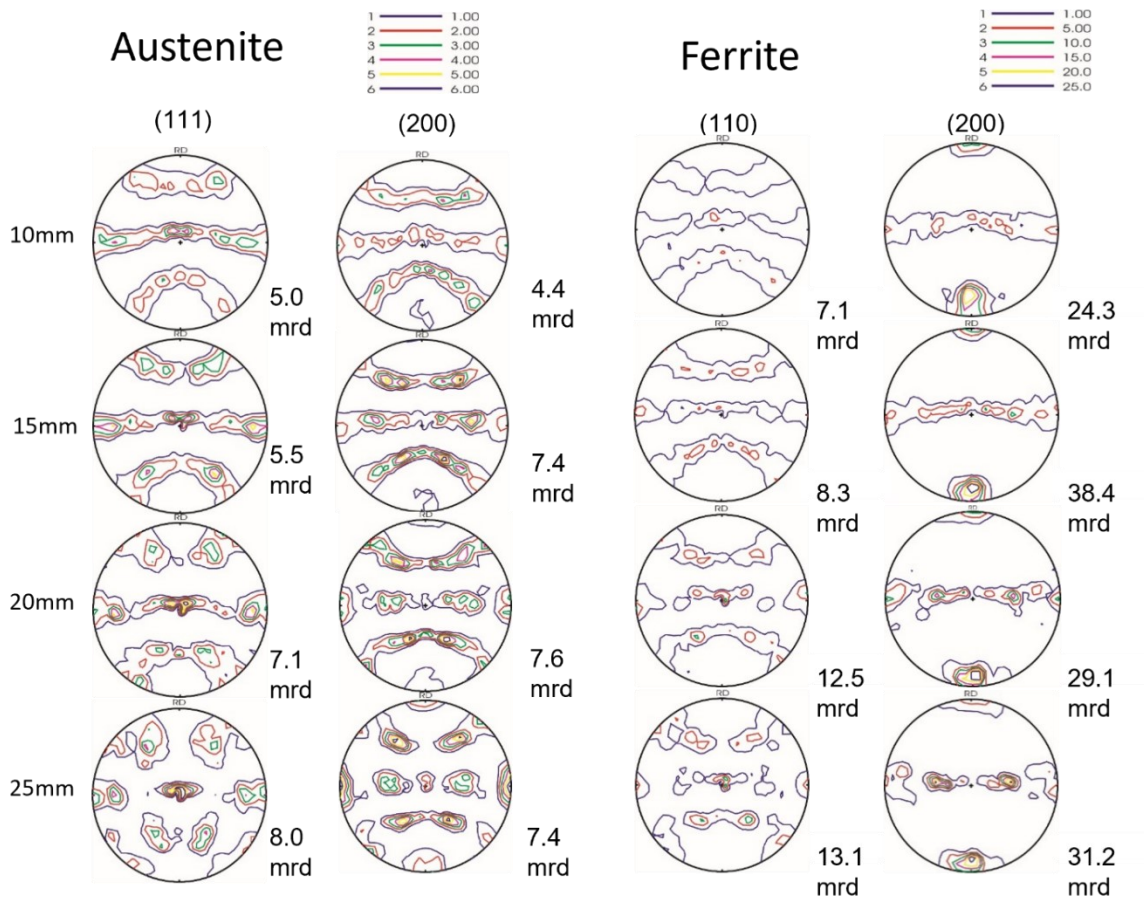

Figure 67: Ordinary pole figures of the P5 specimen.

The results obtained from the high energy X-Ray experiments support the EBSD measurements. The microstructure of the material is the result of the strong directional solidification and heat flow during the process. Epitaxial growth of ferritic grains across layer boundaries was found in accordance with [95,96]. An increased ferrite content at the layer boundaries forms because the solidification and cooling rate is highest at the bottom of the weld track. This region is furthest away from the next track, thereby leading to reduced formation of secondary austenite due to reheating. The epitaxial growth of prior ferrite grains is the result of a fully ferritic equilibrium phase fraction at high temperatures for DSS [37,38,88]. The morphology and phase fraction of the austenitic phase is similar to the morphology reported by Bermejo et al. [96] for the case when using a nitrogen shielding gas. Bermejo et al. [96] did not report the interpass temperature or inter layer wait time during their deposition steps and used approximately twice the laser power (3.5 kW) at comparable welding velocities (0.6 m/min). Since the shielding gas atmosphere, as well as the laser power, are different and the inter layer wait time is unknown, a direct comparison of the results is not possible.

Microhardness Measurements

The results of the microhardness measurements for structures produced with parameter sets P1 and P5 are shown in Figure 68. Parameter sets P1 and P5 resulted in microhardness of 267 ± 6 HV0.1 and 262 ± 7 HV0.1 for position below a height of 75 mm respectively. A 2%

lower average hardness was measured on the specimen produced without pauses. The duplex stainless steel is a two-phase alloy, where the two phases may possess significantly different hardness values. The error bars represent the difference in hardness between the two phases while the average hardness represents the probability of measuring one phase or the other, when the hardness indents are placed randomly. In both specimens, there is a region with slightly reduced hardness directly below the top. Here, the average hardness reduced to 260 ± 6 HV0.1 and 256 ± 7 HV0.1 for parameter sets P1 and P5 respectively. At the top of the parts, the hardness increases sharply up to a value of approx. 312 HV0.1 and 305 HV0.1 for parameter sets P1 and P5 respectively. The standard deviation, maximum and minimum values for the hardness are reported in Table 16.

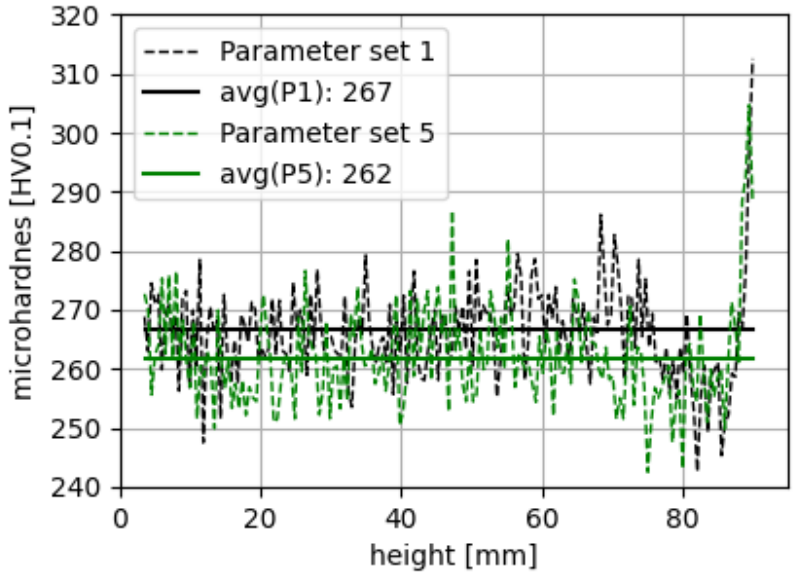

Figure 68: Microhardness profiles of the specimens produced with parameter sets P1 and P5. [21]

Table 16: Statistical description of the hardness measurement results broken down by specimen regions.

Region	Below 75 mm (144 meas.)				75 mm to 85 mm (20 meas.)				Top (11 meas.)			
	Mean	Max.	Min.	Std. Dev.	Mean	Max.	Min.	Std. Dev	Mean	Max	Min	Std. Dev.
P1	267	286	248	6	259	269	243	6	268	313	245	20
P5	262	289	250	7	256	269	243	7	273	305	249	18

The constant hardness along the height of the specimens is a result of the material experiencing a similar repetition of thermal cycles [20]. The observation of constant hardness is a good argument for similar mechanical properties throughout the structure. The uppermost layer experiences no additional thermal cycles. Therefore, no additional austenite precipitates in the ferrite matrix, which explains the higher hardness.

4.2.6 Tensile Tests

Specimens for the tensile tests were extracted from the parts in relevant locations so that potential process-induced defects were located within the gage section. For each type of processing induced discontinuity, one sample was extracted in the vertical and horizontal orientation. Examples of those strategic locations are shown in Figure 69 (a) to (d).

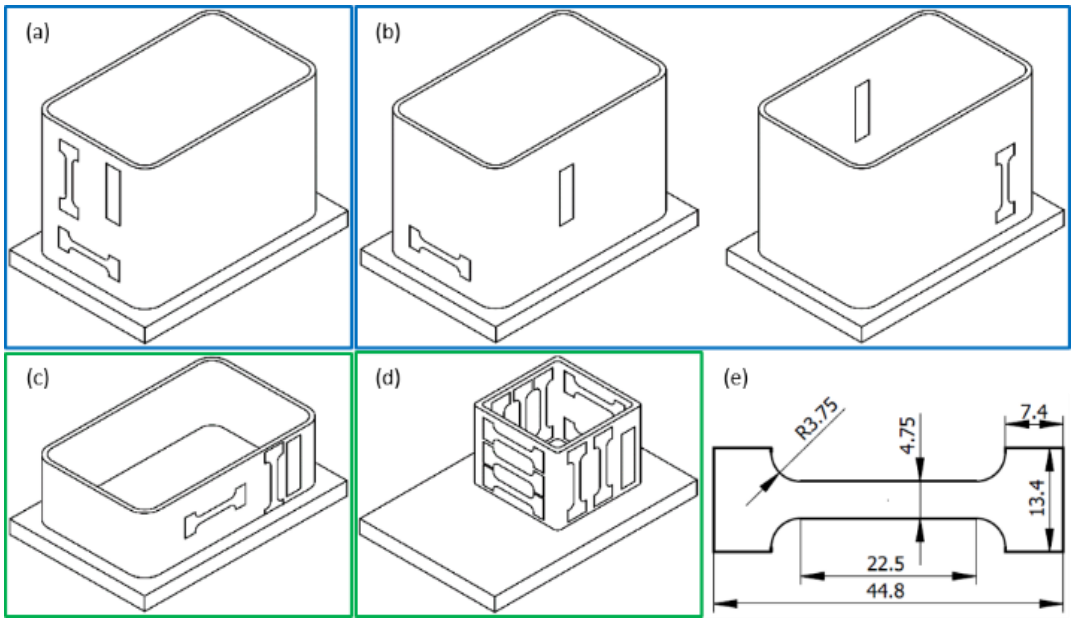

Figure 69: Extraction locations of the specimens for tensile tests and metallographic investigation: (a) Wire stick-out and (b) irregular track formation. Specimens were taken from the front and rear. (c) Optimized process: The build, from which the specimens were taken had to be aborted due to problems with the cooling system of the laser. Another full-size build was done, which was used for the extraction of specimens for fatigue samples. (d) Smaller build with optimized processing parameters for estimation of variation of material properties. (e) Geometry of the tensile test specimens. [21]

The stress-strain curves from the uniaxial tensile tests are shown in Figure 70. All specimens fractured within the gage length and exhibited ductile failure. The resulting yield strengths, ultimate tensile strengths and fracture strains are summarized in Table 17.

Most mechanical properties of the samples extracted from the large, rectangular parts were within 2 standard deviations from results for the sample from the smaller cube-like reference part. The samples extracted from relevant locations to contain potential defect sites did not possess significantly worse properties than the comparison sample and were within 2 standard deviations of the samples from the comparison part. The reduction of part size and its increase in heat accumulation did not lead to a change in mechanical properties.

The material exhibited anisotropy of the tensile properties. The average yield strength in the horizontal and vertical directions for the comparison cube were 586 ± 16 MPa and 481 ± 24 MPa respectively. The lowest ultimate tensile strength for horizontal specimens (768 MPa) was 96 MPa higher than the lowest ultimate tensile strength in vertical specimens (672 MPa) direction. The average fracture strain in the vertical direction (0.466) was 0.228

higher than in the horizontal direction (0.245). Interestingly, the 45° direction exhibited the highest strength and lowest ductility of all measured directions instead of an average of the two.

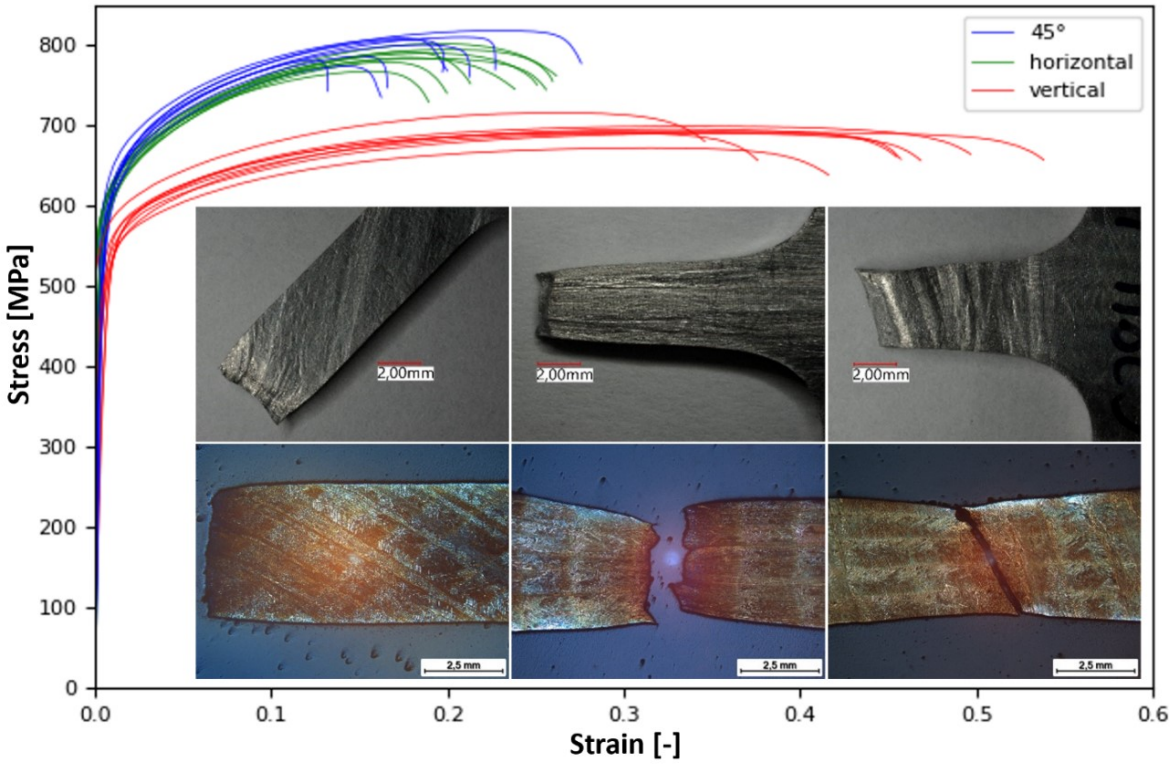

Figure 70: Stress-strain curves from the tensile tests: The legend refers to the load direction with regard to the build direction. Samples with discontinuities are included. The pictures in the first column show the 45° direction, the second column the vertical direction and the third column the horizontal direction.

Etched cross-sections of the fractured tensile specimens (Figure 70) reveal that the strong anisotropy of the microstructure in combination with the texture is the reason for the directional dependence of the tensile properties. Specimens, which were extracted along the horizontal direction, fractured in an intragranular fashion with regard to the prior ferrite grains. The fracture path lies at an angle of approximately 60° towards the load direction. An angled fracture path is typical for ductile fracture, but usually material with isotropic microstructures yields at an angle of 45°, where the shear stresses are maximized. Specimens, which were extracted along the vertical and 45° direction, exhibit a more irregular fracture path, which is oriented at a 90° angle to the load direction. The peaks and valleys of the fracture path coincide with the locations of austenitic seams located at the prior ferrite-ferrite grain boundaries for the horizontal sample. Individual segments of the fracture path lie at an angle with regard to the loading direction, so that they are not perfectly perpendicular.

Table 17: Statistical description of the results from the tensile tests. The difference in terms of the number of standard deviations is given in the standard deviation columns for the single repetition tests.

Parameter		Yield strength [MPa]				Ultimate tensile strength [MPa]				Fracture strain [-]			
		Mean	Max	Min	Std. Dev.	Mean	Max	Min	Std. Dev	Mean	Max	Min	Std. Dev.
vertical	Wire stick out (1 meas.)	470			<1×σ	696			2×	0.481			<1×σ
	Uneven track (1 meas.)	473			<1×σ	717			3×	0.371			<2×σ
	Optimized (1 meas.)	486			<1×σ	692			1×	0.561			<2×σ
	Comparison (5 meas.)	481	517	456	24	689	700	672	10	0.466	0.525	0.398	0.048
horizontal	Wire stick out (1 meas.)	560			<2×σ	802			2×	0.284			<2×σ
	Uneven track (1 meas.)	589			<1×σ	785			1×	0.264			<1×σ
	Optimized (1 meas.)	560			<2×σ	792			1×	0.211			<1×σ
	Comparison (5 meas.)	586	600	561	16	784	795	768	11	0.238	0.268	0.196	0.034
45°	Comparison	631	653	611	31	800	820	775	16	0.192	0.276	0.131	0.042

The material exhibits significant anisotropy with regard to the orientation of the specimens. In the horizontal case, the layer boundaries – with their increased ferrite content – act as fibrous reinforcement, which also limits fracture strain when the limit of deformation for the ferritically enriched parts is reached (Figure 71 (a)). In this case, all regions of the microstructure are subject to the same strain. In the vertical case, the regions with higher austenite content are connected in series with the stronger layer boundaries, allowing them to undergo much higher deformation – albeit at lower loads – before the specimens finally rupture due to strain mismatch between the layer boundaries and the center of the welded tracks (Figure 71 (b)). In this case, all parts of the microstructure are subject to the same stress but can undergo different strains.

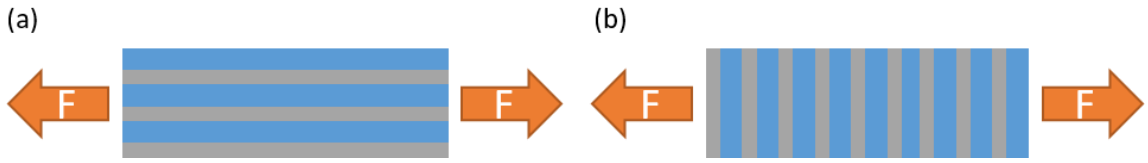

Figure 71: Schematic explaining the applicable laws of mixtures. (a) Horizontal case, where the layer bands and layers are connected in parallel. (b) Vertical case, where the layer bands and layers are connected in series. [21]

Additionally, the yield strength correlates well with the Taylor factors for the ferritic phase. For the horizontal and 45° case the lowest and highest Taylor factors were measured respectively.

The standard deviation of the fracture strain is larger in the vertical than in the horizontal direction. The macrostructure of the material is dominated by large prior ferrite grains, which are regions where the crystal orientation of the ferritic phase is constant and the crystal orientation of the austenitic phase was observed to be determined by the Kurdjumov-Sachs orientation relationship [173]. When the test section of a tensile test specimen only contains a few or one dominant prior ferrite grain, the deformation is dictated by the best orientation of any slip system. An argument against this explanation is, that both ferrite and austenite are cubic lattices, which have a plethora of slip systems so that the variation in Schmid factor with changing orientation is not as large as for example in hexagonal close-packed systems.

ASTM A240 [174] places minimum requirements of 655 MPa ultimate tensile strength, 450 MPa yield strength and 0.25 fracture strain on DSS 2205. The minimum of the yield and ultimate tensile strength exceed the requirements by 34 MPa and 31 MPa respectively in the vertical direction. The minimum fracture strain (0.192, 45° direction) is below the requirement. The orientation with the lowest fracture strain is the one with the highest yield and ultimate tensile strength, which exceed the requirements significantly. Regarding the strength and fracture strain, the material can compete with wrought material of similar chemical composition. Due to the flexibility of the manufacturing setup, it is possible to achieve tailored properties in a part depending on whether high strength or high damage tolerance is needed.

The discontinuities, which appear in the “cold” processing route on the outside of the specimens and due to bending deformation of the specimens during deposition, have no detrimental effect on the microstructure and mechanical properties. The reason for the similarity in microstructure between the region of the unmolten wire and the rest of the structure can be attributed to partial melting of the wire, which ensures good bonding. Additionally, the wire material experiences similar thermal cycles as the rest of the structure, which leads to similar austenite formation.

The additively manufactured material exhibits a strong anisotropy in tensile properties, while still exceeding most requirements for wrought material of a similar alloy composition. The directional dependence can be attributed to the presence of layer bands, consisting of regions with increased ferrite content, which act as a fibrous reinforcement. Instabilities during the manufacturing process cause surface discontinuities, which are not detrimental to the material properties, when they are removed in a machining step.

4.2.7 Closed-loop Control

The previous sections described the results obtained from open loop control of the process parameters. Due to the high experimental effort required for the open loop control, a process control method [22] based on the interaction force between wire and substrate was developed.

The viability of the approach for process control with adaptive layer height was validated by the fabrication of the sample part shown in Figure 72. The sample part is a pipe manifold

with a curvature in the joint region. This part is time-consuming to fabricate conventionally since pipe section must be formed and cut precisely, fixed in position and then welded. It is also challenging to manufacture additively because it has an overhang of approx. 30°.

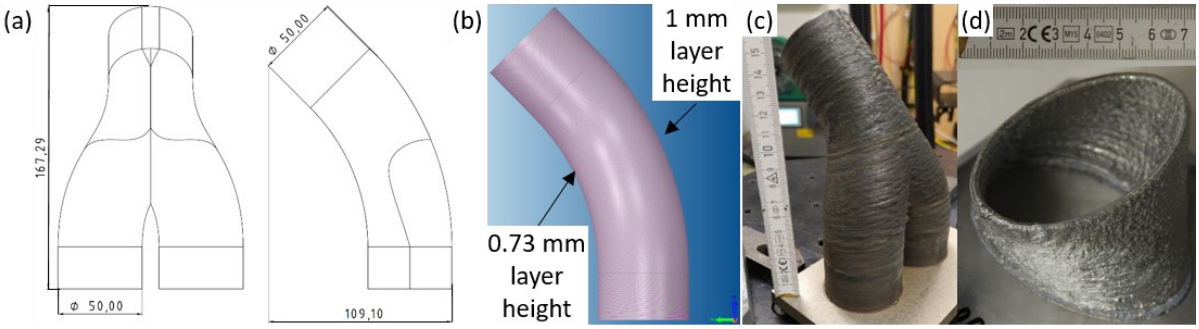

Figure 72: Sample parts produced using closed loop control: (a) Drawing of simplified manifold exhaust pipe, (b) CAD-model (c) part made from DSS 2209 and (d) freeform part made from EN AW-6063 aluminum alloy.

Here, a different manufacturing route to the traditional planar slicing along the Z-axis known from typical 3-axis AM-machines was chosen. The cuts were made perpendicular to the neutral fiber of the bent pipe, resulting in an effective layer height of approx. 0.73 mm and 1 mm on the inside and outside of the sample part respectively. The tool orientation was kept upright during the deposition process, while the positioner moved the part, so that the tools Z-axis was always perpendicular to the tool movement direction and tangential to the surface of the part. The control strategy successfully adapted the wire feed rate according to the local pre-programmed layer height. The control method has also been shown to be applicable to aluminum feedstock material (Figure 72 (d)). The only adjustment that was needed to switch from the stiff steel feedstock material to the much more pliable aluminum feedstock was an adjustment of the controller setpoint to account for the reduced forces and friction inside the wire guides.

Force Control Specific Challenges

Through contact of the wire with the substrate the process control method ensures that the absolute minimum mass specific energy, which can be achieved for the given processing conditions, is employed. Therefore, the bonding to previous layers and the contact angle of the deposited tracks should receive particular attention. Figure 73 shows still frames from high-speed videos (Sprinter CR-S3500® Camera and Cavilux® illumination laser) of the deposition of single tracks on austenitic stainless steel with the focus on the substrate surface and 3 mm below the substrate surface. In the case shown in Figure 73 (a), the low mass specific heat input and the high irradiance on a small area produced an undesirable contact angle with irregular bonding to the substrate. In case shown in Figure 73 (b) the mass specific heat input and the irradiated area are higher, so that the contact angle was improved at the cost of the deposition rate and an increased remelting depth. The reduced deposition rate is caused by the reduced irradiated length of wire.

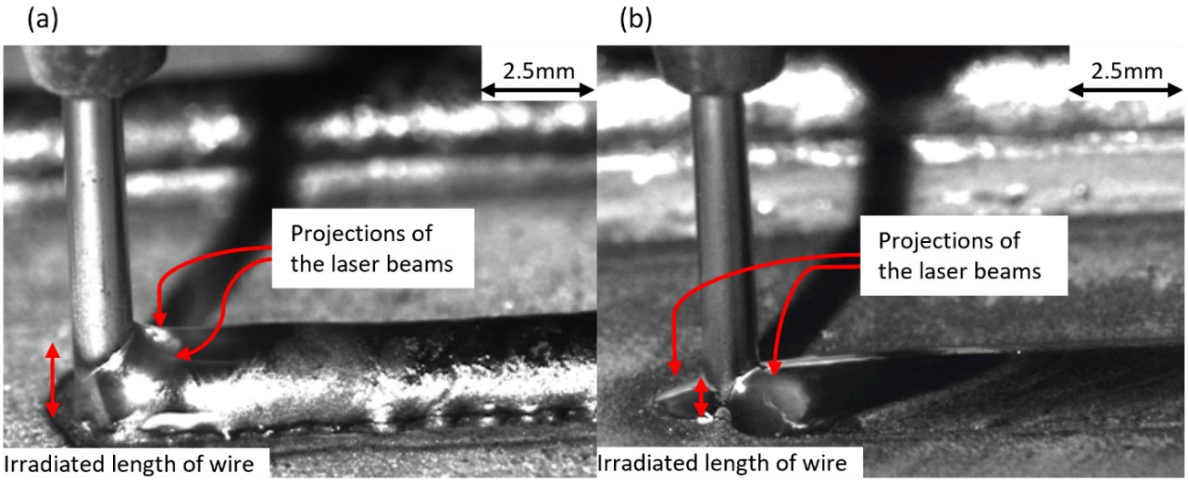

Figure 73: Still frames from high-speed videos of the deposition of a single layer track of DSS 2209 on austenitic stainless steel substrate at a defocus distance of (a) 0 mm and (b) 3mm below the substrate surface.

Figure 74 (a) and (c) show polished sections from the centerline of the track from Figure 73 (a) and (b) respectively The track from Figure 73 (a) exhibits lack of fusion defects, while in the defocused condition intermixing of the feedstock and substrate material with no lack of fusion defects can be observed. In Figure 74 (b) the process signals that correspond to Figure 74 (a) are shown. There is a noticeable likeness between the motor current signal and force signal, supporting the use of the motor current as a control variable for the process, as well as between the occurrence of LoF-defects and an increased force-signal. Conversely, a sufficiently small process force and large irradiated area lead to a stable process and structures without LoF-defects at the bottom or the sides of each deposited track and acceptable amounts of remolten material. The control loop exhibits a time-delay of approx. 150 ms caused by the delay between the set-point change and actuation for the wire feeder. Therefore, the practically achievable welding speeds were limited to approx. 2 m/min.

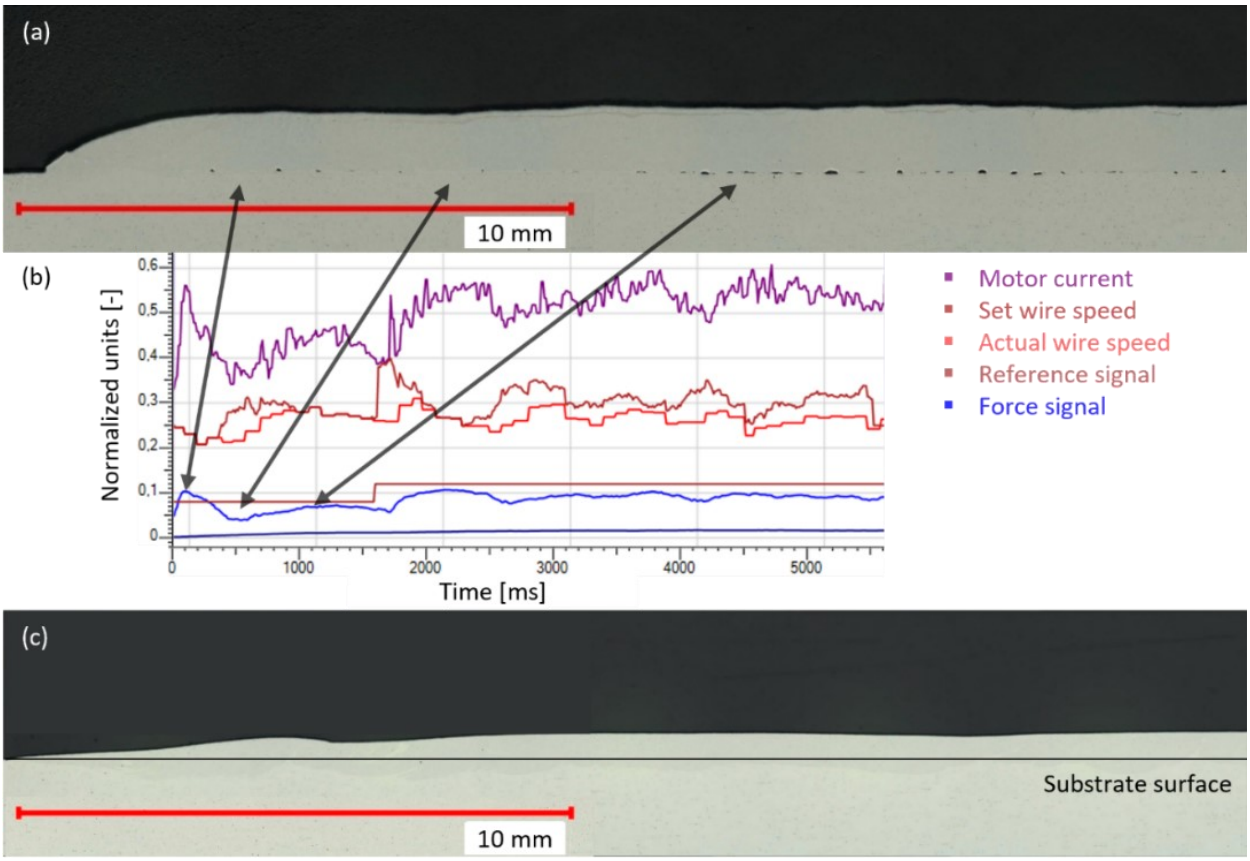

Figure 74: Front quarter of an 80 mm long and one layer high deposition sequence of 1.2 mm DSS 2209 wire on austenitic stainless steel at defocusing distances of 0 mm ((a)) and 3 mm ((c)) below the substrate surface. (b) Shows the process signals corresponding to (a).

4.2.8 Fabrication of Block-like Structures

Block like structures with a length of approx. 130 mm and a thickness of approx. 12 mm were produced using the force feedback process control approach developed during this work. The structures were produced using a constant laser power of 4 kW, welding speed of 2 m/min and height offset of 0.6 mm. The samples were produced by depositing five fill tracks with alternating direction followed by a contour pass. For the IPT100°C parameter set the interpass temperature was limited to 100°C. The absence of pauses led to an interpass temperature under steady state processing conditions of approx. 680°C (IPT680°C parameter set). The only pauses in the production of the IPT680°C sample stemmed from the robot motion from one start-point to the next.

Microstructural Characterization

Figure 75 shows etched micrographs obtained from block-like samples fabricated using the IPT100°C and IPT680°C parameter sets. Using IPT680°C the ferrite fraction varied between 0.07 and 0.35 with an average of 0.23. When the interpass temperature was controlled to 100°C, ferrite fractions varied between 0.32 and 0.79 with an average of 0.60. The low magnification micrographs in Figure 75 (b) and (e) show a fundamental difference between the states. At an Interpass temperature of 680°C layer lines are visible, and nearly the entire layer is homogeneously filled with finely grained needle-like and secondary austenite (Figure 75 (c)). Using IPT100°C results in a gradient of the amount of austenite in every layer. Higher contents can be observed at the top and lower contents at the bottom of each weld-track. Additionally, the samples with controlled interpass temperature exhibit much less secondary austenite.

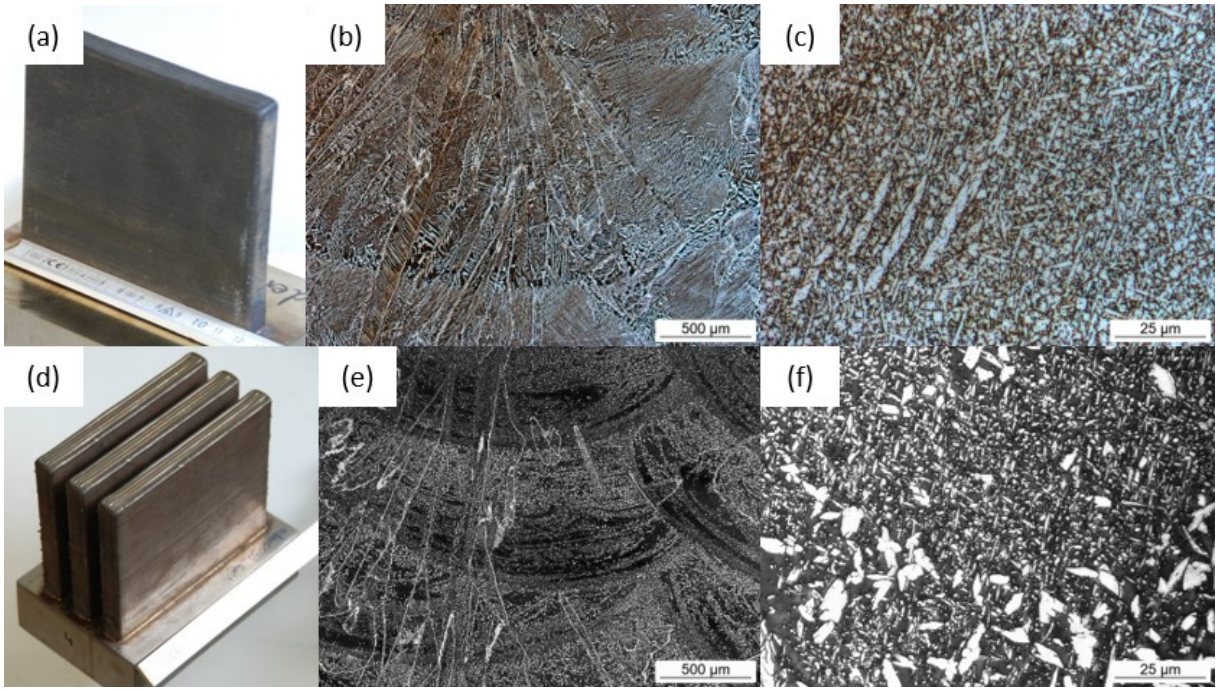

Figure 75: Samples produced at a line energy of 120 J/mm and a layer height of 0.6 mm: (a) to (c) were produced without interpass temperature control (IPT680°C) and (d) to (f) with the interpass temperature set to 100°C (IPT100°C).

Microhardness Maps and Measurements employing the Instrumented Indentation Test

In order to discern the influence of microstructure on the local material properties microhardness maps across the cross-section of approx. two to three weld tracks were measured for the samples produced with parameter sets IPT100°C and IPT680°C (Figure 76). The microhardness mapping yielded 270 HV0.1 to 316 HV0.1 with an average of 290 HV0.1 and 274 HV0.1 to 334 HV0.1 with an average of 296 HV0.1 for the IPT100°C and IPT680°C specimens respectively. The average difference between the process conditions was 6 HV0.1 or approx. 2% of the absolute value. Outlier values of hardness correspond to areas where layer boundaries or prior ferrite-ferrite grain boundaries were present.

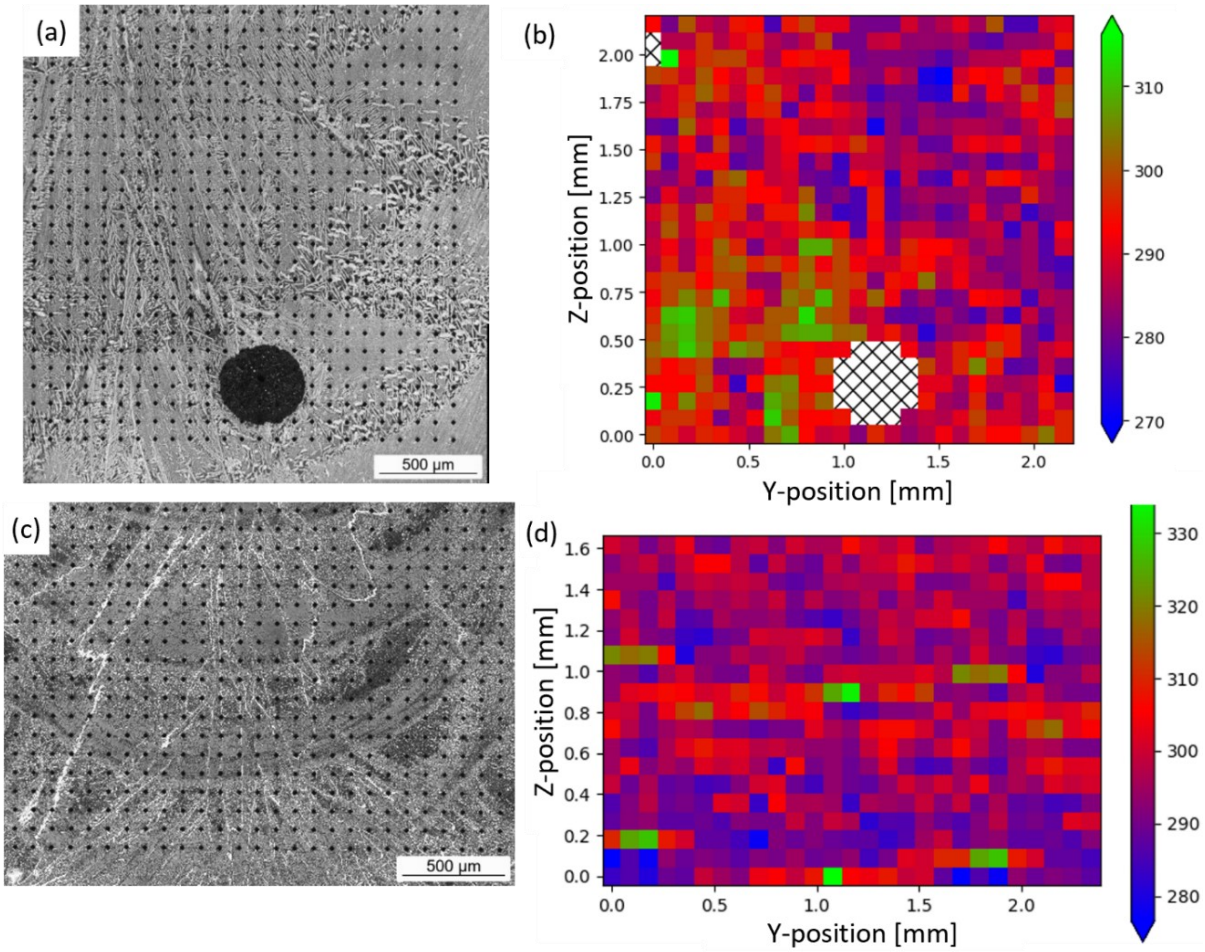

Figure 76: (a) RoI on the 680°C specimen (the black spot is an inclusion of oxide and slag, which is difficult to visualize using X-ray due to the low density difference to the material and thickness of the specimen) and (b) corresponding microhardness map. (c) RoI on the IPT100°C specimen and (d) corresponding microhardness map.

The results of the hardness maps contradict the explanation, that the origin of the difference in yield strength is the banded microstructure with reinforcement in the horizontal direction. To resolve this discrepancy, the relationship between local microstructure and mechanical properties was evaluated in depth by deriving the local yield strength, ultimate tensile strength and fracture strain from the hardness indents using the instrumented indentation method according to DIN SPEC 4864:2019-11.

Due to the high hardness the measurements had to be performed using a weight of 10 kg to generate measurable surface deformation, leading to much larger indents and spacing between the indents compared to the microhardness maps. To compensate, a grid of measurements was performed on both states. The spacing and angle was chosen so that, different positions with regard to the weld tracks were measured (Figure 77 (a)). After the hardness measurements the sample was polished again and color etched using Beraha II. Micrographs of the area surrounding each indent were taken (Figure 77 (b)). The ferrite/ austenite fraction of the surrounding microstructure as well as the total length of phase boundaries in the region of interest (RoI) (Figure 77 (c)) were quantified. The ferrite fraction was determined by the thresholding procedure and the total length of phase boundaries was calculated using the "measure" module of the scikit-image [175] python library and then divided by the area of the RoI to determine the phase boundary density. The phase boundary density was chosen as a parameter in order to estimate a Hall-Petch type parameter because it was not possible to determine a representative grain size from the images. The allotriomorphic austenitic prior ferrite/ferrite grain boundaries and the needles grown into the ferrite grain are essentially evaluated as one grain by all algorithms that were tested. The same applies to the areas with acicular secondary austenite. However, a dislocation passing through these regions has to pass through all the phase boundaries in between, which would not be accounted for. Therefore, the phase boundary density appears to be a better indicator in this case.

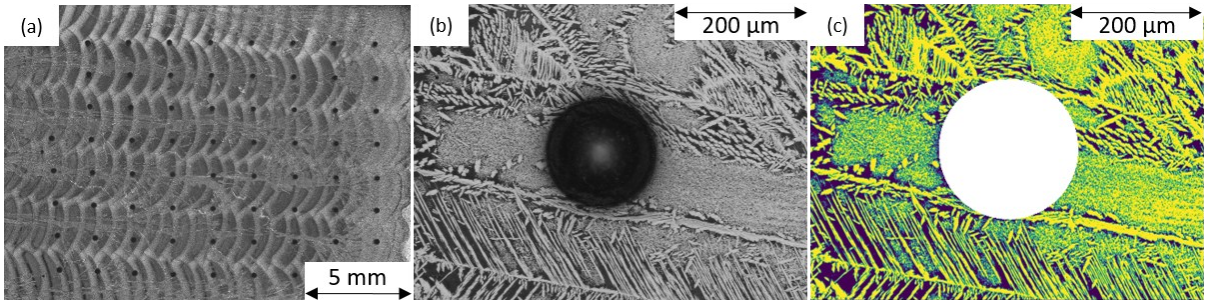

Figure 77: Mechanical properties derived from hardness measurements according to DIN SPEC 4864:2019-11 in dependence of phase composition and grain boundary density. (a) Overview of the measurement position, (b) magnification of a single indent and (c) thresholded image of computation of the phase fraction.

The correlation between the local mechanical properties as determined by the DIN SPEC 4864:2019-11 procedure and the local microstructure is shown in Figure 78. The graphs show a clear clustering of the data from both samples, a positive correlation between the ultimate tensile strength and yield strength with the ferrite fraction and a negative correlation of the fracture stain with the ferrite fraction. The relationship between phase boundary density and ferrite fraction is more complex. The grain boundary density goes to zero for high and low ferrite fractions and there appears to be a maximum at around 35% ferrite in the material.

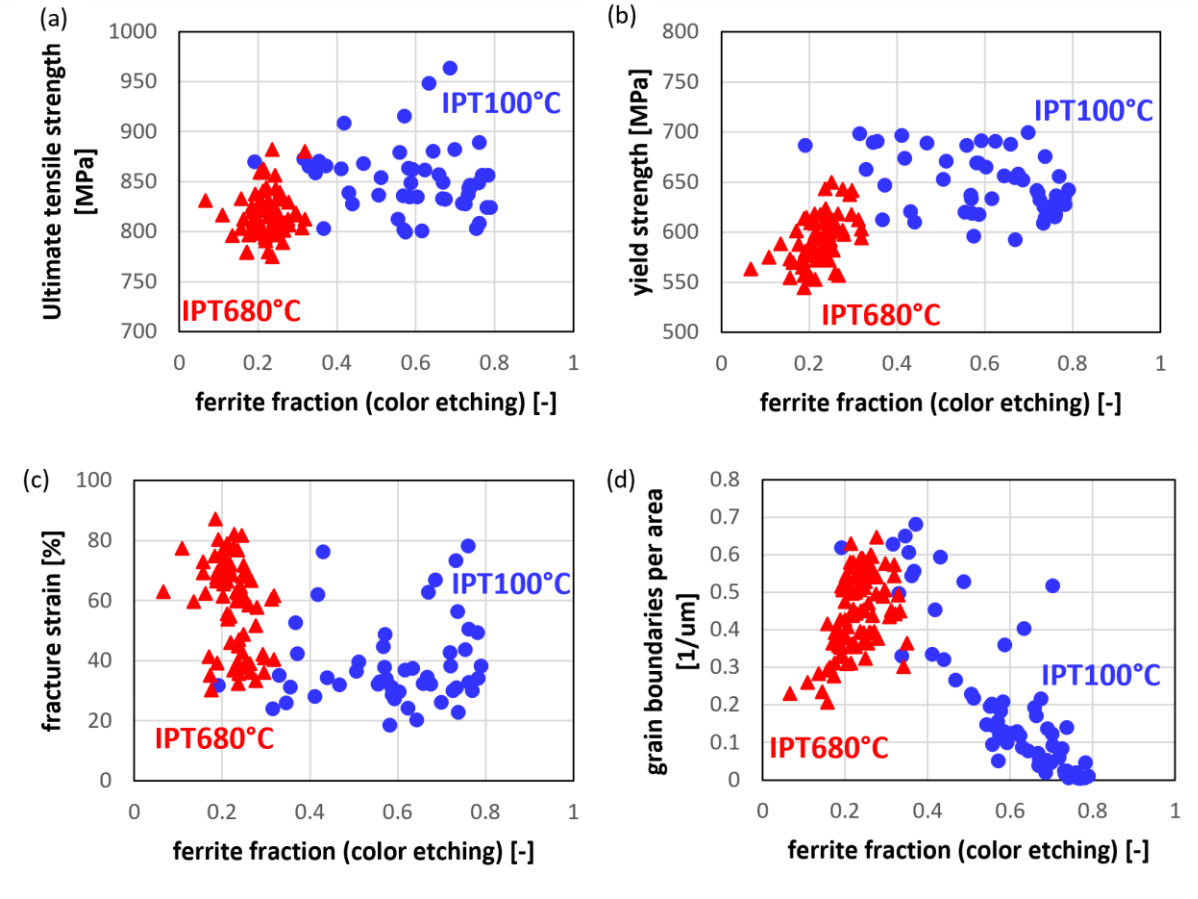

Figure 78: Correlation of mechanical properties and local microstructure. (a) ultimate tensile strength and ferrite fraction, (b) yield strength and ferrite fraction, (c) fracture strain and ferrite fraction and (d) grain boundary density and ferrite fraction

A linear model (Equation (18)) was fitted to the data for the ultimate tensile strength, yield strength and fracture strain using the least square method with ferrite fraction (f) and phase boundary density (p) as independent parameters.

$$k_f \times f + k_p \times p + k_0 = \sigma_{uts}, R_{p0.2}, \varepsilon_f \qquad (18)$$

The values for the fit parameters are shown in Table 18. The fit parameters show that the correlation between ferrite fraction and yield strength is higher than for ferrite fraction and ultimate tensile strength. The fracture strain appears to be negatively correlated with both the ferrite fraction as well as the grain boundary density.

Table 18: Values for fit parameters describing the correlation between mechanical properties and microstructural parameters.

Property	k_f	k_p	k_0
σ_{uts}	108.0 MPa	42 MPa µm	775.3 MPa
$R_{p0.2}$	171.5 MPa	49.3 MPa µm	532 MPa
ε_f	-58.0 %	-8.9 % µm	75.6 %

The dependency of the grain boundary density on the ferrite fraction can be explained analogous to a percolation problem. When there is only ferrite or only austenite, no phase boundaries exist. Therefore, the parameter has to be zero. With increasing fraction of ferrite, the number of phase boundaries increases until the austenite grains start to be connected to each other. At this point the phase boundary density decreases with increasing austenite fraction.

These two competing mechanisms explain the plateau of yield strength and ultimate tensile strength observed in Figure 78 (a) and (b) for increasing ferrite fractions. While the fraction of less deformable phase (ferrite) increases, the obstacles to dislocation movement (grain and phase boundaries) decrease in density preventing further strengthening of the microstructure.

The relationship for fracture strain is clearer. An increase in less deformable phase leads to a decrease in fracture strain. The determination of fracture strain by the indentation method must be regarded carefully, as actual fracture does not occur in the test. The estimated values are also much higher than those determined for additively manufactured material from tensile tests (Table 17).

The observed relationships are in accordance with the results of Kunz et al. [9] for laser powder bed fusion processed DSS 2205 and DSS 2507. Their fully ferritic material in the as-built condition exhibited a yield strength and fracture strain for standard DSS as well as super DSS of 773 MPa, 0.08 and 913 MPa, 0.14 respectively. Balancing the phase fraction by solution annealing led to a decrease in yield strength and increase in fracture strain to values of 558 MPa, 0.28 and 670 MPa, 0.35 respectively. Thereby, the formation of austenite in led to softer material with a higher ductility.

4.2.9 Fatigue Tests

For the application of the fracture mechanics concept, knowledge of the long crack threshold stress intensity factor range ($\Delta K_{th,LC}$) is of vital importance [23]. The results of the relevant fatigue crack propagation threshold tests are shown in Figure 79. One sample from parameter set IPT680°C was tested with constant force after the threshold determination was complete to validate the shape of the curve for increasing stress intensity factor range (ΔK).

The measured $\Delta K_{th,LC}$ is 3.55±0.15 MPa$\sqrt{\mathrm{m}}$, 4.2±0.1 MPa$\sqrt{\mathrm{m}}$ and 2.85 MPa$\sqrt{\mathrm{m}}$ for the material fabricated with IPT680°C, IPT100°C and the material from thin-walled specimens produced with open loop control respectively. The $\Delta K_{th,LC}$, determined for the IPT680°C material is 0.3 MPa$\sqrt{\mathrm{m}}$ or 1 MPa$\sqrt{\mathrm{m}}$ higher than the estimates calculated by Equations 13 and 14 respectively. For the IPT100°C material this difference is approx. 1 MPa$\sqrt{\mathrm{m}}$ or 1.7 1 MPa$\sqrt{\mathrm{m}}$. For the material from the thin walls the measured $\Delta K_{th,LC}$ is between the estimates produced by Equations 13 and 14. As a result, no significant buildup of the resistance against fatigue crack growth with increasing crack length is expected. This means that that cracks are unlikely to be arrested once they start growing from defects. Overall, the material from the thin-walled specimens also exhibits a significantly higher crack growth rate than the material from the

block-like specimens produced with IPT100°C and IPT680°C. It must be noted that the sample for the test on the thin-walled material had a thickness of 3 mm while the samples from the block-like material had a thickness of 10 mm. As a result, the former was subjected to plane stress loading conditions, while the latter experienced plane strain conditions. The size of the plastic zone as well as the stress intensity is increased for thinner specimens. Schijve [176] estimated that the effect of specimen thickness is small for steels. Some of the difference in the results can therefore be attributed to the loading conditions.

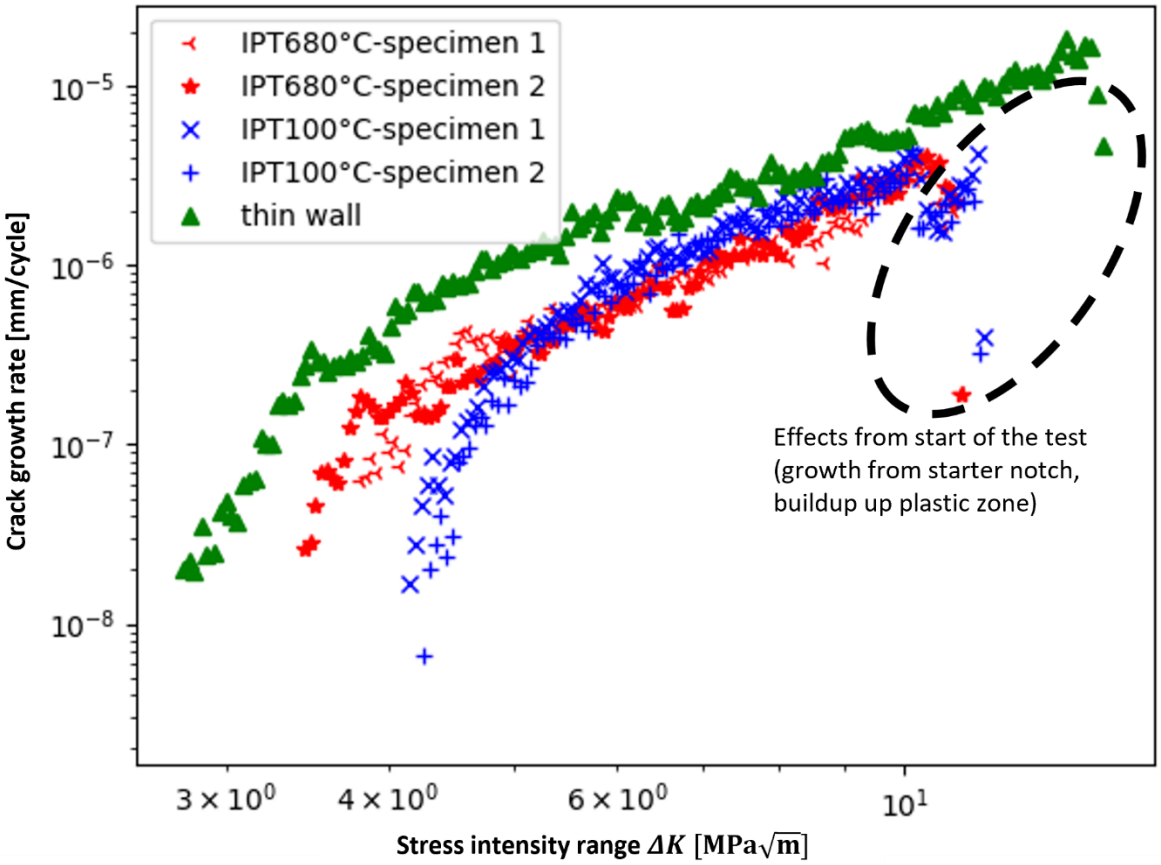

Figure 79: Results of the fatigue crack propagation threshold tests according to ASTM E466-07 for material from thin-walled, IPT100°C and IPT680°C specimens.

For the assessment of failure and residual lifetime of components $\Delta K_{th,LC}$ is a critical parameter. It's consideration in the analysis of a component with a crack (or potential crack assumed from the results of non-destructive testing) is of paramount importance [154]. For example, in welded Ti-6Al-4V a fatigue crack propagation threshold of 2.7 MPa$\sqrt{\mathrm{m}}$ was measured under environmental conditions. However, a calculation of the fatigue life yielded very conservative results, especially with regard to the very high cycle fatigue regime. When considering that, the fatigue crack growth from internal pores takes place in vacuum, where $\Delta K_{th,LC}$ is increased to approx. 6 MPa$\sqrt{\mathrm{m}}$ to 8 MPa$\sqrt{\mathrm{m}}$, an accurate prediction of the fatigue life was possible [158,177]. The same observation was made for wire arc additively manufactured Ti-6Al-4V [23,178]. Another example is the fatigue analysis of a railway axle [179]. Here, consideration of the intrinsic threshold for fatigue crack growth yielded an increase in the prediction of the remaining safe life of 18% or over 400% depending on

whether Equation 13 or 14 was used for the calculation of $\Delta K_{th,eff}$. [154] However, the application of $\Delta K_{th,LC}$ as an assessment criterion for failure from small process induced flaws in additively manufactured material is to be regarded critically because the behavior of small cracks is different to long cracks in some key aspects. A common tool for the assessment of the influence of crack size on the fatigue limit is the Kitagawa-Takahashi diagram [154,180].

Figure 80 shows the results of the fatigue limit tests on the additively manufactured material in the form of a Kitagawa-Takahashi diagram. The diagram shows a negative correlation between the fatigue limit and the defect size for the thin-walled material in the double logarithmic plot. The defect size was determined by measuring the area of the defects on the fracture surface according to the Murakami approach [151]. There is no discernible influence of the loading direction (horizontal (H) or vertical (V)) on the defect tolerance of the material from the thin-walled parts. The highest measured fatigue limit from the thin-walled parts were obtained in the horizontal direction. This correlates well to the results of the tensile tests, where the horizontal direction also exhibited higher strength. The plot does not indicate an upper limit for the fatigue limit for small defect sizes. The material produced with IPT680°C exhibits a fatigue limit at around 500 MPa. One outlier produced a fatigue limit of 590 MPa. The material produced with IPT100°C exhibits a higher defect tolerance compared to the material from the thin-walled structures. For a given defect size the failure stress is increased. Direct comparison of the material produced using IPT100°C and IPT680°C is not possible via the Kitagawa-Takahashi diagram because the defect size distributions for the two states do not overlap.

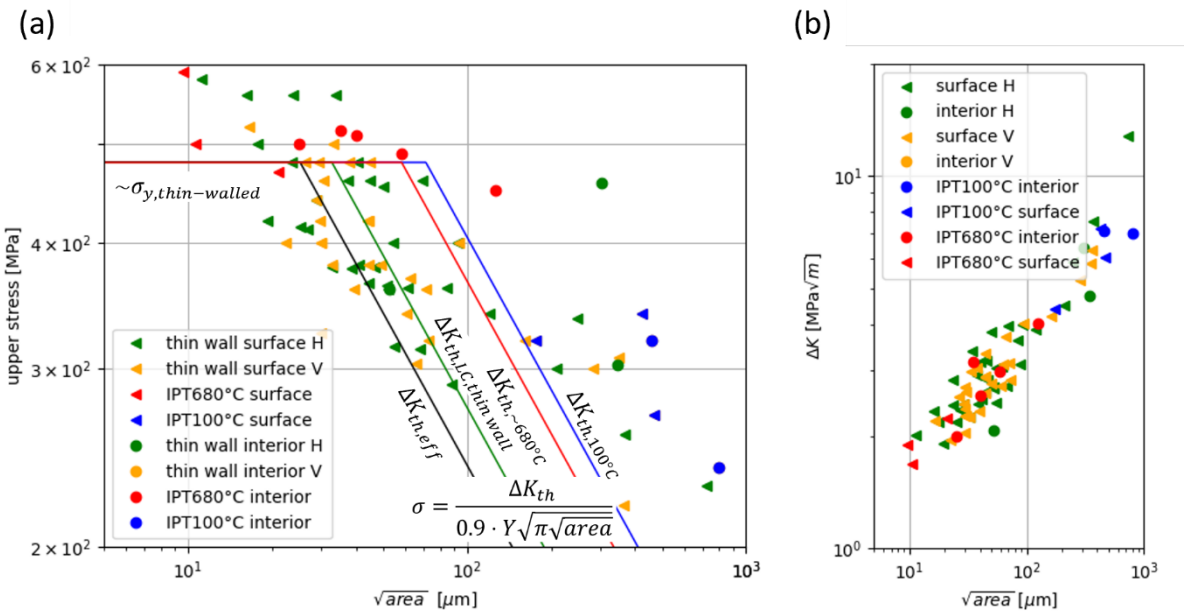

Figure 80: (a) Kitagawa-Takahashi plot from the results of the fatigue tests of the additively manufactured material. The plot includes the fatigue limit stress calculated from Murakami's [151] equation. (b) Defect size plotted against the calculated ΔK-value, that led to specimen failure.

For defects, where the $\sqrt{area}$-parameter is larger than approx. 200 µm and when the stress is below 300 MPa, $\Delta K_{th,LC}$ appears to produce a suitable conservative prediction, as to whether the defect will cause failure. For smaller defects and higher loads applying $\Delta K_{th,eff}$ produces a conservative prediction of the dependence of the fatigue limit on the defect size. The defect sizes that caused failure are homogeneously distributed around the predicted failure threshold in Figure 80 above 300 MPa for the thin-walled material. For the material produced with IPT100°C and IPT680°C, the measured $\Delta K_{th,LC}$ produce good estimates of the fatigue limit in combination with the yield strength of the material.

Figure 80 (b) shows, that the stress intensity factor range, that can be applied to a given defect, is dependent on the size of the defect. The ΔK, that is calculated for a given failure causing defect, increases with increasing size of the defect. This shows, why care must be taken when a uniform threshold stress intensity range is used as a criterion for the assessment of defects.

The short crack effect on the fatigue threshold has been discussed intensely [144–146,180,181]. A modified schematic of the Kitagawa-Takahashi diagram has been proposed by Miller (Figure 81 (a)) [181]. In this diagram a similar difference in behavior between long and short cracks is shown. This difference is attributed to size effects on the fatigue crack growth rate and fatigue crack propagation threshold (Figure 81 (b)). For small cracks the plastic zone ahead of the crack tip is of similar size to the crack, which invalidates the assumptions of linear elastic fracture mechanics and the ΔK-concept. Additionally crack closure effects from crack branching, roughness, oxide debris and local microstructural barriers have a much larger influence than for long cracks.

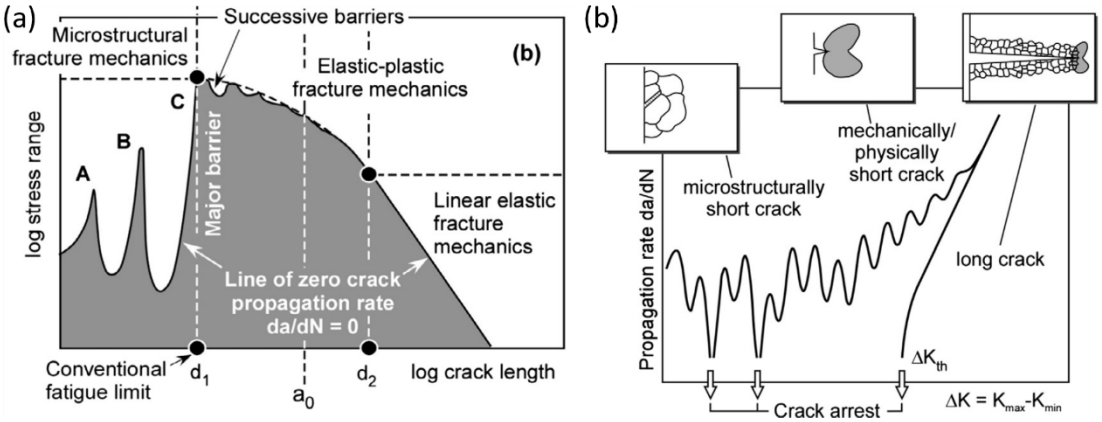

Figure 81: (a) Modified Kitagawa-Takahashi diagram [144] and (b) growths of short cracks [144] according to Miller [181].

Fatigue life tests were performed on the additively manufactured material produced with IPT100°C and IPT680°C0 (Figure 82). For the fatigue life tests, two load levels were chosen in accordance with DIN 50100 [182], so that one load level was above the yield strength and below the ultimate tensile strength of the additively manufactured material and the other load level was just above the 90% survival probability from the fatigue limit tests.

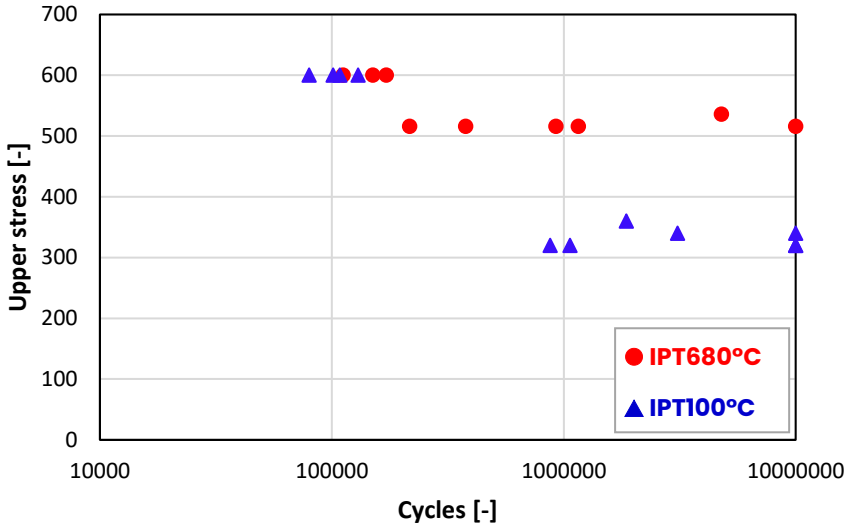

Figure 82: Fatigue life tests on material produced with IPT100°C and IPT680°C.

For the material produced with IPT100°C two specimens did not fracture at the designated stress. They were retested in intervals of 20 MPa until failure. For the material produced with IPT680°C this was the case for one specimen. These specimens have been included in the Kitagawa-Takahashi diagram (Figure 80 (a)).

Analysis of failure mode

Figure 83 shows a histogram of the defect size for the fatigue limit tests. Both orientations from the thin-walled material as well as the material produced with IPT680°C exhibit overlapping distributions of defect sizes. The material produced with IPT100°C contained larger defects. The defects were mainly lack of fusion defects situated in-between tracks of deposited material. One such defect is shown by the cross section through a secondary crack from a high load fatigue life test (Figure 84 (a)).

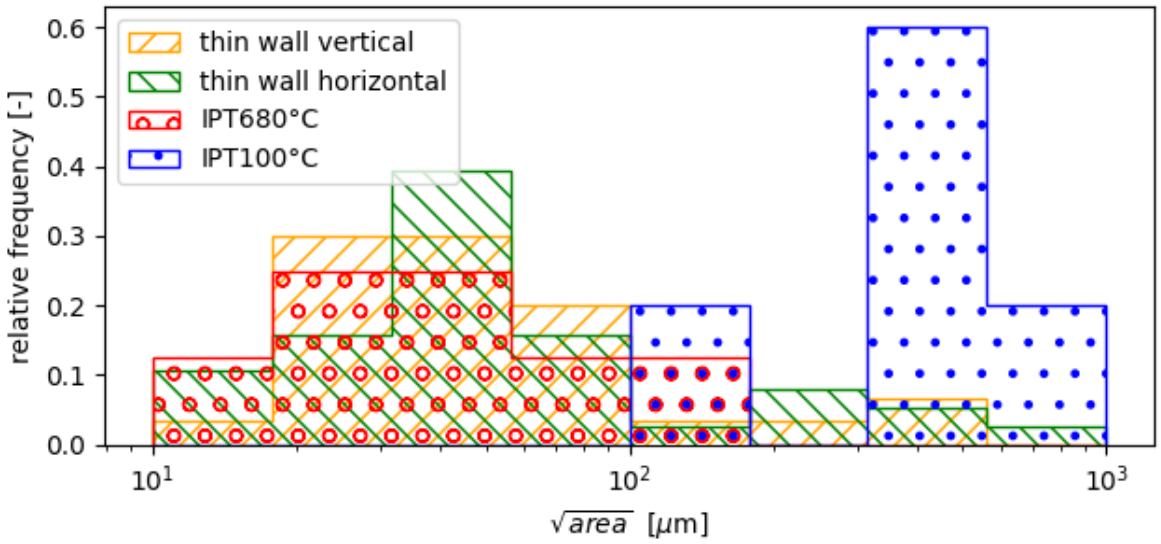

Figure 83: Histogram of the defect sizes. The defect size is given as the square root of the area on the fracture surface.

The specimens, which were tested just above the fatigue limit always exhibited a single origin of failure. The specimens tested above the yield strength of the material exhibited secondary cracks on the surface. A cross-section of such a crack is shown in Figure 84. The crack started at a LoF-defect and grew towards the surface. The direction of the crack follows the austenite rich region (Figure 84 (b)) just after initiation from the defect, preferring to grow in the softer material until crack growth is dominated by the loading direction. Crack growth then occurred perpendicular to the loading direction, where the stress intensity factor range is maximized. This explanation is supported by the $\Delta K_{th,LC}$ measurements presented in Figure 80. At low ΔK the austenite rich regions are less resistant to fatigue crack growths.

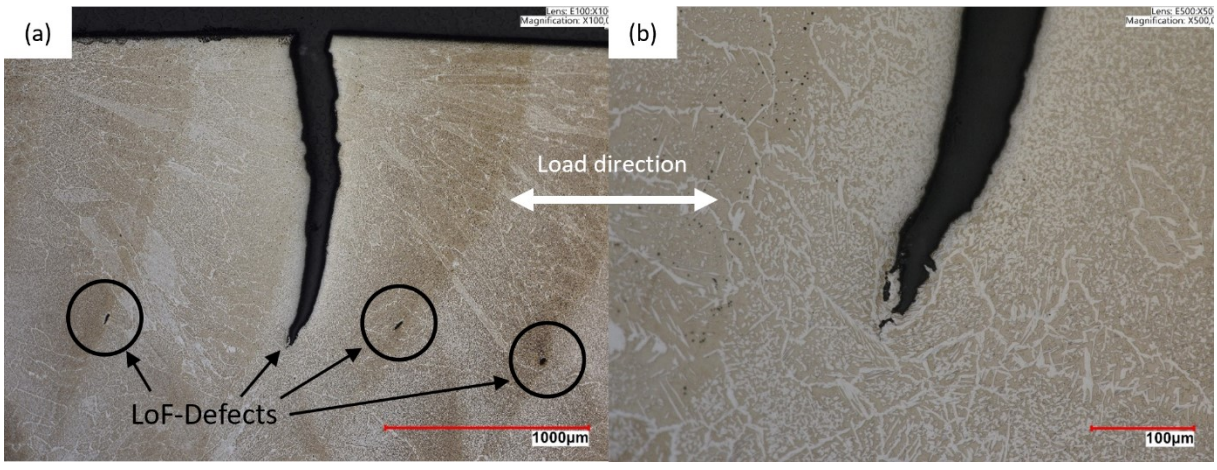

Figure 84: (a) Secondary crack in IPT100°C material growing from defect to the surface of the material and (b) enlarged view of the material in the vicinity of the crack origin.

The constitution of the internal defects was analyzed using optical and scanning electron microscopy. An exemplary defect for the thin-walled material is shown in Figure 85. These

defects, which result in the fatigue failure had an irregular shape with sharp edges. Therefore, the size of the defect only gives an estimate for the actual stress during fatigue loading. This explains the high scatter observed in the Kitagawa-Takahashi plot. Around the internal defect a smoother fatigue fracture surface can be seen, that barely reaches the specimen surface.

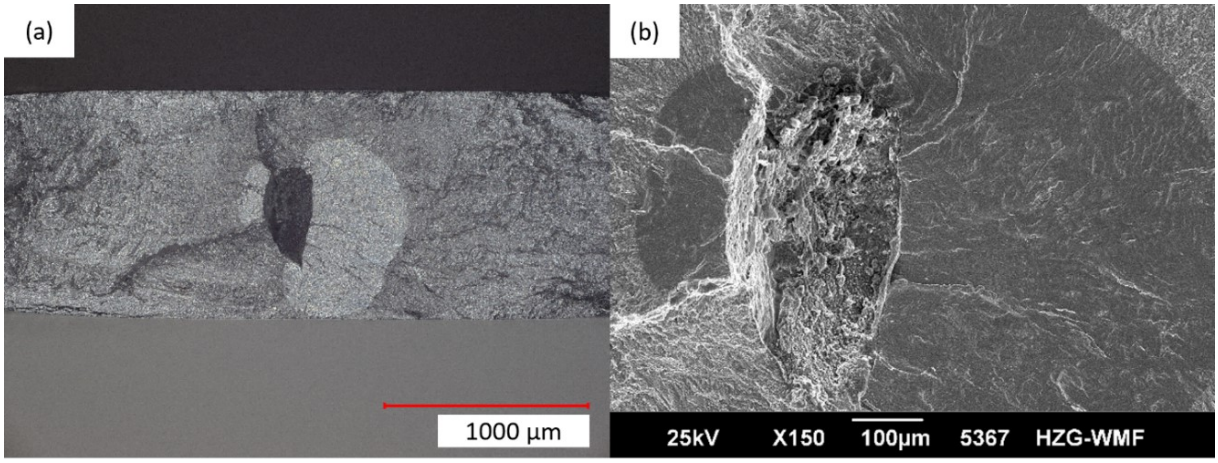

Figure 85: (a) Optical micrograph and (b) SEM image of a material defect leading to fatigue failure of the specimen.

The EDX signal from the area of the interior defects (Figure 86) indicates greatly increased levels of oxygen, chromium, manganese and silicon. The proportions of iron and nickel are reduced compared to the other areas of the fracture surface. The chemical composition of the defects suggests that the defect was part of an oxide and slag layer that was not remolten since it is of a similar chemical composition to the oxide layer investigated in section 4.2.4. In some cases surface defects had increased aluminum and oxygen levels, indicating that surface damage from the grinding procedure was the cause for fatigue failure.

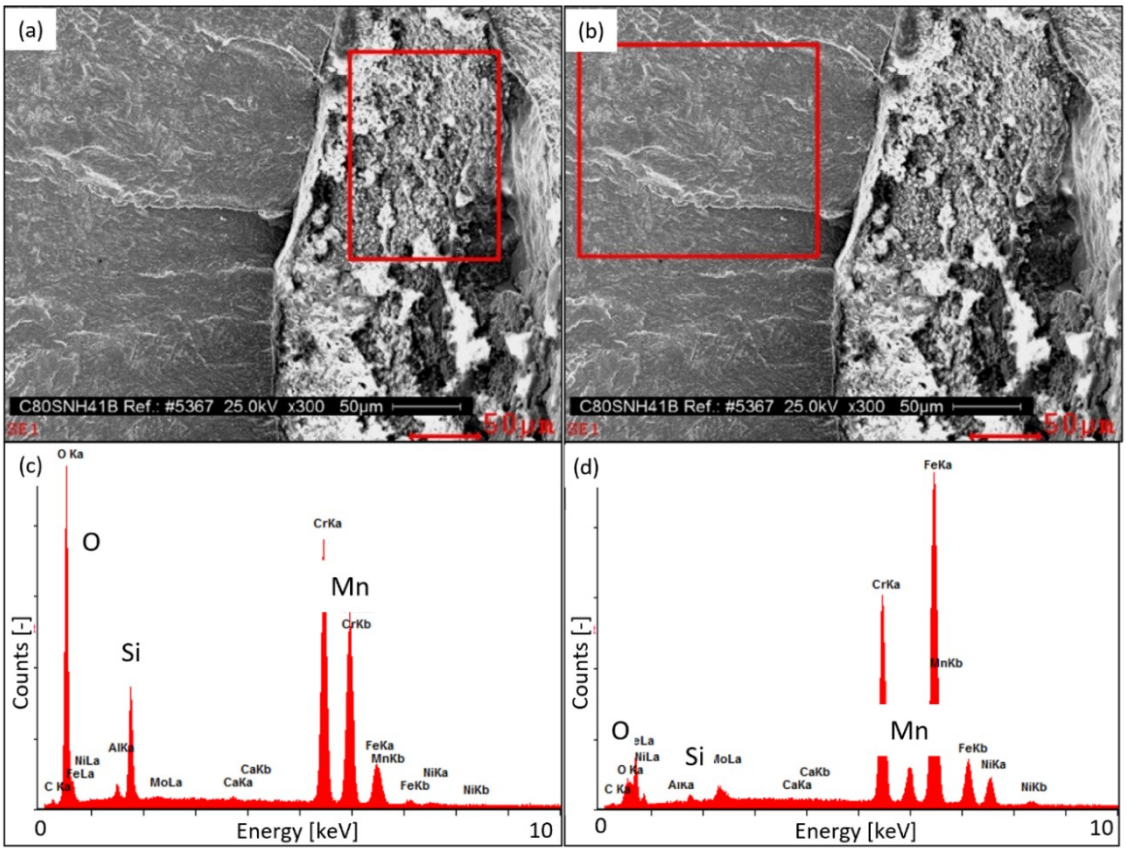

Figure 86: (a) Measurement location on the defect and (b) fracture surface with the corresponding EDX spectra ((c) and (d)) respectively.

Figure 87 shows a fracture surface from a specimen produced with IPT680°C, where the crack started from a pore or circular inclusion. There exist 4 distinctly different areas on the fatigue fracture surface. Figure 87 (a) shows an overview of the residual fracture surface and the fatigue fracture surface, where the crack grew as a surface crack. Figure 87 (b) and (d) show the region, where the crack grew as a subsurface crack. It is clear, that the transition occurred rapidly, when the subsurface crack encountered the surface for the first time. In Figure 87 (c) and (e) the defect at the crack-origin is shown. In the vicinity around the defect there exists another boundary between two areas with different roughness. These areas might be created during subsequent load steps in the fatigue limit test. At load level 1, the crack grew from the defect until it was stopped by the rising resistance from plastic deformation and local microstructure and then grew again, reaching the surface and transforming to a surface crack once the load was increased.

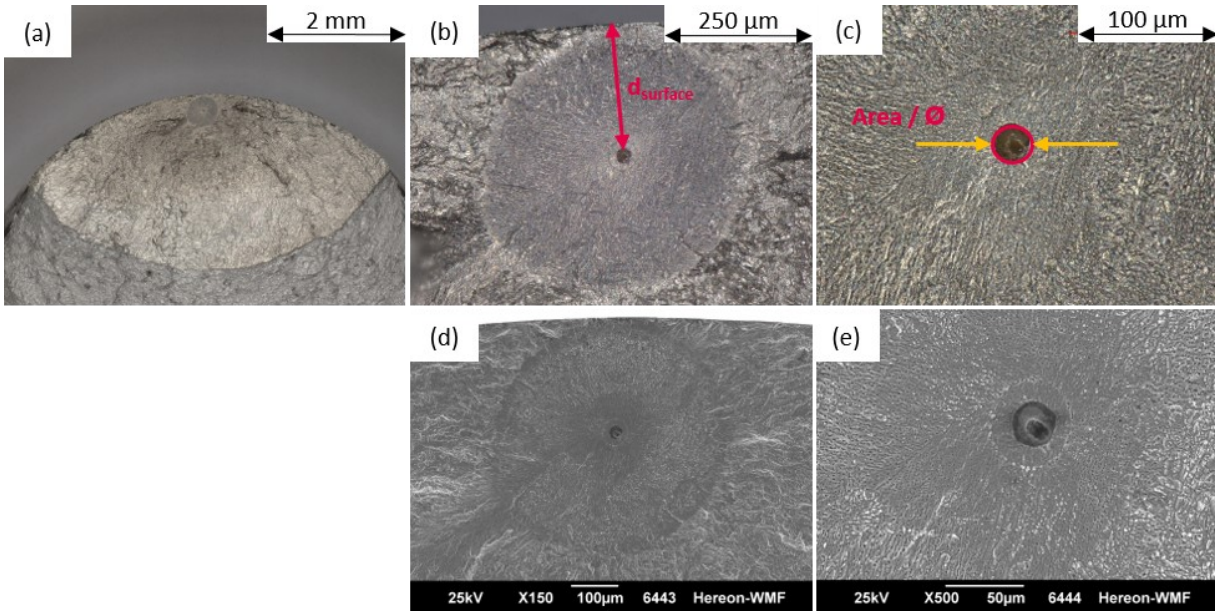

Figure 87: Typical fracture surface of a specimen with an internal defect from a block-like structure manufactured with IPT680°C after fatigue threshold testing showing (a) an overview of the fatigue fracture surface, (b) the region of internal fatigue crack growth and (c) the origin of the fatigue crack. (d) and (e) are SEM-images of the same regions as (b) and (c) respectively. The morphology of the fatigue fracture surface can be discerned more clearly.

Sales et al. [7] and Sales et al. [6] reported significant anisotropy in the fatigue limit of wire arc additively manufactured super duplex stainless steel ER2594. Their material did not exhibit significant anisotropy in tensile properties. Unfortunately, they did not report whether there was an influence of loading direction on defect size. Therefore, no conclusion can be drawn as to whether the observed effect can be attributed to the orientation of defects or an anisotropy in damage tolerance. Measurements of the fatigue crack growth rate and its dependence on the orientation with regard for the welded tracks [97] indicates anisotropy of the crack closure for small cracks. The results presented in this thesis do not show an anisotropy of the fatigue properties with regard to the loading direction. This is because the defect size distribution is similar for the build and weld track directions. The anisotropy of ductility observed in tensile tests does not appear to transfer to an anisotropy in damage tolerance under fatigue loading conditions.

Kunz et al. [9] reported an increase in damage tolerance for increasing austenite fraction in duplex stainless steel material made via laser powder bed fusion. They attribute the increased damage tolerance to the enhanced ductility of the material. This contradicts the findings from measurements of the long crack threshold stress intensity factor range in this thesis. Here, a higher resistance against crack growth at low stress intensity factor values for higher ferrite contents was measured. However, the results of fatigue limit tests also showed a strong dependence of the damage tolerance on the defect size in terms of the stress intensity factor range. For smaller defects the plastic zone ahead of the crack tip is much larger relative to the defect size. Such an effect of small cracks is not captured by the testing scheme employed in this work.

In summary, the results presented in this section qualify the assessment of additively manufactured DSS components containing defects under fatigue loading conditions. The Kitagawa-Takahashi diagram shows a safe life regime for a wide range of defect sizes and loads. The results also show the limitations of using a uniform threshold stress intensity factor range for the assessment of small defects.

4.2.10 Residual Stress Design in Additively Manufactured Parts

In this chapter, the results of process design on the residual stress distribution in additively manufactured DSS pressure vessel structures are presented. The process design was chosen, so that the austenite content is maximized on the inside of the wall to increase the corrosion resistance and the ferrite content on the outer tracks is increased to achieve increased strength while still conforming to the requirements placed on wrought material and weld metal regarding the ferrite content [136,183].

Microstructural Characterization

The tank sample was free of LoF-defects. Optical microscopy measurements of the ferrite content yielded the ferrite fraction presented in Figure 88 (a). Because the interlayer waiting time was omitted for the deposition of the inside track, the highest amounts of austenite were measured at this location. The bottom of the sample exhibited higher amounts of austenite. In this region, the epitaxial ferrite grain growth has not eliminated the grains which were not oriented in the fastest growth direction. Therefore, there is an increased number of ferrite-ferrite grain boundaries, from which austenite precipitated. At the very top, increased amounts of ferrite were measured. This is because this region did not experience repeated reheating cycles.

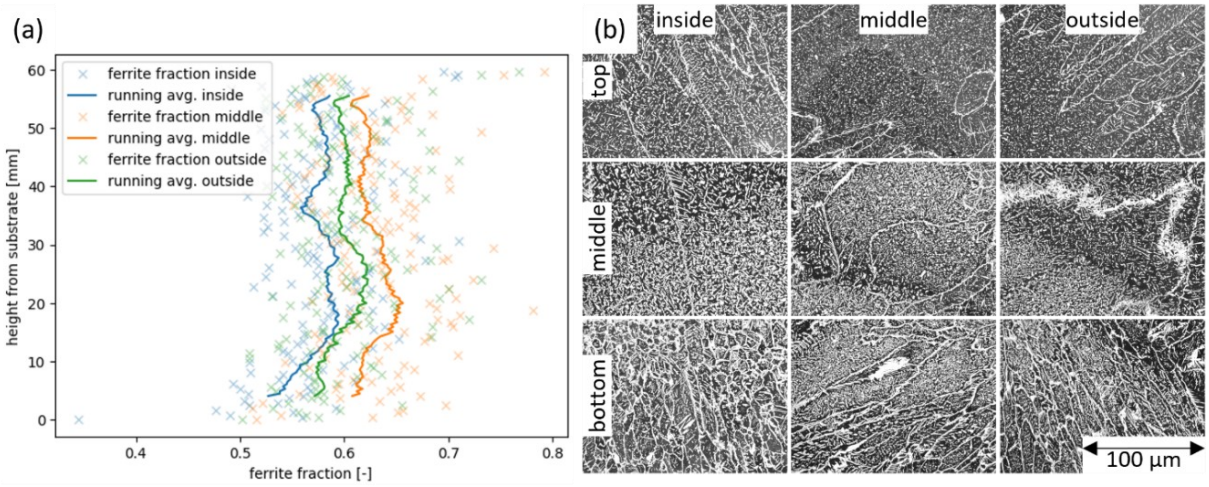

Figure 88: (a) Austenite-ferrite ratio in dependence of the weld track location and height of the sample and (b) etched micrographs corresponding to the location (from left to right: top, middle, bottom) and height of the sample (from top to bottom: approx. 60 mm, 30 mm, 1 mm).

Residual Stress

The results of the residual stress determined from the synchrotron measurements are shown in Figure 89. Due to the missing ϕ-angle for C2 the shear stresses could not be calculated. The results show that there were significant tensile stresses at the top of the sample in the weld track direction (X-axis). The stresses in the track direction became more

compressive towards the bottom of the sample. At the corner of the sample the stresses in the track direction were more tensile. For the build direction (Z-axis), the stresses are more compressive in the center of the part (C1 to C3) of the sample than on the corners (R1 to R3). For the position C1 and R1 at the top of the sample, the stresses are nearly constant along the thickness of the wall. For C2, C3 and R3 the stresses are slightly more tensile towards the outside of the wall along the thickness direction. For R2 the increase in stress is highest. The calculation of the residual stresses yielded results higher than the yield strength of the material. This is likely a result from not using appropriate X-ray elastic constants. However, the results show some interesting trends qualitatively.

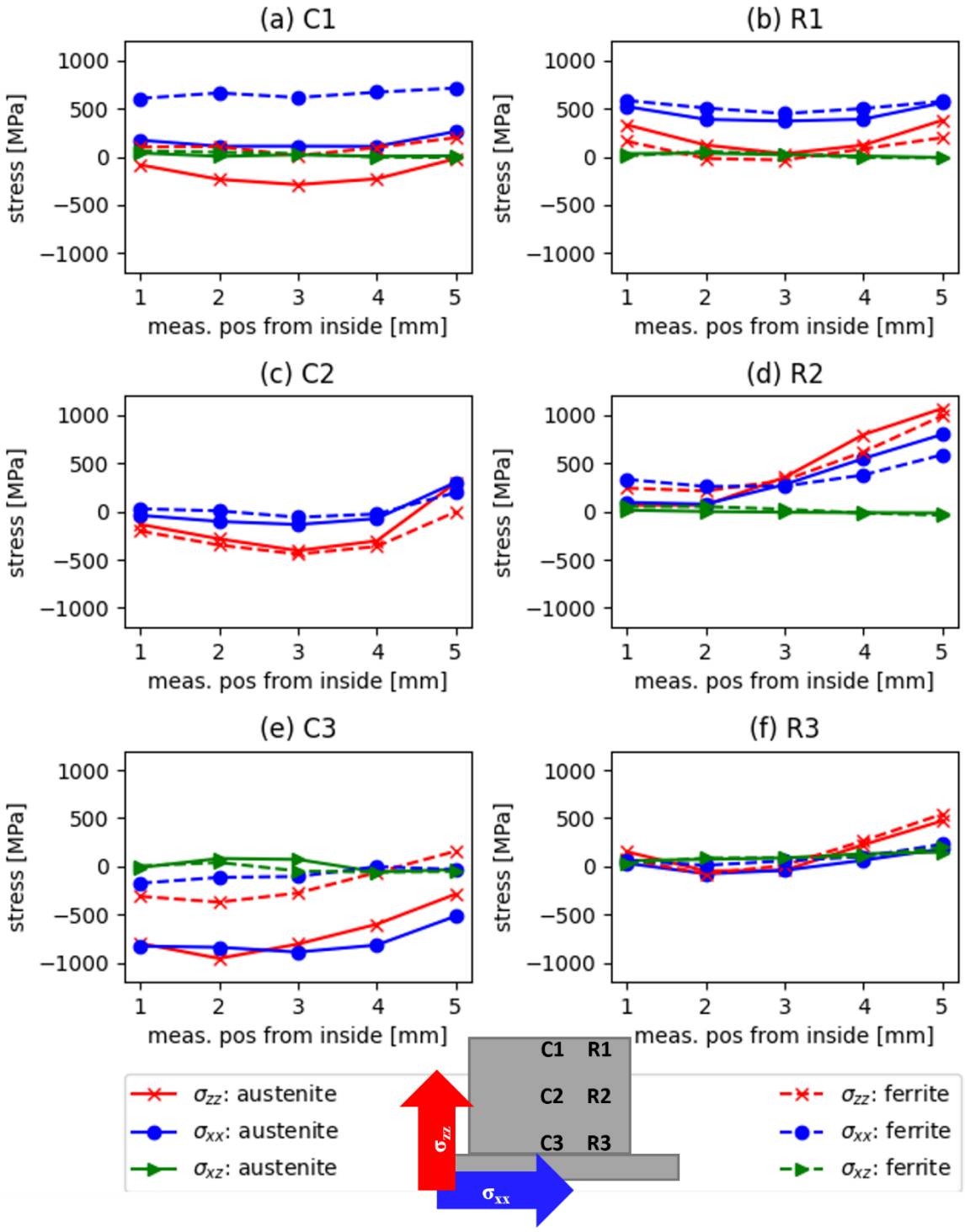

Figure 89: Residual stresses measured on the six positions of the additively manufactured sample.

The overall prediction of the residual stress distribution from the process design was confirmed by the synchrotron results with the calculated stresses qualitatively following the expected trends. However significant residual tensile stresses that exceeded the yield strength measured for the additively manufactured material are still present on the inside of some sections of the sample. The effect of the order of weld tracks had a lower influence on residual stress than the order of layers. The effect for track order from inside to outside is reduced for increasing deposit height. At the C1 and R1 position the residual stresses are

constant across the thickness of the walls of the samples whereas they turn more tensile towards the outside at the remaining measurement positions. The reason might be that succeeding layers also influence on the stress distribution of preceding layers. Newly deposited material places all adjacent material, including the neighboring layer and the layers below, under compressive stresses while being placed under tensile stresses itself.

Lu et al. [132] modelled the residual stress in additively manufactured rectangular hollow parts made from Ti-6Al-4V using the finite element method. They found the highest stresses in the transition area from substrate to additively manufactured parts. This is supported by the results of Ahmad et al. [184] who determined, that the highest residual tensile stresses are formed at the base of thin walled samples made via electron beam additive manufacturing. This is not supported by the results of the current investigation, as compressive residual stresses were found in the corresponding (C3) location. Wu et al. [185] investigated the influence of the deposition pattern on the residual stress distribution in block-like wire arc additive manufactured Ti-6Al-4V and Inconel 718 using the finite element method. One of the deposition patterns investigated was a spiral pattern where the material was deposited from outside to inside. They found high tensile stresses in the center of the component, where the deposition sequences ended and more compressive stresses on the outside. This follows the measured trends observed in this work regarding the deposition sequence. Lee et al. [171] investigated the effect of the tool path strategy on thin Ti-6Al-4V walls made using laser directed energy deposition with wire. They found a concentration of tensile residual stresses in the build direction at the transition from the base plate to the deposited structure. The closest corresponding location in this work are the R3 and R2 positions, where tensile stresses can also be observed.

In summary, the objective of only achieving compressive residual stresses on the inside of the pressure vessel geometry could not be achieved. The severity of the tensile residual stresses could be alleviated by choosing an appropriate process design. The reason for this is, that bending deformation from many successive layers in the build direction dominate the contraction from the track order. Reversing the order of fabrication would have an adverse effect on the load bearing capacity of the pressure vessel.

5 Summary and Outlook

5.1 Summary

The present thesis addresses laser processing of duplex stainless steels focusing on the development of suitable process control methods, processed microstructure, surface state, internal defects, residual stress and their interaction with the mechanical properties. An extensive experimental research program has been carried out to quantify the effect of the laser processes on the properties. The experimental results provide a basis for a deeper understanding between process design decisions, process parameters and the resultant properties. Fundamental material specific properties have been determined and compared across parameters and processes.

As described in the introduction, several global research objectives have been pursued throughout this work. The relationship between the microstructure of the material, the process and the process parameters has been studied. Then the link between microstructure, defects and mechanical properties has been analyzed. Additionally, the influence of processing discontinuities on the mechanical properties was investigated. The influence of process design on the microstructure and residual stress was established. Finally, a process control method for the additive manufacturing with laser and wire has been developed.

1. Weld metal characterization: Laser beam welding and L-DED-wire deposition parameters have been varied to obtain a wide variety of material states. The material states were characterized extensively using optical and scanning electron microscopy as well as high energy X-ray diffraction. In laser beam welding the heat conduction conditions together with the low linear heat inputs lead to high cooling rates, which result in nearly entirely ferritic material. Even when laser surface remelting is performed the ferrite fraction in the material remains high. In additive manufacturing, such high cooling rates cannot be achieved due to the changed thermal boundary conditions. Here, local ferrite contents could be varied between 0.7% and 0.07%. The austenite is formed in two stages. The first fraction forms during cooling of the material after the solidification of the weld track. The remainder is formed by reheating of the material during subsequent deposition sequences. The type of austenite precipitation depends on the welding parameters. At moderate welding speeds, Widmanstädten-like austenite and allotriomorphic grain boundary austenite form. At higher welding speed and lower linear heat inputs increased γ^2–precipitation takes place.

2. Quasi static mechanical properties: Influence of the phase fraction has been studied extensively. Nearly entirely ferritic material exhibits the highest hardness. During tensile tests, these micro-areas deform less. For welded joints, this results in a protection of the joint area from deformation. In additively manufactured material the ferrite rich banded layers act as fibrous reinforcement. This is amplified by the strong solidification texture leading to high Taylor factors and therefore resistance against deformation in the 45° and 0° orientations with regard to the build direction. The microstructural anisotropy in combination with the

texture leads to differences of up to 100 MPa in yield strength and 0.29 in fracture strain. Thereby one direction exhibits nearly three times the ductility of the other.

3. Fatigue properties: In contrast to the quasi-static material properties, the fatigue properties are much more sensitive to defects and geometrical notches. Using laser beam welding, porosity free welds could be produced. In the as-welded state, the joints exhibited worse fatigue properties compared to the base material with increased scatter. Laser surface remelting reduced the scatter and elevated the fatigue properties to the level of the base material by alleviating the notches at the weld root. In additively manufactured material inclusions from the oxide layer and lack of fusion defects are most detrimental to the fatigue properties. The material possesses long crack threshold stress intensity range factors close to the intrinsic threshold stress intensity range factor. Due to the low defect tolerance, even small defects reduce the fatigue limit considerably. The long crack threshold stress intensity factor range depends on the austenite fraction of the material. The evaluation of stress intensity factor range and defects sizes showed that a uniform value is not a viable criterion to assess fatigue failure from small defects.

4. Residual stress: The residual stress distribution qualitatively follows the expected trends with the lower part of deposited structure being placed under compressive stresses by the subsequently deposited material in track direction. This results in more tensile residual stresses in the build direction at the edges of parts and more compressive stresses on the inside. The order of layers has a larger influence on the residual stresses than the order of tracks.

5. Process control: A process control method for the laser and wire additive manufacturing process based on the interaction force between the wire and substrate has been developed. The ability of the method to account for the heat accumulation and changing boundary conditions of the additive manufacturing process to produce complex parts has been demonstrated. The benefit of interpass temperature monitoring to control the microstructure of duplex stainless steels has also been demonstrated.

5.2 Outlook

The present work has given a first understanding between laser fusion processing, the microstructure and the mechanical properties of duplex stainless steels. To enhance that understanding, the phase formation during additive manufacturing should be investigated in more detail, *in-situ,* using high energy X-ray radiation. This way the exact temperature ranges for the formation of different microstructural features in the case of laser welding and additive manufacturing can be identified. This knowledge can serve as a good basis for modeling of the material behavior during the additive manufacturing process, thereby reducing the need for experiments.

The fatigue properties have been assessed using a linear elastic fracture mechanics concept. The shortfalls of this concept for the application to small defects introduced by the additive manufacturing process have been shown. As an extension of this work an elastic-plastic fracture mechanics concept should be developed to account for the short crack effect under fatigue loading. This work has focused on the microstructure and mechanical properties. The corrosion resistance has only been mentioned in the introduction and with regard to the influence of phase fraction and intermetallic phases. In a much broader scope, the influence of the spatial distribution of austenite and ferrite, morphology of the austenitic phase, texture, defects in the material, presence of chromium nitrides, intermetallic phases and lastly residual stresses on the corrosion resistance need to be investigated.

The advantages of the process control method have been demonstrated. However, improvement on the technical side can still be made. At the current stage, the laser spot size can only be varied together with the focal position. If that constraint is lifted by for example the utilization of variable collimation for the laser beam, the irradiated length of wire could be varied independently of the area irradiated by the laser. Another intriguing approach is the combination with an adjustable beam mode laser. This would enable control of energy input into the feedstock material or substrate. Thereby, the formation of defects as well as remelting of the oxide layer could be controlled more precisely leading to a more robust process and additively manufactured parts with improved fatigue properties. Lastly, multiple-wire processes are promising candidates for *in-situ* alloying of the material to achieve the desired properties. This way the alloy composition could be tailored to the specifics of the manufacturing process.

6 References

[1] Günter Schmitt, Michael Schütze, G. F. Hays, Wayne Burns, En-hou. Han, Antoine Pourbaix, Gretchen Jacobson, Global Needs for Knowledge Dissemination, Research, and Development in Materials Deterioration and Corrosion Control, Materials Science, 2009.

[2] TMR Stainless, Practical Guidelines for the Fabrication of Duplex Stainless Steels, London, UK, 2014.

[3] A.H.I. Mourad, A. Khourshid, T. Sharef, Gas tungsten arc and laser beam welding processes effects on duplex stainless steel 2205 properties, Mat Sci Eng a-Struct 549, 2012, 105–113.

[4] J. Chater, The European market for duplex stainless steels: rapid growth expected, 2010, https://www.stainless-steel-world.net/pdf/sswsup1005_duplex_chater.pdf, accessed 26 October 2021.

[5] ThyssenKrupp IndustrialSolutions AG, Air Liquide Global Engineering & Construction Solutions Germany GmbH, Preparation of the iGF-Proposal (BMWK) 1.3828 Aufklärung der Prozess-Eigenschafts-Beziehungen bei der Fertigung von Bauteilen aus korrosionsbeständigen superaustenitischen und Duplexstählen durch drahtbasiertes Laser Directed Energy Deposition. oral, online, 2022.

[6] A. Sales, A. Kotousov, E. Perilli, L. Yin, Improvement of the Fatigue Resistance of Super Duplex Stainless-Steel (SDSS) Components Fabricated by Wire Arc Additive Manufacturing (WAAM), Metals 12, 2022, 1548.

[7] A. Sales, A. Kotousov, L. Yin, Design against Fatigue of Super Duplex Stainless Steel Structures Fabricated by Wire Arc Additive Manufacturing Process, Metals 11, 2021, 1965.

[8] M.L. Köhler, J. Kunz, S. Herzog, A. Kaletsch, C. Broeckmann, Microstructure analysis of novel LPBF-processed duplex stainless steels correlated to their mechanical and corrosion properties, Mat Sci Eng a-Struct 801, 2021, 140432.

[9] J. Kunz, A. Boontanom, S. Herzog, P. Suwanpinij, A. Kaletsch, C. Broeckmann, Influence of hot isostatic pressing post-treatment on the microstructure and mechanical behavior of standard and super duplex stainless steel produced by laser powder bed fusion, Materials Science and Engineering: A 794, 2020, 139806.

[10] Di Zhang, A. Liu, B. Yin, P. Wen, Additive manufacturing of duplex stainless steels - A critical review, Journal of Manufacturing Processes 73, 2022, 496–517.

[11] J.T. Pacheco, A.S.C.M. de Oliveira, Additive manufacturing of duplex stainless steels: assessment of deposition processes, microstructure, and properties, Int J Adv Manuf Technol 127, 2023, 5013–5030.

[12] R. Badji, B. Bacroix, M. Bouabdallah, Texture, microstructure and anisotropic properties in annealed 2205 duplex stainless steel welds, Mater. Charact. 62, 2011, 833–843.

[13] I. Alvarez-Armas, S. Degallaix-Moreuil, Duplex Stainless Steels, John Wiley & Sons, Inc, Hoboken, NJ, USA, 2013.

[14] A. Mateo, F. Heredero, G. Fargas, Failure investigation of a centrifuge duplex stainless steel basket, Eng. Fail. Anal. 18, 2011, 2165–2178.

[15] Lenntech, CPT ANSI Process Pumps, https://www.lenntech.com/Data-sheets/Sulzer-brochure-CPT-en-L.pdf, accessed 10 January 2023.
[16] Manuela Zinke, Erzielung werkstoffspezifischer Eigenschaften beim generativen Schutzgasschweißen fertigkonturnaher Strukturen aus Duplexstahl: zu iGF-Vorhaben Nr. 20.361 BR. Schlussbericht vom 22.11.2021, Magdeburg, 2021.
[17] DIRECTED METAL 3D SL, Metal 3D Printing Applications, https://meltio3d.com/applications/, accessed 25 March 2024.
[18] A. E. Odermatt, L. Pan, V. Ventzke, N. Kashaev, Influence of laser welding defects on the high cycle fatigue behavior of stainless duplex steel 1.4462, Potsdam (Germany), 2020.
[19] A.E. Odermatt, V. Ventzke, F. Dorn, R. Dinsé, P. Merhof, N. Kashaev, Effect of laser beam welding on microstructure, tensile strength and fatigue behaviour of duplex stainless steel 2205, Journal of Manufacturing Processes 72, 2021, 148–158.
[20] A.E. Odermatt, N. Kashaev, Evaluation of steady state via thermography during laser and wire based directed energy deposition, in: Lasers in Manufacturing Conference Proceedings 2021, 2021.
[21] A.E. Odermatt, F. Dorn, V. Ventzke, N. Kashaev, Coaxial laser directed energy deposition with wire of thin-walled duplex stainless steel parts: Process discontinuities and their impact on the mechanical properties, CIRP J. Manuf. Sci. Technol. 37, 2022, 443–453.
[22] A.E. Odermatt, Verfahren zum Betreiben einer drahtbasierten Materialauftragungsvorrichtung und drahtbasierte Materialauftragungsvorrichtung, EP 4 349 600 A1, 2022, Helmholtz-Zentrum Hereon GmbH.
[23] A.E. Odermatt, L. Vázquez, P. Álvarez, N. Kashaev, On the prediction of fatigue life of WAAM-processed Ti-6Al-4V under consideration of manufacturing defects, International Journal of Structural Integrity 2024, under review.
[24] Sebastian Frederik Roth, Thermomechanische FEM-Simulation des laseradditiven Fertigungsprozesses mit Duplexstahldraht. Masterarbeit, Hamburg University of Technology, 2021.
[25] Yasin Balur, Mikrostrukturelle Charakterisierung von additiv gefertigten Duplexstahl-Strukturen. Master Thesis, Leuphana Universität Lüneburg, 2021.
[26] Aljoscha Repczuk, Entwicklung und Validierung zweier Fertigungsstrategien zum drahtbasierten Laserauftragsschweißen eines Wasserstoffdrucktanks aus einem Cr-Ni-Duplexstahl. Masterarbeit, Technische Universität Hamburg harburg, 2022.
[27] R. Esterl, M. Sonnleitner, M. Stadler, G. Wölger, R. Schnitzer, Microstructural Characterization of Ultra-High Strength Martensitic Steels, Practical Metallography 55, 2018, 203–222.
[28] G. Schulze, Die Metallurgie des Schweißens: Eisenwerkstoffe, Nichteisenmetallische Werkstoffe, 4th ed., Springer-Verlag, s.l., 2009.
[29] C.-C. Hsieh, W. Wu, Precipitation of Phase Using General Diffusion Equation with Comparison to Vitek Diffusion Model in Dissimilar Stainless Steels, Journal of Metallurgy 2012, 2012, 1–7.

[30] C.W. Wegst, M. Wegst, Stahlschlüssel: Key to steel = La clé des aciers, 21st ed., Verl. Stahlschlüssel Wegst, Marbach, 2007.
[31] Pierre-Jean Cunat, Alloying elements in stainless steel and other chromium-containing alloys, Euro Inox, Paris, 2004.
[32] A.D. Iams, J.S. Keist, L.A. Giannuzzi, T.A. Palmer, The Evolution of Oxygen-Based Inclusions in an Additively Manufactured Super-Duplex Stainless Steel, Metallurgical and Materials Transactions A 52, 2021, 3401–3412.
[33] Informationsstelle Edelstahl Rostfrei, Nichtrostende Duplex-Stähle, 2021, https://www.edelstahl-rostfrei.de/fileadmin/user_upload/ISER/images/publikationen/ISSF_Duplex-Staehle_final_01.pdf, accessed 8 March 2024.
[34] A. Mateo, L. Llanes, N. Akdut, M. Anglada, High cycle fatigue behaviour of a standard duplex stainless steel plate and bar, Mat Sci Eng a-Struct 319-321, 2001, 516–520.
[35] J.C. de Lacerda, L.C. Cândido, L.B. Godefroid, Effect of volume fraction of phases and precipitates on the mechanical behavior of UNS S31803 duplex stainless steel, Int. J. Fatigue 74, 2015, 81–87.
[36] S. Floreen, H.W. Hayden, The influence of austenite and ferrite on the mechanical properties of two-phase stainless steels having microduplex structures, Asm. Trans. Q. 61, 1968, 489–499.
[37] A.P. Miodownik, N. Saunders, Modelling of materials properties in duplex stainless steels, Mater. Sci. Technol. 18, 2013, 861–868.
[38] I. Calliari, M. Pellizzari, M. Zanellato, E. Ramous, The phase stability in Cr–Ni and Cr–Mn duplex stainless steels, J. Mater. Sci. 46, 2011, 6916–6924.
[39] J.K. Sahu, Effect of 475°C Embrittlement on the Fatigue Behaviour of a Duplex Stainless Steel, University of Siegen, 2008.
[40] U. Krupp, O. Düber, H.J. Christ, B. Künkler, A. Schick, C.P. Fritzen, Application of the EBSD technique to describe the initiation and growth behaviour of microstructurally short fatigue cracks in a duplex steel, J Microsc 213, 2004, 313–320.
[41] U. Krupp, A. Giertler, M. Söker, H. Fu, B. Dönges, H.J. Christ, A. Hüsecken, U. Pietsch, C.P. Fritzen, W. Ludwig, The behavior of short fatigue cracks during Very High Cycle (VHCF) Fatigue of duplex stainless steel, Eng. Fract. Mech. 145, 2015, 197–209.
[42] U. Krupp, I. Alvarez-Armas, Short fatigue crack propagation during low-cycle, high cycle and very-high-cycle fatigue of duplex steel – An unified approach, Int. J. Fatigue 65, 2014, 78–85.
[43] I. Roth, M. Kübbeler, U. Krupp, H.J. Christ, C.P. Fritzen, Crack initiation and short crack growth in metastable austenitic stainless steel in the high cycle fatigue regime, Procedia Eng. (Procedia Engineering) 2, 2010, 941–948.
[44] O. Duber, B. Kunkler, U. Krupp, H. Christ, C. Fritzen, Experimental characterization and two-dimensional simulation of short-crack propagation in an austenitic–ferritic duplex steel, Int. J. Fatigue 28, 2006, 983–992.

[45] G. Winkel, M. Fett, Untersuchung zum Korrosionsverhalten an mittels Laser-und Laser-MSG-hybridgeschweißter Verbindungen aus Duplexstahl 1.4462, in: O. Keßler (Ed.), Fortschritte in der Metallographie: Vortragstexte der 46. Metallographie-Tagung, 19. - 21. September 2012 in Rostock. Vortragstexte der 46. Metallographie-Tagung, DGM, Frankfurt, 2012.

[46] A.-M. El-Batahgy, A.-F. Khourshid, T. Sharef, Effect of Laser Beam Welding Parameters on Microstructure and Properties of Duplex Stainless Steel, MSA 02, 2011, 1443–1451.

[47] T. Omura, T. Kushida, Y. Komizo, Nitrogen distribution on rapid solidification in laser welded duplex stainless steels, Weld. Int. 14, 2000, 288–294.

[48] E. Réka Fábián, Laser Welding Parameters Effect on the Weld Metals Properties at Duplex Stainless Steels, Adv Tech Mat 43, 2018, 7–13.

[49] H.C. Wu, L.W. Tsay, C. Chen, Laser Beam Welding of 2205 Duplex Stainless Steel with Metal Powder Additions, ISIJ Int. 44, 2004, 1720–1726.

[50] ESAB, Hinweise zum Schweißen ferritisch-austenitischer Stähle (Duplex/Super-Duplex), http://www.esab-okhandbuch.de/files/chapter/Schweisshinweise-J.pdf, accessed 12 May 2021.

[51] DVS, Empfehlungen zum Schweißen von nicht rostenden austenitisch-ferritischen Duplex- und Superduplexstählen, Verlag für Schweißen und verwandte Verfahren DVS-Verlag GmbH, Düsseldorf, 2004, https://www.dvs-regelwerk.de/inhalt/172/0946, accessed 8 September 2021.

[52] F. Fomin, On the fatigue behaviour and modelling of fatigue life for laser-welded Ti-6Al-4V, TUHH Universitätsbibliothek, 2019.

[53] M. Bolut, C.Y. Kong, J. Blackburn, K.A. Cashell, P.R. Hobson, Yb-fibre Laser Welding of 6 mm Duplex Stainless Steel 2205, Phys Proc (Physics Procedia) 83, 2016, 417–425.

[54] Peter Merhof, senior welding expert, GEA AG, Keyhole welding of corrosion resistant steels for the food industry. Project meeting, 2020.

[55] J. Blackburn, Laser welding of metals for aerospace and other applications, in: Welding and Joining of Aerospace Materials, Elsevier, 2012, pp. 75–108.

[56] S. Krasnorutskyi, D. Keil, S. Schmigalla, M. Zinke, A. Heyn, H. Pries, Metallurgical Investigations on Electron Beam Welded Duplex Stainless Steels, Weld World 56, 2012, 34–40.

[57] W. Rath, CO_2 Laser - Workhorse for Industrial Manufacturing, Laser Technik Journal (Laser Tech. J.) 6, 2009, 32–38.

[58] R. Soltysiak, Tests of Fracture Toughness of Laser-Welded Joints Made of Duplex 2205 Steel, Solid State Phenom 250, 2016, 191–196.

[59] X. Xie, J. Li, W. Jiang, Z. Dong, S.-T. Tu, X. Zhai, X. Zhao, Nonhomogeneous microstructure formation and its role on tensile and fatigue performance of duplex stainless steel 2205 multi-pass weld joints, Mater Sci Eng A 786, 2020, 139426.

[60] C. Köse, R. Kaçar, Mechanical Properties of Laser Welded 2205 Duplex Stainless Steel*, MP 56, 2014, 779–785.

[61] J. Singh, A.S. Shahi, Metallurgical, impact and fatigue performance of electron beam welded duplex stainless steel joints, J. Mater. Process. Technol. 272, 2019, 137–148.
[62] R. Sołtysiak, Effect of Laser Welding Parameters of DUPLEX 2205 Steel Welds on Fatigue Life, SSP 223, 2014, 11–18.
[63] T. Björk, H. Mettänen, A. Ahola, M. Lindgren, J. Terva, Fatigue strength assessment of duplex and super-duplex stainless steels by 4R method, Weld. World 62, 2018, 1285–1300.
[64] ECRIMESA Group, The characteristics of additive manufacturing and how to use it in the fabrication of metal pieces, 2021, https://ecrimesagroup.com/the-characteristics-of-additive-manufacturing-and-how-to-use-it-in-the-fabrication-of-metal-pieces, accessed 11 March 2024.
[65] S.H. Kang, J. Suh, S.Y. Lim, S. Jung, Y.W. Jang, I.S. Jun, Additive manufacture of 3 inch nuclear safety class 1 valve by laser directed energy deposition, J. Nucl. Mater. 547, 2021, 152812.
[66] DVS, DVS-Technikreport 2018. Forschung und Technik im DVS Mit dem Thema „DVS - Ein Zuhause für die Kunststoffwelt“, 2018.
[67] M. Froend, V. Ventzke, F. Dorn, N. Kashaev, B. Klusemann, J. Enz, Microstructure by design: An approach of grain refinement and isotropy improvement in multi-layer wire-based laser metal deposition, Mater. Sci. Eng., A 772, 2020, 138635.
[68] B. Baufeld, E. Brandl, O. van der Biest, Wire based additive layer manufacturing, J. Mater. Process. Technol. 211, 2011, 1146–1158.
[69] E. Brandl, B. Baufeld, C. Leyens, R. Gault, Additive manufactured Ti-6Al-4V using welding wire: comparison of laser and arc beam deposition and evaluation with respect to aerospace material specifications, Physics Procedia 5, 2010, 595–606.
[70] J.W. Elmer, G. Gibbs, J.S. Carpenter, D.R. Coughlin, P.A.T. Hochnadel, J.A.Y. Vaja, P. Gurung, A. Johnson, M.J. Dvornak, Wire-Based Additive Manufacturing of Stainless Steel Components, Welding J. 99, 2020, 8s-24s.
[71] B.A. Szost, S. Terzi, F. Martina, D. Boisselier, A. Prytuliak, T. Pirling, M. Hofmann, D.J. Jarvis, A comparative study of additive manufacturing techniques, Mater. Des. 89, 2016, 559–567.
[72] V. Luna, L. Trujillo, A. Gamon, E. Arrieta, L.E. Murr, R.B. Wicker, C. Katsarelis, P.R. Gradl, F. Medina, Comprehensive and Comparative Heat Treatment of Additively Manufactured Inconel 625 Alloy and Corresponding Microstructures and Mechanical Properties, JMMP 6, 2022, 107.
[73] G. Casalino, M. Karamimoghadam, N. Contuzzi, Metal Wire Additive Manufacturing: A Comparison between Arc Laser and Laser/Arc Heat Sources, Inventions 8, 2023, 52.
[74] A. Kisielewicz, K. Thalavai Pandian, D. Sthen, P. Hagqvist, M.A. Valiente Bermejo, F. Sikström, A. Ancona, Hot-Wire Laser-Directed Energy Deposition: Process Characteristics and Benefits of Resistive Pre-Heating of the Feedstock Wire, Metals 11, 2021, 634.
[75] W. Carter, C. Masuo, A. Nycz, M. Noakes, D. Vaughan, Thermal process monitoring for wire-arc additive manufacturing using IR cameras, Solid Freeform Fabrication 2019: Proceedings of the 30th Annual International Solid Freeform Fabrication Symposium - An Additive Manufacturing Conference, SFF 2019, 2019.

[76] F. Chen, Y. Yang, H. Feng, Regional Control and Optimization of Heat Input during CMT by Wire Arc Additive Manufacturing: Modeling and Microstructure Effects, Mater. 14, 2021.
[77] A. Heralić, Monitoring and control of robotized laser metal-wire deposition, Chalmers University of Technology, 2012.
[78] P.-Y. Lin, F.-C. Shen, K.-T. Wu, S.-J. Hwang, H.-H. Lee, Process optimization for directed energy deposition of SS316L components, Int J Adv Manuf Technol 111, 2020, 1387–1400.
[79] L. Chechik, N.A. Boone, L.R. Stanger, P. Honniball, F. Freeman, G. Baxter, J.R. Willmott, I. Todd, Variation of texture anisotropy and hardness with build parameters and wall height in directed-energy-deposited 316L steel, Addit. Manuf. 38, 2021, 101806.
[80] C. Charles Murgau, A. Lundbäck, P. Åkerfeldt, R. Pederson, Temperature and Microstructure Evolution in Gas Tungsten Arc Welding Wire Feed Additive Manufacturing of Ti-6Al-4V, Mater. 12, 2019.
[81] M. Froend, V. Ventzke, N. Kashaev, B. Klusemann, J. Enz, Thermal analysis of wire-based direct energy deposition of Al-Mg using different laser irradiances, Addit. Manuf. 29, 2019, 100800.
[82] DIN, Unbefeuerte Druckbehälter: Zusätzliche Anforderungen an additiv gefertigte Druckgeräte und deren Bauteile, Beuth Verlag GmbH, Berlin, 2020.
[83] K. Babkin, E. Zemlyakov, S. Ivanov, A. Vildanov, I. Topalov, G. Turichin, Distortion prediction and compensation in direct laser deposition of large axisymmetric Ti-6Al-4V part, Procedia CIRP 94, 2020, 357–361.
[84] B. Abbes, T. Anedaf, F. Abbes, Y. Li, Direct energy deposition metamodeling using a meshless method, Eng. Comput. (Swansea Wales) ahead-of-print, 2020, 129.
[85] M.H. Farshidianfar, F. Khodabakhshi, A. Khajepour, A.P. Gerlich, Closed-loop control of microstructure and mechanical properties in additive manufacturing by directed energy deposition, Materials Science and Engineering: A 803, 2021, 140483.
[86] M.H. Farshidianfar, F. Khodabakhshi, A. Khajepour, A.P. Gerlich, Closed-loop control of microstructure and mechanical properties in additive manufacturing by directed energy deposition, Materials Science and Engineering: A, 2020, 140483.
[87] M.H. Farshidianfar, F. Khodabakhshi, A. Khajepour, A.P. Gerlich, Closed-loop deposition of martensitic stainless steel during laser additive manufacturing to control microstructure and mechanical properties, Optics and Lasers in Engineering 145, 2021, 106680.
[88] I. Calliari, E. Ramous, P. Bassani, Phase Transformation in Duplex Stainless Steels after Isothermal Treatments, Continuous Cooling and Cold Working, Mater. Sci. Forum 638-642, 2010, 2986–2991.
[89] R. Kaçar, Effect of solidification mode and morphology of microstructure on the hydrogen content of duplex stainless steel weld metal, Mater. Des. 25, 2004, 1–9.
[90] Y. Ohmori, K. Nakai, H. Ohtsubo, Y. Isshiki, Mechanism of Widmanstaetten Austenite Formation in a δ / γ Duplex Phase Stainless Steel, ISIJ International 35, 1995, 969–975.

[91] J. Verma, R.V. Taiwade, Effect of welding processes and conditions on the microstructure, mechanical properties and corrosion resistance of duplex stainless steel weldments—A review, J. Manuf. Proc. (Journal of Manufacturing Processes) 25, 2017, 134–152.
[92] A. Baghdadchi, V.A. Hosseini, M.A. Valiente Bermejo, B. Axelsson, E. Harati, M. Högström, L. Karlsson, Wire laser metal deposition of 22% Cr duplex stainless steel: as-deposited and heat-treated microstructure and mechanical properties, J Mater Sci.
[93] A. Baghdadchi, V.A. Hosseini, M.A. Valiente Bermejo, B. Axelsson, E. Harati, M. Högström, L. Karlsson, Wire Laser Metal Deposition Additive Manufacturing of Duplex Stainless Steel Components-Development of a Systematic Methodology, Materials (Basel, Switzerland) 14, 2021.
[94] A.D. Iams, J.S. Keist, T.A. Palmer, Formation of Austenite in Additively Manufactured and Post-Processed Duplex Stainless Steel Alloys, Metall. Mater. Trans. A 51, 2020, 982–999.
[95] G. Posch, K. Chladil, H. Chladil, Material properties of CMT—metal additive manufactured duplex stainless steel blade-like geometries, Weld. World 61, 2017, 873–882.
[96] M.A. Valiente Bermejo, K. Thalavai Pandian, B. Axelsson, E. Harati, A. Kisielewicz, L. Karlsson, Microstructure of laser metal deposited duplex stainless steel: Influence of shielding gas and heat treatment, Weld. World 65, 2021, 525–541.
[97] A. Sales, A. Khanna, J. Hughes, L. Yin, A. Kotousov, Fatigue Crack Growth Rates and Crack Tip Opening Loads in CT Specimens Made of SDSS and Manufactured Using WAAM, Mater. 17, 2024.
[98] Odermatt, A., Passing, M., Jepsen, J., Klassen, T., Huber, N., Kashaev, N., Wasserstoffkorrosion mittels L-DED-wire gefertigter Duplexstähle, virtual, 2021 - 2021.
[99] C. Örnek, P. Reccagni, U. Kivisäkk, E. Bettini, D.L. Engelberg, J. Pan, Hydrogen embrittlement of super duplex stainless steel – Towards understanding the effects of microstructure and strain, Int. J. Hydrogen Energy 43, 2018, 12543–12555.
[100] P. Koruba, P. Radkiewicz, J. Kędzia, R. Dziedzic, P. Smuga, J. Reiner, Coaxial Laser Wire Deposition of AISI 316L steel - research on influence of processing parameters, Weld. Tech. Rev. 95, 2023, 67–77.
[101] J. Li, H.N. Li, Z. Liao, D. Axinte, Analytical modelling of full single-track profile in wire-fed laser cladding, J. Mater. Process. Technol. 290, 2021, 116978.
[102] F.E. Bock, J. Herrnring, M. Froend, J. Enz, N. Kashaev, B. Klusemann, Experimental and numerical thermo-mechanical analysis of wire-based laser metal deposition of Al-Mg alloys, Journal of Manufacturing Processes 64, 2021, 982–995.
[103] Y. Cai, J. Xiong, H. Chen, G. Zhang, A review of in-situ monitoring and process control system in metal-based laser additive manufacturing, J. Manuf. Syst. 70, 2023, 309–326.
[104] S. Baraldo, A. Vandone, A. Valente, E. Carpanzano, Vision-based control for track geometry optimization of complex AM motion profiles by on-line laser power modulation, Procedia CIRP 95, 2020, 78–82.

[105] Y. Su, Z. Wang, X. Xu, K. Luo, J. Lu, Effect of closed-loop controlled melt pool width on microstructure and tensile property for Fe-Ni-Cr alloy in directed energy deposition, Journal of Manufacturing Processes 82, 2022, 708–721.
[106] L. Peng, J. Shengqin, Z. Xiaoyan, H. Qianwu, X. Weihao, Direct laser fabrication of thin-walled metal parts under open-loop control, International Journal of Machine Tools and Manufacture 47, 2007, 996–1002.
[107] L. Tang, R.G. Landers, Melt Pool Temperature Control for Laser Metal Deposition Processes—Part I: Online Temperature Control, J. Manuf. Sci. Eng. 132, 2010.
[108] Y. Ding, J. Warton, R. Kovacevic, Development of sensing and control system for robotized laser-based direct metal addition system, Additive Manufacturing 10, 2016, 24–35.
[109] T. Shi, B. Lu, T. Shen, R. Zhang, S. Shi, G. Fu, Closed-loop control of variable width deposition in laser metal deposition, Int J Adv Manuf Technol 97, 2018, 4167–4178.
[110] S. Liao, J. Jeong, R. Zha, T. Xue, J. Cao, Simulation-guided feedforward-feedback control of melt pool temperature in directed energy deposition, CIRP Ann.
[111] P. Xu, X. Yao, L. Chen, C. Zhao, K. Liu, S.K. Moon, G. Bi, In-process adaptive dimension correction strategy for laser aided additive manufacturing using laser line scanning, Journal of Materials Processing Technology 303, 2022, 117544.
[112] S. Liao, S. Webster, D. Huang, R. Council, K. Ehmann, J. Cao, Simulation-guided variable laser power design for melt pool depth control in directed energy deposition, Addit Manuf 56, 2022, 102912.
[113] J.T. Hofman, B. Pathiraj, J. van Dijk, D.F.d. Lange, J. Meijer, A camera based feedback control strategy for the laser cladding process, J. Mater. Process. Technol. 212, 2012, 2455–2462.
[114] M. Miyagi, T. Tsukamoto, H. Kawanaka, Adaptive shape control of laser-deposited metal structures by adjusting weld pool size, Journal of Laser Applications 26, 2014.
[115] M.H. Farshidianfar, A. Khajepour, A. Gerlich, Real-time control of microstructure in laser additive manufacturing, Int J Adv Manuf Technol 82, 2016, 1173–1186.
[116] Y. Su, C. Wang, X. Xu, K. Luo, J. Lu, Pore defects and corrosion behavior of AISI 316L stainless steel fabricated by laser directed energy deposition under closed-loop control, Surf Coat Tech 463, 2023, 129527.
[117] D. Tyralla, H. Köhler, T. Seefeld, C. Thomy, R. Narita, A multi-parameter control of track geometry and melt pool size for laser metal deposition, Procedia CIRP 94, 2020, 430–435.
[118] B.T. Gibson, B.S. Richardson, T.W. Sundermann, L.J. Love, Beyond the Toolpath: Site-Specific Melt Pool Size Control Enables Printing of Extra-Toolpath Geometry in Laser Wire-Based Directed Energy Deposition, Appl Sci-Basel 9, 2019, 4355.
[119] B.T. Gibson, Y.K. Bandari, B.S. Richardson, W.C. Henry, E.J. Vetland, T.W. Sundermann, L.J. Love, Melt pool size control through multiple closed-loop modalities in laser-wire directed energy deposition of Ti-6Al-4V, Addit. Manuf. 32, 2020.
[120] D. Tyralla, T. Seefeld, Temperature field based closed-loop control of laser hot wire cladding for low dilution, Procedia CIRP 94, 2020, 451–455.

[121] S. Takushima, N. Shinohara, D. Morita, H. Kawano, Y. Mizutani, Y. Takaya, In-Process Height Displacement Measurement Using Crossed Line Beams for Process Control of Laser Wire Deposition, IJAT 15, 2021, 715–727.
[122] I. Garmendia, J. Pujana, A. Lamikiz, J. Flores, M. Madarieta, Development of an Intra-Layer Adaptive Toolpath Generation Control Procedure in the Laser Metal Wire Deposition Process, Materials (Basel, Switzerland) 12, 2019.
[123] A. Heralić, A.-K. Christiansson, M. Ottosson, B. Lennartson, Increased stability in laser metal wire deposition through feedback from optical measurements, Opt. Lasers Eng. 48, 2010, 478–485.
[124] P. Hagqvist, A. Heralić, A.-K. Christiansson, B. Lennartson, Resistance measurements for control of laser metal wire deposition, Opt. Lasers Eng. 54, 2014, 62–67.
[125] P. Hagqvist, A. Heralić, A.-K. Christiansson, B. Lennartson, Resistance based iterative learning control of additive manufacturing with wire, Mechatronics 31, 2015, 116–123.
[126] E.W. Teichmann, J. Kelbassa, A. Gasser, S. Tarner, J.H. Schleifenbaum, Effect of wire feeder force control on laser metal deposition process using coaxial laser head, Journal of Laser Applications 33, 2021, 12041.
[127] M.F. Steiner, P.H. Lohrer, T. Schopphoven, C.L. Häfner, Setup for electrical resistance measurement for laser material deposition with coaxial wire feed and use for process control, Journal of Laser Applications 35, 2023, 12002.
[128] A. Heralić, A.-K. Christiansson, B. Lennartson, Height control of laser metal-wire deposition based on iterative learning control and 3D scanning, Opt. Lasers Eng. 50, 2012, 1230–1241.
[129] DIN EN 10088-2:2014-12, Nichtrostende Stähle_- Teil_2: Technische Lieferbedingungen für Blech und Band aus korrosionsbeständigen Stählen für allgemeine Verwendung; Deutsche Fassung EN_10088-2:2014, Beuth Verlag GmbH, Berlin.
[130] voestalpine Böhler welding Group GmbH, 3Dprint AM 2209: WAAM solid wire, duplex stainless steel. Material data sheet.
[131] Fraunhofer-Institut für Werkstoff- und Strahltechnik IWS, Laser-Bearbeitungsoptik COAXwire: Beschichten, Reparieren und Generieren mit Massiv- und Fülldraht, https://www.iws.fraunhofer.de/content/dam/iws/de/documents/publikationen/infobla etter/700-2_COAXwire_de.pdf, accessed 26 November 2020.
[132] X. Lu, X. Lin, M. Chiumenti, M. Cervera, Y. Hu, X. Ji, L. Ma, H. Yang, W. Huang, Residual stress and distortion of rectangular and S-shaped Ti-6Al-4V parts by Directed Energy Deposition, Addit. Manuf. 26, 2019, 166–179.
[133] Sebastian Frederik Roth, Thermomechanische FEM-Simulation des laseradditiven Fertigungsprozesses mit Duplexstahldraht. Masterarbeit, Technische Universität Hamburg harburg, 2021.
[134] D. Weisz-Patrault, Residual strains in directed energy deposition additive manufacturing, in: INTERNATIONAL CONFERENCE OF NUMERICAL ANALYSIS AND APPLIED MATHEMATICS ICNAAM 2019, AIP Publishing, 2020, p. 20007.

[135] maxon Switzerland ag, Produktprogramm 2023/2024, 2023, https://online.flippingbook.com/view/623537/.
[136] DIN EN ISO 17781:2017-11, Erdöl-, petrochemische und Erdgasindustrie - Prüfverfahren für die Qualitätslenkung von Mikrostrukturen von ferritisch/austenitisch nichtrostenden Duplexstählen (ISO 17781:2017); Englische Fassung EN ISO 17781:2017.
[137] N. Otsu, A Threshold Selection Method from Gray-Level Histograms, IEEE Trans. Syst., Man, Cybern. 9, 1979, 62–66.
[138] P. Paufler, R. A. Young (ed.). The Rietveld Method. International Union of Crystallography. Oxford University Press 1993. 298 p. Price £ 45.00. ISBN 0–19–855577–6, Cryst. Res. Technol. 30, 1995, 494.
[139] Gleb Dovzhenko, P61AToolkit, Helmholtz-Zentrum hereon GmbH.
[140] DIN SPEC 4864:2019-11, Prüfverfahren zur Ermittlung von Fließkurven und Vergleichskennwerten zum Zugversuch mittels zerstörungsarmem Prüfeindruck, 3D-Vermessung und Finite-Elemente Werkstoffmodell, Beuth Verlag GmbH, Berlin.
[141] DIN EN ISO 6892-2:2018-09, Metallische Werkstoffe - Zugversuch - Teil 2: Prüfverfahren bei erhöhter Temperatur (ISO 6892-2:2018); Deutsche Fassung EN ISO 6892-2:2018, Beuth Verlag GmbH, Berlin.
[142] DIN EN ISO 17636-2:2013-05, Zerstörungsfreie Prüfung von Schweißverbindungen - Durchstrahlungsprüfung - Teil 2: Röntgen- und Gammastrahlungstechniken mit digitalen Detektoren (ISO 17636-2:2013); Deutsche Fassung EN ISO 17636-2:2013, Beuth Verlag GmbH, Berlin.
[143] H. Fu, On the origin of crack initiation in duplex stainless steel during cyclic loading in the VHCF regime. Dissertation, Siegen, Universität, 2017.
[144] U. Zerbst, M. Madia, M. Vormwald, H. Beier, Fatigue strength and fracture mechanics – A general perspective, Eng. Fract. Mech. 198, 2018, 2–23.
[145] U. Zerbst, M. Madia, M. Vormwald, Fatigue strength and fracture mechanics, Procedia Struct. Integrity 5, 2017, 745–752.
[146] J. Maierhofer, S. Kolitsch, R. Pippan, H.-P. Gänser, M. Madia, U. Zerbst, The cyclic R-curve – Determination, problems, limitations and application, Eng. Fract. Mech. 198, 2018, 45–64.
[147] U. Zerbst, M. Madia, Fracture mechanics based assessment of the fatigue strength, Fatigue & Fracture of Engineering Materials & Structures 38, 2015, 1066–1075.
[148] T.L. Anderson, Fracture Mechanics: Fundamentals and Applications, Third Edition, 3rd ed., CRC Press, Hoboken, 2005.
[149] Newman, J. C., Jr., I.S. Raju, Stress-intensity factor equations for cracks in three-dimensional finite bodies subjected to tension and bending loads, United States, 1984.
[150] J.C. Newman, A crack opening stress equation for fatigue crack growth, Int J Fract 24, 1984, R131-R135.
[151] Y. Murakami, Metal fatigue: Effects of small defects and nonmetallic inclusions, 1st ed., Elsevier, Amsterdam, 2002.

[152] P. Paris, F. Erdogan, A Critical Analysis of Crack Propagation Laws, Journal of Basic Engineering 85, 1963, 528–533.
[153] U. Zerbst, M. Madia, M. Vormwald, Applying fracture mechanics to fatigue strength determination – Some basic considerations, Int. J. Fatigue 126, 2019, 188–201.
[154] U. Zerbst, M. Vormwald, R. Pippan, H.-P. Gänser, C. Sarrazin-Baudoux, M. Madia, About the fatigue crack propagation threshold of metals as a design criterion – A review, Eng. Fract. Mech. 153, 2016, 190–243.
[155] R. Pippan, F.O. Riemelmoser, Modeling of Fatigue Crack Growth: Dislocation Models, in: Reference Module in Materials Science and Materials Engineering, 2016.
[156] J. Wasén, E. Heier, Fatigue crack growth thresholds—the influence of Young's modulus and fracture surface roughness, Int J Fatigue 20, 1998, 737–742.
[157] J. Pokluda, R. Pippan, T. Vojtek, A. Hohenwarter, Near-threshold behaviour of shear-mode fatigue cracks in metallic materials, Fatigue Fract Eng Mat Struct 37, 2014, 232–254.
[158] F. Fomin, M. Horstmann, N. Huber, N. Kashaev, Probabilistic fatigue-life assessment model for laser-welded Ti-6Al-4V butt joints in the high-cycle fatigue regime, Int. J. Fatigue 116, 2018, 22–35.
[159] C. Köse, C. Topal, Effect of heat input and post-weld heat treatment on surface, texture, microstructure, and mechanical properties of dissimilar laser beam welded AISI 2507 super duplex to AISI 904L super austenitic stainless steels, Journal of Manufacturing Processes 73, 2022, 861–894.
[160] R. Sołtysiak, T. Giętka, A. Sołtysiak, The effect of laser welding power on the properties of the joint made of 1.4462 duplex stainless steel, Adv. Mech. Eng. 10, 2018, 168781401775194.
[161] J. Pekkarinen, V. Kujanpää, The effects of laser welding parameters on the microstructure of ferritic and duplex stainless steels welds, Physics Procedia 5, 2010, 517–523.
[162] M.C. Young, S. Chan, L.W. Tsay, C.-S. Shin, Hydrogen-enhanced cracking of 2205 duplex stainless steel welds, Materials Chemistry and Physics 91, 2005, 21–27.
[163] C. Köse, Characterization of weld seam surface and corrosion behavior of laser-beam-welded AISI 2205 duplex stainless steel in simulated body fluid, J. Mater. Sci. 55, 2020, 17232–17254.
[164] V. Muthupandi, P. Bala Srinivasan, S.K. Seshadri, S. Sundaresan, Effect of weld metal chemistry and heat input on the structure and properties of duplex stainless steel welds, Materials Science and Engineering: A 358, 2003, 9–16.
[165] E. Haibach, Betriebsfestigkeit: Verfahren und Daten zur Bauteilberechnung, 3rd ed., Springer, Berlin, 2006.
[166] P. Du, W.A. Kibbe, S.M. Lin, Improved peak detection in mass spectrum by incorporating continuous wavelet transform-based pattern matching, Bioinformatics (Oxford, England) 22, 2006, 2059–2065.
[167] The SciPy community, scipy.signal, https://docs.scipy.org/doc/scipy/reference/signal.html, accessed 19 March 2024.

[168] T. DebRoy, H.L. Wei, J.S. Zuback, T. Mukherjee, J.W. Elmer, J.O. Milewski, A.M. Beese, A. Wilson-Heid, A. De, W. Zhang, Additive manufacturing of metallic components – Process, structure and properties, Prog. Mater Sci. 92, 2018, 112–224.

[169] C. Kledwig, H. Perfahl, M. Reisacher, F. Brückner, J. Bliedtner, C. Leyens, Analysis of Melt Pool Characteristics and Process Parameters Using a Coaxial Monitoring System during Directed Energy Deposition in Additive Manufacturing, Materials (Basel, Switzerland) 12, 2019.

[170] W.U.H. Syed, L. Li, Effects of wire feeding direction and location in multiple layer diode laser direct metal deposition, Appl. Surf. Sci. 248, 2005, 518–524.

[171] Y. Lee, Y. Bandari, P. Nandwana, B.T. Gibson, B. Richardson, S. Simunovic, Y. Lee, Y. Bandari, P. Nandwana, B.T. Gibson, B. Richardson, S. Simunovic, Effect of Interlayer Cooling Time, Constraint and Tool Path Strategy on Deformation of Large Components Made by Laser Metal Deposition with Wire, Appl. Sci. 9, 2019, 5115.

[172] J.P. Bergmann, P. Henckell, J. Reimann, A. Yarop, J. Hildebrandt, Grundlegende wissenschaftliche Konzepterstellung zu bestehenden Herausforderungen und Perspektiven für die Additive Fertigung mit Lichtbogen: Studie im Auftrag der Forschungsvereinigung Schweißen und verwandte Verfahren e.V. des DVS, DVS Media GmbH, Düsseldorf.

[173] T.H. Chen, J.R. Yang, Microstructural characterization of simulated heat affected zone in a nitrogen-containing 2205 duplex stainless steel, Mat Sci Eng a-Struct 338, 2002, 166–181.

[174] ASTM A240, Specification for Chromium and Chromium-Nickel Stainless Steel Plate, Sheet, and Strip for Pressure Vessels and for General Applications, ASTM International, West Conshohocken, PA.

[175] S. van der Walt, J.L. Schönberger, J. Nunez-Iglesias, F. Boulogne, J.D. Warner, N. Yager, E. Gouillart, T. Yu, scikit-image: image processing in Python, PeerJ 2, 2014, e453.

[176] J. Schijve, Fatigue of Structures and Materials, 2009.

[177] F. Fomin, N. Kashaev, Probabilistic Reliability Assessment of a Component in the Presence of Internal Defects, Springer International Publishing, Cham, 2020.

[178] N. Kashaev, A. Odermatt, L. Vázquez, P. Álvarez, Fatigue life assessment of WAAM-processed Ti-6Al-4V, Procedia Structural Integrity 54, 2024, 361–368.

[179] U. Zerbst, M. Schödel, H. Beier, Parameters affecting the damage tolerance behaviour of railway axles, Eng Fract Mech 78, 2011, 793–809.

[180] U. Zerbst, G. Bruno, J.-Y. Buffière, T. Wegener, T. Niendorf, T. Wu, X. Zhang, N. Kashaev, G. Meneghetti, N. Hrabe, M. Madia, T. Werner, K. Hilgenberg, M. Koukolíková, R. Procházka, J. Džugan, B. Möller, S. Beretta, A. Evans, R. Wagener, K. Schnabel, Damage tolerant design of additively manufactured metallic components subjected to cyclic loading: State of the art and challenges, Prog. Mater Sci., 2021, 100786.

[181] K.J. Miller, THE TWO THRESHOLDS OF FATIGUE BEHAVIOUR, Fatigue Fract Eng Mat Struct 16, 1993, 931–939.

[182] DIN 50100:2016-12, Schwingfestigkeitsversuch - Durchführung und Auswertung von zyklischen Versuchen mit konstanter Lastamplitude für metallische Werkstoffproben und Bauteile, Beuth Verlag GmbH, Berlin.
[183] DIN EN ISO 15156-3:2015-12, Erdöl- und Erdgasindustrie - Werkstoffe für den Einsatz in schwefelwasserstoffhaltiger Umgebung bei der Öl- und Gasgewinnung - Teil 3: Hochlegierte Stähle (CRAs) und andere Legierungen; Deutsche Fassung EN ISO 15156-3:2015, Beuth Verlag GmbH, Berlin.
[184] B. Ahmad, van der Veen, Sjoerd O., M.E. Fitzpatrick, H. Guo, Measurement and modelling of residual stress in wire-feed additively manufactured titanium, Mater. Sci. Technol. 34, 2018, 2250–2259.
[185] Q. Wu, T. Mukherjee, C. Liu, J. Lu, T. DebRoy, Residual stresses and distortion in the patterned printing of titanium and nickel alloys, Addit Manuf 29, 2019, 100808.